

The Classification of Blazars

Dissertation
zur Erlangung des Doktorgrades
des Fachbereichs Physik
der Universität Hamburg

vorgelegt von
Hermine Landt
aus Rimnik, Rumänien

Hamburg
2003

Gutachterin/Gutachter der Dissertation:	Prof. Dr. Dieter Reimers Prof. Dr. C. Megan Urry
Gutachterin/Gutachter der Disputation:	Prof. Dr. Dieter Reimers Prof. Dr. Sjur Refsdal
Datum der Disputation:	30.1.2003
Vorsitzende/Vorsitzender des Prüfungsausschusses:	Dr. habil. Franz-Josef Zickgraf
Vorsitzende/Vorsitzender des Promotionsausschusses:	Prof. Dr. Günter Huber
Dekanin/Dekan des Fachbereichs Physik:	Prof. Dr. Friedrich-Wilhelm Büßer

Abstract

Blazars are believed to be radio galaxies with their jets oriented at relatively small angles with respect to our line of sight. However, their separation from radio galaxies as well as their division into their subclasses, BL Lacertae objects (BL Lacs) and flat-spectrum radio quasars (FSRQ), is currently not based on strong physical arguments. This thesis searches for the most suitable physical classification scheme for blazars, and, in this respect, represents a physical revision of the current classification scheme proposed by Marchã and collaborators.

In the first part of this thesis I investigate the physical meaning of the dilution of the Ca H&K break in radio-loud active galactic nuclei (AGN), since the value of this stellar absorption feature is currently used to separate radio galaxies and blazars. For this purpose I use ~ 90 BL Lacs and radio galaxies from the Deep X-ray Radio Blazar Survey (DXRBS), the survey at the basis of this thesis, and also from other radio and X-ray surveys available in the literature. The main result of these studies is that the Ca H&K break value of radio-loud AGN is a suitable statistical indicator of orientation. This finding means that average viewing angles for samples of radio-loud AGN can be determined from such a simple (and common) observation as their optical spectra. My studies show that the transition in Ca H&K break value between blazars and radio galaxies is continuous. However, I infer that a Ca H&K break value of $C \sim 0.35$ is suitable to separate core- and lobe-dominated radio-loud AGN. This value is similar to that of $C = 0.4$ proposed by Marchã et al. to separate blazars and radio galaxies.

In the second part of this thesis I investigate if a bimodal distribution is present for the emission lines of radio-loud AGN, since emission line strength is currently the criterion used to distinguish between BL Lacs and FSRQ. In particular, I consider the narrow emission lines [O II] $\lambda 3727$ and [O III] $\lambda 5007$ to search for a bimodality inherent to the entire class of radio-loud AGN. Only the narrow emission lines of radio-loud AGN are believed to be radiated isotropically and so are common to both blazars and radio galaxies. For this purpose I use ~ 100 radio-loud AGN from two radio-flux limited samples, DXRBS and 2 Jy survey.

My studies yield a bimodal distribution for the [O III] emission line. Based on this I separate my sample into radio-loud AGN with *intrinsically* weak and strong [O III] emission lines (referred to as weak- and strong-lined radio-loud AGN respectively) and investigate if further differences exist between the two. In particular, I compare their narrow and broad emission line region luminosities, their distribution in the emission line luminosity – jet power planes, and their state of ionization. These studies give three main results: 1. weak-lined radio-loud AGN have *considerably* less luminous narrow (a factor of ~ 300) and broad (a factor of ~ 70) emission line regions than strong-lined radio-loud AGN; 2. weak-lined sources do not form simply an extension of strong-lined radio-loud AGN to both lower line luminosities *and* jet powers; and 3. the dominant excitation mechanisms for the narrow emission lines of weak- and strong-lined radio-loud AGN might be different, namely (jet-induced) shocks and photoionization respectively.

A consistent scenario emerges from my studies: strong-lined radio-loud AGN have powerful accretion disks which produce luminous narrow and broad emission lines via photoionization. On the other hand, weak-lined radio-loud AGN have accretion disks with only very low ionizing powers (possibly advection-dominated accretion flows [ADAFs]), which, however, can support powerful radio jets. This then favors (jet-induced) shocks as the dominant excitation mechanism for their narrow emission lines.

Zusammenfassung

Wir nehmen an, daß Blazare Radiogalaxien sind, deren Jets unter einem geringen Winkel betrachtet werden. Allerdings sind ihre derzeitige Trennung von Radiogalaxien und ihre Einteilung in die zwei Unterklassen, BL Lacertae Objekte (BL Lacs) und flach-spektrum Radioquasare (FSRQ), nicht streng physikalisch begründet. Die Aufgabe dieser Dissertation ist es, nach dem geeignetesten physikalischen Klassifikationsschema für Blazare zu suchen. Somit repräsentiert diese Arbeit eine physikalische Revision des gegenwärtigen Klassifikationsschemas, das von Marchã et al. vorgeschlagen wurde.

Im ersten Teil dieser Arbeit untersuche ich die Verringerung des Ca H&K Bruchs in radiolauten aktiven Galaxienkernen (AGN), da die derzeitige Trennung von Radiogalaxien und Blazaren auf den Wert dieses stellaren Absorptionsmerkmals gründet. Für diese Arbeit verwende ich ~ 90 BL Lacs und Radiogalaxien aus dem Deep X-ray Radio Blazar Survey (DXRBS), dem Survey, der die Grundlage dieser Dissertation bildet, und auch aus anderen öffentlich zugänglichen Radio- und Röntgensurveys. Das Hauptergebnis dieser Studien ist, daß sich der Wert des Ca H&K Bruchs radiolauter AGN als statistischer Orientierungsanzeiger eignet. Dies bedeutet, daß sich der mittlere Sichtwinkel einer Sammlung dieser Objekte aus einer solch einfachen (und üblichen) Beobachtungsgröße wie ihrem optischen Spektrum bestimmen läßt. Meine Untersuchungen zeigen, daß sich der Ca H&K Bruch beim Übergang von Radiogalaxien zu Blazaren kontinuierlich verringert. Ein Wert von $C \sim 0.35$ scheint jedoch dazu geeignet zu sein, Objekte mit kern- und lobe-dominierter Radiomorphologie zu trennen. Dieser Wert ist dem von $C = 0.4$ ähnlich, der von Marchã et al. zur Unterscheidung von Blazaren und Radiogalaxien vorgeschlagen wurde.

Im zweiten Teil dieser Arbeit untersuche ich, ob die Emissionslinien radiolauter AGN eine bimodale Verteilung besitzen, da die Emissionslinienstärke das derzeitige Kriterium ist, um BL Lacs von FSRQ zu unterscheiden. Insbesondere konzentriere ich mich auf die schmalen Emissionslinien [O II] $\lambda 3727$ und [O III] $\lambda 5007$, um nach einer Bimodalität zu suchen, die der gesamten Klasse von radiolauten AGN zugrundeliegt. Es wird angenommen, daß nur die schmalen Emissionslinien isotropisch ausgestrahlt werden, und somit sind nur diese den Blazaren und Radiogalaxien gemeinsam. Für diese Studien verwende ich ~ 100 radiolauter AGN selektiert aus zwei radiofluß-limitierten Surveys, DXRBS und 2 Jy Survey.

Ich finde eine Bimodalität für die Emissionslinie [O III]. Darauf unterteile ich die Objekte in radiolauter AGN mit *intrinsisch* schwachen und starken [O III] -Linien (genannt schwache- und starke-linien radiolauter AGN) und untersuche, ob zwischen diesen beiden Gruppen weitere Unterschiede bestehen. Insbesondere vergleiche ich ihre Narrow und Broad Line Region Leuchtkräfte, ihre Verteilung in den Linienleuchtkraft – Jetstärke Diagrammen, und ihren Ionisationsstatus. Ich erhalte drei Hauptergebnisse: 1. schwache-linien radiolauter AGN besitzen *enorm* schwächere Narrow (um einen Faktor ~ 300) und Broad (um einen Faktor ~ 70) Line Regions als starke-linien radiolauter AGN; 2. Objekte mit schwachen Linien repräsentieren keineswegs eine Fortsetzung der Objekte mit starken Linien zu geringeren Emissionslinien- und Jetleuchtkräften hin; und 3. die schmalen Emissionslinien der schwache- und starke-linien radiolauter AGN scheinen unterschiedlich angeregt zu sein, nämlich im ersten Fall durch (jet-ingeleitete) Schocks und im zweiten Fall durch Photoionisation.

Daraus ergibt sich folgendes plausible Gesamtbild: starke-linien radiolauter AGN besitzen leuchtkräftige Akkretionsscheiben, die ihre starken schmalen und breiten Emissionslinien durch Photoionisation produzieren. Die Akkretionsscheiben der schwache-linien radiolauter AGN aber besitzen nur eine sehr geringe Ionisationskraft (und sind somit wahrscheinlich advektionsdominierte Akkretionsflüsse [ADAF]), die jedoch gleichzeitig starke Radiojets unterhalten. Dies führt dann dazu, daß die schmalen Emissionslinien in diesen Objekten hauptsächlich durch (jet-ingeleitete) Schocks angeregt werden.

Anyone who has never made a mistake has never tried anything new.

Albert Einstein (1879 - 1955)

Contents

1	Introduction to Radio-Loud AGN	1
1.1	The General AGN Paradigm	2
1.2	Unified Schemes for Radio-Loud AGN	4
1.2.1	Relativistic Beaming	6
1.2.2	Radio Galaxies and Blazars	7
1.3	The Classification of Blazars	11
1.4	A Physical Revision of Blazar Classification	17
2	The Deep X-ray Radio Blazar Survey	21
2.1	Blazar Surveys	21
2.2	Candidate Selection	23
2.3	The Radio Spectral Index	26
2.4	Optical Identifications and Classifications	29
2.5	Sample Properties	31
2.5.1	Redshift Distributions	31
2.5.2	Radio and X-ray Luminosities	34
3	The Separation of BL Lacs and Radio Galaxies	37
3.1	The Optical BL Lac Continuum	38
3.2	From a BL Lac to a Radio Galaxy	41
3.2.1	The Radio Core and X-ray Luminosities	46
3.2.2	Intrinsic Luminosity Variations or Orientation Effects?	47
3.3	The Relation between Ca H&K Break and Viewing Angle	50
3.3.1	Luminosity Ratios and Viewing Angle	50
3.3.2	Ca H&K Break and Viewing Angle	53
3.4	Low- and High-Energy Peaked BL Lacs	53
3.4.1	Viewing Angles	54
3.4.2	Radio and X-ray Luminosity Differences	56
3.5	Discussion	58

4	A New Classification Scheme for Blazars	61
4.1	The Sample	62
4.2	Emission Line Measurements	66
4.3	The Limitations of the Current Classification Scheme	68
4.3.1	The Redshift Effect	69
4.3.2	The Ca H&K Break – Equivalent Width Plane	70
4.4	Weak- and Strong-Lined Radio-Loud AGN	74
4.4.1	The [O III] – [O II] Equivalent Width Plane	74
4.4.2	Emission Line Region Luminosities	83
4.4.3	Emission Line Regions and Jet Powers	85
4.4.4	The Ionization State	90
4.5	Discussion	94
4.5.1	The Bimodality of the [O III] Emission Line	94
4.5.2	The Nature of Weak- and Strong-Lined Radio-Loud AGN	96
4.5.3	A New Classification Scheme for Blazars	100
5	Conclusions and Prospects	103
	BIBLIOGRAPHY	107
A	Positional Information	123
B	Spectroscopic Observations	131
C	Classifications and Redshifts	135
D	Optical Spectra	145

Chapter 1

Introduction to Radio-Loud AGN

Vast numbers of galaxies are known today but only a small fraction ($\approx 1\%$) show phenomena which we refer to as activity, namely 1. a compact core brighter than the one of normal galaxies; 2. continuum radiation of the central core component extending from the radio to the X-ray, and in some cases γ -ray, band; 3. emission lines produced in the central regions by non-stellar processes; 4. highly variable continuum radiation and/or emission lines; and/or 5. non-thermal radio emission emanating from the center in the form of jets. Galaxies which show one or more of these properties are commonly referred to as Active Galactic Nuclei (AGN), a name emphasizing the fact that the activity is confined mainly to their central regions.

The study of AGN started out with the discovery of Seyfert galaxies (Seyfert, 1943) and quasars (Schmidt, 1963) and has grown since to become one of the largest fields of astronomy. Most important for this development was surely the fascinating notion that a super-massive black hole might lie at their center, and the discovery of strong non-thermal radio jets extending over incredibly large distances in some of these. However, a significant contribution to the growth of AGN research came also from the fact that their build-up is very complex and its study only possible in numerous specialised subfields. Moreover, AGN are amongst the strongest emitters at almost all wavelengths which makes them suitable candidates for most ground- and space-based telescopes.

1.1 The General AGN Paradigm

The prevailing picture of the physical structure of AGN is illustrated in Fig. 1.1 (adapted from the review of radio-loud AGN by Urry and Padovani (1995)). According to this, a super-massive ($M \sim 10^6 - 10^{10} M_\odot$, where M_\odot is the mass of the sun) black hole lies at the center, and its strong gravitational potential pulls the surrounding material inwards. Owing to the conservation of angular momentum the infalling material forms an accretion disk, which radiates through the conversion of potential to thermal energy. It is through the highly efficient matter-to-energy conversion of such an accretion flow that AGN can produce in tiny volumes ($\sim 10R_G = 5 \times 10^{-5}$ pc for a 10^8 solar mass black hole, where $R_G = GM/c^2$ is the gravitational radius of the black hole) extraordinary (up to 10^{47} erg s^{-1}) luminosities, which are much higher than can be achieved through ordinary, non-explosive stellar processes. The most common assumption about the state of the plasma within the accretion disk is that it is optically thick and thermal. This then implies that the released energy extends roughly from optical through soft X-ray frequencies with a substantial fraction emitted in the form of ultraviolet (UV) photons. (A blackbody emitting at a significant fraction of the Eddington luminosity on size scales associated with super-massive black holes has a temperature in the UV range.)

In addition to the central black hole and the accretion disk surrounding it, massive clouds of gas move rapidly in the potential well of the black hole at somewhat larger distances. These clouds are illuminated by the radiation of the accretion disk and produce, mainly via the processes of photoionization and collisional excitation, the strong emission lines characteristic of an AGN's spectrum (see Fig. 1.3, lower panel). Clouds closer to the black hole ($\sim 0.001 - 1$ pc) are denser and move more rapidly. These give rise to broad (\gtrsim a few 1000 km s^{-1}) emission lines in the object's spectrum, which are usually permitted transitions. The most prominent of these are the hydrogen lines from the Balmer and Lyman series and transitions of magnesium and carbon ions. These clouds are concertedly referred to as the broad-line region (BLR). Clouds located further out (up to a few kpc; e.g. Schmitt and Kinney, 1996; Bennert et al., 2002) have lower densities and velocities, and form the so-called narrow-line region (NLR). Narrow emission lines can be permitted and, owing to the relatively low electron densities ($n_e \sim 10^{10} m^{-3}$), also forbidden lines. The strongest of the latter type are transitions of ionized oxygen and neon.

Since we do not observe broad emission lines in all AGN, but almost always narrow emission lines, the existence of a thick, dusty torus (or warped disk) has been postulated. This feature is assumed to be located outside the accretion disk and to obscure the BLR at certain orientations of the AGN with respect to our

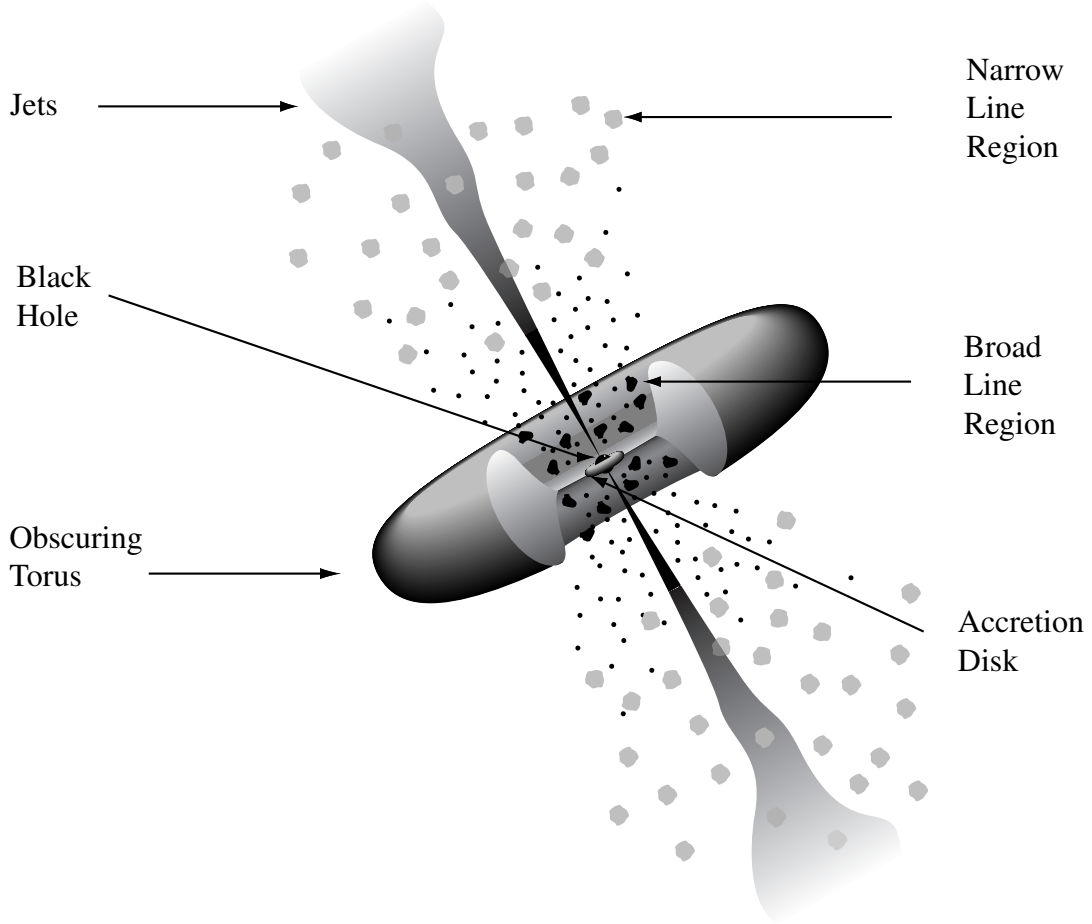


FIGURE 1.1. A schematic diagram of the current paradigm for AGN (not to scale; adapted from Urry and Padovani (1995)). Surrounding the central black hole is a luminous accretion disk. Broad and narrow emission lines are produced in clouds closer (dark blobs) and further away (grey blobs) from the central source respectively. A thick, dusty torus (or warped disk) obscures the broad-line region from transverse lines of sight. Powerful radio jets emanate from the region near the black hole in radio-loud AGN. For a $10^8 M_{\odot}$ black hole, the gravitational radius is $\sim 10^{-5}$ pc, the accretion disk emits mostly from $\sim 3 - 100 \times 10^{-5}$ pc, the broad-line clouds are located within $\sim 5 - 50 \times 10^{-3}$ pc of the black hole, and the inner radius of the dusty torus is perhaps ~ 0.1 pc. The narrow-line region extends approximately from 1 to a few times 10^3 pc, and radio jets have been detected on scales from 0.1 to several times 100 kpc. See text for more details.

line of sight. Strong evidence that such a torus indeed exists comes from direct observations of broad emission lines in the polarized scattered light of numerous narrow-line AGN (e.g. Antonucci and Miller, 1985; Cohen et al., 1999; Lumsden et al., 2001).

Additionally, we observe in radio-loud AGN (and sometimes also in radio-quiet AGN, although on much smaller scales) so-called ‘jets’. These are streams of plasma (most likely electrons and positrons or electrons and protons) that are collimated and accelerated by strong magnetic fields thus radiating via the synchrotron process. The jets emanate from locations close to the central black hole and feed extended lobes at very large distances (up to several 100 kpc) to each side of the central nucleus.

1.2 Unified Schemes for Radio-Loud AGN

The complex and non-spherically symmetric build-up of their central engine has led to the classification of AGN into many apparently different types. Within the class of radio-loud AGN, meaning objects with radio (5 GHz) to optical (B band) flux ratios above ten ($\sim 10\%$ of the entire population; Ivezić et al. (2002)), we currently differentiate between radio galaxies, quasars and BL Lacertae objects (BL Lacs).

Radio galaxies reach the largest linear dimensions at radio frequencies and their (optical) spectra show only narrow emission lines (if any at all). Therefore, these sources are believed to be oriented with their radio jets at relatively large angles with respect to our line of sight. Their BLR is then most likely obscured by the putative circumnuclear dusty torus. An exception to this appeared to be the Broad-Line Radio Galaxies (BLRG), classified as such based on their extended appearance on optical direct images. However, it is now largely accepted that these are simply low-luminosity quasars found preferably at low redshifts where the host galaxy can be easily discerned (e.g. Hardcastle et al., 1998; Dennett-Thorpe et al., 2000).

A landmark in the study of radio galaxies was the demonstration by Fanaroff and Riley (1974) of the existence of a relatively sharp morphological transition at a radio luminosity of $L_{178\text{MHz}} \sim 2 \times 10^{25} \text{ W Hz}^{-1}$. Based on their studies, we now differentiate between Fanaroff-Riley type I (FR I) and type II (FR II) radio galaxies with luminosities below and above this break respectively. Their typical radio morphologies are exemplified in Fig. 1.2. In the case of FR I radio galaxies (upper panel) we observe diffuse radio lobes with their brightest regions within the inner half of the radio source and so these sources are edge-dimmed. FR II radio galaxies (lower panel) are usually straighter, exhibit edge-brightened morphology, and typ-

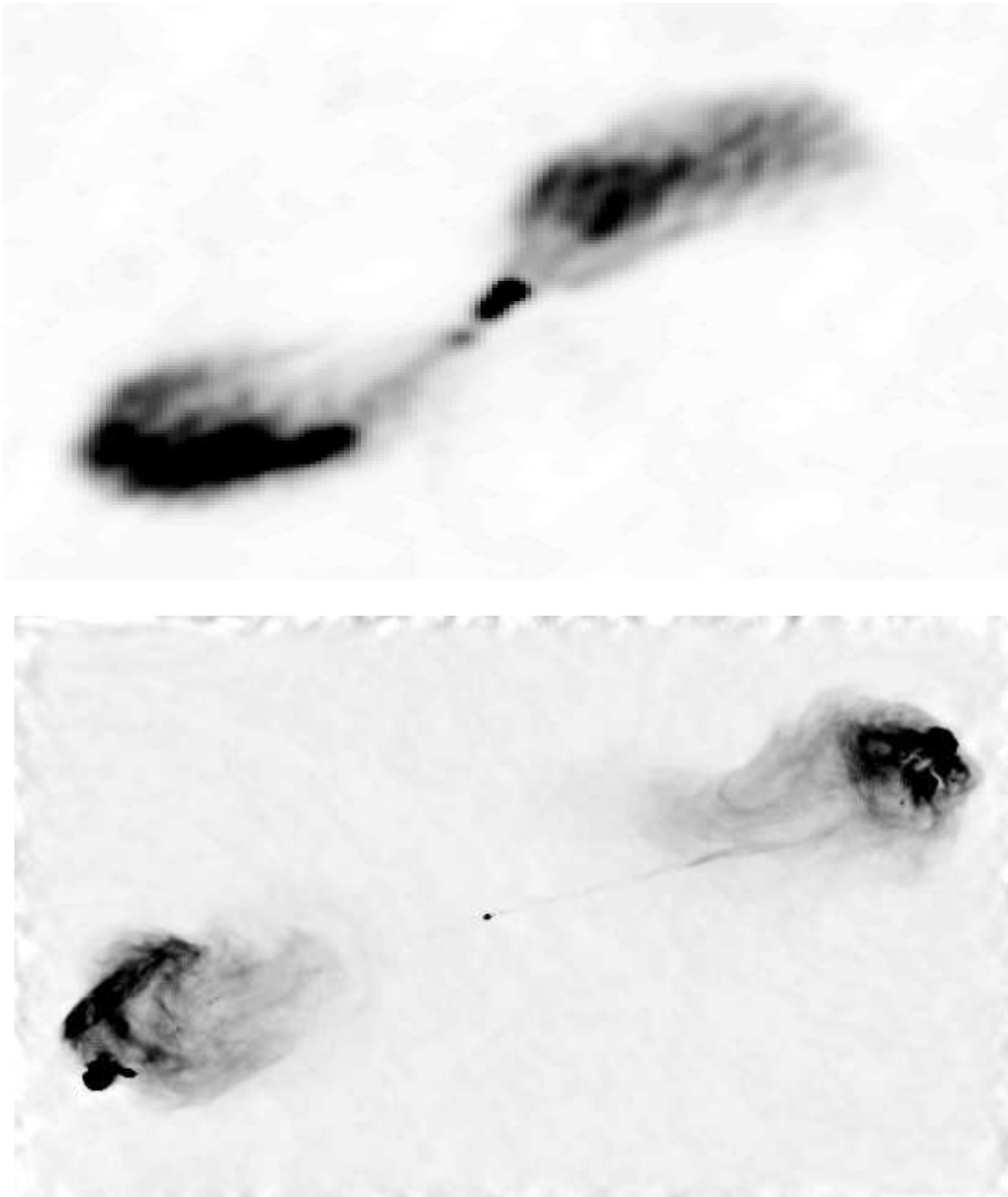


FIGURE 1.2. **Upper panel:** VLA radio image at 21 cm of the FR I radio galaxy Centaurus A (Condon et al., 1996). This galaxy lies at a distance of ~ 3 Mpc and has a linear size of 500×250 kpc. **Lower panel:** VLA radio image at 6 cm of the FR II radio galaxy Cygnus A (Perley et al., 1984). The east-west extent of the radio emission is $127''$ (corresponding to roughly 190 kpc for a Hubble constant of $H_0 = 50 \text{ km sec}^{-1} \text{ Mpc}^{-1}$).

ically contain ‘hot spots’ (i.e. small regions of extremely high surface brightness) near the outer edges of their radio lobes. Their jets are often too faint to see. It was later realized that the critical radio luminosity separating FR Is and FR IIs actually increases with the optical luminosity of the host elliptical galaxy (Owen and Ledlow, 1994).

The origin of the FR I/FR II dichotomy continues to be a much debated issue. Several authors have linked the morphological differences primarily to the transition of an initially supersonic (perhaps relativistic), but relatively weak, jet to a transonic/subsonic flow decelerated substantially through entrainment of the thermal plasma within the inner (~ 1 kpc) region of the host elliptical galaxy (e.g. De Young, 1993; Bicknell, 1995; Kaiser and Alexander, 1997). An alternative approach posits that FR Is and FR IIs differ primarily in the importance of the beam thrust relative to the basic parameters of the ambient medium (Gopal-Krishna and Wiita, 1988, 2001). In this version of the deceleration scenario, the emphasis is on the slowing of the advance of the hot spot, or working surface, at the end of the jet rather than on the slowing of the bulk flow within the jet. In contrast, others have argued in favor of more fundamental differences existing between the two classes, involving the nature of the central engine, such as black hole mass and spin, or the possibility of composition of jet plasma being different (e.g. Celotti and Fabian, 1993; Baum et al., 1995; Reynolds et al., 1996a; Meier, 1999; Ghisellini and Celotti, 2001).

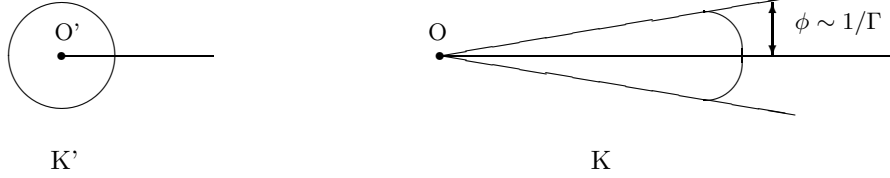
1.2.1 Relativistic Beaming

As first argued by Rees (1966) the plasma within the jets of radio-loud AGN moves at relativistic speed and so transports efficiently the energy from the vicinity of the super-massive black hole to the distant lobes. This, however, has strong implications for an observer who views the jet at relatively small angles as is believed to be the case in BL Lacs and quasars.

Let us assume that a source emits isotropically in its rest-frame K' . Then, in the observer’s frame K , where the sources moves at highly relativistic ($\beta = v/c \sim 1$) speed, three effects occur (adapted from Rybicki and Lightman (1979)):

1. *Light aberration:* The angular distribution of the radiation is highly peaked in the forward direction (see graph below). In particular, since for a particle in a magnetic field the velocity and acceleration are perpendicular (in K'), the emitted photons are observed in K to make an angle given by $\sin \phi = 1/\Gamma$, where $\Gamma = 1/\sqrt{1 - \beta^2}$ is the Lorentz factor of the accelerated particle. This

means that in K half of the photons are concentrated in a cone of semi-aperture angle of $\sim 1/\Gamma$ and are not radiated over the available solid angle of 2π .



2. *Arrival times of the photons:* The emission and arrival time intervals (Δt_e and Δt_a respectively) of photons are different. As measured in the observer's frame K we have $\Delta t_a = \Delta t_e(1 - \beta \cos \phi)$ (simply the Doppler effect). If $\Delta t'_e$ is measured in K' , $\Delta t_e = \Gamma \Delta t'_e$ leading to $\Delta t_a = \Gamma(1 - \beta \cos \phi) \Delta t'_e \equiv \Delta t'_e / \delta$, where δ is the Doppler factor.
3. *Blueshift of frequencies:* Since frequencies are the inverse of times, we just have $\nu = \delta \nu'$.

Owing to the first effect we observe the intensity of the jet to be dramatically enhanced if its velocity vector is closely aligned to our line of sight. This is referred to as 'beaming' or 'Doppler boosting'. In particular, since I_ν/ν^3 is a relativistic invariant, we get for its observed specific intensity $I_\nu(\nu) = \delta^3 I'_\nu(\nu')$ and integration over frequencies yields $I = \delta^4 I'$. Similarly, we have for the received flux, assuming the synchrotron emission spectrum which can be approximated by a power-law of the form $F'_\nu \propto (\nu')^{-\alpha}$, $F_\nu(\nu) = \delta^{p+\alpha} F'_\nu(\nu)$ with $p = 3$ and 2 in the case of a moving, isotropic source and a continuous jet respectively. More complicated cases are also possible (Lind and Blandford, 1985). The effect of beaming is maximized for viewing angles $\phi = 0^\circ$, in which case $\delta \simeq 2\Gamma$. (Relativistic deamplification takes place for angles larger than $\phi = \arccos \sqrt{(\Gamma - 1)/(\Gamma + 1)}$.) The second effect predicts the observation of apparent superluminal motion for objects with their jets oriented at very small viewing angles as first pointed out by Rees (1966).

1.2.2 Radio Galaxies and Blazars

BL Lacs and quasars are strong radio sources characterized by their distinct (optical) spectra. These are exemplified in Fig. 1.3. Whereas in BL Lacs we observe no or very weak emission lines and their continuum emission can often be fitted by a power-law, quasars exhibit both strong narrow and broad emission lines.

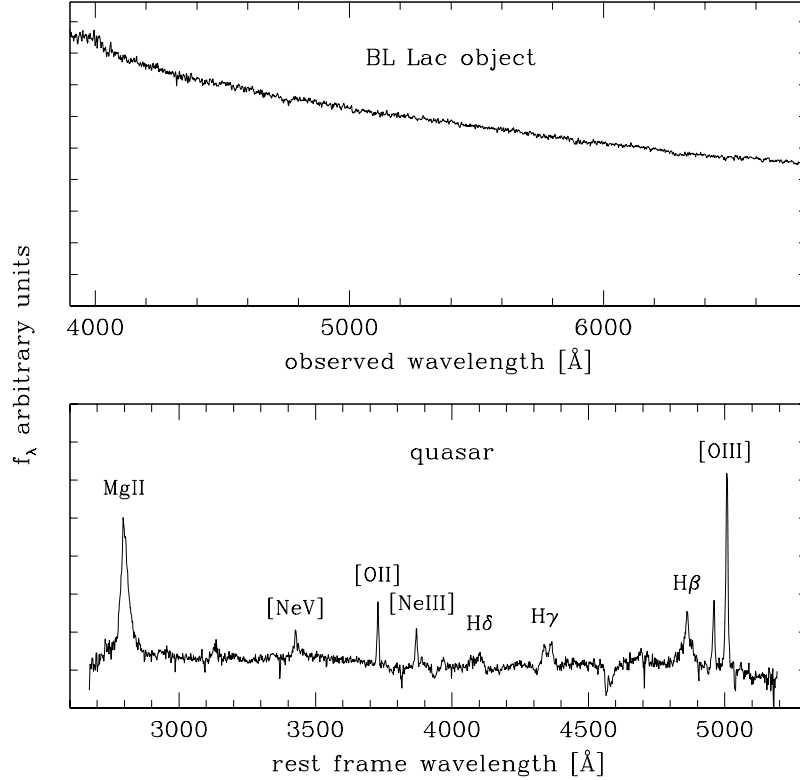


FIGURE 1.3. Blazar spectra. Upper and lower panel show, respectively, the BL Lac object WGAJ0449.4-4349 and the quasar WGAJ1306.6-2428 from the Deep X-ray Radio Blazar Survey (DXRBS). The featureless spectrum of BL Lacs makes a redshift determination often difficult, if not impossible. On the other hand, both strong narrow and broad emission lines are typically seen in quasar spectra.

BL Lacs and quasars are believed to be related to radio galaxies via orientation. In particular, BL Lacs are believed to be the beamed counterparts of FR I radio galaxies (Browne, 1989), whereas FR II radio galaxies are assumed to be viewed as quasars when their jets are pointed close to our line of sight (Barthel, 1989). This scenario is referred to as ‘unified schemes for radio-loud AGN’. Within the quasar class we further differentiate between steep- (SSRQ) and flat-spectrum radio quasars (FSRQ), defined as quasars with radio spectral indices $\alpha_r > 0.5$ (where $S_\nu \propto \nu^{-\alpha}$) and $\alpha_r \leq 0.5$ respectively. The different radio spectra are the signature of their distinct morphologies: SSRQ have weaker radio cores and show extended (steep-spectrum) radio lobes similar to the ones of radio galaxies (although on smaller

linear scales), whereas the emission of FSRQ is dominated by the (flat-spectrum) core component. Based on this FSRQ and SSRQ are believed to be FR II radio galaxies oriented at small and intermediate viewing angles respectively (Browne, 1989). (The former Optically Violently Variable (OVV) quasars, Highly Polarized Quasars (HPQ), and Core-Dominated Quasars (CDQ) are now often grouped under the FSRQ class.)

A subclass of BL Lacs similar to SSRQ, meaning BL Lacs oriented at intermediate angles, is currently not known (X-ray selected BL Lacs had been first considered as likely candidates but were later ruled out, see Section 1.3) and this thesis brings for the first time evidence for such a population (Chapter 3). In general, BL Lacs showed extreme properties more similar to the ones of FSRQ, which led to their common name of ‘blazars’. (The word ‘blazar’ was coined by Ed Spiegel in 1978 and combines BL (Lac) with (qu)asar. Its use in the literature, however, is most likely due to the review of optical polarisation in extragalactic objects by Angel and Stockman (1980).)

The unified schemes for radio-loud AGN in general, i.e. their unification based on orientation, and in particular the BL Lac/FR I and quasar/FR II associations can be tested in at least three ways. First, strongly beamed sources are expected to have multiwavelength properties dominated by a Doppler-boosted jet emission. This is what is observed: blazars (BL Lacs and FSRQ) have a core-dominated radio morphology; their continuum emission is mostly non-thermal and extends from radio to X-ray and in some case up to γ -ray frequencies; their emission is strongly ($> 3\%$) polarized at most wavelengths (a property related directly to the nature of synchrotron emission); and they exhibit rapid variability (on timescales down to hours). In addition, these sources often show apparent superluminal motion.

Second, the isotropic (i.e. orientation independent) properties of BL Lacs and quasars, such as extended radio emission, luminosity of narrow emission lines, luminosity and type of host galaxy, and environment have to be similar to those of their assumed parent populations. In this respect, radio-loud AGN are generally found to reside in luminous ellipticals (e.g. McLure et al., 1999; Urry et al., 2000) which supports the unification of blazars and radio galaxies in general but does not provide a test for the BL Lac/FR I and quasar/FR II associations in particular. Studies of the environmental properties of radio-loud AGN are somewhat inconclusive. Quasars and FR IIs are found to reside in clusters of similar richness (e.g. Wold et al., 2000). On the other hand, Wurtz et al. (1997) found for a relatively large (45 sources) sample of BL Lacs that their environments were more similar to those of quasars and FR IIs rather than of FR Is. However, it is not clear if the

environments of FR Is and FR IIs differ at all. Prestage and Peacock (1988) found for a sample of ~ 200 radio sources with redshifts $z < 0.25$ that FR I radio galaxies laid in richer clusters than FR II radio galaxies. But at higher redshifts ($z \simeq 0.5$) their environments were found to be similar (Hill and Lilly, 1991). And more recent studies albeit for much smaller samples of radio-loud AGN conclude that also at low redshifts ($z \simeq 0.2$) radio-loud AGN have similar cluster environments (McLure and Dunlop, 2001). In any case a common result of these studies is that the cluster properties of all types of radio-loud AGN span a large range.

As regards their extended radio emissions and narrow line luminosities, we observe a discrepancy. Quasars are found to have extended radio powers (and morphologies) typical of FR II radio galaxies (e.g. Murphy et al., 1993; Fernini et al., 1997). BL Lacs, however, can have extended radio powers typical of both FR Is and FR IIs (e.g. Kollgaard et al., 1992; Murphy et al., 1993; Cassaro et al., 1999; Rector and Stocke, 2001). As regards their narrow emission lines, these are relatively weak or absent in FR I radio galaxies as observed for BL Lacs (one of their defining criteria). On the other hand, quasars have (by definition) strong narrow emission lines, whereas these can be both weak and strong in FR II radio galaxies (e.g. Laing et al., 1994; Tadhunter et al., 1998). Therefore, our current view that BL Lacs are solely beamed FR I radio galaxies appears problematic. This is directly related to our current classification scheme for blazars and radio galaxies and I will expand on this issue in Section 1.4.

Finally, Urry and Shafer (1984) have developed a formalism that allows one to derive the luminosity functions and number counts of the beamed populations from those of the unbeamed ones. Urry and Padovani (1995) (but see also Padovani and Urry (1992)) have successfully applied this model to the observed radio luminosity functions of quasars (FSRQ and SSRQ) and FR II radio galaxies from the 2 Jy sample. A similar test of the BL Lac/FR I unification scheme is more subtle. BL Lacs not only are much rarer than quasars and, therefore, complete samples suffer from small number statistics, but their almost featureless spectra make a redshift determination often difficult if not impossible. Nevertheless, comparisons of luminosity functions of BL Lacs and FR I radio galaxies at radio, optical and X-ray frequencies showed (within the errors) good agreement with the beaming hypothesis (Padovani and Urry, 1990, 1991; Urry et al., 1991).

1.3 The Classification of Blazars

Radio galaxies are separated into FR Is and FR IIs based on their radio morphology (and so roughly on radio power). Blazars, on the other hand, are defined as strongly polarized and highly variable compact radio sources and are separated into BL Lacs and FSRQ based on the strengths of their emission lines. The reason that we have different classification schemes for beamed and unbeamed radio-loud AGN is twofold. First, a morphological classification of the extended lobe emission is difficult (if not impossible) if the jet is viewed at small angles. At such orientations not only is the core emission strongly enhanced by relativistic beaming and can then outshine the extended emission, but also projection effects become important. The second reason is historical and goes hand in hand with the discovery of BL Lacs.

The first member of this class to be discovered and which gave it its name was BL Lacertae (BL Lac). This was a compact and highly variable radio source that had been first identified with a star. However, its optical spectrum was rather unusual, it was featureless and the continuum emission was steeply rising to infrared wavelengths. Therefore, BL Lac continued to draw the attention of researchers, and it was not until OVV quasars were discovered and their multiwavelength properties, such as high polarization and rapid variability, recognized to be similar, that its spectrum could be explained as simply the signature of a Doppler-boosted jet emission (Blandford and Rees, 1978). After the discovery of BL Lac a handful (~ 30) of other similar objects were found, and Strittmatter et al. (1972) suggested that they formed a new class of extragalactic radio sources. (Since their featureless spectra made a redshift determination difficult, their extragalactic origin could be firmly established only when nebulosities often surrounding their bright nuclei were identified with elliptical galaxies.)

Nevertheless, although a beamed jet overlaying the host galaxy accounted for the lack of absorption lines and shape of the continuum of BL Lacs, it did not provide a convincing explanation for why strong emission lines typically seen in quasar spectra were missing. Blandford and Rees (1978) first proposed that BL Lacs were strongly beamed versions of quasars, which explained their low emission line equivalent widths, but later no further evidence could be found in support of this scenario. Therefore, finding such an explanation and so understanding the connection between BL Lacs and quasars became (and remains to this day) one of the most important issues considering the physics of radio-loud AGN.

For example, astrophysical jets appear to be ubiquitously associated with accretion processes, as are in general super-massive black holes. A lack of emission lines in BL Lacs, however, could mean a lack of emission line clouds or of an accretion disk

(or both). Both of these possibilities, if true, would have strong implications for our fundamental understanding of AGN. The emission line clouds most likely supply the material that is finally accreted, and the existence of accretion disks without such clouds could pose severe problems for accretion disk formation theories. If, however, no accretion disk existed, current jet formation models (e.g. Blandford and Znajek, 1977) would have to be revisited. In this respect, BL Lacs are considered an important link in our progress to understand what triggers the formation of powerful jets in some AGN, a mechanism only poorly understood and directly related to the present radio-loud/radio-quiet dichotomy. In the light of these considerations it is then not surprising that establishing a classification scheme for blazars consistent with that for radio galaxies was less important.

Originally, Strittmatter et al. (1972) defined BL Lacs as strongly variable and highly polarized compact radio sources with completely featureless spectra, i.e. neither absorption nor emission lines. However, many BL Lacs turned out to have temporarily weak emission lines (e.g. Ulrich, 1981; Sitko and Junkkarinen, 1985; Corbett et al., 1996), especially when in a faint state, and this started to blur their distinction from quasars. Therefore, the first surveys to produce complete and sizeable samples of BL Lacs, the 1 Jy radio survey and the *EINSTEIN* Medium Sensitivity Survey (EMSS) at X-ray frequencies, introduced a well-defined limit on their emission line strength.

The 1 Jy radio survey defined its BL Lacs as flat-spectrum ($\alpha_r \leq 0.5$) radio sources with emission lines with rest-frame equivalent widths $W_\lambda < 5 \text{ \AA}$. The flat radio spectrum ensured that the objects were relatively core-dominated and therefore beamed. The other two blazar properties, strong polarization and rapid variability, were not included as classification requirements. Nevertheless, optical polarization studies, available at the time, gave values above 3% for almost all objects (Kühr and Schmidt, 1990), and their strong and irregular variability was quantified later by Heidt and Wagner (1996). The 1 Jy radio survey covered almost the entire sky down to a flux limit of 1 Jy at 5 GHz and yielded 34 BL Lacs with magnitude ≤ 20 (Stickel et al., 1991; Rector and Stocke, 2001).

The EMSS X-ray survey, on the other hand, did not use any radio information to classify its objects as BL Lacs (allowing for the existence of radio-quiet X-ray emitting BL Lacs, which could not be found), and chose similarly to the 1 Jy survey an (in this case observer's frame) equivalent width value of 5 \AA to separate BL Lacs from emission-line AGN (Stocke et al., 1991). In order to ensure a substantial beaming and so to separate BL Lacs from radio galaxies in clusters which were unresolved X-ray sources and from normal galaxies, the EMSS required a Ca H&K break value

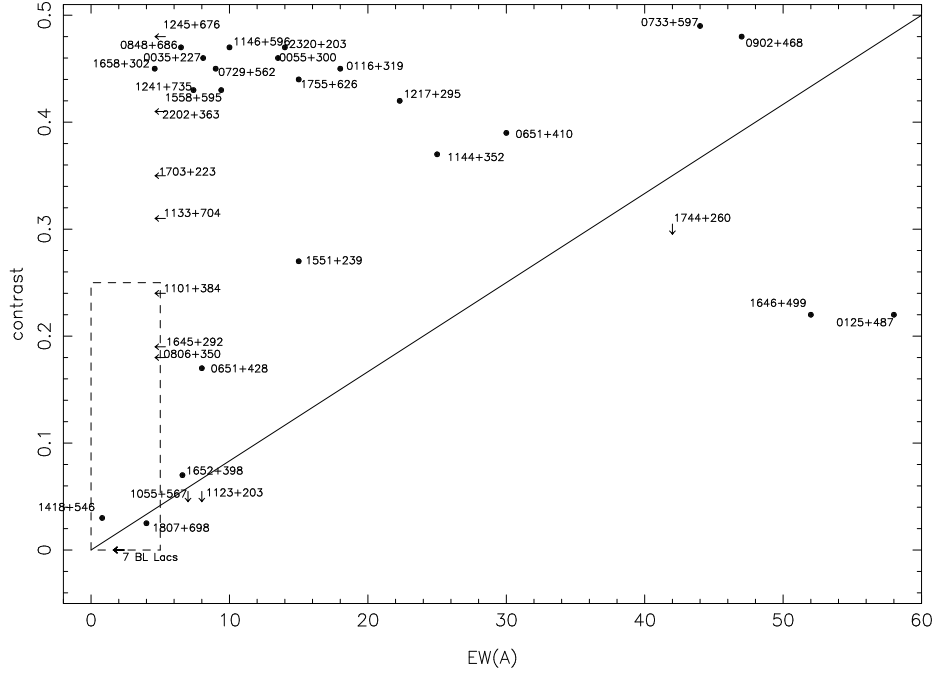


FIGURE 1.4. The Ca H&K break value versus the rest-frame equivalent width of the strongest observed emission line for radio-loud sources from the 200 mJy sample. Arrows indicate upper limits. The diagonal line represents the simulated increase of emission line strength with decreasing non-thermal jet emission for the BL Lac object 3C 371 and was suggested to separate BL Lacs (left of the line) from FSRQ (right of the line). The area enclosed by the dashed line corresponds to equivalent width values $W_\lambda \leq 5 \text{ \AA}$ and Ca H&K break values $C \leq 0.25$ proposed by Stocke et al. to classify BL Lacs (from Marchã et al. (1996)).

below 25%. This was based on the finding that this stellar absorption feature was on average $\sim 50\%$ in non-active elliptical galaxies (Dressler and Shectman, 1987). As regards polarization (Stocke et al., 1991; Jannuzi et al., 1994) and variability (Heidt and Wagner, 1998), EMSS BL Lacs were found to have somewhat lower values than the ones typical of 1 Jy BL Lacs. However, similarly to the 1 Jy survey, these properties were not included as classification criteria. The EMSS, being a sample of serendipitous X-ray sources from pointed observations, covered an area of ~ 700 square degrees with (0.3 – 3.5 keV) X-ray flux limits down to a few $10^{-13} \text{ erg cm}^{-2} \text{ s}^{-1}$ and yielded 44 BL Lacs (Stocke et al., 1991; Morris et al., 1991; Rector et al., 2000).

The classification scheme for BL Lacs introduced by the EMSS and 1 Jy survey was revised by Marchã et al. (1996). These authors used a low-redshift sample of flat-spectrum radio sources (with fluxes $f_r \geq 200$ mJy at 8.4 GHz and $V \leq 17$ mag) in order to investigate ‘natural’ differences between BL Lacs and other flat-spectrum radio sources unaffected by pre-imposed classification criteria. Based on their studies, they then argued that any source with Ca H&K break values $C \leq 40\%$ was likely to have an extra component of non-thermal emission and should be classified as a blazar. Additionally, they pointed out that the strength of emission lines in radio-loud AGN will depend strongly on the contribution from non-thermal jet emission, and, therefore, on the Ca H&K break value. They then simulated the increase in equivalent width with decreasing non-thermal continuum (i.e. increasing Ca H&K break value) for the strongest observed emission line ($H\alpha \lambda 6562$) of the classical BL Lac object 3C 371 and obtained a diagonal line in the Ca H&K break – equivalent width plane (Fig. 1.4). This diagonal line together with the line of constant $C = 40\%$ defined a triangular region in this plane, which, these authors argued, should be used to separate BL Lacs both from radio galaxies (objects with $C > 40\%$) and quasars (to the right of the diagonal line). BL Lacs selected according to these extended criteria were termed ‘BL Lac candidates’ in order to distinguish them from those fulfilling the classical criteria used by the EMSS and the 1 Jy survey.

The classification scheme of Marchã et al. is currently employed by most large blazar surveys, such as, e.g., Deep X-ray Radio Blazar Survey (DXRBS; Perlman et al. (1998); Landt et al. (2001)), which is the survey at the basis of this thesis, RGB (ROSAT All Sky Survey [RASS]-Green Bank) survey (Laurent-Muehleisen et al., 1998, 1999), REX (Radio-Emitting X-ray sources) survey (Caccianiga et al., 1999, 2000), and Sedentary Survey (Giommi et al., 1999)). Its revision is the main topic of this work.

Spectral Energy Distributions

The EMSS and 1 Jy survey, most likely owing to their widely different selection frequencies and relatively high flux limits, yielded BL Lacs with distinct broad-band spectral properties. BL Lacs selected at radio frequencies (RBL) had lower X-ray-to-radio flux ratios, were more core-dominated in the radio, had higher polarizations at radio and optical wavelengths, and varied more rapidly than X-ray selected BL Lacs (XBL; e.g. Urry and Padovani (1995) and references therein). In addition, RBL and XBL had different evolutionary properties. The cosmological evolution of samples with single and multiple flux limits is in general quantified using the

V/V_{\max} (Schmidt, 1968) and V_e/V_a methods (Avni and Bahcall, 1980) respectively, where V (V_e) and V_{\max} (V_a) are the enclosed and maximum available volumes. A mean value of $\langle V/V_{\max} \rangle = 0.5$ (or $\langle V_e/V_a \rangle = 0.5$) indicates no evolution, whereas significantly lower or higher mean values suggest a sample with negative (i.e. sources were less luminous and/or less numerous in the past) or positive evolution (i.e. sources were more luminous and/or more numerous in the past) respectively. In this respect, quasars show in general a strong positive evolution, and a weak positive evolution was found also for the 1 Jy BL Lacs ($\langle V/V_{\max} \rangle = 0.60 \pm 0.05$; Stickel et al. (1991)). EMSS BL Lacs, on the other hand, appeared to evolve negatively ($\langle V_e/V_a \rangle = 0.43 \pm 0.05$; Rector et al. (2000)), although both results were consistent with no evolution at the $\sim 2\sigma$ level.

Since the spectral energy distributions (SEDs) of BL Lacs are assumed to be dominated at almost all wavelengths by the enhanced jet emission, the presence of apparently two different BL Lac populations was an important finding relevant for our general understanding of the formation and acceleration of relativistic jets as well as the related beaming phenomenon. In this respect, it became crucial to explain the connection between RBL and XBL.

So far, two competing scenarios have been put forward. The first one proposed that RBL and XBL were viewed at smaller and larger angles respectively (Maraschi et al., 1986). This was based on the fact that their X-ray luminosities were similar, whereas their radio luminosities differed considerably. Then, in this scenario the X-ray emission was more isotropic than the radio one (due to either a smaller bulk Lorentz factor (Ghisellini and Maraschi, 1989) or a weaker collimation of the plasma producing the X-ray photons (Celotti et al., 1993)), and RBL having higher radio luminosities than XBL were simply more strongly beamed. The fact that RBL also had more extreme multiwavelength properties than XBL seemed to support this interpretation. In conclusion it was then argued that objects detected in X-ray surveys were more representative of the BL Lac population as a whole, and XBL predicted to outnumber RBL by a factor of ~ 10 (derived from the ratio of RBL to XBL at a given X-ray flux).

A very different scenario was proposed by Padovani and Giommi (1995). These authors argued that the primary difference between BL Lacs detected in radio and X-ray surveys was not orientation but rather the (intrinsic) shape of their SEDs. This was based on previous studies of multifrequency spectra of large samples of BL Lacs (Giommi et al., 1995) which found that the radio-to-infrared spectra of RBL and XBL were similar, but that the spectral energy cut-off of RBL was located at lower frequencies than that of XBL. Then, starting from the radio luminosity function

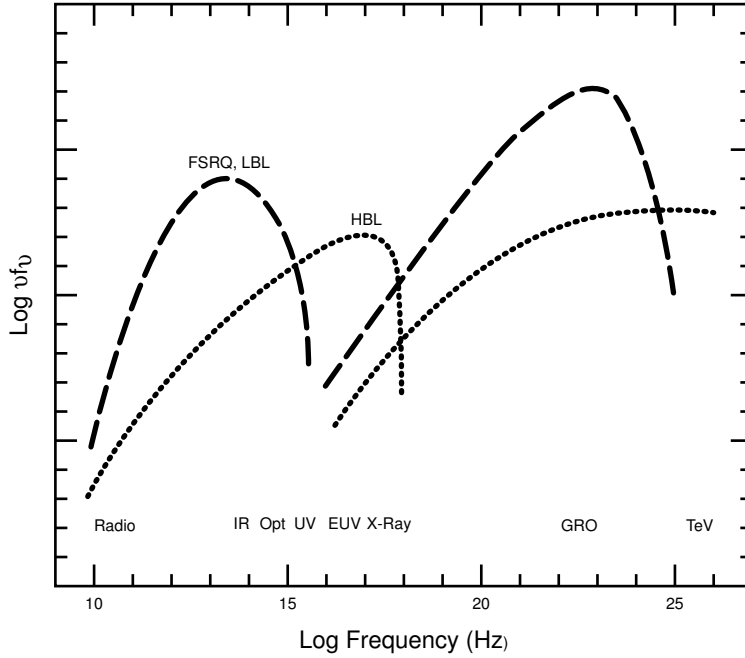


FIGURE 1.5. Characteristic double-peaked SED of blazars plotted as νf_ν versus frequency ν . The low-energy component, due to synchrotron radiation, peaks in the IR/optical band for LBL and (known) FSRQ (dashed line) and at UV/soft-X-ray energies for HBL (dotted line). The corresponding high-energy components, most likely produced by the inverse Compton process, peak at GeV or TeV energies respectively (from Urry (1998)).

and radio-to-X-ray flux ratio distribution of 1 Jy BL Lacs they could reproduce the X-ray number counts and luminosity function, as well as the radio flux distribution of EMSS BL Lacs. However, they failed to reproduce their redshift distribution and so could not explain the different cosmological evolution of RBL and XBL. This, however, is important in order to clarify if they represent a single population. The slightly more extreme properties of RBL compared to those of XBL were fitted into this scenario by assuming that X-ray surveys simply sampled the low end of the radio luminosity function of BL Lacs, and so were likely to select on average less beamed objects than radio surveys. They then concluded that radio- rather than X-ray-selected samples of BL Lacs were unbiased, and, since BL Lacs with spectral energy cut-offs at relatively high frequencies made up only $\sim 10\%$ of the objects discovered in radio surveys, that XBL were by this factor less numerous than RBL. In Chapter 3, I will present results in support of their interpretation that the primary difference between the two BL Lac subclasses is intrinsic rather than orientation.

Following Padovani and Giommi (1995) we now separate BL Lacs into low- (LBL)

and high-energy peaked BL Lacs (HBL). Fig. 1.5 shows their characteristic SEDs. These exhibit two pronounced emission peaks, a lower-frequency one attributed to synchrotron emission and a higher-frequency one produced by inverse Compton emission (i.e. scattering of photons by electrons). LBL and HBL are defined as BL Lacs with a synchrotron emission peak located at IR/optical and UV/soft-X-ray frequencies respectively, or equivalently, X-ray emission dominated by inverse Compton and synchrotron emission respectively. In practice, however, the division between LBL and HBL is based on their X-ray-to-radio flux ratios. Originally, a value of $f_x/f_r = 10^{-11}$ (with f_x in $\text{erg cm}^{-2} \text{s}^{-1}$ in the energy range 0.3 – 3.5 keV and f_r in Jy at 5 GHz) was proposed as a dividing line (meaning that most known RBL were also LBL and all known XBL were HBL). Later, based on their studies of X-ray spectra of BL Lacs (Padovani and Giommi, 1996) this ratio was changed to a value of $f_x/f_r = 10^{-11.5}$ (corresponding to a radio-to-X-ray effective spectral index of $\alpha_{\text{rx}} = 0.78$).

A similar split for the more powerful blazar subclass, the FSRQ, did not exist so far. All known FSRQ were found to have SEDs similar to the ones of LBL. However, there is mounting evidence that current deep blazar surveys, like, e.g., the Deep X-ray Radio Blazar Survey (DXRBS) which forms the basis of this thesis, do contain FSRQ with broad-band spectral properties similar to those of HBL (Padovani et al., 2002). This could then mean that AGN in general produce relativistic jets with a wide range of spectral energy cut-offs.

1.4 A Physical Revision of Blazar Classification

The scheme we choose to classify astrophysical objects is our first and most fundamental stepping stone toward understanding their properties and their relation to each other. Therefore, a classification scheme based on physical arguments is to be sought rather than one developed phenomenologically or even historically. In this respect this thesis represents the search for the most suitable physical classification scheme for blazars and is, therefore, a revision of the current scheme proposed by Marchã et al. (1996).

Marchã et al. increased the dividing line between blazars and radio galaxies from a Ca H&K break value of $C = 0.25$, as initially introduced by Stocke et al. (1991) for the EMSS BL Lacs, to a value of $C = 0.4$. This change was based on the argument that less than 5% of the sample of more than 700 early-type (non-active) galaxies of Dressler and Shectman (1987) had a Ca H&K break value $C \leq 0.4$. However, Marchã et al. did not investigate what *caused* the dilution of the Ca H&K break in

radio-loud AGN. It was clear that a strong dilution of this feature was caused by the superposition of the non-thermal jet component over the thermal host galaxy spectrum. But the strength of the jet component, and so the dilution of the Ca H&K break, could be due to intrinsic variations as well as relativistic beaming effects (and so a change in viewing angle). Without such an understanding, however, the most (physically) appropriate value to separate blazars and radio galaxies cannot be determined and any suggested value has to remain arbitrary.

In Chapter 3, I investigate reasons for the dilution of the Ca H&K break in BL Lacs and low-luminosity radio galaxies. An additional motivation for this study, besides its obvious purpose, came from the understanding that, if the Ca H&K break was indeed diluted by beaming effects, the average orientation of a sample of radio-loud AGN could be determined from such a simple observation as their optical spectra. The only such indicator currently known is the radio core dominance parameter (defined as the ratio between core and extended radio power), and its measurement requires dedicated radio observations.

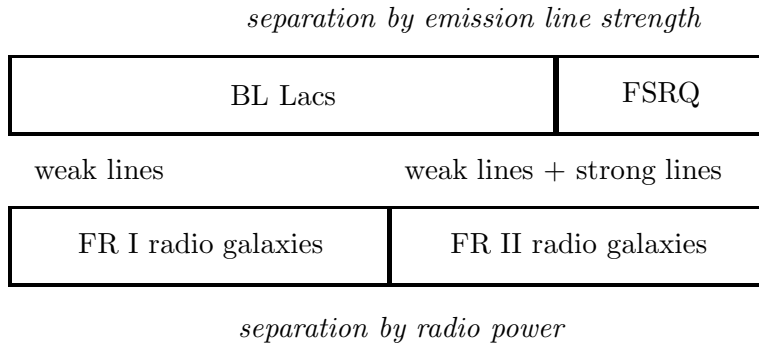
As already noticed by Marchã et al. the diagonal line suggested to separate blazars into BL Lacs and FSRQ was plain arbitrary and only based on the judgement that the BL Lac object 3C 371 was representative of the class as a whole. However, a separation of blazars based on their emission line strength can only be physically justified if there existed a bimodality. No such bimodality has been reported so far and so the possibility still existed that the (historical) separation of blazars was rather forced. In fact, Scarpa and Falomo (1997) showed that there was a continuity in optical continuum and emission line luminosities between BL Lacs and FSRQ. Using measurements of the Mg II $\lambda 2798$ emission line they found that they had similar line luminosities but that the emission lines of BL Lacs appeared weaker due to their stronger optical continua. Based on this they then concluded that from the point of view of emission line strengths it was not necessary to invoke two different populations of blazars. It is important to point out, however, that Scarpa & Falomo used an heterogeneous sample of BL Lacs and FSRQ and so in any case the classification of blazars had to be revisited using a homogeneous sample, i.e. a sample selected in an uniform and therefore presumably unbiased way.

Such a sample is used in this thesis. This is the Deep X-ray Radio Blazar Survey (DXRBS), which is the faintest and largest homogeneous blazar sample available today with nearly complete optical identification. During my thesis I have worked on its spectroscopic identification and I present its selection and identification criteria as well as its properties in the next chapter. The most appropriate separation of BL Lacs and FSRQ is investigated in Chapter 4. Additionally I have included in these

studies radio galaxies (and quasars) from the 2 Jy survey in order to find a more consistent picture for the emission line properties of radio-loud AGN than would have been possible using DXRBS alone.

I want to stress that finding a physically justified classification scheme for blazars is particularly crucial for the class of BL Lacs. These are very rare sources, only a few hundred are known compared to several thousands of quasars (Véron-Cetty and Véron, 2001). In addition, their spectral energy distributions as well as (perhaps) their evolutionary behaviour are different for sources first discovered in radio and X-ray surveys and the impact of the classification scheme in this respect can be enormous.

I want to turn now to the general inconsistency of our present classification scheme for radio-loud AGN. As detailed earlier we separate blazars and radio galaxies into their subclasses based on different criteria, namely emission line strength and radio morphology (and so radio power) respectively. However, observations of *both* blazars and radio galaxies show that a separation of radio-loud AGN based on radio power is not equivalent to one based on line luminosity (see Section 1.2).



This discrepancy (illustrated in the diagram above) has gained not enough attention so far. Nevertheless, a consistent classification scheme for blazars and radio galaxies, i.e. a classification scheme that correctly assigns the subclasses within the beamed and unbeamed populations, is indispensable for all our future studies of radio-loud AGN. Only with such a classification scheme can we be confident that we compare the properties of the same subclasses at different orientations. And such comparisons are necessary in order to find answers to fundamental questions such as ‘How do emission line regions of AGN form?’, ‘Do all AGN have accretion disks?’ and ‘What triggers the formation of jets in AGN?’.

For example, the broad emission line gas is a direct tracer of the accretion disk

power, but can only be observed in objects oriented at relatively small angles. The narrow line regions, on the other hand, might provide the initial fuel that finally gets accreted. These, however, are often extended and their origin is then best determined from observations of objects oriented at large angles. The SED of the jet, which is very relevant for our understanding of jet formation and acceleration mechanisms, can be easily observed in blazars where it is enhanced by relativistic beaming effects. An understanding of the propagation and in-situ acceleration of relativistic jets, however, can only be gained from observations of radio galaxies. The knowledge of both of these is necessary for a complete picture. Moreover, a consistent classification scheme would allow us to study how properties of radio-loud AGN change with viewing angle, and so help us determine which of these are indeed isotropic, and would also deepen our understanding of the relativistic beaming phenomenon. Finally, we could disentangle orientation effects and study the number counts and luminosity functions of radio-loud AGN with improved statistics.

The discrepancy in our current classification scheme for radio-loud AGN can only be reconciled if we classify both radio galaxies and blazars uniformly, i.e. based either on their emission line strengths or on their radio morphologies. However, a general decision might not be required and not even desired (some studies will rather need information on emission lines, whereas radio measurements will be more important to others) if we had a method to disentangle orientation effects at radio *and* optical frequencies. The radio core dominance parameter can be used for radio observations and this thesis has made an effort to find optical viewing angle indicators.

Chapter 2

The Deep X-ray Radio Blazar Survey

The studies presented in this thesis are largely based on sources selected from the Deep X-ray Radio Blazar Survey (DXRBS). DXRBS is the faintest and largest sample of flat-spectrum radio sources existing today with nearly complete ($\sim 90\%$) optical identification. It contains ~ 350 sources and reaches 5 GHz radio fluxes ~ 50 mJy and 0.1 – 2.0 keV X-ray fluxes a few $\times 10^{-14}$ erg cm $^{-2}$ s $^{-1}$. The survey has been published so far in two parts as Perlman et al. 1998, “The Deep X-ray Radio Blazar Survey I. Methods and First Results” (AJ 115, 1253), and Landt et al. 2001, “The Deep X-ray Radio Blazar Survey (DXRBS) II. New Identifications” (MNRAS 323, 757).

2.1 Blazar Surveys

Owing to their preferred orientation with respect to our line of sight blazars represent a very rare class of objects, making up only $\sim 5\%$ of all AGN (Padovani, 1997). For this reason, large area sky surveys are better suited than pencil beam surveys to find these sources. Until very recently all existing blazar samples were drawn from surveys with a small sky coverage and/or relatively high flux limits. These so-called ‘classical’ blazar samples are:

- 1 Jy BL Lac sample, sky coverage 9.81 sr, radio fluxes $f_{5\text{GHz}} > 1$ Jy, radio spectral index cut $\alpha_r \leq 0.5$, $V < 20$; complete sample 34 objects (Stickel et al., 1991; Rector and Stocke, 2001)
- EMSS BL Lac sample, sky coverage ~ 700 square degrees, X-ray fluxes $f_{0.3-3.5\text{keV}} \gtrsim 2 \times 10^{-13}$ erg cm $^{-2}$ s $^{-1}$; total sample 44 objects (Stocke et al., 1991; Morris et al., 1991; Rector et al., 2000)
- *Einstein* Slew BL Lac sample, sky coverage ~ 10 sr, X-ray fluxes $f_{0.2-4\text{keV}} \gtrsim 2 \times 10^{-11}$ erg cm $^{-2}$ s $^{-1}$; complete sample 51 objects (Perlman et al., 1996a)
- 2 Jy FSRQ sample, sky coverage 9.81 sr, radio fluxes $f_{2.7\text{GHz}} > 2$ Jy; complete sample 52 objects (Wall and Peacock, 1985; Padovani and Urry, 1992)

Most of our current understanding of the blazar phenomenon is based on these samples, which means on a relatively small number of intrinsically luminous sources. In other words, we have only sampled the tip of the iceberg of the blazar population. For example, the radio luminosity function of FSRQ derived by Urry and Padovani (1995), although based on 52 sources, included only one source at $L_r < 10^{26.5}$ W Hz $^{-1}$, the power which coincides roughly with the predicted flattening of the luminosity function of blazars (Urry and Shafer, 1984). The need for deeper and larger blazar samples to test unified schemes and to gain extensive knowledge of the physical properties of blazars is obvious.

DXRBS provides such a sample. Other groups are also tackling the task of assembling large and deep blazar samples, the main ones being RGB (ROSAT All Sky Survey [RASS]-Green Bank) survey (Laurent-Muehleisen et al., 1998, 1999), REX (Radio-Emitting X-ray sources) survey (Caccianiga et al., 1999, 2000), Sedentary Survey (Giommi et al., 1999), and CLASS (Cosmic Lens All Sky Survey) blazar sample (Marchã et al., 2001; Caccianiga et al., 2002) (see Padovani (2002) for a detailed list of current blazar surveys). However, compared to other on-going surveys, DXRBS has several advantages:

1. Its optical identification is almost ($\sim 90\%$) complete. In comparison, the identification fractions for other published samples are, e.g., $\sim 40\%$ for RGB ($\sim 1,500$ sources), $\sim 30\%$ for the REX sample ($\sim 1,600$ sources), $\sim 50\%$ for the Sedentary Survey (155 candidates), and $\sim 70\%$ for the CLASS sample (325 sources).
2. It contains a large number of *both* blazar types. In this respect, RGB has concentrated so far mainly on BL Lacs (33 objects in complete sample, 127 in

whole sample), but see Padovani et al. (2002) for an independent extraction of FSRQ from this survey. Similarly, the Sedentary Survey was designed solely to select high-energy peaked BL Lacs (two-point spectral index selection criterion $\alpha_{\text{rx}} \lesssim 0.56$ and $\alpha_{\text{ro}} > 0.2$).

3. It reaches, with REX, the lowest X-ray fluxes. RGB and the Sedentary Survey employ similarly to DXRBS a correlation of radio and X-ray catalogues. However, the Sedentary Survey and RGB are based on the RASS Bright Source Catalogue (BSC; $f_{0.1-2.4\text{keV}} \gtrsim 10^{-12}$ erg cm⁻² s⁻¹) and RASS ($f_{0.1-2.4\text{keV}} \gtrsim 3 \times 10^{-13}$ erg cm⁻² s⁻¹) respectively.
4. It does not have an optical magnitude cut which allows it to reach a relatively high completion level down to its radio and X-ray flux limits. Most other surveys have restricted their candidates to the brightest sources, e.g., RGB has an optical magnitude cut of $B < 18$, whereas the CLASS sample includes only $R < 17.5$ sources.

2.2 Candidate Selection

The DXRBS takes advantage of the fact that all blazars are relatively strong X-ray and radio emitters, and that one of their defining properties is a flat radio spectrum. Therefore, the strategy for candidate selection adopted by DXRBS was to cross-correlate an X-ray catalogue with several radio catalogues, and to impose an upper limit on the radio spectral index of $\alpha_r = 0.7$ (where $S_\nu \propto \nu^{-\alpha}$).

In order to select the largest possible number of blazar candidates the DXRBS made use of the catalogues with the lowest possible flux limits publicly available in 1995 (the year the survey was started). These were the *ROSAT* X-ray database WGACAT and the radio catalogues from the 20 cm and 6 cm Green Bank surveys NORTH20CM and GB6 (for the northern sky) and the 6 cm Parkes-MIT-NRAO survey PMN (for the southern sky). WGACAT is a point source catalogue generated by White et al. (1995) from all *ROSAT* Position Sensitive Proportional Counter (PSPC) pointed observations and comprises $\sim 60,000$ objects (Version 1). It covers $\sim 18\%$ of the sky and its flux limit varies, depending on the length of each individual exposure and the distance from the center of the PSPC field, between $\sim 10^{-14}$ and $\sim 10^{-12}$ erg cm⁻² s⁻¹. The positional errors of the sources depend on their distance from the PSPC center and are listed in Table 2.1 (see Perlman et al. (1998)). In order to avoid problematic detections DXRBS selected from the WGACAT database only sources with quality flag ≥ 5 .

North of the celestial equator ($\delta > 0^\circ$) the WGACAT database was first correlated with the GB6 catalogue. This comprises $\sim 75,000$ sources with declinations in the range $0^\circ < \delta < +75^\circ$ and reaches fluxes down to ~ 20 mJy (Gregory et al., 1996). A correlation radius of $1'$ was chosen. The resulting sample, which included 1,119 sources, was then correlated with the NORTH20CM. The NORTH20 catalogue comprises $\sim 30,000$ sources with declinations in the range $-5^\circ < \delta < +82^\circ$ and reaches fluxes down to ~ 100 mJy (White and Becker, 1992). This time a correlation radius of $3'$ was chosen due to the considerably worse positional uncertainties ($160''$ at the 90% level). This produced a list of 570 sources. Of these, 148 met the additional DXRBS candidate requirements of having a radio spectral index $\alpha_r \leq 0.7$ and being off the Galactic plane ($|b| > 10^\circ$).

TABLE 2.1. **X-ray Positional Errors**

PSPC		WGACAT
Center	Offset	Positional Error
	$0' - 10'$	$13.0''$
	$10' - 20'$	$18.1''$
	$20' - 30'$	$28.6''$
	$30' - 40'$	$36.1''$
	$40' - 50'$	$42.0''$
	$50' - 60'$	$53.4''$

South of the celestial equator the WGACAT database was correlated with the PMN catalogue. This comprises $\sim 50,000$ sources with declinations in the range $-87.5^\circ < \delta < +10^\circ$ (Griffith and Wright, 1993). The flux limit of the PMN is declination dependent and averages ~ 50 mJy. Again, a correlation radius of $1'$ was used. This produced a list of 541 objects. Of these, 148 sources met the additional DXRBS selection requirements.

Since the positional accuracy of radio catalogues decreases with flux, the possibility was investigated that a $1'$ cross-correlation radius might not be large enough at lower radio fluxes and/or large PSPC center offsets. Therefore, the cross-correlation of the WGACAT with the GB6 and PMN radio catalogues was done with a $1.5'$ radius. The significance of the (mis)match was quantified by the ratio between the X-ray/radio offset (the distance between the X-ray and radio position) and the 1σ combined positional error. This quantity gives the probability that the X-ray/radio match is spurious. Then, a correlation radius of $1.5'$ corresponds roughly to 2σ for

a source with PSPC offset $\sim 30'$ and radio flux ~ 50 mJy.

The results of the expansion of the cross-correlation radius are as follows. For the WGACAT/PMN correlation, the number of X-ray/radio sources increased by 40%. Dividing the WGACAT sample in an inner (PSPC offset $\leq 30'$) and outer (PSPC offset $> 30'$) region, there was a 38% increase in the inner region and a 45% increase in the outer region. In the inner region most of the increase was due to ‘spurious’ associations, which were defined for the purpose of this experiment as those matches with ratio between offset and positional error > 2 . Of the 144 new sources, 104 were spurious, with a net increase of ‘good’ sources $\sim 12\%$. In the outer region, of the 81 new sources, only 13 were spurious, so the number of good sources increased by $\sim 38\%$. This simply reflects the fact that WGACAT sources with larger PSPC offsets have larger positional uncertainties and ‘real’ matches can have X-ray/radio offsets $> 1'$. For the WGACAT/GB6 correlation the results were slightly different: the increase was only 25%, practically independent of WGACAT offset. The net increase of ‘good’ matches was only $\sim 4\%$ in the inner region of the PSPC and $\sim 21\%$ in the outer one. That is, as the GB6 positions are better than the PMN ones, increasing the correlation radius has a bigger effect on the WGACAT/PMN ‘real’ matches than it has on the WGACAT/GB6 matches. As a result of this experiment, in order to increase the completeness of the DXRBS the correlation radius was expanded to $1.5'$ for the inner $45'$ of the PSPC field of view, excluding sources with $\sigma > 2.5$ in the PSPC region $0' - 30'$ and $\sigma > 2$ in the PSPC region $30' - 45'$. A somewhat larger significance of the mismatch was allowed in the inner $30'$ PSPC region, since this did not increase the number of the DXRBS candidates exuberantly.

The DXRBS complete sample contains at the time of writing 350 sources (108 previously known objects, 211 newly identified objects, and 31 unidentified objects). The detailed X-ray, radio and optical positional information for the 211 newly identified sources can be found in Appendix A. Appendix A also lists 22 additional sources that have been identified in the course of time but that do not meet all DXRBS selection criteria (‘low priority sources’).

2.3 The Radio Spectral Index

One of the selection criteria that makes DXRBS most efficient at finding blazars is its imposed cut on the radio spectral index of $\alpha_r = 0.7$. This limit ensures that DXRBS: 1. selects all FSRQ (defined by $\alpha_r \leq 0.5$); 2. selects basically all BL Lacs ($\alpha_r = 0.7$ is the limiting value for the BL Lacs with X-ray-to-radio flux ratios typical of DXRBS within the multiwavelength AGN catalogue of Padovani et al. (1997)), and 3. excludes the large majority of radio galaxies. Ideally, the candidate selection should have been done on radio core-dominance, the ratio between core and extended radio flux, known to be $\gtrsim 1$ in blazars (e.g. Murphy et al., 1993), but derivation of this parameter requires dedicated radio observations. Therefore, DXRBS uses simply the fact that a flat radio spectrum is a direct indicator of radio core dominance (Impey and Tapia, 1990).

The radio spectral index was obtained for the northern sources directly from the cross-correlation of the GB6 and NORTH20CM catalogues and covers the range 6 – 20 cm. For objects south of the celestial equator, where a survey at a frequency different from the one of the PMN was missing when the project was started (the NVSS [Condon et al. (1998)], now available, reaches in any case only $\delta = -40^\circ$), a snapshot survey was conducted with the Australia Telescope Compact Array (ATCA) at 3.6 and 6 cm. The ATCA observations were originally requested at 6 and 20 cm in order to match the northern part of the sample, but the time allocation committee decided otherwise based on the instrumental configuration. In the declination range $-40^\circ < \delta < 0^\circ$ both ATCA observations and NVSS-PMN data (6 – 20 cm range) are available. Nevertheless, for consistency with the northern part of the survey it was decided to use radio spectral indices derived from the latter. In summary, the radio spectral indices for the DXRBS sources have been derived as follows:

- $\delta > 0^\circ$: α_r from the GB6 and NORTH20 catalogues and covers the range 1.4 – 5 GHz (6 – 20 cm);
- $-40^\circ < \delta < 0^\circ$: α_r from NVSS and PMN catalogues and covers the range 1.4 – 5 GHz (6 – 20 cm);
- $\delta < -40^\circ$: α_r from ATCA snapshot survey and covers the range 4.8 – 8.6 GHz (3.6 – 6 cm);

Besides allowing the selection of candidates for spectroscopy in advance of the completion of the NVSS, the original stated purpose of the ATCA observations was to help to gauge the effect of using non-simultaneous data to derive spectral

indices, and hence to include in the DXRBS true blazars which might otherwise be excluded. The ATCA data gives radio spectral indices unaffected by variability, since the observations at both frequencies are truly simultaneous, but in a higher frequency range than that used for the northern objects. On the other hand, radio spectral indices derived from PMN-NVSS data cover the more standard 1.4 – 5 GHz and are less affected by either spatial filtering or poor (u, v) coverage, but involve non-simultaneous data and have angular resolution no better than $\sim 15''$ (Condon et al., 1998). The PMN-NVSS radio spectral indices were derived by summing up all NVSS sources within $3'$ from the PMN position, given the different beam sizes of the two surveys. (Padovani et al., in preparation, show that this procedure is robust and gives radio spectral indices in very good agreement with those derived from single dish measurements.) The values of α_{ATCA} are expected to be correlated with $\alpha_{\text{PMN-NVSS}}$, with perhaps a small offset indicative of steepening in the synchrotron spectrum at higher frequencies.

Fig. 2.1 compares the values of α_{ATCA} and $\alpha_{\text{PMN-NVSS}}$ for all sources in the declination range $-40^\circ < \delta < 0^\circ$. The locus of equal spectral indices is represented by a dotted line. As expected, while the scatter is fairly large, probably due to variability and the different spatial scales sampled by the PMN/NVSS surveys and the ATCA (see below), the two spectral indices are well correlated ($P > 99.9\%$).

The mean values of the two spectral indices are, however, somewhat different. We find $\langle \alpha_{\text{ATCA}} \rangle = 0.62 \pm 0.06$ while $\langle \alpha_{\text{PMN-NVSS}} \rangle = 0.36 \pm 0.04$, and a mean difference of $\langle \Delta\alpha \rangle = \langle \alpha_{\text{ATCA}} - \alpha_{\text{PMN-NVSS}} \rangle = 0.26 \pm 0.04$. This comparison includes all sources and is therefore not appropriate: an extended source, which will typically have a relatively steep $\alpha_{\text{PMN-NVSS}}$, will be resolved out more at 8.6 GHz than at 4.8 GHz with the ATCA, due to the smaller primary beam area at the higher frequency. Such a source will therefore have an even steeper α_{ATCA} . A more meaningful comparison is that between the two spectral indices for relatively compact sources, which are the ones we are interested in. For this purpose, we estimated a core-dominance parameter, i.e., the ratio between core and extended flux, from our ATCA data at 4.8 GHz. Note that only a lower limit is available for the extended flux and therefore our core-dominance parameters are upper limits to the true value.

Keeping all this in mind, Figure 2.1 shows the distribution of the two spectral indices for sources with core-dominance parameter at 4.8 GHz $R_{4.8} > 1$ (filled points) and $R_{4.8} < 1$ (open points). As expected, most of the lobe-dominated ($R_{4.8} < 1$) sources have both α_{ATCA} and $\alpha_{\text{PMN-NVSS}} > 0.5 - 0.7$. The difference between the two spectral indices is clearly reduced for core-dominated objects. We find $\langle \alpha_{\text{ATCA}} \rangle = 0.36 \pm 0.05$, while $\langle \alpha_{\text{PMN-NVSS}} \rangle = 0.23 \pm 0.04$, and a mean difference of

$$\langle \Delta\alpha \rangle = 0.13 \pm 0.04.$$

In the case of a direct proportionality between the two spectral indices, all sources should populate the two areas of the diagram defined by $\alpha_{\text{ATCA}} < 0.7$, $\alpha_{\text{PMN-NVSS}} < 0.7$ and $\alpha_{\text{ATCA}} > 0.7$, $\alpha_{\text{PMN-NVSS}} > 0.7$ (the bottom-left and top-right areas, denoted in Figure 2.1 by the two dashed lines). This is “almost” the case: only 23/138 (17%) of the sources fall outside these regions. By choosing as our selection criterion for inclusion in the sample $\alpha_{\text{PMN-NVSS}} < 0.7$, we are conservatively including most (19/23) of these outliers. Ten of these sources, however, have $R_{4.8} < 1$ and their blazar classification might be questionable. As regards the four sources in the top-left part of the figure, excluded by our criterion, one has $R_{4.8} < 1$, while the maps of the other three show that they are at least partially extended.

Thus our conclusion is that among our sources we observe a steepening in spectral index between 1.4 – 5.0 GHz and 4.8 – 8.6 GHz of $\langle \Delta\alpha \rangle \sim 0.25$, which reduces to 0.13 when considering only the sources likely to be compact. By applying the same

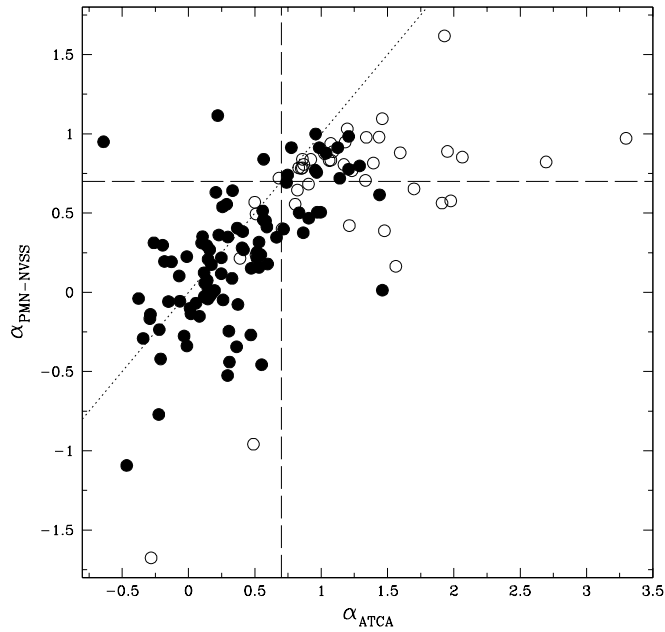


FIGURE 2.1. The radio spectral index derived from PMN - NVSS data (1.4–5 GHz) compared with the radio spectral index from the ATCA observations (4.8–8.6 GHz). The dotted line represents the locus of $\alpha_{\text{PMN-NVSS}} = \alpha_{\text{ATCA}}$, while the dashed lines indicate $\alpha_r = 0.7$ derived in each way. Objects with ATCA core dominance parameter at 4.8 GHz $R_{4.8} > 1$ are plotted as filled circles, while open circles indicate sources with $R_{4.8} < 1$.

cut of $\alpha_r = 0.7$ in the declination range $\delta < -40^\circ$, where we have only 4.8 – 8.6 GHz spectral indices available for our candidate selection, we are missing no more than three blazar candidates, included otherwise if $\alpha_{\text{PMN-NVSS}}$ were available and less than 0.5 (as the majority of our blazars are FSRQ). We estimate this number by considering the sources included in Fig. 2.1 with $\alpha_{\text{ATCA}} > 0.7$. Of these, only 7% have $\alpha_{\text{PMN-NVSS}} < 0.5$ and $R_{4.8} > 1$. Therefore, the use of higher resolution data in a slightly different frequency range does not affect strongly our selection of blazar candidates.

Some of the sources in Fig. 2.1 with flat $\alpha_{\text{PMN-NVSS}}$ but marked ($\gtrsim 0.6$) steepening at high frequencies could be Gigahertz peaked-spectrum (GPS) sources (e.g. O’Dea, 1998). For these sources, and for those with $\alpha_{\text{ATCA}} > 0.7$, the α_{ATCA} values are listed as footnotes to the tables in Appendix C.

2.4 Optical Identifications and Classifications

The full sample of DXRBS sources comprises 233 objects that have been newly identified in the course of several observing runs. For these objects accurate ($\lesssim 3''$) positions to pinpoint the optical counterpart and to allow spectroscopical identification were obtained from the NVSS or from the ATCA observations. The chance radio/optical identification in our case is expected to be very small. If a circle with radius $3''$ is assumed for each source, the number of previously unidentified sources in DXRBS (~ 250) as the number of circles, and a background density of stellar objects and galaxies from faint UK Schmidt plates of 2.1 stars and 1.2 galaxies per square-arcmin (e.g. Jauncey et al., 1982), one obtains ~ 6 chance coincidences (or $\sim 2\%$).

Finders were produced using the Digitized Sky Survey (DSS) via SkyCat (Albrecht et al., 1997). Magnitudes were derived for relatively bright objects ($B \lesssim 22$, $R \lesssim 20$) from the Cambridge APM project (Irwin et al., 1994) for the northern sources and Edinburgh COSMOS catalogue for the southern objects (Drinkwater et al., 1995). Candidates without counterparts on DSS plates were imaged at the KPNO 0.9 m, WIYN 3.5 m, CTIO 0.9 m, and ESO 2.2 m and 3.6 m telescopes.

Spectroscopic observations were conducted at several telescopes. These telescopes together with the properties of the grisms used during the observing runs are listed in Table 2.2. A list with the observational details for the single object can be found in Appendix B. Since most of the DXRBS sources were expected to be quasars, the exposure times have been calculated based on this assumption and are rather low. This rendered the identification of weak emission and absorption fea-

TABLE 2.2. **Grism Properties**

Telescope	Disp. [Å/pix]	Range [Å]	Telescope	Disp. [Å/pix]	Range [Å]
CTIO 1.5 m	5.4	3600 – 10000	ESO 2.2 m	8.4	3400 – 9200
CTIO 4 m	1.2	3800 – 7300	ESO 3.6 m	6.3	3185 – 10940
KPNO 2.1 m	4.6	4000 – 10000		25.0	3600 – 11000
KPNO 4 m	9.1	4300 – 10000		6.3	3740 – 6950
	4.3	4300 – 8500		2.1	3860 – 8070
	4.3	4800 – 9500	VLT 8 m	2.7	4450 – 8650
Lick 3 m	1.8	3700 – 8300		5.5	4450 – 11000
MMT 4.5 m	2.0	3800 – 9000			

tures in the obtained spectra somewhat difficult. The spectra acquired during the September 1998 and February 1999 runs have a fairly low SNR due to bad weather conditions. Spectra observed with the Lick, MMT, CTIO 4 m, ESO 3.6 m, and KPNO 4 m were taken at parallactic angle, except in cases where the radio/X-ray error circle contained two candidates and therefore a rotation of the slit was necessary. Observations at parallactic angle were not attempted at the CTIO 1.5 m, ESO 2.2 m, and KPNO 2.1 m telescopes, since these observatories require a time consuming manual slit rotation.

The acquired spectra were reduced using standard IRAF routines. The data were bias-subtracted and flatfielded using programs in the IRAF package *noao.imred.ccdred*. The spectra were extracted, wavelength and flux-calibrated using programs in the package *noao.twodspec*. Cosmic rays were removed in the one- and two-dimensional data by hand. A dereddening correction was applied to the data using the IRAF routine *noao.onedspec.dered* and assuming Galactic values of extinction derived from 21-cm measurements (Stark et al., 1992). The final spectra are shown in Appendix D.

We have classified sources in the DXRBS based on their optical spectra as BL Lacs, quasars (FSRQ and SSRQ) and radio galaxies following Marchã et al. (1996). Stars have not been detected most likely due to their weak radio emission (Helfand et al., 1999) with average fluxes below the limits of the radio catalogues employed in our survey. Sources having both narrow and broad emission lines have been classified as blazars. We have adopted a dividing value of the full width at half maximum $\text{FWHM} = 1000 \text{ km s}^{-1}$ to quantify the terms ‘narrow’ and ‘broad’. For

sources previously known we have adopted the classification given in the literature. Redshifts and classifications, as well as optical magnitudes, radio and X-ray fluxes and radio spectral index for the DXRBS sample are listed in Appendix C. The DXRBS complete sample (319 sources) contains at the time of writing 40 BL Lacs, 252 quasars (195 FSRQ and 57 SSRQ), and 27 radio galaxies. The 22 low priority sources split as follows: 4 BL Lacs, 9 quasars (6 FSRQ and 3 SSRQ), and 9 radio galaxies. (Note, however, that DXRBS radio galaxies have a relatively flat radio spectral index and therefore their jets are expected to be oriented closer to our line of sight than the ones of classical lobe-dominated radio galaxies.)

2.5 Sample Properties

2.5.1 Redshift Distributions

Fig. 2.2 displays the fractional redshift distribution of the DXRBS quasars compared to the quasars found in the S4 ($f_{5\text{GHz}} > 0.5$ Jy) and 1 Jy ($f_{5\text{GHz}} > 1$ Jy) surveys (Stickel et al., 1994; Stickel and Kühr, 1994). Note that DXRBS quasars have been selected to have $\alpha_r \leq 0.7$. Therefore the S4 and 1Jy distributions shown here comprise the quasars from these samples defined on the same basis.

While for the S4 and 1 Jy surveys the area of the sky covered is the same at all fluxes (5,624 and 32,208 deg² respectively), this is not the case for DXRBS. Due to the serendipitous nature of the survey and the variable sensitivity of the *ROSAT* PSPC detector across the field of view, the area in which faint X-ray sources could be detected is smaller than that for brighter X-ray sources. The DXRBS redshift distribution has therefore been deconvolved with the appropriate sky coverage and this is what is shown in Fig. 2.2. Namely, each bin represents $\sum 1/\text{Area}(f_x)$ for all the sources in that bin, where $\text{Area}(f_x)$ is the area accessible at its X-ray flux, divided by the total surface density of sources. Error bars represent the 1σ range based on Poisson statistics. The sky coverage is difficult to determine in the parts of the PSPC field of view affected by the rib structure ($13' < \text{offset} < 24'$). That area, and the sources within, have therefore been excluded from the analysis presented here. Moreover, only sources with $f_{5\text{GHz}} > 51$ mJy have been included since the sky coverage of the PMN survey below this flux has not been computed so far.

As the radio flux limit of the quasar samples drops from 1 Jy to ~ 0.05 Jy, the approximate limit of the DXRBS, a progression towards higher redshifts is clearly seen, as expected. The mean redshift, in fact, moves from $\langle z \rangle = 1.18 \pm 0.05$ for the 1 Jy, to $\langle z \rangle = 1.30 \pm 0.07$ for the S4, to $\langle z \rangle = 1.56 \pm 0.06$ for the DXRBS sample. A Kolmogorov-Smirnov test shows that the DXRBS redshift distribution

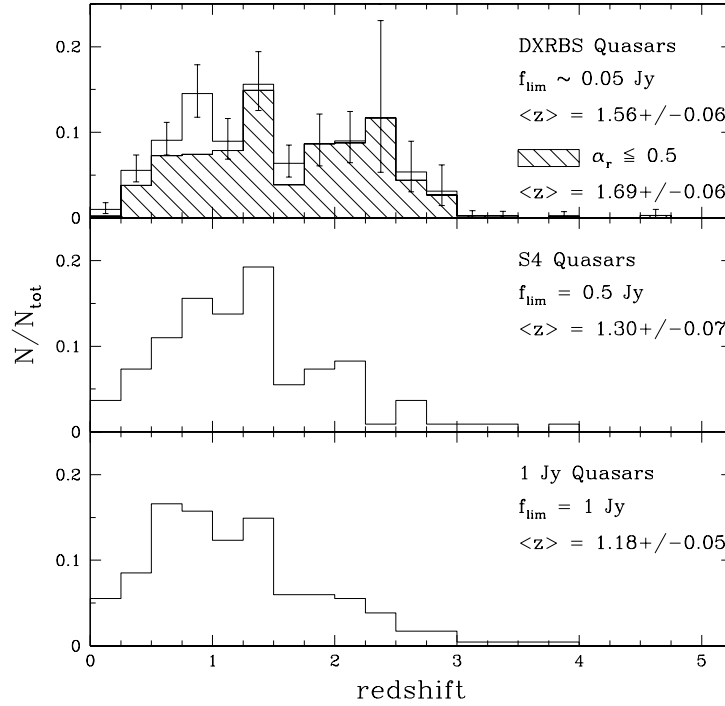


FIGURE 2.2. Fractional redshift distributions for the 171 DXRBS, 109 S4, and 235 1 Jy quasars with $\alpha_r \leq 0.7$. The shaded area represents the redshift distribution for the 134 DXRBS FSRQ. The DXRBS distributions have been deconvolved with the appropriate sky coverage. Error bars represent the 1σ range based on Poisson statistics.

is significantly different ($P > 99\%$) from the 1 Jy and S4 distributions. The mean values are also different at the same significance level. Considering that the DXRBS complete sample is $\sim 90\%$ identified and that the missing sources are likely to be at relatively high ($z \gtrsim 1.5$) redshift, we expect the final mean redshift to be even higher. Compared to the S4 and 1 Jy samples, a larger fraction of DXRBS quasars are at relatively high redshift. In fact, DXRBS finds $\sim 35\%$ of its quasars at $z > 2$ (once the effect of the WGACAT sky coverage is taken into account), whereas only $\sim 15\%$ of the S4 and 1 Jy quasars lie above this redshift. Fig. 2.2 shows also the redshift distribution of FSRQ (shaded diagram). For these we get a mean value of $\langle z \rangle = 1.69 \pm 0.06$, not significantly different from that of the total sample.

Fig. 2.3 displays the redshift distribution of the DXRBS BL Lacs, compared to that of the 1 Jy and EMSS samples. The DXRBS and EMSS redshift distributions have been deconvolved with the appropriate sky coverage (the sky coverage for the EMSS was taken from Gioia et al. (1990) and Morris, private communication). BL

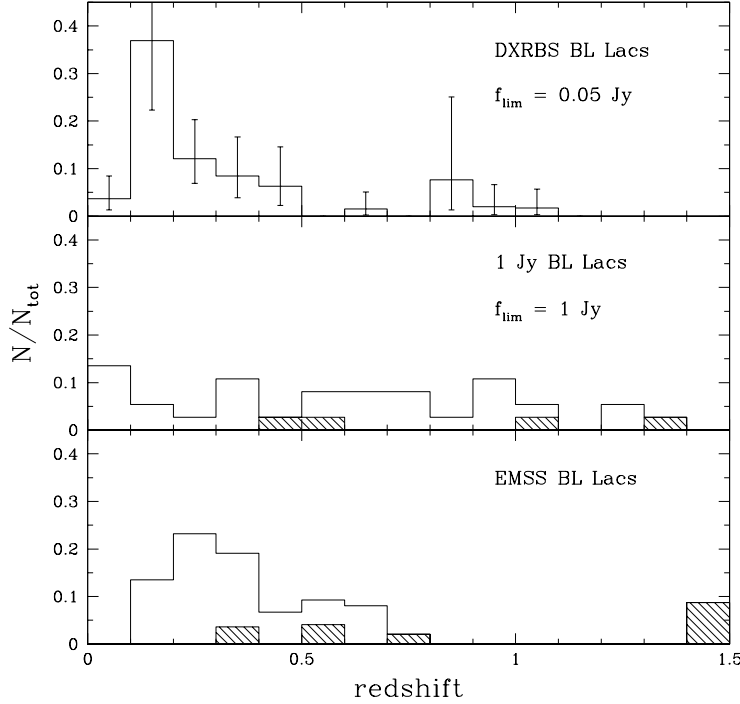


FIGURE 2.3. Fractional redshift distribution for the 22 DXRBS, 32 1 Jy, and 38 EMSS BL Lacs. The DXRBS and EMSS distributions have been deconvolved with the appropriate sky coverages. The hatched areas represent lower limits (1 Jy) and uncertain values (EMSS). Error bars represent the 1σ range based on Poisson statistics.

Lacs from the *Einstein* Slew Survey have not been included in this plot because the detailed sky coverage of that survey is not fully known yet. Five EMSS redshifts are uncertain, while four 1 Jy redshifts are lower limits (hatched areas; five more 1 Jy sources have a lower limit on their redshift of 0.2 based on the non-detection of their host galaxies on the optical image). Note that the fraction of BL Lacs with redshift information ranges from 93% and 86% for the EMSS and 1 Jy samples respectively to 73% for DXRBS. The majority of the DXRBS BL Lacs without a determined redshift are previously known objects, and therefore have not been spectroscopically observed by us.

The mean redshift for the three BL Lac samples is 0.35 ± 0.06 for DXRBS, 0.46 ± 0.06 for the EMSS, and 0.63 ± 0.07 (including lower limits) for the 1 Jy. Notably, the redshift distributions of both the DXRBS and EMSS samples are peaked (at $z = 0.2$ and $z = 0.3 - 0.4$ respectively), whereas the redshift distribution of the 1

Jy sample is essentially flat with a significant number of sources at larger redshifts (10/32 1 Jy BL Lacs are at $z > 0.8$ and 5 at $z > 1$). In contrast to the quasars, no progression to higher redshifts is seen for the BL Lacs as the radio flux limit drops from 1 Jy, for the 1 Jy sample, to 0.05 Jy for the DXRBS. Similarly, no progression of this kind is seen as the X-ray flux limit drops from a few $\times 10^{-13}$ erg cm $^{-2}$ s $^{-1}$ for the EMSS to a few $\times 10^{-14}$ erg cm $^{-2}$ s $^{-1}$ for the DXRBS. However, caution is advisable when making such comparisons, since the BL Lac classification criteria were somewhat different in each of these surveys. While the spectroscopic criteria employed for the DXRBS and EMSS were identical (once the EMSS sample was expanded to take into account the classification proposed by Marchã et al. (1996); Rector et al. (1999)), the EMSS did not require a flat radio spectrum to classify an X-ray source as a candidate BL Lac. The 1 Jy survey, on the other hand, required a flat ($\alpha_r \leq 0.5$) radio spectral index and did not impose a restriction on the Ca break value. In addition, the 1 Jy survey was often inconsistent in applying its selection criteria (as noted by, e.g., Marchã and Browne, 1995; Perlman et al., 1998; Rector et al., 1999). Finally, DXRBS is basically equivalent to a radio flux-limited sample (Padovani, 2001), so a comparison with a purely X-ray flux limited sample like the EMSS is not straightforward.

Noteworthy is also the striking difference in redshift range between BL Lacs and quasars, the latter reaching $z \sim 4.7$, the former only getting up to $z \sim 1.5$. Note that, while $\sim 28\%$ of DXRBS BL Lacs lack a redshift determination, that is not the case for the EMSS and 1 Jy samples for which redshifts are available for $\sim 90\%$ of the sources. Although one cannot exclude the possibility that the missing redshifts are all relatively high, the point remains that the mean redshift values for BL Lacs and quasars *belonging to the same sample* are significantly different.

Finally, the redshift distribution for the radio galaxies in DXRBS reaches only $z \sim 0.8$ and is skewed towards low redshifts, with $\langle z \rangle = 0.26$.

2.5.2 Radio and X-ray Luminosities

Because it reaches much lower fluxes than any previously published sample of FSRQ (by a factor $\sim 10 - 20$ in radio flux and by a factor ~ 10 in X-ray flux), DXRBS has vastly expanded the coverage of parameter space for FSRQ in complete samples. These expansions occur in two regions of the L_x, L_r plane (see Fig. 2.4): 1. at low luminosities; and 2. at high L_x/L_r values, with the discovery of a new class of X-ray bright FSRQ.

At the low luminosity end, DXRBS includes at present ~ 5 times more quasars with $L_r < 10^{33.5}$ erg s $^{-1}$ Hz $^{-1}$ than the S4 and 1 Jy samples combined. About 40

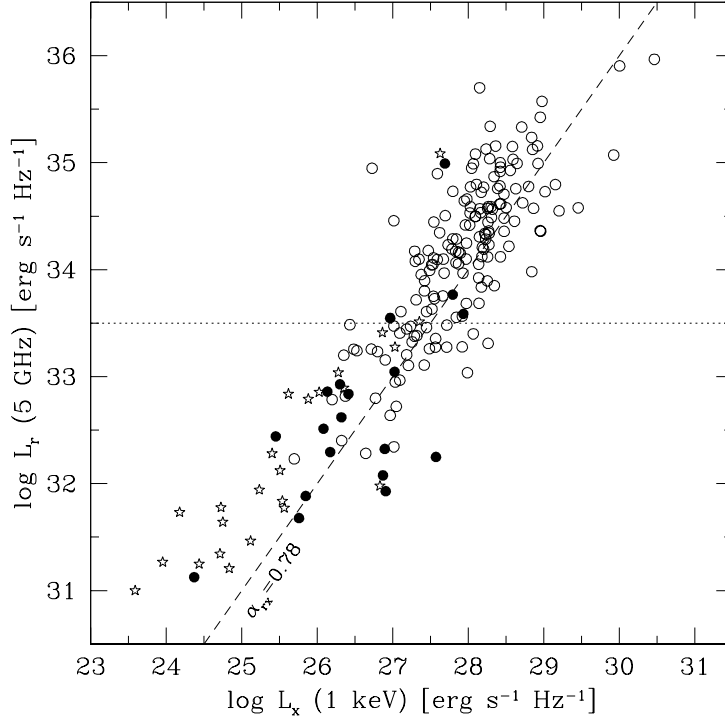


FIGURE 2.4. The radio luminosity at 5 GHz versus the X-ray luminosity at 1 keV for the DXRBS complete sample. Open circles, filled circles and stars denote quasars, BL Lacs and radio galaxies respectively. The dashed line indicates the locus of constant $\alpha_{\text{rx}} = 0.78$ separating low- (to the left of the line) and high-energy peaked blazars (to the right of the line). The dotted line represents the locus of constant $L_r = 10^{33.5} \text{ erg s}^{-1} \text{ Hz}^{-1}$, a power which coincides roughly with the predicted flattening of the quasar radio luminosity function based on unified schemes (Urry and Padovani, 1995)

DXRBS quasars in the complete sample are in fact currently known at these low powers, and this will put strong constraints on the quasar radio luminosity function. For comparison, the radio luminosity function derived by Urry and Padovani (1995) from the 2 Jy sample (the only published high frequency sample with relatively complete redshift information) included only one source at $L_r < 10^{33.5} \text{ erg s}^{-1} \text{ Hz}^{-1}$, a power which coincides roughly with the predicted flattening of the luminosity function based on unified schemes. Four of these low-power objects are in a luminosity range never before reached for quasars: $10^{31.5} < L_r < 10^{32.5} \text{ erg s}^{-1} \text{ Hz}^{-1}$, the former being the expected minimum luminosity of quasars assuming these objects are beamed FR II radio galaxies.

Perlman et al. (1998) discussed the finding of a large fraction ($\sim 25\%$) of X-ray bright ($\log L_x/L_r > -6$ or $\alpha_{rx} < 0.78$) FSRQ in the DXRBS, and termed them high-energy peaked FSRQ (HFSRQ), stressing the similarity in their broad-band spectral shapes to the high-energy peaked BL Lacs. The fraction of HFSRQ in the DXRBS is now $\sim 25\%$, taking into account the effect of the WGACAT sky coverage. By comparison, the previously known complete samples included very few of these objects (3% in total). The reason for this discrepancy is because DXRBS is the first X-ray survey which included the radio spectral slope in its identification process, thus for the first time allowing the identification of a sample of X-ray emitting FSRQ. But further research on other samples has shown that the X-ray/radio luminosity distribution of DXRBS FSRQ is not anomalous. A slightly larger percentage of these objects is found among the FSRQ in the RGB survey, which goes to somewhat larger values of L_x/L_r but at higher X-ray flux than DXRBS (Padovani et al., 2002). Moreover, subsequent archival research on the *Einstein* EMSS and Slew samples has also shown similar fractions of HFSRQ (Perlman et al., 2001; Wolter and Celotti, 2001).

As regards BL Lacs, DXRBS will be providing the first complete radio-selected sample down to ~ 50 mJy, an improvement of a factor of 20 in flux over the 1 Jy sample, still the only sizeable BL Lac radio-selected sample. The similar improvement in radio powers will allow us to extend the radio luminosity function of radio-selected BL Lacs down to $L_r \sim 10^{30} - 10^{31}$ erg s $^{-1}$ Hz $^{-1}$, again getting close to the expected minimum powers according to unified schemes. Moreover, due to their low X-ray fluxes, DXRBS BL Lacs are also reaching more than an order of magnitude lower L_x than, for example, the EMSS or Slew samples.

Chapter 3

The Separation of BL Lacs and Radio Galaxies

Most current blazar surveys separate BL Lacs and radio galaxies based on their Ca H&K break value following Marchã et al. (1996). These authors proposed to expand the Ca H&K break limit for BL Lacs from 25%, the value previously suggested by Stocke et al. (1991) for BL Lacs in the EMSS, up to 40% in order to additionally include in surveys radio sources with a strong host galaxy contribution which might hide (intrinsically) weak BL Lacs.

The Ca H&K break values proposed by both Stocke et al. and Marchã et al. were rather arbitrary. Based on the studies of Dressler and Sheckman (1987), who showed that non-active elliptical galaxies had a Ca H&K break value of $\sim 50\%$, the EMSS chose a limit of 25% for BL Lacs to ensure the presence of a ‘substantial’ non-thermal jet continuum in addition to the thermal emission from the host galaxy. Marchã et al. examined the data of Dressler and Sheckman and found that less than 5% of their galaxies had a Ca H&K break value below 40%. Based on this they argued that it was reasonable to assume that *all* radio galaxies with Ca H&K break values less than 40% had some extra source of continuum.

The motivation for the work presented in this chapter was to show for the first time what determines the strength of the Ca H&K break in BL Lacs and radio galaxies, and so to assess which value discriminates between the two classes in a physically meaningful way. I start by simulating optical BL Lac continua and by

relating the Ca H&K break value of BL Lacs to their optical core emissions (Section 3.1). Then I expand these studies also to the radio and X-ray band (Section 3.2). I conclude that the Ca H&K break value of BL Lacs and radio galaxies is a suitable indicator of orientation and determine a possible relation between the Ca H&K break value and viewing angle (Section 3.3). Finally, I apply the results to the two BL Lac subclasses, LBL and HBL (Section 3.4). I summarize and discuss the results in Section 3.5. The work presented in this chapter has been recently published as Landt, Padovani & Giommi 2002 (MNRAS 336, 945) .

3.1 The Optical BL Lac Continuum

According to current unified schemes for radio-loud AGN, BL Lacs are beamed FR I radio galaxies. Therefore, in their optical spectra we see the amplified non-thermal emission from the jet in addition to thermal emission from the underlying host galaxy, normally a luminous elliptical (e.g. Wurtz et al., 1996). The non-thermal and thermal components have different shapes, and their relative strengths determine the observed BL Lac continuum. The jet component can be locally best described by a single power law of the form $S_\nu \propto \nu^{-\alpha_\nu}$ (or equivalently $S_\lambda \propto \lambda^{-\alpha_\lambda}$, where $\alpha_\lambda = 2 - \alpha_\nu$). The spectrum of the host galaxy, on the other hand, has an approximate black body shape and contains absorption features typical of ellipticals.

For my studies I have simulated possible BL Lac continua. For this purpose, I assumed the jet overlaying the elliptical host galaxy to vary in intensity and optical spectral slope. I used values between 0.2 and 100 for the jet/galaxy ratio (defined at 5500 Å), and assumed for the optical spectral slope the three cases $\alpha_\nu = 0, 1, 2$, following the results of Falomo et al. (1994), and included additionally the extreme case of $\alpha_\nu = 4$.

Fig. 3.1 shows the resulting simulated BL Lac spectra representatively for a jet of optical spectral slope $\alpha_\lambda = \alpha_\nu = 1$. As the jet steadily increases relative to the galaxy, two effects are visible. The shape of the BL Lac continuum resembles more and more a power-law spectrum and the galactic absorption features become weaker. One prominent absorption feature typically seen in the spectra of elliptical galaxies is the Ca H&K break located at ~ 4000 Å rest frame wavelength. This feature, also referred to as “Ca II break” or “contrast”, is defined as $C = (f_+ - f_-)/f_+$, where f_- and f_+ are the fluxes in the rest frame wavelength regions 3750 – 3950 Å and 4050 – 4250 Å respectively. Its value in normal non-active elliptical galaxies is found to be on average ~ 0.5 (Dressler and Shectman, 1987). In BL Lacs, the value of the Ca H&K break is decreased by the non-thermal jet emission. Note that the Ca

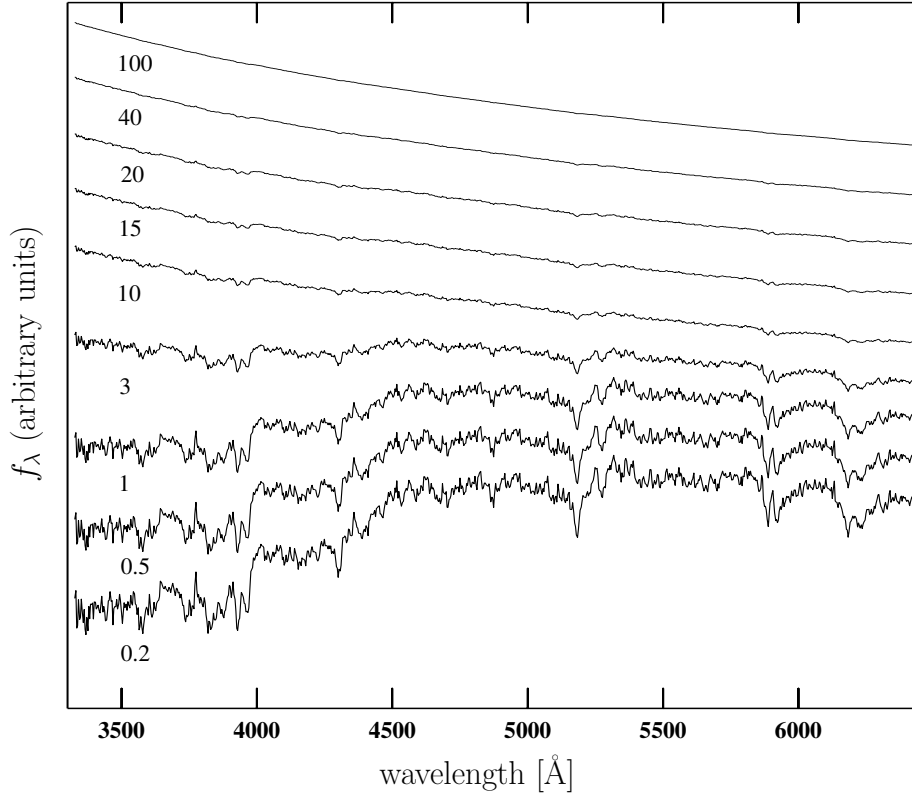


FIGURE 3.1. Simulated BL Lac spectra f_λ vs. λ for a jet of optical spectral slope $\alpha_\lambda = \alpha_\nu = 1$ and of increasing flux relative to the underlying host galaxy. The assumed jet/galaxy ratios (defined at 5500 Å) are from bottom to top: 0.2, 0.5, 1, 3, 10, 15, 20, 40, and 100.

H&K break value is related to the discontinuity at 4000 Å ($D(4000)$; Bruzual, 1983) by $C = 1 - 1/D(4000)$, and is measured in spectra plotted as f_ν versus ν . However, if measured in spectra plotted as f_λ versus λ , the relation $C_\nu = 0.14 + 0.86 \cdot C_\lambda$ can be used to convert one to the other.

In order to quantify how the amplified jet emission changes the Ca H&K break value, I measured this feature in each of the simulated spectra. In the case where the jet dominates the object's spectrum, the Ca H&K break value was set equal to zero (its minimum possible value in these simulations). For every case of α_ν , there is a significant ($P > 99.99\%$) linear anticorrelation between the assumed jet/galaxy ratio and the Ca H&K break value (dotted lines in Fig. 3.2, left panel).

To assess how well this result is reproduced by observations information is required on Ca H&K break value and jet/galaxy ratios for a sizeable sample of BL Lacs. Observational jet/galaxy ratios were obtained from the imaging studies of

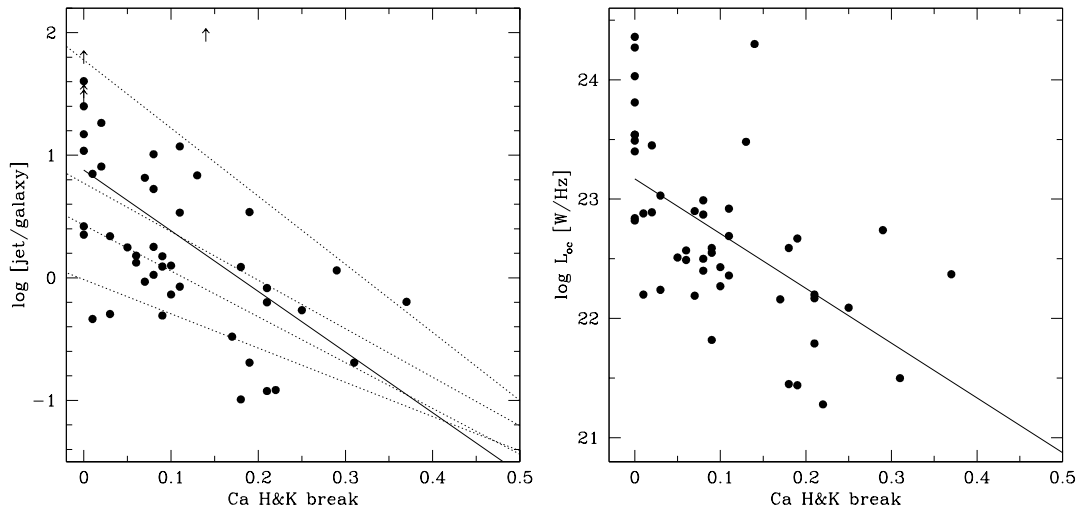


FIGURE 3.2. **Left panel:** The jet/galaxy flux ratio (at 5500 Å) versus the Ca H&K break value for BL Lacs from Urry et al. (2000). Arrows indicate lower limits on the jet/galaxy ratio. The solid line represents the observed correlation. Dotted lines represent the correlations obtained from the simulations for optical spectral slopes $\alpha_\nu = 0, 1, 2, 4$ (from bottom to top). **Right panel:** The optical core luminosity versus the Ca H&K break value for BL Lacs from Urry et al. (2000). The solid line represents the observed correlation.

Urry et al. (2000) which allow the separation of the core flux from that of the host galaxy. These authors used the *HST* Wide Field Planetary Camera 2 (WFPC 2) to image in snapshot mode a sample of 132 BL Lacs from different radio and X-ray surveys. Most of their images were taken in the F702W filter (similar to Cousin R filter), but those already observed in F814W during an earlier *HST* cycle were reobserved in F606W (a filter similar to Johnson V). Jet/galaxy ratios at 5500 Å were derived by converting R magnitudes to V magnitudes. A value $V - R = 0.3$ was assumed for the core component (Urry et al., 2000), while for the host galaxy magnitudes I used the redshift-dependent $V - R$ values as tabulated by Urry et al. (2000) (see their Table 2). Ca H&K break values for 48 of these sources were derived from the literature and also from my own measurements (see Section 3.2).

For these BL Lacs Fig. 3.2, left panel, plots the jet/galaxy ratio versus Ca H&K break value. An analysis using the ASURV package (Feigelson and Nelson, 1985), which was employed in this work whenever censored data were present, shows that these two quantities are significantly ($P > 99.99\%$) anticorrelated, in agreement with the simulations. Furthermore, a partial correlation analysis using the algorithms for

censored data sets developed by Akritas and Siebert (1996) shows that this correlation is not induced by a common redshift dependence. Fig. 3.2, left panel, plots the observed correlation between optical jet/galaxy ratio and Ca H&K break value (solid line) in addition to the correlations obtained from the simulations (dotted lines). A comparison between the two indicates that the scatter in the observed correlation (~ 0.6) is likely induced by jets of different optical spectral slopes.

Using both simulations and observational data I have shown that the Ca H&K break value in BL Lacs anticorrelates with optical jet/galaxy ratio. At this point the question arises if this correlation could possibly mask a correlation between jet emission and Ca H&K break value or between host galaxy emission and Ca H&K break value. Urry et al. (2000) find that the distribution of the absolute magnitudes of BL Lac host galaxies has a relatively small dispersion $\Delta M_R = 0.6$ mag. This result is based on detected host galaxies of a very large number of BL Lacs (72 sources) covering the redshift range $0.024 \leq z \leq 0.7$. The relatively small dispersion found by Urry et al. implies that the luminosity of BL Lac host galaxies can be regarded as roughly constant. Therefore, the observed increase in jet/galaxy ratio (with decreasing Ca H&K break) can be related directly to an increase in jet power. Indeed, for the sample under study I find that, on one hand, the optical core luminosity (from Urry et al. (2000)) is significantly ($P > 99.9\%$) anticorrelated with the Ca H&K break value (see Fig. 3.2, right panel), and that, on the other hand, no significant ($P = 88\%$) correlation is present between host galaxy luminosity and Ca H&K break value.

3.2 From a BL Lac to a Radio Galaxy

In the previous section, I have shown that the Ca H&K break value in BL Lacs is decreased due to an increase in optical jet power. Here I want to investigate this further by relating the Ca H&K break value also to the radio and X-ray properties of both BL Lacs and low-luminosity (FR I) radio galaxies.

For this purpose I have collected from the literature and from our own data information on the Ca H&K break value, *ROSAT* X-ray band (0.1 – 2.4 keV) flux, total radio flux at 1.4 (NVSS) and 5 GHz, and core radio flux. From these I have computed the luminosities, radio core dominance parameter and radio spectral index α_r which are listed in Table 3.1 (see footnotes to Table 3.1 for details). Table 3.1 also gives the references for the Ca H&K break value, and the radio core and X-ray fluxes. The radio core flux measurements are largely based on observations with the Very Large Array (VLA). The total radio flux at 5 GHz was obtained from the

GB6 survey (Gregory et al., 1996), with the following exceptions: for the 1 and 2 Jy objects the values given in Stickel et al. (1994) and Wall and Peacock (1985) were used, for the EMSS objects I used the measurements given in Stocke et al. (1991), for Slew objects not detected in the GB6 the values given in Perlman et al. (1996a) were taken, and for southern DXRBS sources the total radio flux at 5 GHz from the PMN survey (Griffith and Wright, 1993) is given.

The BL Lacs and FR I radio galaxies have been selected from the following surveys: 1 Jy survey (Stickel et al., 1994), 2 Jy survey (Tadhunter et al., 1993), 200 mJy sample (Marchã et al., 1996), EMSS (Rector et al., 1999, 2000), Slew survey (Perlman et al., 1996a), RGB (Laurent-Muehleisen et al., 1998), and DXRBS (Perlman et al., 1998; Landt et al., 2001). From these surveys I chose in fact all objects with a rest frame equivalent width of the strongest emission line $< 60 \text{ \AA}$, an available Ca H&K break value, and *both* a radio core and X-ray flux measurement. Available fluxes in both radio and X-ray band were required in order to avoid comparing two different sets of objects in the luminosity – Ca H&K break plane (see following subsection). However, while for a particular object it is always possible to obtain an upper limit on its *ROSAT* X-ray luminosity from the exposure maps of the RASS (Voges et al., 1999), this is not the case for its radio core luminosity and the object will not be included in this sample. The limit on the emission line strength is based on the results of Marchã et al. (1996) and was chosen to exclude quasars.

An exclusion of objects whose power is typical of FR II radio galaxies can be based on the value of the extended radio emission. Following the results of Owen and Ledlow (1994), a value of $L_{\text{ext}} = 10^{25.6} \text{ W Hz}^{-1}$ (transformed from 1400 MHz using a radio spectral index $\alpha_r = 0.8$) was chosen to separate the less luminous FR I radio galaxies from the more luminous FR II radio galaxies. These authors find that basically only FR II radio galaxies have an extended radio emission above this value. The extended radio power was computed as $L_{\text{ext}} = L_{\text{tot}} - L_{\text{rc}}$, where L_{tot} and L_{rc} are the object's total and core radio powers at 5 GHz respectively. Note that it is *assumed* that these low-power radio galaxies are FR Is, although no information on their radio morphology is available. Bondi et al. (2001) have indeed shown that the nuclear properties of the weak-lined radio galaxies in the 200 mJy sample are consistent with those of FR Is, although their radio morphology might not be consistent in all cases with an FR I classification. The sample under study comprises 83 objects. However, in Table 3.1, I additionally list 7 objects that meet the current classification criteria for a BL Lac but have extended radio powers typical of FR II radio galaxies. These sources will be used only for the comparison studies presented in Section 3.4.

I measured the Ca H&K break values for objects from the 1 Jy, 2 Jy, Slew survey, and DXRBS on the reduced and calibrated spectra. For sources from the 200 mJy sample, EMSS, and RGB, I used the Ca H&K break values listed in the literature. Note that I excluded from this study sources with errors on the Ca H&K break value > 0.2 . The error on the Ca H&K break listed in Table 3.1 represents the 1σ limit and was computed based on the signal-to-noise ratio (SNR) blueward and redward of the feature. The error is on average 0.07 for the sources included in this study. No errors were available for sources from the 200 mJy sample and RGB. Nevertheless, the spectra of the RGB objects are quoted to have a SNR $\gtrsim 30$ (Laurent-Muehleisen et al., 1998) and therefore the error on the Ca H&K break value for these sources is expected to be small.

The sample under study is highly heterogeneous, being a collection of surveys with different selection bands and flux limits. However, similarly to the studies of Padovani and Giommi (1996), this approach offers the possibility to maximize the coverage of the parameter space and therefore to look for correlations in a way which would not be possible by considering individual samples separately. This approach is acceptable whenever the parameter values or correlations studied are not strongly influenced by the sample selection.

TABLE 3.1. BL Lacs and Radio Galaxies

Survey	Name	z	C	σ	Ref. C	$\log L_x$ 1 keV [W/Hz]	Ref. f_x	$\log L_{rc}$ 5 GHz [W/Hz]	Ref. f_{rc}	Radio array	$\log L_{ext}$ 5 GHz [W/Hz]	$\log R$ 5 GHz	α_r
(1)	(2)	(3)	(4)	(5)	(6)	(7)	(8)	(9)	(10)	(11)	(12)	(13)	(14)
1 Jy	0118–272	0.559	0.00	0.02	v	20.45	a	26.94	m	IV	26.81	0.13	–0.16
1 Jy	0138–097	0.733	0.00	0.03	v	20.56	a	27.12	m	IV	26.99	0.13	–0.50
1 Jy	0218+357	0.685	0.12	0.09	v	< 20.51	A	27.25	o	XI	27.07	0.18	0.31
1 Jy	0828+493	0.548	0.08	0.06	v	< 20.29	A	26.55	y	II	26.78	–0.23	–0.88
1 Jy	1538+149	0.605	0.00	0.03	v	20.77	x	27.13	y	II	27.19	–0.06	–0.28
1 Jy	1823+568	0.664	0.02	0.03	v	21.02	x	27.05	y	II	27.31	–0.26	–0.13
2 Jy	0625–53	0.054	0.15	0.12	v	19.32	b	23.75	p	IX	25.37	–1.62	1.06
2 Jy	0915–11	0.054	0.36	0.01	w	19.84	b	24.45	p	VII	26.24	–1.79	0.82
200 mJy	0055+300	0.015	0.46		u	< 16.87	A	23.22	n	X	22.93	0.29	0.90
200 mJy	0116+319	0.060	0.45		u	< 18.09	A	25.09	n	X	25.11	–0.02	0.42
200 mJy	0149+710	0.022	0.33		u	17.86	c	23.78	q	III	23.87	–0.09	–0.10
200 mJy	0210+515	0.049	0.15		u	19.19	c	24.22	q	III	24.09	0.13	0.04
200 mJy	0651+410	0.021	0.39		u	< 17.19	A	23.74	o	IV	23.39	0.35	–0.51
200 mJy	0651+428	0.126	0.17		u	18.93	c	24.97	q	III	24.55	0.42	0.06
200 mJy	0733+597	0.041	0.49		u	< 17.88	A	24.23	q	III	23.97	0.26	0.36
200 mJy	1055+567	0.410	≤ 0.05		u	20.77	c	26.11	q	III	25.76	0.35	–0.10
200 mJy	1101+384	0.031	0.24		u	20.28	d	24.40	q	VIII	23.71	0.69	0.05

TABLE 3.1. BL Lacs and Radio Galaxies

Survey	Name	z	C	σ	Ref. C	$\log L_x$ 1 keV [W/Hz]	Ref. f_x	$\log L_{rc}$ 5 GHz [W/Hz]	Ref. f_{rc}	Radio array	$\log L_{ext}$ 5 GHz [W/Hz]	$\log R$ 5 GHz	α_r
(1)	(2)	(3)	(4)	(5)	(6)	(7)	(8)	(9)	(10)	(11)	(12)	(13)	(14)
200 mJy	1133+704	0.046	0.31		u	19.79	d	24.11	q	III	24.09	0.02	0.15
200 mJy	1144+352	0.063	0.37		u	18.07	d	24.75	q	III	24.75	0.00	-0.03
200 mJy	1217+295	0.002	0.42		u	17.76	A	21.69	q	VIII	20.86	0.83	0.13
200 mJy	1241+735	0.075	0.43		u	< 15.00	A	24.52	n	X	24.70	-0.18	-0.13
200 mJy	1418+546	0.151	0.03		u	19.20	d	26.10	q	VIII	25.46	0.64	-0.62
200 mJy	1652+398	0.031	0.07		u	19.59	d	24.79	m	IV	23.46	1.33	0.10
200 mJy	1744+260	0.147	≤ 0.3		u	< 18.74	A	25.11	n	X	25.09	0.02	0.23
200 mJy	1807+698	0.046	0.03		u	18.43	d	25.14	m	IV	24.79	0.35	-0.12
200 mJy	2320+203	0.038	0.47		u	17.63	d	23.85	q	III	24.18	-0.33	0.03
EMSS	MS0011.7+0837	0.162	0.30	0.04	e	19.01	e	24.64	e	II	24.80	-0.16	1.13
EMSS	MS0122.1+0903	0.338	0.22	0.18	s	19.18	f	23.88	s	II	< 23.74	> 0.14	
EMSS	MS0158.5+0019	0.298	0.09	0.02	s	20.56	f	24.37	z	II	24.35	0.02	0.13
EMSS	MS0257.9+3429	0.246	0.25	0.06	s	19.13	f	24.34	z	II	23.70	0.64	0.10
EMSS	MS0317.0+1834	0.190	0.21	0.06	s	19.57	f	24.05	z	II	24.21	-0.16	0.24
EMSS	MS0419.3+1943	0.516	0.11	0.07	s	20.64	f	24.92	s	II	24.23	0.69	0.09
EMSS	MS0607.9+7108	0.267	0.09	0.04	s	19.04	f	24.52	z	II	24.43	0.09	0.31
EMSS	MS0737.9+7441	0.314	0.00	0.01	s	20.51	f	24.86	z	II	24.48	0.38	-0.02
EMSS	MS0922.9+7459	0.638	0.20	0.07	s	20.57	f	24.88	s	II	< 24.03	> 0.85	
EMSS	MS1019.0+5139	0.141	0.23	0.05	s	19.73	e	23.31	s	V	22.29	1.02	0.61
EMSS	MS1050.7+4946	0.140	0.32	0.07	s	19.46	e	24.50	s	V	24.18	0.32	0.15
EMSS	MS1154.1+4255	0.172	0.33	0.10	s	18.95	e	24.08	e	V	23.17	0.91	0.57
EMSS	MS1207.9+3945	0.616	0.07	0.04	s	20.90	f	25.53	s	V	24.59	0.94	0.95
EMSS	MS1209.0+3917	0.602	0.15	0.13	s	20.27	e	25.28	e	V	< 24.31	> 0.97	0.67
EMSS	MS1221.8+2452	0.218	0.02	0.02	s	19.51	f	24.60	z	II	24.14	0.46	-0.02
EMSS	MS1229.2+6430	0.164	0.18	0.09	s	20.16	f	24.56	z	II	24.18	0.38	0.27
EMSS	MS1235.4+6315	0.297	0.05	0.07	s	19.87	f	24.62	s	V	< 23.24	> 1.38	0.47
EMSS	MS1407.9+5954	0.496	0.10	0.05	s	20.12	f	25.15	z	II	24.97	0.18	0.64
EMSS	MS1443.5+6349	0.298	0.22	0.06	s	19.98	f	24.40	z	II	24.40	0.00	0.39
EMSS	MS1458.8+2249	0.235	0.00	0.01	s	20.14	f	24.69	z	II	24.37	0.32	0.07
EMSS	MS1534.2+0148	0.311	0.11	0.06	s	20.29	f	25.00	z	II	24.84	0.16	0.61
EMSS	MS1552.1+2020	0.273	0.13	0.09	s	20.71	f	24.94	z	II	24.73	0.21	0.60
EMSS	MS1757.7+7034	0.406	0.01	0.00	s	20.68	f	24.78	s	II	< 24.27	> 0.51	
EMSS	MS2143.4+0704	0.235	0.10		j	19.94	f	24.93	z	II	24.70	0.23	0.57
EMSS	MS2347.4+1924	0.515	0.18	0.16	s	20.28	s	24.57	s	II	23.88	0.69	0.36
SLEW	1ES0120+340	0.272	0.00	0.04	v	21.41	h	25.03	r	VI	24.01	1.02	0.24
SLEW	1ES0229+200	0.139	0.21	0.07	v	20.34	g	24.60	r	VI	22.97	1.63	0.48
SLEW	1ES0502+675	0.416*	0.00	0.04	v	21.70	h	25.21	q	I	24.52	0.69	0.04
SLEW	1ES0806+524	0.138	0.00	0.04	v	20.31	h	25.01	q	III	24.63	0.38	0.03
SLEW	1ES0927+500	0.188	0.03	0.07	v	20.73	i	24.36	q	III	24.04	0.32	-0.02
SLEW	1ES1255+244	0.140	0.08	0.11	v	20.92	r	23.80	r	VI	22.65	1.15	0.55
SLEW	1ES1426+428	0.129	0.01		j	20.75	h	24.20	q	I	24.09	0.32	0.35
SLEW	1ES1440+122	0.162	0.18		j	20.22	h	24.73	q	VIII	23.71	1.02	0.26
SLEW	1ES1741+196	0.083	0.12	0.05	v	19.55	h	24.67	q	III	24.73	-0.06	-0.07
SLEW	1ES1853+671	0.212	0.09	0.05	v	20.20	r	24.37	r	VI	< 22.87	> 1.50	-0.07
SLEW	1ES2326+174	0.213	0.06	0.05	v	20.50	r	24.55	r	VI	24.23	0.32	-0.03
RGB	RGBJ0110+418	0.096	0.32		j	19.08	j	23.88	q	I	23.88	0.00	0.70

TABLE 3.1. BL Lacs and Radio Galaxies

Survey	Name	z	C	σ	Ref. C	log L_x 1 keV [W/Hz]	Ref. f_x	log L_{rc} 5 GHz [W/Hz]	Ref. f_{rc}	Radio array	log L_{ext} 5 GHz [W/Hz]	log R 5 GHz	α_r
(1)	(2)	(3)	(4)	(5)	(6)	(7)	(8)	(9)	(10)	(11)	(12)	(13)	(14)
RGB	RGBJ0152+017	0.080	0.29		j	19.22	j	24.26	q	VIII			0.12
RGB	RGBJ0314+247	0.054	0.30		j	18.50	j	22.88	q	VIII	23.65	-0.77	-1.16
RGB	RGBJ0656+426	0.059	0.36		j	18.84	j	24.33	q	III	24.72	-0.39	0.53
RGB	RGBJ0710+591	0.125	0.22		j	20.49	j	24.39	q	I	24.54	-0.15	0.54
RGB	RGBJ0806+728	0.098	0.16		j	19.23	j	23.93	q	I	23.67	0.26	0.39
RGB	RGBJ0820+488	0.130	0.41		j	18.96	j	23.59	q	I	24.84	-1.25	0.59
RGB	RGBJ1136+676	0.136	0.20		j	20.45	j	24.50	q	I	23.81	0.69	-0.04
RGB	RGBJ1253+509	0.121	0.49		j	18.93	j	23.67	q	I	24.33	-0.66	0.51
RGB	RGBJ1324+576	0.115	0.41		j	19.36	j	24.16	q	I	23.98	0.18	0.04
RGB	RGBJ1417+257	0.237	0.00		j	20.95	j	25.05	q	VIII			0.67
RGB	RGBJ1427+541	0.105	0.39		j	18.68	j	24.07	q	VI	23.65	0.42	0.24
RGB	RGBJ1516+293	0.130	0.32		j	19.30	j	24.41	q	I			
RGB	RGBJ1532+302	0.064	0.29		j	19.09	j	23.92	q	III	23.16	0.76	-0.01
RGB	RGBJ1745+398	0.267	0.17		j	19.86	j	25.64	q	III	25.70	-0.06	0.75
RGB	RGBJ1750+470	0.160	0.29		j	19.71	j	24.08	q	I	24.66	-0.58	0.59
RGB	RGBJ1823+334	0.108	0.49		j	19.27	j	23.22	q	I	24.50	-1.28	0.91
RGB	RGBJ1841+591	0.530	0.17		j	20.24	j	24.94	q	I			
RGB	RGBJ2241+048	0.069	0.45		j	18.36	j	23.94	q	III	24.14	-0.20	0.42
RGB	RGBJ2250+384	0.119	0.07		j	19.76	j	24.56	q	III	24.56	0.00	-0.11
RGB	RGBJ2322+346	0.098	0.33		j	19.05	j	24.10	q	I	24.30	-0.20	0.17
RGB	RGBJ2323+205	0.041	0.48		j	17.70	j	23.92	q	III	24.25	-0.33	0.03
DXRBS	WGAJ0032.5-2849	0.324	0.22	0.08	k	19.11	k	25.79	t	IX	24.88	0.91	0.08
DXRBS	WGAJ0340.8-1814	0.195	0.40	0.08	k	17.85	k	24.53	t	IX	25.37	-0.84	0.57
DXRBS	WGAJ0428.8-3805	0.150	0.32	0.05	k	17.99	k	24.50	t	IX	24.24	0.26	-0.03
DXRBS	WGAJ0528.5-5820	0.254	0.38	0.18	l	18.76	k	25.01	t	IX	25.29	-0.28	0.46
DXRBS	WGAJ0624.7-3230	0.252	0.22	0.05	k	19.26	k	24.72	t	IX	25.29	-0.47	-0.54
DXRBS	WGAJ0816.0-0736	0.040	0.37	0.18	k	16.98	k	23.41	t	IX	23.20	0.21	-0.28
DXRBS	WGAJ1057.6-7724	0.181	0.48	0.18	l	18.14	k	25.38	t	IX	25.66	-0.28	0.71
DXRBS	WGAJ1311.3-0521	0.160	0.33	0.12	l	18.61	l	24.53	t	IX	24.30	0.23	0.37
DXRBS	WGAJ1457.9-2124	0.319	0.45	0.20	l	19.57	l	25.25	t	IX	25.80	-0.55	0.79
DXRBS	WGAJ2317.4-4213	0.056	0.52	0.08	k	16.58	k	23.28	t	IX	24.22	-0.94	0.53

columns: (1) survey, (2) object name, (3) redshift, (4) Ca H&K break value (measured in spectra f_λ vs. λ), (5) 1σ error on the Ca H&K break value, (6) reference for Ca H&K break measurement, (7) X-ray luminosity at 1 keV (*ROSAT* X-ray band (0.1 - 2.4 keV) flux transformed to 1 keV and luminosity k-corrected assuming spectral index $\alpha_x = 1.2$), (8) reference for *ROSAT* X-ray band flux, (9) radio core luminosity at 5 GHz (transformed to 5 GHz and k-corrected assuming α_r from column (14) or else $\alpha_r = 0.3$), (10) reference for radio core flux, (11) radio array used for observations of radio core flux (see below), (12) extended radio luminosity at 5 GHz, (13) radio core dominance, (14) radio spectral index between 1.4 (NVSS) and 5 GHz (computed from the object's total fluxes)

radio array: (I) VLA A at 5 GHz, (II) VLA A at 1.5 GHz, (III) VLA BnA at 5 GHz, (IV) VLA B at 5 GHz, (V) VLA B at 1.5 GHz, (VI) VLA CnB at 5 GHz, (VII) VLA C at 5 GHz, (VIII) VLA D at 5 GHz, (IX) ATCA at 5 GHz, (X) MERLIN at 5 GHz, (XI) VLBI at 1.5 GHz

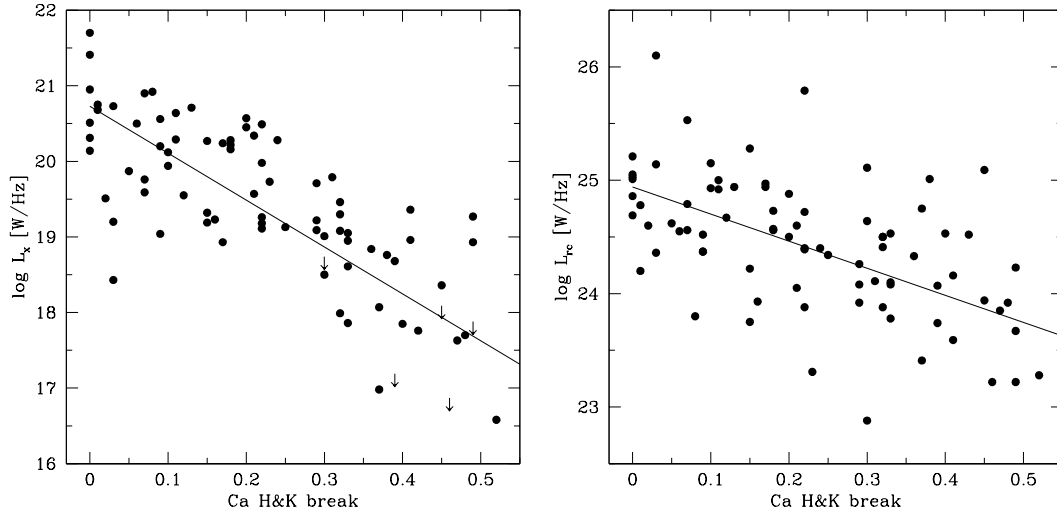


FIGURE 3.3. The 1 keV X-ray luminosity (left panel) and the radio core luminosity at 5 GHz (right panel) versus the Ca H&K break value. Arrows denote upper limits. The solid lines represent the observed correlations. Object 1241+735 is off the plot in the left panel.

references: (a) Siebert et al. (1998), (b) Brinkmann et al. (1994), (c) Brinkmann et al. (1997), (d) Brinkmann et al. (1995), (e) Rector et al. (1999), (f) Perlman et al. (1996b), (g) Nass et al. (1996), (h) Laurent-Muehleisen et al. (1999), (i) Bade et al. (1998), (j) Laurent-Muehleisen et al. (1998), (k) Perlman et al. (1998), (l) Landt et al. (2001), (m) Cassaro et al. (1999), (n) Augusto et al. (1998), (o) Taylor et al. (1996), (p) Morganti et al. (1993), (q) Laurent-Muehleisen et al. (1997), (r) Perlman et al. (1996a), (s) Rector et al. (2000), (t) from ATCA observations of the DXRBS, (u) Marchã et al. (1996), (v) measured on spectrum, (w) Owen et al. (1996), (x) RASS/NVSS-ASDC catalogue (Giommi et al. in prep.), (y) Murphy et al. (1993), (z) Perlman and Stocke (1993), (A) ROSAT All Sky Survey (Voges et al., 1999); upper limit estimated from exposure maps

* this redshift is different from the one published by Perlman et al. (1996a) and was obtained after a careful reinspection of the electronic spectral file

3.2.1 The Radio Core and X-ray Luminosities

In the optical band, the spectrum of a BL Lac is made up of two components, a thermal (galaxy) and a non-thermal (jet) one. But this is not the case for the radio and X-ray bands, where we observe mainly the jet emission. (Though in the X-ray case extended emission from cluster- or group-scale gas can contribute to the observed luminosity.) Therefore, following the results from the previous section, we expect the radio core and X-ray luminosities to increase as the Ca H&K break decreases. Fig. 3.3 shows that this is indeed the case. The Ca H&K break value

is significantly anticorrelated with both the X-ray ($P > 99.9\%$) and radio core luminosity ($P > 99.9\%$). The correlations remain in both cases very strong ($P > 99.9\%$) even if objects with Ca H&K break values $C > 0.4$ are excluded, i.e., objects currently defined as radio galaxies. In addition, I have verified by means of a partial correlation analysis that all significant luminosity - Ca H&K break correlations were not induced by a common redshift dependence. Note also that, since the sources in the sample under study were required to have information on both radio core and X-ray luminosity, the left and right panel of Fig. 3.3 include the *same* number of objects (83 sources).

A similarly strong ($P > 99.9\%$) anticorrelation is present between Ca H&K break value and X-ray luminosity if only BL Lacs and radio galaxies from the DXRBS (21 objects) are considered. Note that not all of these sources have a measured radio core luminosity. Additionally, Caccianiga et al. (1999) found a significant correlation between Ca H&K break value and X-ray luminosity for the BL Lacs and radio galaxies from the REX survey, once sources residing in clusters of galaxies were excluded. Since both the DXRBS and REX are homogeneous flux-limited samples, these results suggest that the luminosity - Ca H&K break correlations present in the sample used in this work are unlikely to be caused by selection effects.

3.2.2 Intrinsic Luminosity Variations or Orientation Effects?

So far I have shown by using observations in the optical, radio and X-ray band that the decrease in Ca H&K break is due to an increase in the object's jet power. In the following I want to investigate *why* BL Lac objects with a low Ca H&K break have more powerful jets than those with higher Ca H&K break values. There are two possible explanations: 1. the spread in jet luminosities is intrinsic to the BL Lac class, and/or 2. the spread in jet luminosities (and Ca H&K break value) is induced by orientation effects.

Which of these two possibilities causes the Ca H&K break value to correlate with jet luminosity can be best determined by using information in the radio band. In this range, measurements on both core and extended jet luminosities are available. This is important, since the two powers are affected in a different way by orientation, but similarly if the jet luminosity range is intrinsic. Beaming, i.e., a change in viewing angle, is known to cause only an increase in core luminosity, but not to affect extended power, since the latter is believed to be radiated isotropically. A change in intrinsic luminosity, on the other hand, would be apparent as an increase in both core and extended radio power (e.g. Giovannini et al., 1988) with decreasing Ca H&K break value. For the objects in the sample under study, no significant

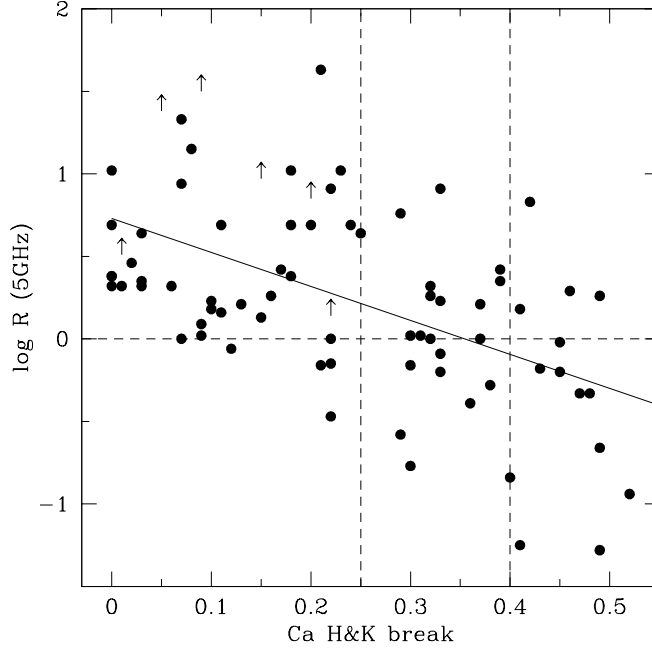


FIGURE 3.4. The core dominance parameter at 5 GHz versus the Ca H&K break value. Arrows denote lower limits. The solid line represents the observed correlation. The horizontal dashed line represents the locus of constant $R = L_{\text{rc}}/L_{\text{ext}} = 1$. The vertical dashed lines represent Ca H&K break values of $C = 0.25$ and 0.4 suggested by Stocke et al. (1991) and Marchã et al. (1996) respectively to discriminate between BL Lacs and radio galaxies.

($P \sim 46\%$) correlation is present between Ca H&K break value and extended radio power L_{ext} . Note that, though the extended radio powers of the selected objects have been limited to $L_{\text{ext}} < 10^{25.6} \text{ W Hz}^{-1}$, the distributions of both core and extended radio powers have similar dispersions $\sigma = 0.7$ and 0.8 respectively. Therefore, a priori there is no reason why the Ca H&K break value should correlate with radio core but not with extended radio emission.

On the other hand, if the Ca H&K break value can indeed be related to the object's viewing angle, it is expected to also correlate with the radio core dominance parameter, thought to be a good orientation indicator. Fig. 3.4 plots for the objects in the sample under study the radio core dominance parameter at 5 GHz versus the Ca H&K break value. The former is defined as $R = L_{\text{rc}}/L_{\text{ext}}$. A significant ($P > 99.9\%$) linear anticorrelation, albeit with a large scatter, is present between the two quantities. The correlation remains very strong even if objects with Ca H&K break values $C > 0.4$ are eliminated.

Wolter et al. (2001) presented a plot similar to the one shown in Fig. 3.4 for BL Lacs and FR I radio galaxies from the REX survey. They obtained for their sample (~ 40 objects) that Ca H&K break value and radio core dominance parameter (at 5 GHz) are only weakly anticorrelated. However, they noted that their radio galaxies were more core-dominated than classical FR Is. In fact, all their objects had radio core dominance parameters $\log R \geq 0$. If I include only the core-dominated objects of the present sample, also the correlation between Ca H&K break value and radio core dominance parameter shown in Fig. 3.4 becomes insignificant ($P = 85\%$).

Fig. 3.4 shows further that the transition between core- and lobe-dominated objects, i.e., between BL Lacs and FR I radio galaxies, seems to occur rather smoothly as the Ca H&K break value (and therefore the viewing angle) changes. In fact, in the range formerly defined as the BL Lac regime ($0 \leq C \leq 0.25$) only 11% of the objects are lobe-dominated ($\log R < 0$), whereas this ratio increases in the Ca H&K break value ranges $0.25 < C \leq 0.4$ and $C > 0.4$ to 40% and 69% respectively. Therefore, the objects newly included by Marchã et al. (1996) with Ca H&K break values $0.25 < C \leq 0.4$ seem to represent the long-sought population intermediate between the ‘classical’ BL Lacs and the FR I radio galaxies.

Further support for the assumption that the range in Ca H&K break values represents a range in viewing angles can be found by using the results of Zirbel and Baum (1995) and Hardcastle and Worrall (1999). Zirbel and Baum (1995) obtained for a sample of 81 FR I radio galaxies a mean logarithmic radio core luminosity of $23.4 \pm 1.0 \text{ W Hz}^{-1}$. This is consistent with the value of $\log L_{\text{rc}} = 23.8 \pm 0.3 \text{ W Hz}^{-1}$ that the correlation in Fig. 3.3, right panel, gives for $C = 0.5$, i.e., for the radio galaxies. Hardcastle and Worrall (1999) could detect in *ROSAT* pointed observations a core in the X-ray band for 15 of the FR I radio galaxies studied (see their Table 4). For these I obtain a mean *ROSAT* X-ray core luminosity $\log L_x = 17.2 \pm 0.9 \text{ W Hz}^{-1}$. This is in good agreement with the value of $\log L_x = 17.6 \pm 0.5 \text{ W Hz}^{-1}$ that the correlation in Fig. 3.3, left panel, gives for $C = 0.5$. Therefore, the luminosity - Ca H&K break correlations obtained including both BL Lacs and FR I radio galaxies seem to reproduce well the average radio and X-ray luminosities of (larger samples of) FR I radio galaxies.

3.3 The Relation between Ca H&K Break and Viewing Angle

3.3.1 Luminosity Ratios and Viewing Angle

I now want to investigate how the Ca H&K break value might be used to constrain the viewing angle. I have then simulated for the radio and X-ray band the expected luminosity ratio between the BL Lac object and the parent radio galaxy as the viewing angle ϕ_{GAL} changes. For this purpose I have used the formula given in Capetti and Celotti (1999):

$$L_{\text{BL}}/L_{\text{GAL}} = [(1 - \beta \cdot \cos\phi_{\text{GAL}})/(1 - \beta \cdot \cos\phi_{\text{BL}})]^{(p+\alpha)},$$

where β is the bulk velocity in units of the speed of light and ϕ the angle between the velocity vector of the jet and the line of sight. I chose the case of a continuous jet ($p = 2$). For the simulations in the radio band I assumed a radio spectral index $\alpha_{\text{r}} = 0.2$, corresponding to the mean value for the objects in the sample under study, while for the X-ray band $\alpha_{\text{x}} = 1.4$ has been chosen, following the results of Padovani and Giommi (1996). The simulations were performed assuming the three cases $\phi_{\text{BL}} = 0^\circ$, 10° , and 20° , and a changing ϕ_{GAL} up to a maximum value of 90° . In these studies, the quantity ϕ_{BL} is fixed and represents the angle below which the jet/galaxy ratio is so high that the Ca H&K break value is constant and equal to zero. Only ϕ_{GAL} is assumed to change as the Ca H&K break value increases. For each case of ϕ_{BL} jet Lorentz factors $\Gamma = 1/\sqrt{1 - \beta^2} = 2, 3$ and 4 were assumed. The results for the radio and X-ray band are shown in Fig. 3.5, representatively for the case of $\phi_{\text{BL}} = 10^\circ$ and Lorentz factor $\Gamma = 3$.

TABLE 3.2. **Average viewing angles of radio galaxies**

BL Lac angle:	0°	10°	20°
$\Gamma = 4$	32°	40°	58°
$\Gamma = 3$	44°	50°	66°
$\Gamma = 2$	72°	77°	$> 90^\circ$

The best fits in Fig. 3.3 give a maximum ratio of $\log L_{\text{BL}}/L_{\text{GAL}} = 3.11 \pm 0.30$ and 1.20 ± 0.20 for the X-ray and radio band respectively, where L_{BL} is the luminosity at the Ca H&K break value $C = 0$ and L_{GAL} the luminosity at $C = 0.5$. The simulations show that in all three cases assumed for ϕ_{BL} and Γ it is possible to reproduce these two ratios within their 2σ errors simultaneously, i.e., with the same

Lorentz factor and approximately with the same maximum viewing angle. The resulting values are listed in Table 3.2. The derived viewing angles represent the angles under which we expect to observe on average an FR I radio galaxy with a Ca H&K break value of $C = 0.5$. These are not to be confused with maximum viewing angles for FR I radio galaxies, which can be larger, or with the critical viewing angle, i.e., the angle separating BL Lacs from FR I radio galaxies. From Table 3.2 we see that the case of a starting BL Lac viewing angle $\phi_{\text{BL}} = 20^\circ$ and a Lorentz factor $\Gamma = 2$ is unphysical, since it gives typical viewing angles for radio galaxies above 90° . Higher Lorentz factors than the ones simulated here would result in smaller angles for the radio galaxies. Similarly for the case of $p = 3$, describing a moving, isotropic source.

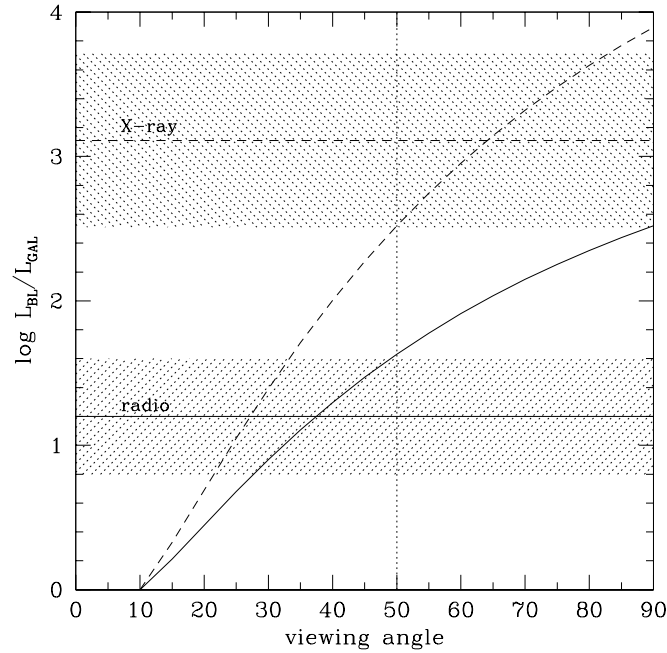


FIGURE 3.5. Simulated $L_{\text{BL}}/L_{\text{GAL}}$ ratios in the X-ray (dashed line) and radio band (solid line) for a Lorentz factor $\Gamma = 3$, assuming a fixed BL Lac viewing angle $\phi_{\text{BL}} = 10^\circ$ and a changing FR I galaxy viewing angle ϕ_{GAL} (see text for details). Horizontal lines indicate the ratios inferred from Fig. 3.3 in the X-ray (dashed line) and radio band (solid line) respectively. The 2σ error on the ratios is shown by the shaded areas. The vertical dotted line represents the FR I galaxy viewing angle at which the observed $L_{\text{BL}}/L_{\text{GAL}}$ ratios in the radio and X-ray band are reproduced approximately simultaneously.

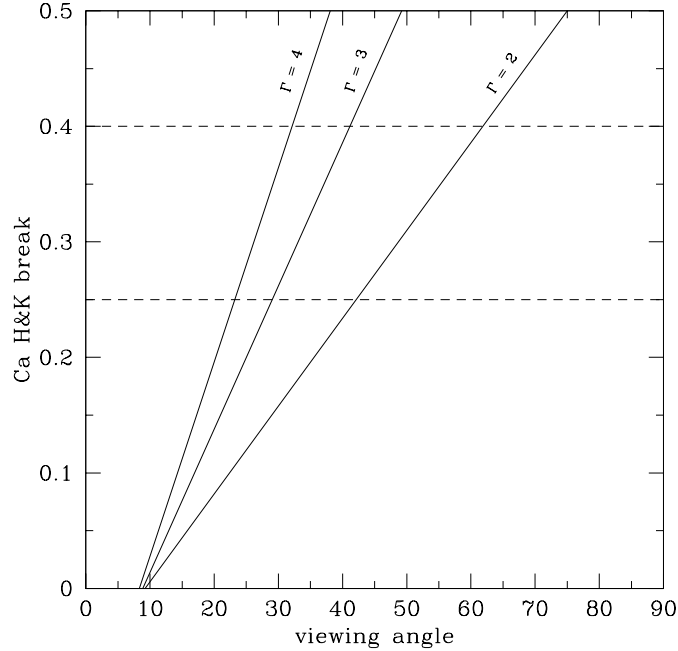


FIGURE 3.6. The correlation Ca H&K break value versus viewing angle for a starting viewing angle $\phi_{\text{BL}} = 10^\circ$ and Lorentz factors $\Gamma = 2, 3$ and 4 as obtained from connecting the correlations in Fig. 3.3 with the simulations exemplified in Fig. 3.5.

The resulting viewing angles and Lorentz factors for FR I radio galaxies agree with values obtained using independent methods, validating the Ca H&K break value as a suitable orientation indicator. Giovannini et al. (2001) constrained the Lorentz factor for parsec-scale jets in both low- and high-power radio galaxies to $\Gamma = 3 - 10$ based on the scatter of their correlation between core and total radio power. Urry and Padovani (1995) obtained from luminosity function studies of BL Lacs and FR I radio galaxies average Lorentz factors of $\Gamma = 3 - 7$ and critical angles $\phi_c = 12 - 30^\circ$. The latter transform to average viewing angles for the FR Is in the range $58 - 63^\circ$ if we use their equation (A12). Chiaberge et al. (2000) derived from the observed differences in core power between BL Lacs and FR Is with similar extended radio powers average Lorentz factors $\Gamma \sim 5$, if maximum viewing angles $\phi = 1/\Gamma$ and 60° are assumed for BL Lacs and FR Is respectively. Verdoes Kleijn et al. (2002) used the correlation between radio core and $\text{H}\alpha + [\text{NII}]$ core emission for their sample of FR I radio galaxies and constrained the average Lorentz factors to $\Gamma \sim 2 - 5$, assuming viewing angles in the range $\phi = [30^\circ, 90^\circ]$.

3.3.2 Ca H&K Break and Viewing Angle

I now want to investigate how the Ca H&K break value can be converted to viewing angle. For this purpose, I determine from the correlations in Fig. 3.3 for a range of Ca H&K break values the ratio L_{BL}/L_C in the X-ray and radio band. I assume L_{BL} to be the luminosity at the Ca H&K break value $C = 0$, and define L_C as the luminosity at $C = 0.1, 0.2, 0.3, 0.4$ and 0.5 . I then convert the L_{BL}/L_C ratios observed in the two bands to a viewing angle using the simulations exemplified in Fig. 3.5. Since each L_{BL}/L_C ratio pair also corresponds to an individual Ca H&K break value, a correlation between Ca H&K break and viewing angle is obtained in this way. These correlations are shown in Fig. 3.6 for a jet of Lorentz factor $\Gamma = 2, 3$ and 4 , and assuming for $C = 0$ a starting viewing angle of $\phi_{\text{BL}} = 10^\circ$.

From Fig. 3.6, we see that by extending the ‘classical’ Ca H&K break value of 0.25 to 0.4 as proposed by Marchã et al. (1996), BL Lac surveys include sources seen at larger viewing angles, and therefore less beamed. This is supported by the recent results of Dennett-Thorpe and Marchã (2000), who find that BL Lac objects with $C > 0.25$, the so-called BL Lac candidates, are significantly less polarized at 8.4 GHz than BL Lacs with $C < 0.25$.

3.4 Low- and High-Energy Peaked BL Lacs

The BL Lac class is currently divided into two subclasses: low- (LBL) and high-energy peaked BL Lacs (HBL), i.e., objects with a synchrotron emission peak located in the IR/optical and UV/soft X-ray band respectively. This division was introduced by Padovani and Giommi (1995) after it was realized that BL Lacs detected in radio (RBL) and X-ray surveys (XBL) had different radio-to-X-ray flux ratios, and that this was due to the fact that their spectral energy distributions (SED) had different shapes (Giommi et al., 1995).

As of today the question of how the two BL Lac subclasses are connected with each other regarding, e.g., their physical properties or evolutionary behaviour, is a matter of fervent debate. A finding that shaped strongly our perception of BL Lacs was made by Maraschi et al. (1986). These authors found that radio- and X-ray-selected blazars differed considerably in their radio luminosities, but had similar X-ray powers. Based on this, they concluded that the X-ray radiation was less beamed than the radio one, and that XBL being radio-weak were objects viewed at larger angles than RBL. However, Sambruna et al. (1996) later showed that the typical SED of an XBL cannot be obtained from the SED of an RBL simply by changing the viewing angle alone.

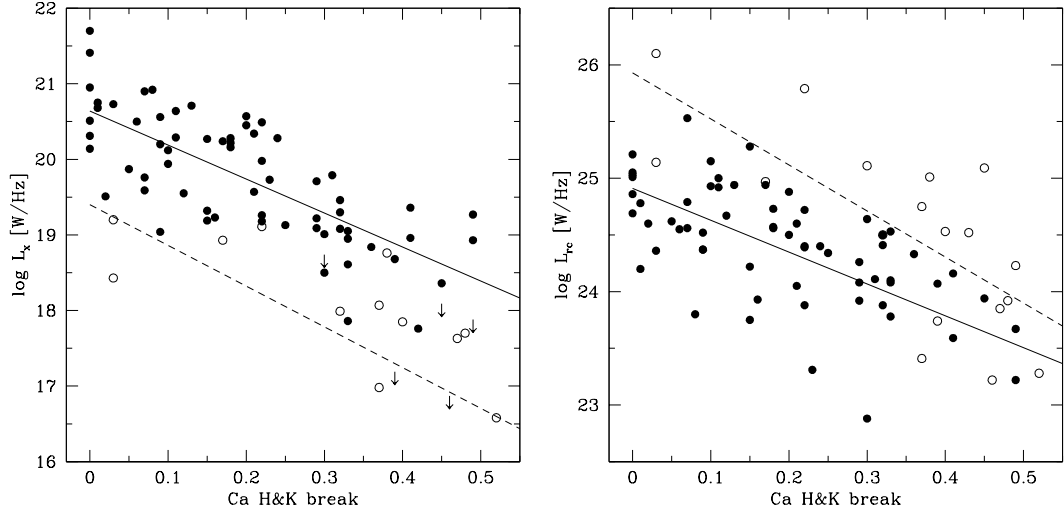


FIGURE 3.7. The 1 keV X-ray luminosity (left panel) and the radio core luminosity at 5 GHz (right panel) versus the Ca H&K break value. Open and filled circles denote LBL ($\log L_{\text{rc}}/L_x \geq 6$) and HBL ($\log L_{\text{rc}}/L_x < 6$) respectively. Arrows indicate LBL with upper limits on the X-ray luminosity. Solid and dashed lines represent the observed correlations for HBL and LBL respectively. Object 1241+735 is off the plot in the left panel.

If I divide the objects in the present sample into LBL (defined by $\log L_{\text{rc}}/L_x \geq 6$ [Padovani and Giommi (1996)]; 18 objects) and HBL (defined by $\log L_{\text{rc}}/L_x < 6$; 65 objects), I get similarly to the entire sample that their X-ray and radio core luminosities are strongly anticorrelated with Ca H&K break value (Fig. 3.7). Note that all objects in the sample have been subdivided, i.e., independently of Ca H&K break value. This approach is justified since the radio core instead of the total radio power is used to define LBL and HBL. The significance level is $P > 99.9\%$ for all four correlations.

This finding allows now, on one hand, the derivation of typical viewing angles for LBL and HBL, and, on the other hand, a comparison of their luminosities at different orientations.

3.4.1 Viewing Angles

The simulations described in Section 3.3 have been performed individually for the two BL Lac subclasses.

The LBL and HBL in the sample under study have mean radio spectral indices $\alpha_r = 0.1 \pm 0.1$ and 0.3 ± 0.1 respectively, not significantly different ($P = 93.7\%$) according to a Student's t-test. Therefore, I assumed for the simulations in the

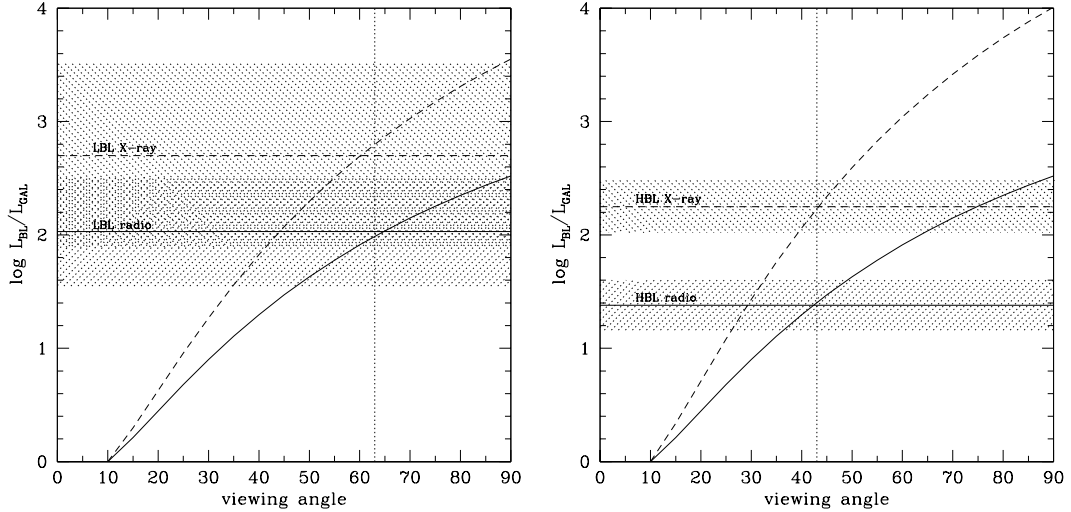


FIGURE 3.8. Simulated $L_{\text{BL}}/L_{\text{GAL}}$ ratios for LBL (left panel) and HBL (right panel) in the X-ray (dashed line) and radio band (solid line) for a changing viewing angle and a Lorentz factor $\Gamma = 3$. Horizontal lines indicate the ratios inferred from Fig. 3.7 in the X-ray (dashed line) and radio band (solid line) respectively. The 1σ error on the ratios is shown by the shaded areas. The vertical dotted line represents the viewing angle at which the observed $L_{\text{BL}}/L_{\text{GAL}}$ ratios for LBL and HBL in the radio and X-ray band are reproduced approximately simultaneously.

radio band for both LBL and HBL a radio spectral index $\alpha_r = 0.2$. On the other hand, the X-ray spectral index is known to be different for the two types of BL Lacs. Therefore, I performed the simulations in the X-ray band independently for LBL and HBL and used, following the results of Padovani and Giommi (1996), $\alpha_x = 1.1$ and 1.5 respectively.

The best fits in Fig. 3.7 give for LBL a maximum ratio of $\log L_{\text{BL}}/L_{\text{GAL}} = 2.70 \pm 0.81$ and 2.03 ± 0.48 for the X-ray and radio band respectively, where L_{BL} is the luminosity at the Ca H&K break value $C = 0$ and L_{GAL} the luminosity at $C = 0.5$. For HBL, the best fits in Fig. 3.7 give ratios $\log L_{\text{BL}}/L_{\text{GAL}} = 2.25 \pm 0.26$ and 1.38 ± 0.22 for the X-ray and radio band respectively. The simulations show that in all cases assumed for ϕ_{BL} and Γ (see Section 3.3) it is possible to reproduce for both LBL (Fig. 3.8, left panel) and HBL (Fig. 3.8, right panel) their ratios in the radio and X-ray band simultaneously, i.e., with the same Lorentz factor and the same maximum viewing angle. The viewing angles obtained in this way are similar to the ones listed in Table 3.2. Note that in the case of LBL somewhat higher viewing angles are obtained than for HBL. However, this difference is not significant

($P = 77.0\%$). A significantly larger range in viewing angles would imply that LBL were more beamed than HBL. This becomes clear if one recalls that in the performed simulations the same Lorentz factor was assumed for LBL and HBL. Alternatively, I could have fixed the range in viewing angles, which would have resulted in larger Lorentz factors for LBL.

3.4.2 Radio and X-ray Luminosity Differences

The use of the Ca H&K break value as a statistical viewing angle indicator allows for the first time the evaluation and comparison of the radio and X-ray luminosities of LBL and HBL at different orientations.

Table 3.3 lists the X-ray and radio core powers resulting from the correlations in Fig. 3.7 for LBL and HBL at small ($C = 0$) and large ($C = 0.5$) Ca H&K break values and therefore viewing angles. These show that at large viewing angles LBL and HBL have similar radio core and X-ray powers, i.e., they reside in FR I radio galaxies with similar properties (radio core and X-ray luminosities), while at relatively small viewing angles the two BL Lac subclasses differ significantly in their luminosities. In this case LBL are ≈ 10 times more luminous in the radio and by a similar factor less luminous in the X-ray band than HBL. I stress that the objects used in this work form an heterogeneous sample of sources from different surveys with widely different flux limits. Therefore, although these luminosity differences should be indeed genuine, their precise values can depend on the selected objects. In the following I want to expand on the influence of selection effects on the luminosity differences between LBL and HBL.

For this purpose I have also included BL Lacs with extended radio powers more typical of FR II radio galaxies ($L_{\text{ext}} > 10^{25.6} \text{ W Hz}^{-1}$). Furthermore, I distinguished between the following three cases: 1. a comparison between HBL (65 objects) and LBL (18 objects), where both have extended radio emissions typical of FR I radio

TABLE 3.3. Radio core and X-ray luminosities* of BL Lacs

		LBL	HBL	P_{diff}
$C = 0$	$\log L_x$	19.40 ± 0.59	20.65 ± 0.12	96.4%
	$\log L_{\text{rc}}$	25.93 ± 0.36	24.90 ± 0.11	98.8%
$C = 0.5$	$\log L_x$	16.71 ± 1.00	18.39 ± 0.28	89.0%
	$\log L_{\text{rc}}$	23.90 ± 0.60	23.51 ± 0.25	45.1%

*derived from correlations in Fig. 3.7; in units of $[\text{W Hz}^{-1}]$

TABLE 3.4. Mean radio core and X-ray luminosities*

	FR I HBL	FR I LBL	P	FR I&II LBL	P	FR II LBL	P
$\log L_x$	19.77 ± 0.10	17.49 ± 0.34	> 99.9%	18.04 ± 0.36	> 99.9%	19.71 ± 0.50	8.0%
$\log L_{rc}$	24.36 ± 0.08	24.51 ± 0.19	57.9%	25.14 ± 0.26	99.3%	26.77 ± 0.25	> 99.9%
z	0.21 ± 0.02	0.10 ± 0.02	> 99.9%	0.23 ± 0.05	37.3%	0.57 ± 0.07	> 99.9%

*in units of [W Hz⁻¹]

galaxies; 2. a comparison between HBL (65 objects) and LBL (25 objects), where the latter are selected independent of extended radio emission; and 3. a comparison between HBL (65 objects) and LBL (7 objects), where the latter have extended radio emissions typical of FR II radio galaxies. The most important difference between these three cases is that HBL and LBL are compared that are first matched and then not matched in extended radio power, i.e., have a similar parent population. For the three cases, I obtain the following results, illustrated in Table 3.4:

1. In the first case, where LBL and HBL with similar extended radio powers are compared, their mean radio core luminosities are similar, while HBL have higher mean X-ray luminosities than LBL. In this case, LBL have a significantly lower mean redshift than HBL.
2. In the second case, where LBL and HBL with somewhat different extended radio powers are compared, LBL have higher mean radio core luminosities and lower mean X-ray luminosities than HBL. In this case, LBL and HBL have similar mean redshifts.
3. In the third case, where LBL with high extended radio powers and HBL with low extended radio powers are compared, the two BL Lac subclasses have similar mean X-ray luminosities, while LBL have higher mean radio core luminosities than HBL. In this case, LBL have a significantly higher mean redshift than HBL.

These comparisons show that the resulting luminosity differences between LBL and HBL seem to depend strongly on the samples chosen. In particular, these three cases illustrate that, the more LBL and HBL differ in their extended radio powers, the less they differ in their X-ray powers. Note that these luminosity differences cannot be due only to a redshift effect. If that were the case, in fact, higher-redshift samples would be more luminous in all bands, contrary to what observed.

These selection effects can be further illustrated by using two different samples: the sample of Maraschi et al. (1986) that contains LBL and HBL with similar X-ray powers, and the complete sample of BL Lacs from the DXRBS which is radio-flux limited and therefore contains LBL and HBL with similar radio powers. Nearly half of the objects in the sample used by Maraschi et al. are strong-lined objects, i.e., radio quasars. Therefore, in order to compare their results with the ones from this work I selected from their sample only the BL Lac objects. Similarly to their results for radio- and X-ray-selected blazars, I get that their LBL (17 objects) and HBL (11 objects) have similar mean X-ray powers, but significantly different ($P > 99.9\%$) mean (total) radio luminosities $\log L_r = 26.61 \pm 0.25$ and 24.56 ± 0.08 W Hz⁻¹ respectively. The mean redshifts are $z = 0.35 \pm 0.08$ and 0.12 ± 0.03 for LBL and HBL respectively, different at the 98.8% level. This result is similar to the above case 3, indicating that these authors have compared radio-strong LBL with radio-weak HBL.

For the sample of DXRBS BL Lacs, I get that LBL (20 objects) and HBL (12 objects) have similar mean radio powers, but significantly different ($P = 98.7\%$) mean X-ray powers $\log L_x = 18.98 \pm 0.23$ and 20.00 ± 0.32 W Hz⁻¹ respectively. In this case LBL and HBL have similar mean redshifts. This result shows that case 1 can be reproduced with a radio-flux limited sample.

Now the question arises: ‘Which is the best approach to clarify what are the intrinsic luminosity differences between LBL and HBL in a given band?’. I believe that this can be answered in a physically meaningful way by comparing LBL and HBL with a similar parent population, i.e., with similar extended radio powers. Ideally, if information on the Ca H&K break value is available, one should also take into account orientation effects by separating sources according to viewing angle.

3.5 Discussion

In this chapter I have suggested that the Ca H&K break value of BL Lacs and low-luminosity radio galaxies is a direct indicator of viewing angle. This was based on the strong anticorrelations observed between Ca H&K break value and optical, radio, and X-ray jet powers, as well as radio core dominance parameter. The possibility that the observed ranges in jet powers and Ca H&K break values were due to intrinsic variations (and not to a difference in viewing angle) was excluded based on the fact that no similarly strong correlation between Ca H&K break value and extended radio emission was present for the sample under study.

The main result of these studies most relevant for blazar classification is that

the transition in Ca H&K break value from BL Lacs to radio galaxies is rather continuous. This then means that the extension of the allowed Ca H&K break value for blazars from 25% (initially proposed by Stocke et al. (1991)) to 40% as suggested by Marchã et al. (1996) simply leads to the inclusion of less strongly beamed BL Lacs in current blazar surveys. These objects with Ca H&K break values $0.25 \leq C \leq 0.4$, termed by Marchã et al. ‘BL Lac candidates’, however, represent the long-sought population of BL Lacs with viewing angles intermediate between the ‘classical’ BL Lacs and FR I radio galaxies. Such a population was postulated by current unified schemes for radio-loud AGN but was not known so far. FR II radio galaxies, on the other hand, were known to be viewed as steep-spectrum radio quasars (SSRQ) and flat-spectrum radio quasars (FSRQ) when their jet were oriented at intermediate and relatively small angles with respect to our line of sight respectively.

Which limit on the Ca H&K break value should be chosen to separate BL Lacs from FR I radio galaxies? In general, BL Lacs are those objects viewed at angles smaller than a certain critical angle, which has been defined in the literature as the angle for which the radio core dominance parameter is equal to 1 (Urry and Padovani, 1995). From the correlation between the radio core dominance parameter and Ca H&K break value illustrated in Fig. 3.4, I infer that a Ca H&K break value ~ 0.35 would then be appropriate to separate BL Lacs (core-dominated) from radio galaxies (lobe-dominated). Note that this value is very close to the value of 0.4 proposed by Marchã et al. (1996), however, it has now a more physical meaning.

An important result of these studies relevant for all future studies of radio-loud AGN is that the Ca H&K break value is a suitable statistical indicator of orientation. So far, only one other such indicator was known: the radio core dominance parameter. However, the determination of this quantity usually requires dedicated radio observations, which are time consuming and not always available. Therefore, the result that the viewing angles of samples of BL Lacs and FR I radio galaxies can be constrained from such a simple astrophysical observation as their optical spectra will be a considerable advantage in our studies of unified schemes.

A first application of the Ca H&K break value as a statistical orientation indicator has shown that radio and X-ray jets of BL Lacs and FR I radio galaxies have similar Lorentz factors and are viewed under similar angles, which means that their radio and X-ray Doppler factors are the same (within the errors). This result becomes even more significant if the sample is separated into low- (LBL) and high-energy peaked BL Lacs (HBL). In addition, I have shown that the jets of both LBL and HBL have similar Lorentz factors and are viewed under similar angles, i.e., their Doppler factors are similar. This result is in agreement with the scenario proposed

by Padovani and Giommi (1995), which claims that the main difference between LBL and HBL is the frequency position of their synchrotron emission peak. Moreover, these authors have attributed the more extreme properties of radio-selected BL Lacs, such as higher percentage of polarization, shorter variability time scales and higher radio-core dominance, as compared to those of X-ray selected BL Lacs to the fact that X-ray surveys simply sample the low-luminosity end of the radio luminosity function of BL Lacs. Therefore, X-ray surveys (which include mostly HBL) are likely to select less strongly beamed sources than radio surveys (which select mainly LBL). A hint in the data presented in this work indicates that LBL might be more beamed than HBL, i.e., they might have either larger Lorentz factors or span a larger range in viewing angles, however, not significantly so. This is in accordance with the conclusions of Padovani and Giommi (1995).

The finding that the Ca H&K break value is directly related to viewing angle made for the first time the comparison of the luminosities of the two types of BL Lacs at different orientations possible. These showed that FR I radio galaxies harbouring LBL and HBL have similar radio core and X-ray luminosities. At small viewing angles, LBL have radio cores ≈ 10 times more powerful than HBL ones, while the opposite is true in the X-ray band. These two results combined appear to be at odds with the previous result that LBL and HBL have similar Doppler factors. This apparent contradiction is most likely due to small number statistics. Note in fact that HBL-like and LBL-like FR Is also differ in their powers in the same sense as HBL and LBL but their differences are not significant owing to the larger statistical errors at $C \sim 0.5$.

Chapter 4

A New Classification Scheme for Blazars

Currently blazars are classified as either BL Lacs or flat-spectrum radio quasars (FSRQ) based on the strength of their emission lines. This quantitative distinction between blazar subclasses was prompted by observations of temporal weak emission lines in BL Lacs, since these objects had been previously defined as compact, radio-loud sources with completely featureless optical spectra.

A first (and rather arbitrary) limit on the equivalent width of emission lines of BL Lacs was introduced by surveys that selected the first complete samples of these objects, namely the 1 Jy radio survey (Stickel et al., 1991) and *EINSTEIN* Medium Sensitivity Survey (EMSS) at X-ray frequencies (Stoche et al., 1991). Both these surveys chose a value of 5 Å for the maximum equivalent width of BL Lac emission lines, however, applied to the rest and observed frame respectively. Later, this limit was revised by Marchã et al. (1996), who argued that the strength of blazar emission lines depended on the strength of the non-thermal jet continuum overlaying the host galaxy spectrum, and so on the dilution of the Ca H&K break. Based on this, they proposed to classify blazars in the Ca H&K break – equivalent width plane (see Fig. 1.4).

In order to separate BL Lacs and FSRQ in this plane, Marchã et al. proposed to use a diagonal line, which they obtained by simulating the equivalent width decrease for the H α λ 6562 emission line of the BL Lac object 3C 371 as the contribution from

the non-thermal jet emission decreased. But the source 3C 371 was chosen rather arbitrarily. It was adopted on the grounds that it was widely accepted as a ‘genuine’ BL Lac. Later, Scarpa and Falomo (1997) showed that there was a continuity in optical continuum and emission line luminosities between BL Lacs and FSRQ and argued that from the point of view of emission line strengths it was not necessary to invoke two different populations of blazars. However, it is important to point out that Scarpa and Falomo, contrary to Marchã et al., used a heterogeneous sample of BL Lacs and FSRQ.

The rather arbitrary separation of blazars proposed by Marchã et al. and the results of Scarpa and Falomo in favor of a continuity between blazar subclasses make the revision of blazar classification highly necessary. In this respect, a physical revision of blazar classification using a homogeneous sample of blazars is required. This is accomplished by the work presented in this chapter. However, the main motivation for the studies presented here was to substantially contribute to an answer to the important question which has troubled researchers since the discovery of BL Lacs: ‘Why do BL Lac objects lack strong emission lines otherwise seen in optical spectra of quasars?’

In Section 4.1 and 4.2, I present the sample of DXRBS sources used for this study and describe the emission line measurements. A discussion of the limitations of the current blazar classification scheme is presented in Section 4.3, and a possible new classification scheme for blazars is investigated in Section 4.4. In Section 4.5, I discuss the main results. The work presented in this chapter will be shortly submitted to the *Monthly Notices of the Royal Astronomical Society* as Landt, Padovani, Perlman & Giommi 2003 “A New Classification Scheme for Blazars”.

4.1 The Sample

For this study I have selected BL Lacs and FSRQ from the Deep X-ray Radio Blazar Survey (DXRBS). I have selected all DXRBS BL Lacs, but have restricted the sample of FSRQ to objects with redshifts $z \leq 2.2$. This was done in order to compare BL Lacs and FSRQ that have the same kind of emission lines. The strongest emission lines common to both are typically Mg II $\lambda 2798$, [O II] $\lambda 3727$, H β $\lambda 4861$, [O III] $\lambda 5007$, and H α $\lambda 6563$. Then, $z \sim 2.2$ represents the maximum redshift for which Mg II can be observed in the range of $\sim 4000 - 9000 \text{ \AA}$ typically covered by our optical spectra.

The Sample of BL Lacs

We have an available optical spectrum for 28 of the 44 DXRBS BL Lacs. Additionally, I could find in the literature information on emission lines for one more source (4C 55.17). Out of the 28 BL Lacs observed by us 5 objects do not have a determined redshift and have been excluded from this analysis. Therefore, the BL Lac sample under study includes 24 objects and is listed in Table 4.1.

TABLE 4.1. **DXRBS BL Lacs**

Name	z	MgII		[OII]		H β		[OIII]		H α		L_{NLR} [erg/s]	L_{BLR} [erg/s]
		W_λ	log L										
		[\AA]	[erg/s]										
WGAJ0023.6+0417	0.100					< 9.8	<39.56	< 7.0	<39.43	<16.4	<39.82	<40.81	<40.76
WGAJ0032.5-2849	0.324					< 1.6	<41.36						<42.76
WGAJ0043.3-2638	1.002	6.5	43.50	< 0.6	<42.28	7.5	43.01					<43.71	44.61
WGAJ0100.1-3337	0.875	10.1	42.71										43.93
WGAJ0245.2+1047	0.070			15.0	41.08	< 2.3	<40.72	20.6	41.67	20.6	41.65	42.50	42.50
WGAJ0313.9+4115	0.029					< 1.7	<40.12	1.9	40.24	19.4	41.17	41.37	42.03
WGAJ0428.8-3805	0.150			< 1.9	<40.19	< 1.7	<40.50	< 1.1	<40.32	< 2.2	<40.66	<41.37	<41.64
WGAJ0431.9+1731	0.143					< 9.8	<39.97	< 4.7	<39.70	<13.3	<40.20	<40.99	<41.15
WGAJ0528.5-5820	0.254					< 2.2	<40.81	12.0	41.55			42.40	<42.21
WGAJ0533.6-4632	0.332					< 2.4	<40.71						<42.11
WGAJ0558.1+5328	0.036					< 2.7	<40.35	8.7	40.84	11.6	41.05	41.82	41.91
WGAJ0624.7-3230	0.252			< 2.2	<40.87	< 2.0	<41.05	< 2.0	<41.07	< 6.5	<41.49	<42.08	<42.37
WGAJ0816.0-0736	0.040			< 5.0	<39.85	< 2.5	<39.93	< 1.2	<39.63	< 2.2	<39.92	<40.92	<40.98
WGAJ0847.2+1133	0.199			< 1.1	<40.35	< 2.2	<40.50	< 1.8	<40.40	< 7.3	<40.76	<41.50	<41.70
WGAJ1204.2-0710	0.185					< 4.5	<41.58	5.1	41.71			42.54	<42.98
WGAJ1311.3-0521	0.160			< 2.7	<40.50	< 1.6	<40.60	< 1.2	<40.47	< 1.9	<40.63	<41.62	<41.67
WGAJ1320.4+0140	1.235	15.2	43.01										44.24
WGAJ1744.3-0517	0.310			< 3.5	<40.60	< 3.3	<40.72	< 2.6	<40.62			<41.74	<42.12
WGAJ1834.2-5948	0.435			<13.0	<40.86	<12.2	<40.84	< 8.0	<40.68			<41.94	<42.24
WGAJ1840.9+5452	0.646	<15.3	<42.83	5.5	42.38	< 8.1	<42.53	10.9	42.63			43.61	<44.00
WGAJ1936.8-4719	0.264			< 0.5	<40.79	< 0.9	<41.04	< 0.9	<40.95			<41.98	<42.44
WGAJ2258.3-5525	0.479	1.4	41.90	< 0.8	<41.48	< 3.2	<41.95	< 1.7	<41.67			<42.68	43.11
WGAJ2330.6-3724	0.279			0.8	40.18	< 1.4	<40.45	2.4	40.63			41.52	<41.85
4C55.17	0.909	1.6	43.39	0.5	42.92	4.2	43.62	9.4	43.95			44.68	44.77

The Sample of FSRQ

We have an available optical spectrum for 107 of the 178 DXRBS FSRQ with redshifts $z \leq 2.2$ (71 objects were previously known sources, which we did not reobserve). Out of these I have included in this analysis 91 objects. I have excluded

objects that: 1. had a spectrum whose wavelength range did not cover the location of any of the emission lines analyzed here (6 objects); 2. had a spectrum covering the location of Mg II λ 2798 only, but either the signal-to-noise ratio (S/N) was below 3 (4 objects) or telluric A band was present (2 objects) in that region; 3. had a spectrum that was not taken at parallactic angle and the loss in flux at the location of all emission lines under study was larger than 30% (4 objects; see next section for more details). Additionally, I could find in the literature information on emission lines for 15 of the previously known sources. The FSRQ sample under study includes 106 objects and is listed in Table 4.2.

TABLE 4.2. DXRBS FSRQ

Name	z	MgII		[OII]		H β		[OIII]		H α		L_{NLR} [erg/s]	L_{BLR} [erg/s]
		W_{λ} [Å]	log L [erg/s]										
WGAJ0010.5–3027	1.190	55.7	44.16										45.25
WGAJ0012.5–1629	0.151					22.6	41.87	14.8	41.69	145.1	42.42	42.52	43.26
WGAJ0029.0+0509	1.633	41.4	44.49										45.68
WGAJ0106.7–1034	0.469			9.5	42.53	138.2	43.47					43.96	44.87
WGAJ0110.5–1647	0.781	34.8	44.20	< 3.1	<42.85							<44.28	45.41
WGAJ0126.2–0500	0.411	89.3	42.68	17.7	41.87	36.1	42.00	62.4	42.21			43.15	43.76
WGAJ0136.0–4044	0.649	87.3	42.78	8.5	41.78							43.21	43.99
WGAJ0143.2–6813	1.223	101.7	43.56										44.71
WGAJ0217.7–7347	1.234	93.1	43.99										45.13
WGAJ0253.3+0006	1.339	53.9	42.65										43.86
WGAJ0258.6–5052	0.834	191.9	42.63	4.9	41.65	<21.6	<42.18					43.09	43.85
WGAJ0259.4+1926	0.544	157.4	43.18	6.5	41.70	79.7	42.63	36.3	42.27			43.11	44.25
WGAJ0304.9+0002	0.563	74.9	43.62	2.6	42.01	35.8	42.76	62.1	42.98			43.72	44.65
WGAJ0312.3–6610	1.384	50.3	43.37										44.53
WGAJ0314.4–6548	0.636	106.4	43.54	< 1.9	<41.63	56.9	42.97	11.6	42.28			43.11	44.59
WGAJ0322.1–5205	0.416					115.8	43.21	25.4	42.59	615.1	43.69	43.33	44.56
WGAJ0322.2–5042	0.651	66.6	43.34	< 2.3	<41.66	69.1	42.91	27.9	42.44			43.27	44.47
WGAJ0322.6–1335	1.468	93.2	43.44										44.61
WGAJ0357.6–4158	1.271	115.4	43.83										45.03
WGAJ0411.0–1637	0.622	49.3	44.39	0.6	42.30	28.4	43.41	8.6	42.81			43.67	45.43
WGAJ0427.2–0756	1.375	88.4	44.07										45.77
WGAJ0435.1–0811	0.791	105.5	43.74	1.7	41.69	35.7	42.46	55.3	42.50			43.27	44.76
WGAJ0441.8–4306	0.872	127.7	42.46	19.8	41.74							43.17	43.67
WGAJ0447.9–0322	0.774	52.4	44.85	1.1	42.97			4.5	43.05			44.13	46.06
WGAJ0448.6–2203	0.496	127.0	42.03	39.4	41.39							42.82	43.24
WGAJ0510.0+1800	0.416	55.8	42.95	5.7	42.18							43.61	44.09
WGAJ0535.1–0239	1.033	83.1	44.30										45.58
WGAJ0539.0–3427	0.263					263.7	41.91		169.4	41.82			42.92
WGAJ0546.6–6415	0.323			0.8	42.08	93.0	43.84	24.9	43.25	442.2	44.28	43.96	45.15
WGAJ0600.5–3937	1.661	20.7	44.25										45.62
WGAJ0631.9–5404	0.193			4.2	41.82	77.1	42.96	33.5	42.59	378.0	43.50	43.37	44.34

TABLE 4.2. DXRBS FSRQ

Name	z	MgII		[OII]		H β		[OIII]		H α		L_{NLR} [erg/s]	L_{BLR} [erg/s]
		W_λ [\AA]	log L [erg/s]										
WGAJ1911.8–2102	1.420	14.5	43.80										45.22
WGAJ1938.4–4657	0.805	48.8	41.70	14.4	41.34							42.77	42.91
WGAJ2109.7–1332	1.226	69.6	44.75	< 5.0	<43.41							<44.84	45.96
WGAJ2154.1–1502	1.208	39.4	44.87	< 1.4	<43.17							<44.60	46.28
WGAJ2157.7+0650	0.625			39.4	42.18	132.9	42.69	187.1	42.83			43.65	44.09
WGAJ2304.8–3624	0.962	139.1	43.12	23.5	42.36							43.79	44.33
WGAJ2320.6+0032	1.894	61.9	43.52										45.49
WGAJ2322.0+2113	0.707	45.1	44.18	< 1.6	<42.55			12.3	42.73			43.56	45.40
WGAJ2329.0+0834	0.948	70.3	43.05										44.26
WGAJ2333.2–0131	1.062	90.7	43.86										44.94
WGAJ2349.9–2552	0.844	108.5	43.74	6.0	42.34							43.78	44.95
WGAJ2354.2–0957	0.989	57.8	42.76	12.1	42.02							43.45	43.97
1Jy 0112–017	1.381	21.0	43.68										44.98
1Jy 0119+041	0.637	36.0	43.82				43.25		42.80			43.63	44.87
1Jy 0514–459	0.194					6.7	42.33	5.0	42.18	35.2	43.00	42.95	43.83
1Jy 0850+581	1.322	25.8	45.20	0.4	43.15							44.58	46.34
1Jy 0859+470	1.462	30.1	44.84	1.2	43.20							44.64	46.07
1Jy 1637+574	0.750	11.4	44.39	1.1	43.04		44.57	6.9	43.72			44.52	45.79
1Jy 1638+398	1.666	2.3	43.39										44.65
1Jy 1725+044	0.293								42.15		43.82	42.93	44.67
1Jy 2344+092	0.673	41.2	44.62		42.92		44.45					44.36	45.99
S5 0743+74	1.629	12.6	44.19										45.40
S5 1027+74	0.123			3.6	40.46	39.2	41.91	49.9	42.01		42.37	42.69	43.20
3C345	0.594	35.1	44.86	0.6	42.58		43.23	3.1	43.48			44.23	45.95
4C38.41	1.814	10.3	45.15										46.67
PKS 2059+034	1.013	34.3	44.26										45.49
OY-106	0.618	17.9	43.19	9.3	42.84			38.3	43.39			44.24	44.40

4.2 Emission Line Measurements

Tables 4.1 and 4.2 list the rest frame equivalent widths and line luminosities for Mg II λ 2798, [O II] λ 3727, H β λ 4861, [O III] λ 5007, and H α λ 6562 for the DXRBS BL Lacs and FSRQ included in this analysis.

In the individual spectra a cubic spline has been first fitted interactively to the continuum over the full wavelength range covered using the IRAF task *noao.onedspec.sfit*. The equivalent widths (W_λ) and line fluxes have then been measured using the IRAF task *noao.onedspec.splot*. The continuum of a few objects showed the black body shape typical for elliptical galaxies. In these cases a local continuum has been fitted to the single lines. The 1σ uncertainties on the equivalent width and line flux values

induced by the placement of the continuum are estimated to be typically $\sim 30\%$ and $\sim 20\%$ respectively. The ‘small bump’ (which spans the 2000 – 4000 Å rest frame wavelength region and is a blend of Fe II lines and Balmer continuum emission) was present in only 11 of the objects with a clearly detected [O II] $\lambda 3727$ emission line. In these cases the [O II] equivalent width has been determined by taking the line flux relative to the continuum including this feature as well as to the (lower) one fitted to the entire spectrum. For these objects I get a typical difference between the two equivalent width values of $\sim 20\%$. Since this difference is rather low compared to the measurement errors and the feature is not present in most objects, for consistency reasons also for these sources the ‘uncorrected’ values are listed. Owing to the medium S/N of our spectra I have not attempted to quantify the iron contamination of the [O III] $\lambda 5007$ emission line. Gaussian line profiles have been assumed for the narrow emission lines [O II] $\lambda 3727$ and [O III] $\lambda 5007$. In the case of the broad emission lines Mg II $\lambda 2798$, H β $\lambda 4861$, and H α $\lambda 6562$ I have not assumed a specific line profile but have integrated the line flux over the entire emission line range. This range has been determined for each object individually using the quasar composite of Francis et al. (1991) as a guide.

I have derived 2σ upper limits on the rest frame equivalent widths and line fluxes when the lines were not detected but their position covered by the spectrum. In the case of narrow emission lines I have determined non-detection limits only if the resolution of the spectrum was high enough to allow for a detection. The non-detection limits have been calculated assuming a rectangular emission line. The emission line width has been assumed to be 1000 km s^{-1} for the narrow lines [O II] and [O III]. In the case of the broad lines Mg II, H β , and H α I have assumed for FSRQ values 5800 km s^{-1} , 4000 km s^{-1} , and 4500 km s^{-1} respectively, and for BL Lacs values 4100 km s^{-1} , 1500 km s^{-1} , and 1500 km s^{-1} respectively. These correspond to the average values for the detections. I have not attempted to derive upper limits if the S/N at the position of the line was $\lesssim 3$.

The spectra of a number of DXRBS sources have not been observed at parallactic angle. I have chosen to include in this analysis line measurements based on these spectra only if the flux loss due to atmospheric differential refraction at the position of the line was not greater than 30%. The expected loss in flux has been computed for our sources following the calculations of Filippenko (1982).

The narrow line region (NLR) luminosity for the sample of objects included here has been calculated following Rawlings and Saunders (1991) as

$$L_{\text{NLR}} = 3 \times (3 \times L_{[\text{O II}]} + 1.5 \times L_{[\text{O III}]}) \tag{4.1}$$

where $L_{[\text{O II}]}$ and $L_{[\text{O III}]}$ are the line luminosities of $[\text{O II}] \lambda 3727$ and $[\text{O III}] \lambda 5007$ respectively. For objects with redshifts $z < 0.5$ for which the spectrum did not cover the position of $[\text{O II}]$, $L_{[\text{O II}]}$ has been calculated from the linear correlation between the ratio $L_{[\text{O II}]} / L_{[\text{O III}]}$ and $\log L_{[\text{O III}]}$ found by Saunders et al. (1989). In all other cases the relation $L_{[\text{O III}]} = 4 \times L_{[\text{O II}]}$ has been used when only one of the two emission lines was observed. The broad line region (BLR) luminosity was calculated following Celotti et al. (1997) as:

$$L_{\text{BLR}} = \sum_i L_{i,obs} \frac{\langle L_{\text{BLR}}^* \rangle}{\sum_i L_{i,est}^*}, \quad (4.2)$$

where $\sum_i L_{i,obs}$ is the sum of the measured luminosities of the observed broad lines scaled by the ratio of the estimated total broad line region luminosity L_{BLR}^* to the estimated luminosities of the observed broad lines. Both estimates were taken from the results of Francis et al. (1991), and in the case of $\text{H}\alpha \lambda 6562$ from Gaskell et al. (1981).

4.3 The Limitations of the Current Classification Scheme

We have initially classified blazars in the DXRBS sample as BL Lacs and FSRQ following the scheme proposed by Marchã et al. (1996). However, using the Ca H&K break – equivalent width plane to classify blazars the way it was suggested by these authors is problematic for the following reasons:

1. The diagonal line that separates BL Lacs from FSRQ is not only arbitrary but if applied to the strongest *observed* emission line, as suggested by Marchã et al., prevents the classification of blazars as BL Lacs at higher redshifts ($z > 0.4$) (see below).
2. If the Ca H&K break – equivalent width plane is to be used to separate blazars from radio galaxies it can only be applied to narrow emission lines (and not to the strongest *observed* emission line), since only these are common to both.
3. In any case, the rest frame equivalent width of broad emission lines is not necessarily expected to decrease with decreasing Ca H&K break value, if this is indeed a suitable viewing angle indicator (see previous Chapter).

In the following subsections I will expand on these points.

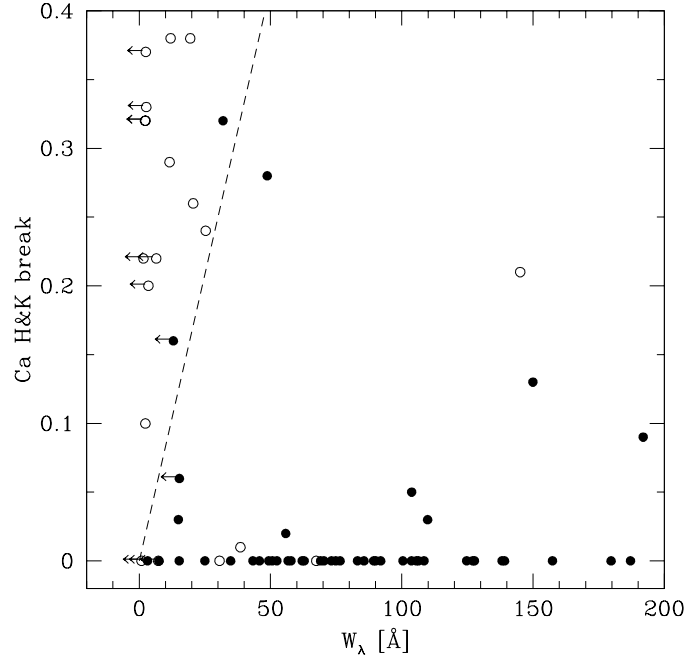


FIGURE 4.1. The Ca H&K break value versus the rest frame equivalent width of the strongest observed emission line for DXRBS BL Lacs and FSRQ. Open and filled circles indicate objects with redshifts $z < 0.4$ and $z \geq 0.4$ respectively. Arrows indicate upper limits. WGAJ0322.1-5205, WGAJ0539.0-3427, WGAJ0546.6-6415, and WGAJ0631.9-5404 are off the plot to the right. The dashed line represents the division between BL Lacs and FSRQ proposed by Marchã et al. (1996).

4.3.1 The Redshift Effect

Fig. 4.1 plots the Ca H&K break value versus the rest frame equivalent width of the strongest observed emission line for the objects in the sample under study. The Ca H&K break is observable in the optical spectrum up to a redshift of $z \sim 1.2$. Therefore, Fig. 4.1 includes all BL Lacs and FSRQ from the current sample with redshifts below this value, with the exception of 13 objects (the spectrum of 7 objects does not cover the Ca H&K break location, and for 6 objects the Ca H&K break is located at the position of strong telluric absorption or is sampled with poor S/N). Owing to the redshift restriction the strongest emission lines observed in these objects are the narrow lines [O II] $\lambda 3727$ and [O III] $\lambda 5007$, and the broad lines Mg II $\lambda 2798$, H β $\lambda 4861$, and H α $\lambda 6562$.

Of the 70 objects plotted in Fig. 4.1, 48 have a redshift $z \geq 0.4$ (filled circles). This is the mean redshift value for the BL Lacs listed in Table 4.1. Out of these we

see that only four objects have a Ca H&K break value $C > 0.1$, and only 10 objects have a Ca H&K break value $C > 0$. This means that if we use the diagonal line proposed by Marchã et al. to classify our objects $\sim 90\%$ of our high-redshift sources have to be classified as FSRQ if one of their emission lines is as weak as $\sim 10 \text{ \AA}$ (the value the diagonal line gives for $C = 0.1$), and $\sim 80\%$ have to be classified as FSRQ if they have emission lines at all (note that the diagonal line does not allow any emission line for $C = 0$; I have considered the Ca H&K break to have reached its minimum value of zero when the flux blueward of this feature was equal to or larger than the one redward).

4.3.2 The Ca H&K Break – Equivalent Width Plane

I now want to investigate if it is in general physically meaningful to separate BL Lacs and FSRQ using the Ca H&K break – equivalent width plane.

In the previous Chapter I have shown that the Ca H&K break value of BL Lacs and low-luminosity radio galaxies decreases with viewing angle. This, however, means that only the equivalent widths of narrow emission lines, believed to be radiated isotropically, are expected to decrease with Ca H&K break value. The broad emission lines, on the other hand, will be obscured by the putative circumnuclear dusty torus at relatively large viewing angles, and will come progressively into our line of sight as the viewing angle, and therefore the Ca H&K break, decreases. Simultaneously we also expect the continuum flux to increase (owing to the beamed jet component). This combination of emission line and continuum flux increase renders the resulting equivalent width and its dependence on the Ca H&K break value difficult to quantify and the possibility that the equivalent widths of broad emission lines *increase* with Ca H&K break value cannot be excluded. Moreover, if the Ca H&K break – equivalent width plane is to be used to separate also radio galaxies and blazars (as was suggested by Marchã et al.) it is obvious that it can be applied to narrow emission lines only. Thus the question that I want to answer becomes: Is it physically justified to separate BL Lacs and FSRQ in the Ca H&K break – equivalent width plane using their *narrow* emission lines?

For my studies I have first simulated the decrease in equivalent width with increasing contribution from non-thermal jet emission. For this purpose I have assumed at $C = 0.5$ starting equivalent width values $W_\lambda = 1, 5, 10, 20, 50, 100, 200, 300, \text{ and } 500 \text{ \AA}$, and have increased the non-thermal jet emission f_{jet} . I have then calculated the Ca H&K break value C using the relation $\log f_{\text{jet}}/f_{\text{gal}} = -3.74 \times C + 0.43$, where f_{gal} is the flux of the underlying host galaxy, assumed to be constant. This relation results from the simulations presented in Section 3.1 for a jet of optical

spectral index $\alpha_\nu = 1$, assuming a jet spectrum of the form $S_\nu \propto \nu^{-\alpha}$ (see also Fig. 3.2). The resulting correlations between Ca H&K break value and equivalent width are represented by the dotted lines in Fig. 4.2, left panel. Note that contrary to the results of Marchã et al. the above relation between Ca H&K break and jet emission gives a non-linear dependence between the Ca H&K break and equivalent width values.

These simulations show that the equivalent width range of objects with high Ca H&K break values determines the (maximum) equivalent width range of objects with low Ca H&K break values. (Note that it is the maximum range since an increasing jet emission can further decrease the equivalent width, although the Ca H&K break value has reached its minimum value of zero.) In other words, the equivalent width range of blazars will depend on the (intrinsic) equivalent width range of their parent radio galaxy populations. Then, a discrimination between BL Lacs and FSRQ using, e.g., one of the simulated dashed lines, would be physically justified only if there existed two populations of radio galaxies with significantly different [O II] and/or [O III] equivalent width distributions. This means that we need to observe a bimodal [O II] and/or [O III] line luminosity distribution intrinsic to the entire class of radio-loud AGN, which is expected to manifest itself as a bimodal equivalent width distribution at any given orientation. Note that the equivalent width, although orientation dependent in radio-loud AGN, is independent of redshift and so more appropriate than the line luminosity itself to quantify in a meaningful way such a bimodality.

In order to investigate the existence of such a bimodality we need a large number of radio galaxies and blazars that span a wide range of equivalent widths and Ca H&K break values. Therefore, I have additionally included in this study the radio galaxies from the DXRBS (listed in Table 4.3). However, given its radio spectral index cut ($\alpha_r \leq 07$) DXRBS selects against most radio galaxies. Therefore, I have included also the sample of radio galaxies and quasars from the 2 Jy survey presented by Tadhunter et al. (1993) and Morganti et al. (1997). The spectra of the 2 Jy sources were kindly made available to us by Clive Tadhunter. For these additional sources I have measured the equivalent widths of [O II] $\lambda 3727$ and [O III] $\lambda 5007$, and the Ca H&K break values. Upper limits on equivalent widths have been derived as described in Section 4.2. Note that the use of objects from radio surveys with different flux limits is warranted and should not introduce any bias since line flux was not part of the selection criteria.

Fig. 4.2, left panel, plots for radio galaxies and blazars from the DXRBS and the 2 Jy survey the Ca H&K break value versus the rest frame equivalent width

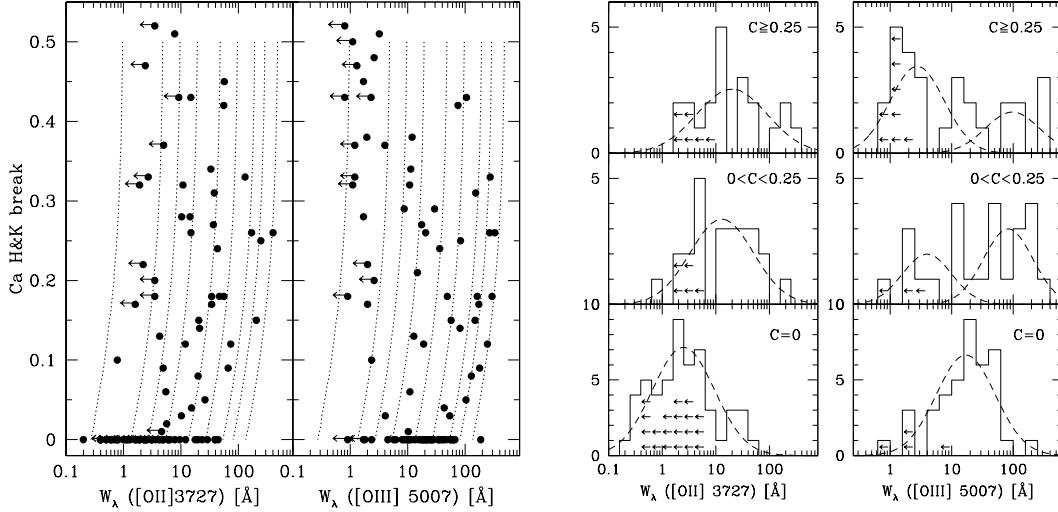


FIGURE 4.2. **Left panel:** The Ca H&K break value versus the [O II] $\lambda 3727$ and [O III] $\lambda 5007$ rest frame equivalent widths for DXRBS and 2 Jy objects. Arrows indicate upper limits. Dotted lines represent the simulated rest frame equivalent width decrease with increasing non-thermal jet continuum for starting values (at $C = 0.5$) of $W_\lambda = 1, 5, 10, 20, 50, 100, 200, 300,$ and 500 \AA (from left to right). **Right panel:** The [O II] $\lambda 3727$ and [O III] $\lambda 5007$ rest frame equivalent width distributions for objects from the left panel with $C = 0, 0 < C < 0.25,$ and $C \geq 0.25$. Arrows indicate upper limits. The dashed curves represent the best-fit Gaussian models.

of [O II] $\lambda 3727$ and [O III] $\lambda 5007$. The panel for the [O II] ([O III]) emission line includes 59 (48) and 39 (45) sources from the DXRBS and 2 Jy sample respectively. Note that sources with errors on the Ca H&K break value > 0.2 have been excluded from these studies. Fig. 4.2, right panel, shows the equivalent width distributions for these objects, binned into three groups of Ca H&K break values $C = 0, 0 < C < 0.25$ and $C \geq 0.25$. These groups comprise 52, 25 and 21 objects respectively in the case of [O II], and 40, 25 and 28 objects respectively in the case of [O III].

In order to quantify a possible bimodality in these distributions I have used the k_{MM} algorithm developed by Ashman et al. (1994). The k_{MM} algorithm computes for a given univariate dataset the confidence level at which the single Gaussian model can be rejected in favour of a two Gaussian model. I have fitted homoscedastic groups (i.e., groups with similar covariances), and only if the resulting confidence level was below 95% I have also considered the heteroscedastic case. For the distributions in Fig. 4.2, right panel, I get a high confidence level for the rejection of the single Gaussian model in the case of [O III] for objects with $C \geq 0.25$ ($P = 98.4\%$) and

TABLE 4.3. DXRBS Radio Galaxies

Name	z	[OII]		[OIII]		L_{NLR} [erg/s]	C	σ
		W_λ [Å]	$\log L$ [erg/s]	W_λ [Å]	$\log L$ [erg/s]			
WGAJ0204.8+1514	0.833	49.1	42.35	85.7	42.93	43.77	0.21	0.37
WGAJ0247.9+1845	0.301	< 5.8	<40.71	< 1.8	<40.63	<41.82	0.47	0.26
WGAJ0500.0–3040	0.417	20.5	42.12	57.2	42.77	43.58	0.15	0.08
WGAJ0605.8–7556	0.458	39.8	41.21	32.9	41.18	42.33	0.03	0.24
WGAJ1120.4+5855	0.158			43.2	42.71	43.44		
WGAJ1229.4+2711	0.490	74.5	42.69	53.0	42.57	43.78	0.42	0.53
WGAJ1420.6+0650	0.236	33.2	41.69	11.3	41.63	42.81	0.34	0.10
WGAJ1835.5–6539	0.554	< 4.8	<40.46	42.5	41.53	42.36	0.11	0.23
WGAJ2131.9–0556	0.085	< 9.2	<39.64	< 2.3	<39.53	<40.74	0.43	0.20
WGAJ2205.2–0004	0.827	41.1	42.15			43.59	0.36	0.75
WGAJ2303.5–5126	0.426	11.9	41.70	18.9	42.06	42.99	0.12	0.19

$0 < C < 0.25$ ($P = 94.7\%$). In all other cases a single Gaussian model is the better fit. The resulting best-fit Gaussians are overlaid as dashed lines in Fig. 4.2, right panel. Note that, although a relatively large number (9/28 or 32%) of objects with $C \geq 0.25$ have only upper limits on their [O III] equivalent widths, the limits only increase the significance of the bimodality but do not cause it. If these are excluded, the bimodal [O III] equivalent width distribution remains significant ($P = 95.6\%$).

The single Gaussian models for the [O II] equivalent width distributions give mean values of about 20, 13, and 3 Å for objects with $C \geq 0.25$, $0 < C < 0.25$, and $C = 0$ respectively. This observed decrease in equivalent width is well reproduced by the simulations that give at $C = 0$ a value of ~ 5 Å if a starting value of ~ 20 Å at $C = 0.5$ is assumed. This confirms the use of the Ca H&K break as a statistical indicator of orientation. In the case of [O III] the two best-fit Gaussians give mean values of ~ 3 and 100 Å for objects with $C \geq 0.25$, and ~ 4 and 80 Å for objects with $0 < C < 0.25$. For a starting value of ~ 100 Å the simulations predict a value of ~ 25 Å at $C = 0$. This is similar to the mean of ~ 20 Å observed for objects with $C = 0$. On the other hand, for a starting value of ~ 5 Å a value of ~ 1.5 Å at $C = 0$ is expected. This group of objects seems to be absent in the sample under study. These could be the featureless BL Lacs with no available redshift. In the DXRBS there are 13 such objects (5 of which have been observed by us) that have been excluded from this analysis. Tadhunter et al. (1993) failed to identify recognizable

features for 11 sources out of their complete sample of 87 objects.

The presence of a bimodality for the [O III] emission line could indicate the existence of two physically distinct classes of radio-loud AGN, thus allowing a refinement of the present classification scheme for blazars. This I want to investigate in the remainder of this chapter.

4.4 Weak- and Strong-Lined Radio-Loud AGN

In this section, I want to split the entire sample of objects (blazars and radio galaxies) from the DXRBS and 2 Jy survey into sources with *intrinsically* weak and strong [O III] emission lines, which I will refer to as weak- and strong-lined radio-loud AGN respectively, and investigate if they differ in other properties, such as NLR and BLR luminosities, radio and X-ray jet powers, and/or ionization state.

4.4.1 The [O III] – [O II] Equivalent Width Plane

One option to split the sample would be to use as a dividing line one of the above simulated lines in the Ca H&K break – [O III] equivalent width plot. Then, one could think to use simply the simulated line corresponding at $C = 0.5$ to the value of the intersection point of the two best-fit Gaussians for objects with $C \geq 0.25$. However, a large fraction (40/93 or 43%) of the sources included in Fig. 4.2 have a Ca H&K break $C = 0$. For these objects the dividing value at $C = 0$ resulting from the presented simulations could be problematic, since, as mentioned earlier, the equivalent width will continue to decrease with increasing jet emission, although the Ca H&K break has reached its minimum value. In other words, at $C = 0$ extremely beamed strong-lined AGN can cross the dividing line and invade the region of weak-lined AGN or, said differently, a way needs to be found to distinguish at $C = 0$ between ‘intrinsically’ weak-lined sources and those appearing weak because they are strongly beamed. In this respect, the Ca H&K break – equivalent width plane simply does not offer the dynamic range necessary for a meaningful separation of the entire sample under study into weak- and strong-lined radio-loud AGN.

Such a separation, however, has to be based in any case on the [O III] equivalent width. The [O III] line luminosity is not an option, since it depends strongly on redshift. The use of the [O III] equivalent width, on the other hand, requires a method to disentangle orientation effects if radio galaxies and blazars are included. I suggest that this is possible using an [O III] – [O II] equivalent width plot. Since the equivalent widths of both these emission lines are expected to decrease with viewing angle, in such a plot objects viewed at larger and smaller angles are expected

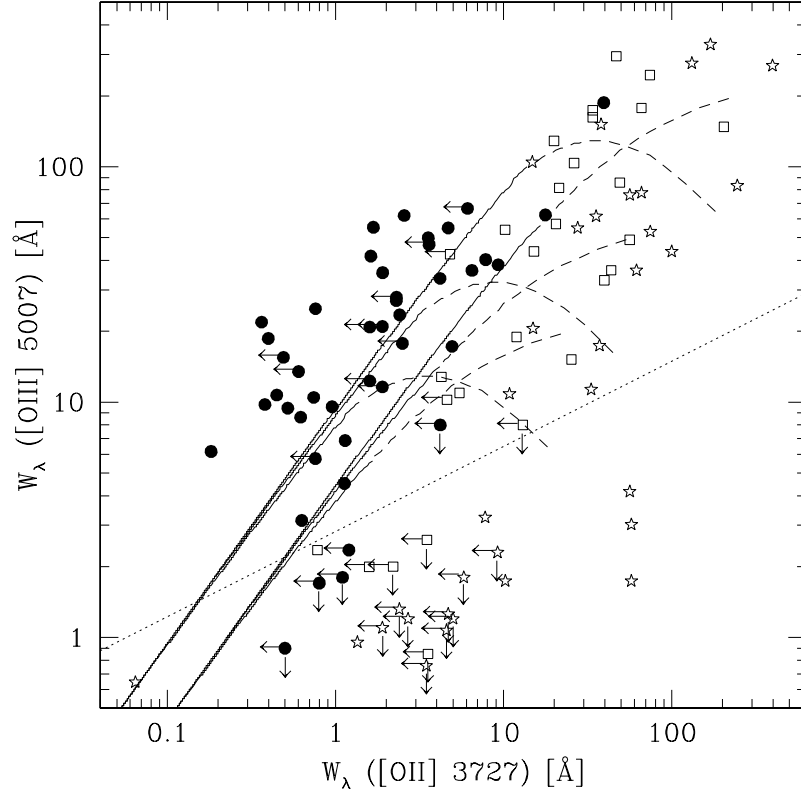


FIGURE 4.3. The rest frame equivalent widths of [O III] $\lambda 5007$ versus [O II] $\lambda 3727$ for objects from the DXRBS and 2 Jy survey. Filled circles, open squares and stars represent sources with Ca H&K break values $C = 0$, $0 < C < 0.25$ and $C \geq 0.25$ respectively. Arrows indicate upper limits. The dashed and solid lines represent simulated loci of objects with $C > 0$ and $C = 0$ respectively. The right and left set of simulations assume a constant and an increasing [O III] line flux with decreasing viewing angle respectively. The dotted line separates weak- (below the line) and strong-lined radio-loud AGN (above the line) as defined in these studies. See text for details.

to be concentrated at higher and lower [O II] and [O III] equivalent width values respectively, and so to populate distinct regions of the plane.

Fig. 4.3 plots the [O III] $\lambda 5007$ versus the [O II] $\lambda 3727$ rest frame equivalent widths for objects from the DXRBS and 2 Jy survey (105 objects). In order to increase the number statistics I have now additionally included objects with errors on their Ca H&K break values > 0.2 (15 sources; mean error 0.3), and objects with no available Ca H&K break measurement (8 sources). Objects with Ca H&K break values $C \geq 0.25$, $0 < C < 0.25$ and $C = 0$ are plotted as stars (31 objects), open

squares (28 objects), and filled circles (38 objects) respectively. In cases where a Ca H&K break measurement was not available, objects were assumed to be viewed at relatively small angles if broad emission lines were present in their optical spectra (6 objects, grouped with sources with $C = 0$ and plotted as filled circles), and to be viewed at relatively large angles if only narrow lines had been observed (2 objects, grouped with sources with $C \geq 0.25$ and plotted as stars).

Fig. 4.3 first shows that sources with relatively high and low Ca H&K break values, i.e. radio galaxies and blazars respectively, indeed populate distinct regions of the plane. Second, as argued in the previous section, the majority of the blazars under study appear to be beamed radio galaxies with strong [O III] emission lines, since it is mostly this type of radio galaxies which have [O III] and [O II] equivalent widths higher than the ones of blazars. (Note that these quantities are expected to decrease with viewing angle only if the radio galaxies and blazars are part of the same population.) However, a few blazars might be beamed radio galaxies with weak [O III] emission lines. Therefore, we need a general approach to separate in this plane *both* the radio galaxy and blazar populations into weak- and strong-lined radio-loud AGN.

For this purpose I have simulated the relation between the [O II] and [O III] equivalent widths as the jet emission increases relative to the host galaxy. I have assumed starting [O III] equivalent width values $W_{[\text{OIII}]} = 200, 50$ and 20 \AA and a constant line luminosity ratio $L_{[\text{OII}]} / L_{[\text{OIII}]} = 0.3$ (the mean value for the 72 objects in the current sample with both a detected [O II] and [O III] emission line). For the jet I have assumed a power-law spectrum with spectral index $\alpha_\nu = 1$. The results are shown in Fig. 4.3 as the right set of dashed and solid lines, indicating loci of objects with Ca H&K break values $C > 0$ and $C = 0$ respectively.

These simulations seem to reproduce well the equivalent width decrease for objects with $C > 0$ as well as the position at which sources start to have a Ca H&K break value of zero. However, the predicted relation between the [O II] and [O III] equivalent widths for objects with $C = 0$ appears to be steeper than the observed one. In the performed simulations the Ca H&K break is diluted to its minimum value of zero when the jet emission dominates at all optical wavelengths. Then, as the jet emission further increases both the [O II] and [O III] equivalent widths decrease in a similar way, resulting in a correlation between the two with a slope of one. This is shown by the solid lines in Fig. 4.3 that converge irrespective of the starting [O III] equivalent width values. The observations, however, seem to indicate that the [O II] and [O III] equivalent widths of objects with $C = 0$ do not decrease in the same way. In fact they seem to have a similar decrease as the ones

of sources with $C > 0$. This is evidenced by the clear-cut envelope in the upper left part of Fig. 4.3 stretching from radio galaxies to blazars for which I get roughly a slope of ~ 0.4 . A slope flatter than one for sources with $C = 0$ then means that with orientation either their [O III] equivalent widths decrease less than the ones of [O II], or their [O II] equivalent widths decrease more than the ones of [O III].

A lower decrease of the [O III] emission line equivalent width compared to that of [O II] is only possible if we assume that the [O II]/[O III] line luminosity ratio decreases with viewing angle. This could be the case if, e.g., the [O III] emission was radiated anisotropically (Hes et al., 1996). Indeed, for the objects in the current sample with a detection of at least one of the two emission lines I find a strong ($P > 99.9\%$) correlation between $L_{[\text{OII}]} / L_{[\text{OIII}]}$ and Ca H&K break value, albeit with a large scatter. I have checked also by means of a partial correlation analysis that this relation is not induced by the common redshift dependence. I have used here and in the following the ASURV analysis package (Isobe et al., 1986) and the algorithms for partial correlation analysis developed by Akritas and Siebert (1996) whenever censoring was present in the data.

In order to test if an increase of the [O III] line flux with orientation can in fact account for the distribution of the points in Fig. 4.3 I have repeated the simulations. I have now assumed starting [O II] (and not [O III] as before) equivalent widths $W_{[\text{O II}]} = 200, 50$ and 20 \AA and increased the [O III] line flux in dependence of the Ca H&K break value using the above correlation between the $L_{[\text{OII}]} / L_{[\text{OIII}]}$ ratio and Ca H&K break. The results are shown in Fig. 4.3 as the left set of dashed and solid lines, indicating loci of objects with Ca H&K break values $C > 0$ and $C = 0$ respectively. However, this new set of simulations seems to reproduce the equivalent width decrease for objects with $C > 0$ worse than the earlier one. Moreover, it still cannot account for the flatter decrease observed for objects with $C = 0$. This is because the increase in jet emission ‘catches up’ with the [O III] line flux increase, causing the [O II] and [O III] equivalent widths to decrease in a similar way as soon as the Ca H&K break is diluted to its minimum value. I will expand on the subject of the [O II]/[O III] emission line ratios in Section 4.4.4.

The second possibility, that with orientation the [O II] equivalent width decreases more than the one of [O III], implies that the continuum at the position of [O II] increases with decreasing viewing angle more than the one at the position of [O III]. This, however, is only possible if we assume the presence of a third component that starts to dominate the high frequency continuum of radio-loud AGN at the smallest viewing angles. In order to assess if this is indeed the case I have built composite spectra for objects with Ca H&K break values $C \geq 0.25$, $0 < C < 0.25$ and

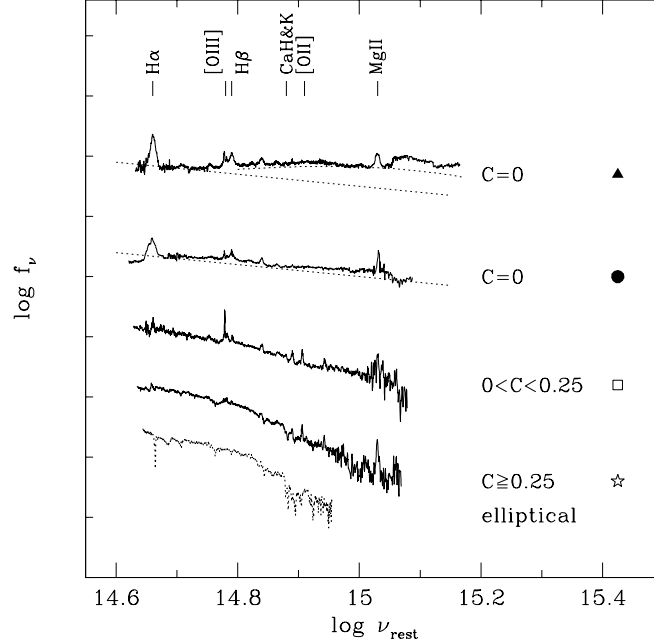


FIGURE 4.4. Composite spectra for objects from the DXRBS and 2 Jy survey grouped according to their Ca H&K break value. Also shown is the spectrum of an elliptical galaxy. A power law continuum with slope $\alpha_\nu = 1$ and a Balmer continuum are underlaid as dotted lines to the composites for objects with Ca H&K break value $C = 0$. Objects included in the composites are plotted in Fig. 4.5 with symbols shown on the right side. $C = 0$ sources are separated into sources with ratios between their [O II] and [O III] continuum luminosities above (top, triangle) and below (bottom, circle) $\log L_{c[\text{O II}]} / L_{c[\text{O III}]} = 0.15$ (corresponding roughly to an optical spectral slope of $\alpha_\nu = 1$).

$C = 0$, the latter separated also into sources with ratios between their [O II] and [O III] continuum luminosities below and above a value of $\log L_{c[\text{O II}]} / L_{c[\text{O III}]} = 0.15$ (corresponding roughly to an optical spectral slope of $\alpha_\nu = 1$). Before combining, the spectra have been shifted to their rest frame wavelength, normalized at 5500 \AA and trimmed off noisy edges. The spectra have been merged building an average with the IRAF task *noao.onedspec.scombine*. The resulting four composites are displayed in Fig. 4.4. From top to bottom these contain 29, 10, 27 and 33 objects.

The composites show that the continuum of radio-loud AGN indeed flattens with decreasing Ca H&K break value. And this flattening can be very well interpreted as being caused by distinct components dominating the continuum emission at different

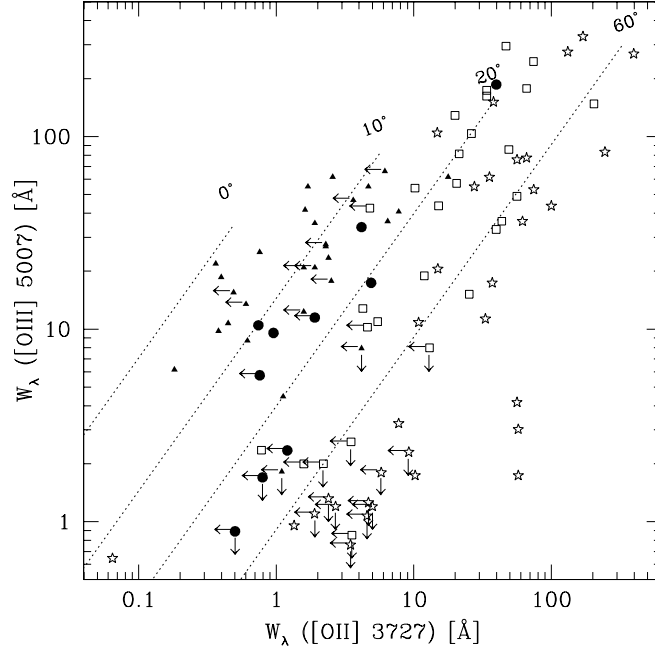


FIGURE 4.5. The rest frame equivalent widths of [O III] $\lambda 5007$ versus [O II] $\lambda 3727$ for objects from the DXRBS and 2 Jy survey. Stars and open squares represent sources with Ca H&K break values $C \geq 0.25$ and $0 < C < 0.25$ respectively. Filled circles and triangles represent sources with Ca H&K break values $C = 0$ included in the lower and upper composite of Fig. 4.4 respectively. Arrows indicate upper limits. Dotted lines represent loci of constant viewing angle as labeled (see text for details).

orientations. A comparison between the composite for objects with $C \geq 0.25$ and the spectrum of an elliptical galaxy (dotted spectrum in Fig. 4.4) suggests that this is the dominant component at relatively large viewing angles. Then, as the viewing angle decreases and relativistic beaming enhances the jet emission, the continuum flattens (composite for objects with $0 < C < 0.25$), until the jet emission dominates (lower composite for objects with $C = 0$ to which a power-law spectrum with slope $\alpha_\nu = 1$ is overlaid as dotted line). Finally, at even smaller viewing angles we observe an additional component dominating the continuum emission at UV frequencies.

This additional component is the ultraviolet excess often observed in AGN, which is generally interpreted as Balmer continuum/Fe II emission (e.g. Malkan and Sargent, 1982). Following Wills et al. (1985), I have then calculated the Balmer continuum for a temperature of 15,000 K. The resulting spectrum is overlaid as dotted curve to the upper composite for objects with $C = 0$. A remarkable agreement is

evident. But is it feasible to assume that the Balmer continuum emission increases with decreasing viewing angle? Observations indicate that the Balmer continuum is located within the BLR (Maoz et al., 1993). Therefore, as the broad emission lines themselves, we expect the Balmer continuum to be obscured by the putative circumnuclear dusty torus at large viewing angles and to come into our line of sight only if the AGN is oriented at relatively small viewing angles. Indeed, a strong correlation is present between the BLR luminosity and the $[\text{O II}]/[\text{O III}]$ continuum luminosity ratio (Fig. 4.7, lower panel), which will be discussed in detail in Section 4.4.2. Note that the $[\text{O II}]/[\text{O III}]$ continuum luminosity ratio is directly related to the Ca H&K break, the $[\text{O II}]$ and $[\text{O III}]$ emission lines being located blue- and redward of this feature respectively, and so is also expected to be a suitable orientation indicator.

The composites shown in Fig. 4.4 are very similar to the ones presented by Baker and Hunstead (1995) for a sample of quasars selected from the Molongolo survey. These authors grouped their sources according to the radio core dominance parameter R (defined as the ratio between the core and extended radio flux), which is assumed to be a suitable indicator of orientation. The trends observed with increasing R are similar to the ones observed with decreasing Ca H&K break value, namely a flattening of the continuum emission, markedly stronger appearance of the Balmer continuum, and a decrease of the $[\text{O II}]$ and $[\text{O III}]$ equivalent widths. This confirms the use of the Ca H&K break value as a statistical orientation indicator. However, Baker (1997) concluded that the main cause for the flattening of the continuum of quasars at small viewing angles was a decreased obscuration by the putative circumnuclear dusty torus. Or reversed, the larger the viewing angle, the more the continuum is steepened by dust extinction. In support of this interpretation Baker (1997) argued the strong correlation observed between the $\text{H}\alpha/\text{H}\beta$ emission line ratios and optical spectral index. The amount of extinction predicted by this correlation seemed to explain the observed decrease in $[\text{O II}]$ and $[\text{O III}]$ equivalent widths with R and the observed range of optical spectral slopes.

However, an orientation-dependent obscuration as the primary cause for the change of the continuum shape of radio-loud quasars with viewing angle is ruled out by the fact that this trend is observed with decreasing Ca H&K break value. The Ca H&K break can only be decreased by the presence of an additional component, assumingly the jet, but not by obscuration. In any case, the observed continuum shapes are in good agreement with those of the expected main components in radio-loud AGN, namely host galaxy and jet. On the other hand, obscuration might play a role in the observed Balmer decrement decrease. In fact, we have measurements on both $\text{H}\alpha$ and $\text{H}\beta$ emission lines for 11 objects from the sample plotted in Fig. 4.3

and for these, similar to the results of Baker (1997), an anticorrelation ($P = 97.7\%$) is present between the $H\alpha/H\beta$ emission line and $[O\text{ II}]/[O\text{ III}]$ continuum luminosity ratios.

To explain the distribution of the points in Fig. 4.3, I have then repeated the simulations assuming now three components for the continuum emission of radio-loud AGN, namely host galaxy, jet and Balmer continuum, and increased the flux of the latter two with decreasing viewing angle. I have simulated the change in orientation by increasing the jet flux relative to the host galaxy emission (jet/galaxy ratio defined at 5500 \AA) and calculated from this viewing angles using the results presented in the last Chapter. In particular I have used from these studies the linear relations between jet/galaxy ratio and Ca H&K break value for a jet with spectral slope $\alpha_\nu = 1$ (Section 3.1), and between Ca H&K break value and viewing angle for a jet with Lorentz factor $\Gamma = 3$ (Section 3.3). The flux increase of the Balmer continuum with decreasing viewing angle has been adjusted interactively to give a slope of ~ 0.4 for the correlation between the logarithmic $[O\text{ III}]$ and $[O\text{ II}]$ equivalent

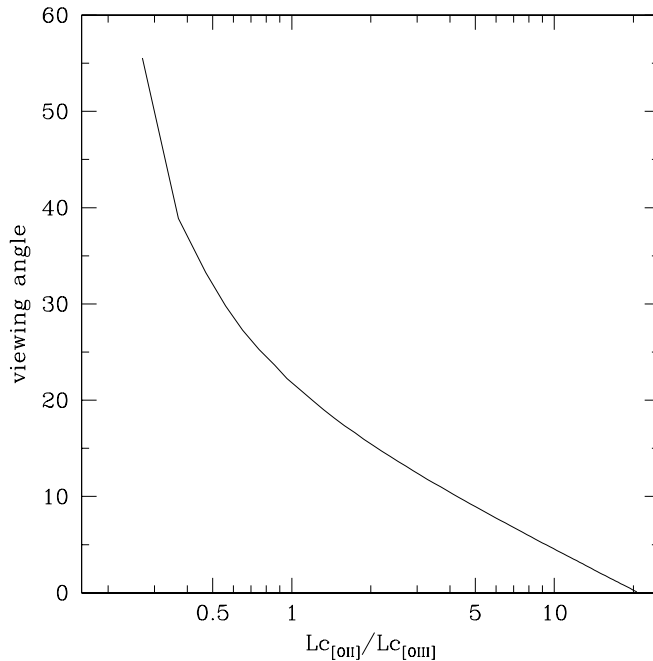


FIGURE 4.6. The relation viewing angle versus ratio between continuum luminosities at the position of $[O\text{ II}]\ \lambda 3727$ and $[O\text{ III}]\ \lambda 5007$ as obtained from the simulations assuming three components for the continuum emission of radio-loud AGN, namely host galaxy, jet and Balmer continuum (see text for details). Continuum luminosities are in $\text{erg s}^{-1}\ \text{\AA}^{-1}$.

widths. This is the approximate slope of the upper envelope to the data in Fig. 4.3. The resulting loci of constant viewing angle are shown as dotted lines in Fig. 4.5. These have a slope of one, since I have assumed for simplicity a constant line luminosity ratio $L_{[\text{O II}]} / L_{[\text{O III}]}$ which does not change with viewing angle, but the envelope of these lines follows the slope of the envelope to the data points.

These new simulations predict that the continuum flux at the position of $[\text{O II}]$ is dominated by emission from the host galaxy, jet and Balmer continuum for objects viewed at angles $\phi \gtrsim 35^\circ$, $15^\circ \lesssim \phi \lesssim 35^\circ$ and $\phi \lesssim 15^\circ$ respectively. Fig. 4.5 also plots the objects included in the four composites with different symbols. From this we see in particular that objects with $C = 0$ included in the upper and lower composites indeed cluster around the predicted values. Therefore, the relation between the logarithmic $[\text{O II}]$ and $[\text{O III}]$ equivalent widths of radio-loud AGN seems to follow indeed a slope of ~ 0.4 and their continuum appears to change with viewing angle mainly at the position of $[\text{O II}]$. The latter makes the $[\text{O II}]/[\text{O III}]$ continuum luminosity ratio a suitable orientation indicator and Fig. 4.6 shows its relation to viewing angle as it results from the described simulations. Its advantage over the Ca H&K break value is that it offers a much higher dynamical range. Note again that weak-lined sources at small angles w.r.t. the line of sight seem to be lacking in the bottom left corner of Fig. 4.5. This might be simply a selection effect. Sources in this region, in fact, which should be strongly beamed, intrinsically weak-lined objects, would have extremely small equivalent widths ($\sim 0.1 - 1$), which can be easily washed out in low S/N spectra, preventing a redshift determination.

Now I want to use the $[\text{O III}] - [\text{O II}]$ equivalent width plane to separate the entire sample of DXRBS and 2 Jy sources into (intrinsically) weak- and strong-lined radio-loud AGN. The objects plotted in Fig. 4.3 have $[\text{O III}]$ and $[\text{O II}]$ equivalent width distributions similar to the ones shown in Fig. 4.2. For the intersection point of the two best-fit Gaussians in the case of objects with $C \geq 0.25$, I now find $W_{[\text{O III}]} \sim 10 \text{ \AA}$. Then for the purpose of this study I define the line dividing weak- and strong-lined radio-loud AGN in this plane to have a slope of 0.4 (assumed to represent the relation between the $[\text{O II}]$ and $[\text{O III}]$ equivalent widths as the viewing angle changes), and to separate objects with $C \geq 0.25$ and $[\text{O III}]$ equivalent width values below and above 10 \AA respectively (dotted line in Fig. 4.3). This results in a total of 25 and 80 objects in the sample under study being defined as weak- and strong-lined radio-loud AGN respectively. Of the weak- and strong-lined AGN 12 (13) and 43 (37) sources respectively are part of the DXRBS (2 Jy) survey. Out of the 12 weak-lined radio-loud AGN from the DXRBS, 8 are currently classified as BL Lacs, 2 as FSRQ, and 2 as radio galaxies. Out of the 43 strong-lined radio-loud

AGN from the DXRBS, 32 are currently classified as FSRQ, 4 as BL Lacs, and 7 as radio galaxies.

Note that Tadhunter et al. (1998) have similarly classified objects in their sample from the 2 Jy survey as weak-line radio galaxies (WLRG) if their spectra were dominated by stellar absorption features from the host galaxy and their [O III] emission lines were weaker than 10 \AA . In this respect, although objects from the 2 Jy have been included in these studies and 11/16 sources with $C > 0.25$ and $W_{[\text{O III}]} < 10 \text{ \AA}$ are from this survey, only 4 objects are in common with the subsample used by Tadhunter et al. (1998).

4.4.2 Emission Line Region Luminosities

In the following I want to investigate if there exist other differences between weak- and strong-lined radio-loud AGN besides their [O III] emission line strengths. I want to start by comparing their narrow and broad line region luminosities.

The broad line region of radio-loud AGN, contrary to their narrow line region, is located much closer to the central black hole, and so can be (partially or fully) obscured by the thick, dusty torus believed to surround the nucleus at relatively large viewing angles. Therefore, the BLR luminosity, unlike the NLR luminosity, is expected to be strongly aspect dependent and any studies involving this quantity need to disentangle orientation effects first. In the previous section, I have argued that the [O II]/[O III] continuum luminosity ratio represents a suitable statistical orientation indicator for radio-loud AGN. In order to further test this Fig. 4.7 plots for the sample of weak- (filled circles) and strong-lined AGN (open circles) the NLR and BLR luminosities versus this quantity.

In the sample under study broad emission lines have been detected only for objects with Ca H&K break values $C \lesssim 0.35$ (with the exception of 2Jy 1514+07, which has a narrow $\text{H}\alpha$ emission line with broad wings, however, its Ca break has a large error, $C = 0.6 \pm 0.5$). Therefore, only these are included in Fig. 4.7, lower panel, and I have assumed that this is the maximum Ca H&K break value (i.e. the maximum viewing angle) for which we can expect to observe broad emission lines in the object's spectrum (note that this value turns out to be the same as the one in Section 3.5 inferred to be appropriate to separate core- and lobe-dominated radio-loud AGN). Non-detection limits on the BLR luminosity have then been derived (as described in Section 4.2) only for objects with $C \leq 0.35$. The NLR luminosity has been considered as a non-detection limit if both the [O II] and [O III] emission lines were absent (15 weak- and 2 strong-lined AGN) and also if only the [O II] emission line could not be detected (2 weak- and 13 strong-lined AGN).

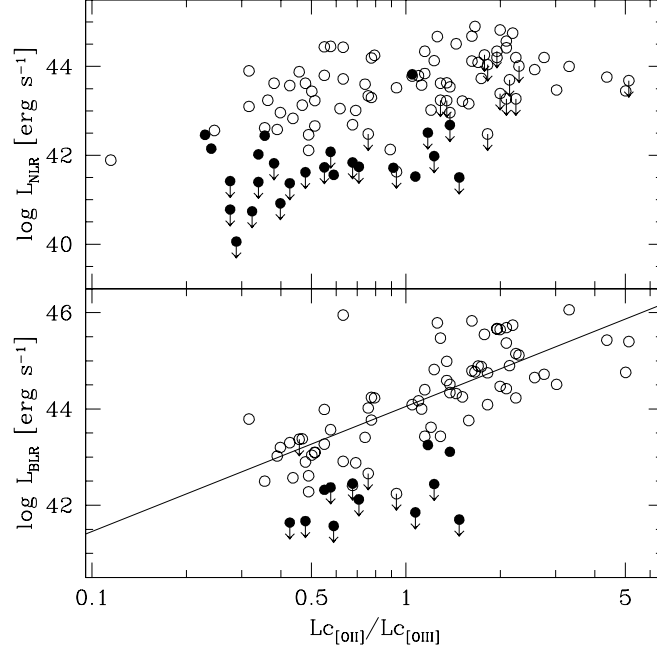


FIGURE 4.7. The narrow line (upper panel) and broad line region (lower panel) luminosities versus the ratio of the continuum luminosities at the locations of [O II] and [O III] for objects from the DXRBS and 2 Jy survey. Filled and open circles denote weak- and strong-lined radio-loud AGN respectively (see text for definition). Arrows indicate upper limits. The solid line represents the observed correlation for the strong-lined radio-loud AGN.

For the population of strong-lined AGN a strong ($P > 99.9\%$) correlation is present between BLR luminosity and [O II]/[O III] continuum luminosity ratio with a slope of ~ 3 (solid line in Fig. 4.7). The correlation remains very strong even if the common dependence on redshift is excluded. Note that a redshift dependence of the [O II]/[O III] continuum luminosity ratio is expected if it is indeed a beaming indicator. In a radio flux-limited sample strongly beamed sources will have higher powers and so will be detected on average at higher redshifts than weakly beamed ones. On the other hand, no significant ($P = 68.3\%$) correlation is present between their NLR luminosities and [O II]/[O III] continuum luminosity ratios once the common redshift dependence is excluded. This result is in support of the interpretation that the [O II]/[O III] continuum luminosity ratio, similar to the Ca H&K break value, is a suitable statistical orientation indicator. Owing to their large number of upper limits I have not attempted a similar analysis for the weak-lined sources.

I now want to compare the NLR and BLR luminosities of weak- and strong-lined

radio-loud AGN. From Fig. 4.7 we see that weak-lined AGN reach lower maximum $[\text{O II}]/[\text{O III}]$ continuum luminosity ratios than strong-lined sources. Therefore, in order to compare their BLR luminosities at similar viewing angles I have considered only strong-lined AGN with $[\text{O II}]/[\text{O III}]$ continuum luminosity ratios in the range spanned by the weak-lined sources. I then get that weak- (12 sources) and strong-lined radio-loud AGN (43 sources) have mean BLR luminosities $\log L_{\text{BLR}} = 41.82 \pm 0.16$ and $43.67 \pm 0.14 \text{ erg s}^{-1}$ respectively, a factor of ~ 70 apart. For the NLR luminosities of (the entire sample of) weak- and strong-lined radio-loud AGN, I get mean values $\log L_{\text{NLR}} = 40.92 \pm 0.25$ and $43.44 \pm 0.09 \text{ erg s}^{-1}$ respectively, a factor of ~ 300 apart. Here and in the following I have calculated means using the ASURV analysis package whenever censored data were included.

These comparisons show that in the viewing angle range considered here strong-lined radio-loud AGN appear to have narrow and broad line regions similar (only a factor of ~ 2 apart) in luminosity. On the other hand, the NLR luminosities of weak-lined sources appear to be on average a factor of ~ 10 lower than their BLR luminosities. This suggests that weak-lined radio-loud AGN have rather underluminous narrow than broad emission line regions. However, no strong conclusions are possible in this respect, since only upper limits are available for the majority of weak-lined sources (9/12 and 17/25 of the sources with values of the BLR and NLR luminosities respectively).

4.4.3 Emission Line Regions and Jet Powers

Next, I want to investigate relations between emission line region luminosities and radio and X-ray jet powers for weak- and strong-lined radio-loud AGN.

Fig. 4.8 plots the narrow line region luminosity versus the extended radio luminosity at 151 MHz (left panel) and versus the total X-ray luminosity at 1 keV (right panel) for the sample of objects under study. For sources from the 2 Jy survey I have used the radio and X-ray information given in Morganti et al. (1993) and Siebert et al. (1996) respectively. I have calculated the extended radio luminosity at 151 MHz for the sample under study from the total radio luminosity at 5 GHz as follows. I have first used the relation between radio core dominance parameter and radio spectral index given in D’Elia et al. (2003) to compute the extended radio luminosity at 5 GHz from the total radio luminosity at this frequency and the radio spectral index. I have then transformed the extended radio luminosity at 5 GHz to 151 MHz assuming a radio spectral index $\alpha_r = 0.8$ (where $f_\nu \propto \nu^{-\alpha}$). I have used the extended radio luminosity at 151 MHz since from this an estimate of the jet power can be derived, as $L_{\text{jet}} \propto L_{151}^{6/7}$ (Willott et al., 1999). For objects from the 2

Jy survey the *ROSAT* X-ray band (0.1 – 2.4 keV) luminosity has been transformed to 1 keV assuming an X-ray spectral index $\alpha_x = 1$.

For the strong-lined radio-loud AGN a significant ($P > 99.9\%$) correlation is present between the narrow line region luminosity and the extended radio luminosity at 151 MHz (solid line in Fig. 4.8, left panel). I have verified also by means of a partial correlation analysis that the luminosity - luminosity correlation is not induced by a common redshift dependence. The large number of upper limits in the case of weak-lined radio-loud AGN do not allow for a similar investigation. Therefore, I want to quantify their relation to the strong-lined sources only qualitatively. For this purpose Fig. 4.8, left panel, plots also the dispersion ($2\sigma = 1.16$) around the best-fit line for the observed correlation (dashed lines). This gives that 44% (11/25) of the weak-lined AGN fall below the 2σ region of the correlation followed by the strong-lined sources. Moreover, the majority (70% or 10/14) of the remaining sources nominally within this region have only upper limits on their NLR luminosities. Therefore, it appears that weak- and strong-lined radio-loud AGN form a parallel sequence in this luminosity - luminosity plane rather than weak-lined AGN being merely an extrapolation of the strong-lined sources down to lower emission line luminosities and radio jet powers. In fact, whereas weak- and strong-lined objects have mean NLR luminosities a factor of ~ 300 apart, their mean extended radio luminosities differ only by a factor of ~ 10 ($\log L_{151} = 33.51 \pm 0.18$ and 34.49 ± 0.10 erg s $^{-1}$ Hz $^{-1}$ respectively). This means that weak-lined radio-loud AGN have underluminous narrow emission lines rather than weak radio jets.

Fig. 4.8, right panel, plots the NLR luminosity versus the total X-ray luminosity at 1 keV for the sample of objects under study. The X-ray emission of radio-loud AGN, contrary to their emission at radio frequencies, is believed to be made up of two components with different origins: an isotropic one, produced by the ambient hot gas (presumably from the group or cluster possibly associated with the source), and an anisotropic one, associated with the nucleus (e.g. Siebert et al., 1996). Then, which of these two components dominates the observed X-ray power will strongly depend on the object's orientation with respect to our line of sight. At relatively large viewing angles, i.e. in the case of radio galaxies, we expect to observe mainly the isotropic component of the X-ray emission, while at relatively small viewing angles, i.e. for blazars, we expect the X-ray emission to be dominated by the (beamed) nuclear component (e.g. Baker et al., 1995). Therefore, I have split in this case the sample not only into weak- and strong-lined radio-loud AGN, but also into objects with Ca H&K break values $C = 0$ (circles) and $C > 0$ (squares), i.e. viewed at smaller and larger angles respectively. (Note that a similar split is shown for the

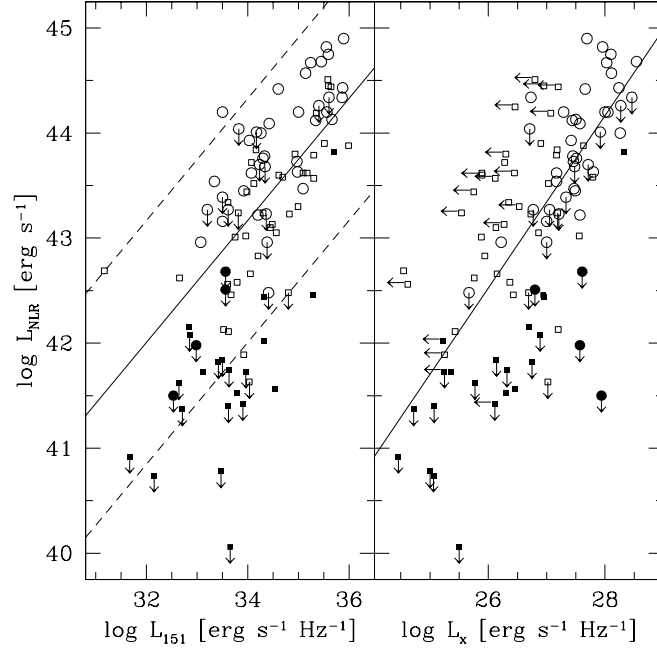


FIGURE 4.8. The narrow line region luminosity versus the extended radio luminosity at 151 MHz (left panel) and the total X-ray luminosity at 1 keV (right panel) for objects from the DXRBS and 2 Jy surveys. Filled and open symbols indicate weak- and strong-lined radio-loud AGN respectively. Circles and squares indicate objects with Ca H&K break values $C = 0$ and $C > 0$ respectively. Arrows indicate upper limits. The solid line represents the observed correlation for the strong-lined radio-loud AGN (left panel) and the strong-lined radio-loud AGN with $C = 0$ (right panel). The dashed lines indicate the 2σ dispersion of the correlation.

objects in the left panel of Fig. 4.8, although only for consistency reasons.)

For the strong-lined radio-loud AGN with $C = 0$ (40 objects) a strong ($P > 99.9\%$) correlation is present between NLR luminosity and total X-ray luminosity, which remains significant if the common redshift dependence is excluded (solid line in Fig. 4.8, right panel). On the other hand, for the objects with $C > 0$ from this group (40 sources) only a marginal ($P = 94\%$) correlation is present once the common redshift dependence is excluded. This suggests that mainly in objects with Ca H&K break values $C = 0$ (i.e. objects dominated by the jet emission; see composites in Fig. 4.4) we observe the nuclear component as the dominant source of X-ray emission. Note that only this component is assumed to be directly related to the object's radio jet power and so expected to scale with emission line luminosity

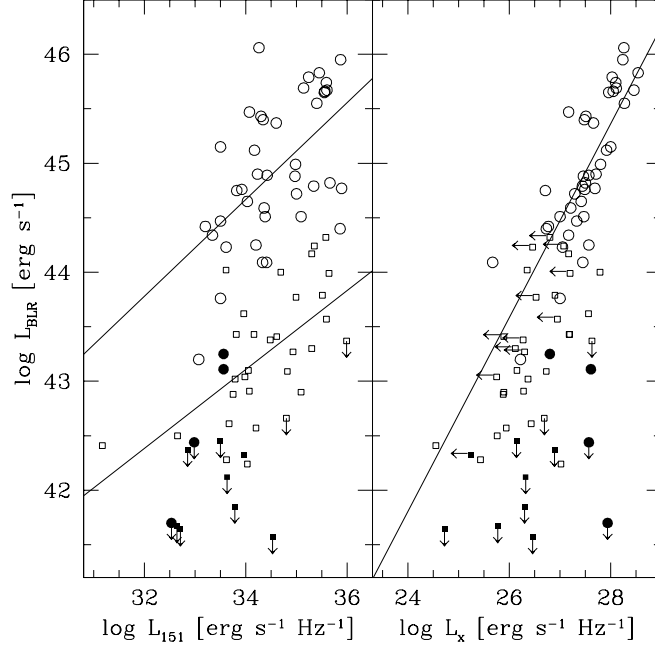


FIGURE 4.9. The broad line region luminosity versus the extended radio luminosity at 151 MHz (left panel) and the total X-ray luminosity at 1 keV (right panel) for objects from the DXRBS and 2 Jy surveys. Symbols are the same as in Fig. 4.8. The upper and lower solid lines in the left panel represent the observed correlations for strong-lined radio-loud AGN with Ca H&K break values $C = 0$ and $C > 0$ respectively. The solid line in the right panel represents the observed correlation for strong-lined radio-loud AGN with Ca H&K break values $C = 0$.

(Rawlings and Saunders, 1991). In objects with Ca H&K break values $C > 0$, on the other hand, the X-ray emission seems to be predominantly thermal in origin. Now, in order to assess if weak- and strong-lined radio-loud AGN differ in the strength of their nuclear X-ray emission, and so X-ray jet power, we would need to compare only objects viewed at relatively small angles. In the current sample only 4 weak-lined objects have $C = 0$. For these I get a mean X-ray luminosity $\log L_x = 27.48 \pm 0.24 \text{ erg s}^{-1} \text{ Hz}^{-1}$, which is very similar to the mean value for the strong-lined objects with $C = 0$ of $\log L_x = 27.51 \pm 0.09 \text{ erg s}^{-1} \text{ Hz}^{-1}$. Therefore, also in the X-ray band it appears that the difference between weak- and strong-lined radio-loud AGN lies mainly in their emission line luminosities rather than their jet powers.

We now want to turn to the broad emission lines. Fig. 4.9 plots the BLR luminosity versus the extended radio luminosity at 151 MHz (left panel) and total

X-ray luminosity at 1 keV (right panel) for the sample under study. Fig. 4.7, lower panel, has shown that a large scatter is expected in any logarithmic plot involving BLR luminosity, if orientation effects are not accounted for properly. Therefore, in order to do so I have split the weak- and strong-lined radio-loud AGN additionally into objects with $C = 0$ (4 and 40 sources) and $C > 0$ (8 and 31 sources). I find that for both strong-lined radio-loud AGN with $C = 0$ and $C > 0$ the BLR luminosity is significantly ($P > 99.9\%$) correlated with the extended radio luminosity at 151 MHz (solid lines in Fig. 4.9, left panel). Both these correlations remain very strong even if the common redshift dependence is excluded. The two correlations have similar slopes 0.44 ± 0.11 and 0.36 ± 0.09 for objects with $C = 0$ and $C > 0$ respectively. Furthermore, these slopes are similar to the one of 0.58 ± 0.08 for the correlation between NLR luminosity and extended radio power (Fig. 4.8, left panel), suggesting that both the NLR and BLR luminosities scale with radio jet power in a similar way.

The dispersion of the two observed correlations is $\sigma = 0.45$ and 0.38 for objects with $C = 0$ and $C > 0$ respectively, and comparable to the dispersion of $\sigma = 0.58$ that is obtained for the correlation between NLR luminosity and extended radio power. Therefore, it seems that it is indeed crucial to first disentangle orientation effects in studies involving BLR luminosity. Comparing the weak- and strong-lined radio-loud AGN (now separately for $C = 0$ and $C > 0$) I get similarly to the findings in Fig. 4.8, left panel, that the weak-lined objects do not form merely a continuation of the strong-lined ones to lower BLR luminosities and radio jet powers. However, in this case the number statistics are considerably reduced owing to the separation in Ca H&K break value. But, e.g., I get that weak- and strong-lined radio-loud AGN with $C > 0$ (for which a larger number is available) reach maximum BLR luminosities $L_{\text{BLR}} \sim 10^{44.5}$ and $\sim 10^{42.5}$ erg s $^{-1}$ respectively, a factor of ~ 100 apart, whereas their mean extended radio powers differ only by a factor of ~ 10 ($\log L_{151} = 33.45 \pm 0.24$ and 34.43 ± 0.18 erg s $^{-1}$ Hz $^{-1}$ respectively). Therefore, this finding also suggests that the difference between weak- and strong-lined radio-loud AGN is mainly in emission line luminosity.

Considering the BLR luminosity versus the total X-ray luminosity (Fig. 4.9, right panel) I find that, once the common redshift dependence is excluded, a significant correlation is only present for strong-lined radio-loud AGN with Ca H&K break values $C = 0$ (solid line), but not for those with $C > 0$. Therefore, the BLR luminosity, similarly to the NLR luminosity, seems to correlate with the nuclear X-ray emission only.

All DXRBS sources for which an optical spectrum was not available have been

excluded from this analysis. Out of these, 37 have a redshift $z < 0.8$, the maximum value for which the [O III] emission line can be observed in the optical range, and so could have been in principle included. For these I get mean values of $\log L_{151} = 33.81 \pm 0.18 \text{ erg s}^{-1} \text{ Hz}^{-1}$ and $\log L_x = 26.50 \pm 0.20 \text{ erg s}^{-1} \text{ Hz}^{-1}$ respectively, well within the luminosity ranges of the objects included. Therefore, the exclusion of these sources is not expected to have biased the current results.

4.4.4 The Ionization State

Finally, I want to investigate the [O III]/[O II] emission line ratios of weak- and strong-lined radio-loud AGN. This quantity is known to be ionization-sensitive in that it is assumed to correlate with the ionizing power of the central AGN (e.g. Saunders et al., 1989). Furthermore, it is often used in relation with other emission line ratios as a diagnostic to discriminate between the two emission line excitation mechanisms believed to be important in radio-loud AGN, namely photoionization by a power-law continuum and ionization by shock-wave heating (e.g. Baldwin et al., 1981; Veilleux and Osterbrock, 1987).

Since the [O III] emission line can be produced in regions that are denser than the ones giving rise to [O II], it has been argued that a significant contribution to the integrated [O III] emission line flux might come from a transition region between the classical narrow and broad line regions, which could be partially obscured at certain viewing angles (Hes et al., 1996). This would then render the [O II]/[O III] line ratio aspect dependent. In fact, Baker (1997) found for their sample of radio quasars a strong correlation between the [O II]/[O III] flux ratio and radio core dominance parameter.

In order to test the (an)isotropy of the [O III] emission for weak- and strong-lined sources Fig. 4.10 plots the [O II]/[O III] line luminosity ratios versus the [O II]/[O III] continuum luminosity ratios, assuming the latter quantity a suitable statistical indicator of orientation. Note that objects with upper limits on both the [O II] and [O III] line luminosities have been excluded from this analysis. For the strong-lined radio-loud AGN only a marginal ($P = 92.9\%$) correlation is present between the two quantities (dashed line), whereas a strong ($P = 97.3\%$) correlation is found for weak-lined sources (solid line), which remains significant even if the common redshift dependence is excluded. Therefore, obscuration seems to play a role in both weak- and strong-lined sources, in agreement with the previous result in Section 4.4.1, where for the entire sample a similarly strong correlation was present between $L_{[\text{O II}]} / L_{[\text{O III}]}$ and Ca H&K break value.

However, obscuration of [O III] emission at large viewing angles cannot be the

main factor that introduces the observed correlation between the $L_{[\text{O II}]} / L_{[\text{O III}]}$ and $Lc_{[\text{O II}]} / Lc_{[\text{O III}]}$ luminosity ratios for weak-lined objects. The best-fit line gives in their case a slope of -1.89 ± 0.56 , which is significantly steeper than the slope of -0.39 ± 0.15 for the correlation of the strong-lined sources. Therefore, this interpretation would imply that weak-lined sources are in fact more obscured than strong-lined AGN, a scenario which is problematic for the following reasons.

First, from the intersection point of the observed correlations it results that weak- and strong-lined AGN have a similar ratio of $L_{[\text{O II}]} / L_{[\text{O III}]} = 0.2$ for a continuum luminosity ratio of $Lc_{[\text{O II}]} / Lc_{[\text{O III}]} = 1$, which corresponds roughly to a viewing angle of $\sim 20^\circ$. Then, e.g., at $Lc_{[\text{O II}]} / Lc_{[\text{O III}]} = 0.3$, which corresponds roughly to a viewing angle of $\sim 50^\circ$, the two correlations give values of $L_{[\text{O II}]} / L_{[\text{O III}]} = 3$ and 0.3 for weak- and strong-lined sources respectively. Assuming now that the change of the line luminosity ratio is only due to obscuration of $[\text{O III}]$ emission at large viewing

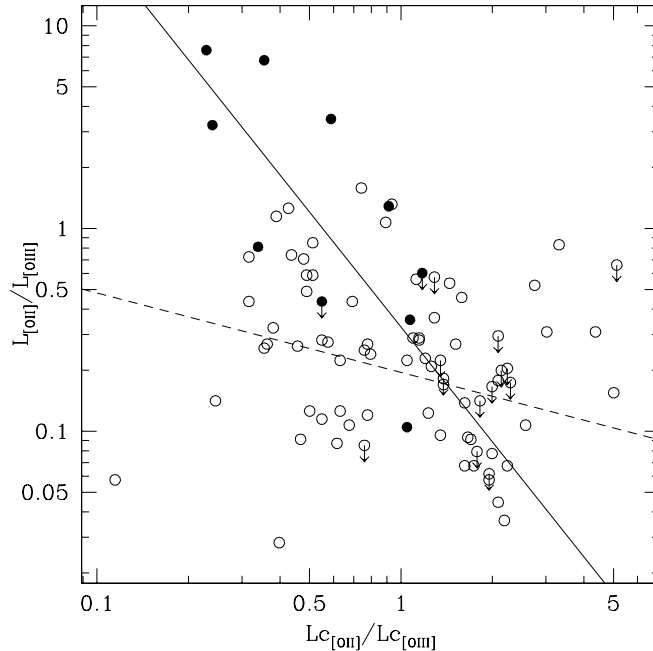


FIGURE 4.10. The ratio between the $[\text{O II}] \lambda 3727$ and $[\text{O III}] \lambda 5007$ line luminosities versus their continuum luminosity ratios for objects from the DXRBS and 2 Jy survey. Filled and open circles denote weak- and strong-lined radio-loud AGN respectively (see text for definition). Arrows indicate upper limits. The solid line represents the observed correlation for the weak-lined radio-loud AGN. The dashed line indicates the marginally significant correlation for the strong-lined radio-loud AGN.

angles, this then implies that the [O III] line luminosity of strong-lined sources barely changes with viewing angle, whereas the one of weak-lined AGN has decreased at large viewing angles by a factor of ~ 15 . In other words, not only has the obscuration to be more severe in weak- than in strong-lined sources, but, if we assume that the obscuration is indeed caused by the dusty torus presumably surrounding the nuclear regions of AGN, then the bulk of the [O III] emission of weak-lined AGN would be in fact located within this feature, and the [O III] emission from their extended, isotropic narrow line regions would be negligible. This is an unlikely scenario.

Second, if the obscuration in weak-lined sources was indeed more severe than in strong-lined sources it would affect in particular their X-ray emission. From Fig. 4.8, right panel, I get that out of the weak- and strong-lined sources with $C > 0$ respectively, i.e. objects oriented at larger viewing angles and so expected to be affected by obscuration, 14% (3/21) and 38% (15/40) respectively have upper limits on their X-ray luminosity. Note that this comparison is meaningful since within both groups sources with $C > 0$ with a detected X-ray flux and a non-detection limit have similar mean redshifts ($\langle z \rangle = 0.155 \pm 0.031$ and 0.097 ± 0.014 respectively in the case of the weak-lined AGN, and $\langle z \rangle = 0.371 \pm 0.042$ and 0.314 ± 0.048 respectively in the case of the strong-lined AGN). Therefore, if anything, strong-lined sources are more obscured.

Then, assuming the effect of obscuration on their narrow emission line ratios to be similar in weak- and strong-lined AGN, the differences in $L_{[\text{O II}]} / L_{[\text{O III}]}$ at any given viewing angle could be interpreted as representative of the differences in their intrinsic physical conditions, such as, e.g., state of ionization. The $L_{[\text{O II}]} / L_{[\text{O III}]}$ values of weak-lined sources viewed at large angles can be reconciled with current photoionization models only if rather low ionization parameters are assumed ($U \sim 10^{-3} - 10^{-4}$), and coincide well with the range of $\sim 3 - 15$ predicted by models invoking ionization by pure shocks (e.g. Dopita and Sutherland, 1995; Allen et al., 1999; Evans et al., 1999). On the other hand, their values at small viewing angles as well as those for the strong-lined radio-loud AGN at both larger and smaller viewing angles lie well within the range typical for photoionization by a central power-law continuum ($U \sim 10^{-2}$, assuming a power-law spectral index $\alpha \sim 1$). Clearly, the underlying line excitation mechanism cannot be unambiguously constrained using the $L_{[\text{O II}]} / L_{[\text{O III}]}$ line ratio alone. Note, however, that even using combinations of line diagnostic diagrams it is in principle difficult to distinguish, on one hand, between excitation by pure shocks and photoionization with a low ionization parameter, and, on the other hand, between shocks+precursor models and photoionization with a higher ionization parameter (e.g. Evans et al., 1999).

If we assume photoionization as the dominant line excitation mechanism in both weak- and strong-lined sources, the fact that we observe the $L_{[\text{O II}]} / L_{[\text{O III}]}$ ratio to change dramatically with viewing angle in weak-lined radio-loud AGN would imply that their ionization parameter changes with orientation. This change would then be roughly a factor of 100 between objects viewed at $\sim 20^\circ$ and those viewed at angles of $\sim 50^\circ$. However, if these represent indeed the same population of objects there is no likely explanation for why the photoionization parameter should be different in the beamed and unbeamed sources.

An alternative scenario could be that photoionization dominates in strong-lined sources, whereas the narrow emission lines of weak-lined AGN are excited mainly via (jet-induced) shocks. Then, the higher and lower $L_{[\text{O II}]} / L_{[\text{O III}]}$ values of weak-lined AGN viewed at larger and smaller angles would be indicative of a pure shock and shock+precursor respectively (e.g. Dopita and Sutherland, 1995; Allen et al., 1999; Evans et al., 1999). However, this scenario implies that the gas excited by the shock precursor dominates the line emission when the jet is viewed at small angles, whereas the one excited by the shock itself becomes gradually more important at larger orientations.

Such a change in ionization gradient for shock induced emission line excitation has indeed been argued by Sutherland et al. (1993) to occur due to projection effects. When our line of sight passes through more of the precursor zone, which is expected to be the case when the jet is viewed at small angles, the $[\text{O III}]$ emission will be enhanced (see their Fig. 4). In their Table 8, they list relative $[\text{O II}]$ and $[\text{O III}]$ line intensities for precursor dominance values of 75%, 50% and 25%. Using the correlation for weak-lined sources in Fig. 4.10 and the relation between $Lc_{[\text{O II}]} / Lc_{[\text{O III}]}$ and viewing angle shown in Fig. 4.6, I then derive for each of these three precursor dominance values a corresponding viewing angle. And with just these three points I readily obtain a strong ($P > 99.9\%$) linear anticorrelation between viewing angle and precursor dominance value. Furthermore, an extrapolation of this relation to lower values gives that the precursor dominance is decreased to a value of zero for viewing angles of $\sim 35^\circ$. From emission line diagnostic diagrams (e.g. Evans et al., 1999) we see that the transition from a shock+precursor to a pure shock occurs at a value of $L_{[\text{O II}]} / L_{[\text{O III}]} \sim 2.5$. The correlation for the weak-lined sources in Fig. 4.10 gives for this a value of $Lc_{[\text{O II}]} / Lc_{[\text{O III}]} \sim 0.35$, which corresponds roughly to a viewing angle of $\sim 40^\circ$, in good agreement with the extrapolated value.

Therefore, the ionization gradient expected for shock-excited emission lines as the general plane of the collisions becomes more and more oblique to our line of sight seems to be a plausible explanation for the steep slope of the correlation observed be-

tween the $L_{[\text{O II}]} / L_{[\text{O III}]}$ and $Lc_{[\text{O II}]} / Lc_{[\text{O III}]}$ luminosity ratios of weak-lined radio-loud AGN. In this respect, note that the fact that we observe a strong correlation in the case of weak-lined AGN although only ten data points are included suggests that the general underlying correlation is in fact very tight and so the $L_{[\text{O II}]} / L_{[\text{O III}]}$ ratio is expected to scale directly with viewing angle rather than the observed correlation being introduced by a third (unknown) physical parameter. However, 15/25 weak-lined sources have been excluded from this analysis since only upper limits were available for both their $[\text{O II}]$ and $[\text{O III}]$ emission lines. Therefore, the results obtained in this section need to be verified using a larger sample of weak-lined AGN with detected emission lines. Since the emission lines of these sources are generally extremely weak such follow-up studies would require spectra with a relatively high resolution and S/N.

4.5 Discussion

4.5.1 The Bimodality of the $[\text{O III}]$ Emission Line

The studies presented in this Chapter have shown that the $[\text{O III}]$ emission line distribution of radio-loud AGN is bimodal and that this bimodality might suggest the existence of two classes of radio-loud AGN with different dominant excitation mechanism for their narrow emission lines: photoionization and ionization by (jet-induced) shock-wave heating. A bimodal distribution has not been reported so far for any emission line of radio-loud AGN, and, therefore, I want to answer the following questions.

- *Is the significance of the $[\text{O III}]$ bimodality real?*

The bimodality of the $[\text{O III}]$ equivalent width distribution was highly significant in the case of sources with Ca H&K break values $C \geq 0.25$, whereas the significance was only marginal for objects with $0 < C < 0.25$ and a single Gaussian model was the better fit for objects with $C = 0$ (however, this latter result is most likely due to the missing weak-lined sources with no available redshift). Nevertheless, in strong support of the interpretation that the observed $[\text{O III}]$ bimodality has physical reality is the fact that simulations of relativistic beaming give values in good agreement with the observed decrease of the mean of the two modes with Ca H&K break. In fact, assuming no bimodality for objects with $C \geq 0.25$ results in a best-fit single Gaussian model with a mean of $\sim 10 \text{ \AA}$, which is *smaller* than the mean of $\sim 20 \text{ \AA}$ that results for the best-fit single Gaussian model for objects with $C = 0$. In other

words, only a bimodality for objects with $C \geq 0.25$ can account for the values observed in blazars within the beaming scenario.

On the other hand, the possibility remains that the [O III] bimodality is sample-dependent. The significance of the bimodality as quantified by the KMM algorithm depends on the overlap region of the two best-fit Gaussians, which again depends on the separation of the peaks and the dispersion of the two Gaussians. For this reason the bimodality for objects with $C \geq 0.25$ could become non-significant if additional sources were present at large [O III] equivalent width values. In fact, I get that, e.g., only 3 sources with [O III] equivalent width values of $\sim 20 \text{ \AA}$ would suffice to reduce the significance of the observed bimodality to $\sim 90\%$ (but again the mean of this unimodal distribution would not agree with the beaming scenario). This then brings us to the next question.

- *Which other surveys can test this result?*

In order to test the presence of a bimodality for the [O III] emission line intrinsic to the class of radio-loud AGN one needs a large sample of *both* radio galaxies and blazars. In addition, these have to have relatively low redshifts (the [O III] emission line is observed in an optical spectrum up to redshifts of $z \sim 1$) and should span a large range of [O III] equivalent width values. Currently existing radio surveys that contain a considerable number of radio galaxies and/or blazars with relatively low redshifts are the 3CR survey (Spinrad et al., 1985) and 1 Jy survey (Stickel et al., 1994). Measurements of the [O III] emission line luminosity are available for ~ 100 3CR radio galaxies and quasars (compiled on Chris Willott's homepage; <http://www-astro.physics.ox.ac.uk/cjw/>), however, large numbers of equivalent width values have not been published. Such measurements would then not only be hard to get from existing observations since these have been acquired by numerous different authors, but these stem from different epochs (as far back as the 1970s) and so the quality of the spectra is not uniform. In comparison, the findings presented in this study are based on a sample of ~ 90 sources with uniform measurements.

The 1 Jy survey catalogue contains ~ 500 sources, however, $\sim 40\%$ of these are also part of the 2 Jy survey, of which the low-redshift galaxies have been included in this study. Of the remaining sources not in common with the 2 Jy survey ~ 150 have a redshift $z \leq 1$. However, for the majority of these objects the spectral classification has been gathered from the literature and so measurements on the equivalent width of [O III] (which are in any case seldom

published) would also be time-consuming to obtain from existing data. In this respect, current on-going surveys are more promising, such as, e.g., RGB (ROSAT All Sky Survey (RASS)-Green Bank; Laurent-Muehleisen et al., 1998, 1999), REX (Radio-Emitting X-ray sources; Caccianiga et al., 1999, 2000), and the low-redshift selected CLASS (Cosmic Lens All Sky Survey) sample of blazars (Marchã et al., 2001; Caccianiga et al., 2002)

4.5.2 The Nature of Weak- and Strong-Lined Radio-Loud AGN

The studies presented in Section 4.4 yielded three main differences between weak- and strong-lined radio-loud AGN: 1. weak-lined radio-loud AGN have *considerably* less luminous narrow (a factor of ~ 300) and broad (a factor of ~ 70) emission line regions than strong-lined AGN; 2. weak-lined sources do not form simply an extension of strong-lined radio-loud AGN to both lower line luminosities *and* jet powers; and 3. the dominant excitation mechanisms for the narrow emission lines of weak- and strong-lined radio-loud AGN might be different, namely (jet-induced) shocks and photoionization respectively.

From all these three results it is possible to construct a consistent scenario: the central engine of weak-lined radio-loud AGN has only a very low ionizing power (possibly due to an accretion disk with low radiative efficiency or a complete lack of such a feature), however, fairly luminous jets can exist in these sources which then excite material in the ambient medium via shocks. Strong-lined radio-loud AGN, on the other hand, most likely have powerful accretion disks which produce luminous narrow and broad emission lines via photoionization. In their case excitation induced by jet-cloud collisions is expected to have a small net effect on their total emission line flux. In the following I want to corroborate this scenario.

In Section 4.4.2, I obtained mean broad line region luminosities for the weak- and strong-lined sources (viewed at similar angles) of $L_{\text{BLR}} = 10^{41.8}$ and $10^{43.7}$ erg s^{-1} respectively. Then using the relation $L_{\text{ion}} = f_{\text{cov}}^{-1} L_{\text{BLR}}$, where L_{ion} is the ionizing power of the central source and f_{cov} the covering factor, which I assume to be $\sim 10\%$ (e.g. D’Elia et al., 2003), I get for the weak- and strong-lined sources average ionizing luminosities of $L_{\text{ion}} = 10^{42.8}$ and $10^{44.7}$ erg s^{-1} respectively. The accretion rate of mass onto the central black hole, \dot{M} , is related to the ionizing power of the central source via $L_{\text{ion}} = \epsilon \dot{M} c^2$, where ϵ is the efficiency parameter and c the speed of light. Assuming that black holes in radio-loud AGN are rapidly rotating I choose $\epsilon = 0.3$ (Malkan, 1983). This gives average accretion rates for weak- and strong-lined AGN of $\dot{M} \sim 4 \times 10^{-4}$ and $\sim 3 \times 10^{-2} M_{\odot}/\text{yr}$ respectively.

However, the resulting values are fairly low since I have used for these calcu-

lations only the strong-lined sources spanning viewing angles similar to those of weak-lined AGN, i.e. viewed at larger angles. Therefore, their typical BLR luminosity is clearly underestimated and the true value is expected to be the one of sources viewed at the smallest angles. Using the relation between their BLR luminosity and continuum luminosity ratio $L_{c[\text{O II}]} / L_{c[\text{O III}]}$ (Fig. 4.7), I then derive for a value of $L_{c[\text{O II}]} / L_{c[\text{O III}]} = 5$, which corresponds roughly to a viewing angle of $\sim 10^\circ$, a BLR luminosity of $L_{\text{BLR}} = 10^{45.9} \text{ erg s}^{-1}$. Therefore, the true average accretion rate for this object class is expected to be rather $\sim 5 M_\odot/\text{yr}$. D’Elia et al. (2003) obtained for a large (136 sources) sample of DXRBS FSRQ an average value of $0.4 M_\odot/\text{yr}$. A similar value can be derived if I consider instead $L_{c[\text{O II}]} / L_{c[\text{O III}]} = 2$, which corresponds roughly to a viewing angle of $\sim 15^\circ$. The accretion rate of weak-lined AGN would increase under similar considerations to a value of $6 \times 10^{-2} M_\odot/\text{yr}$. This value, however, represents only an upper limit, since for the majority (9/12) of weak-lined AGN in fact no broad emission lines have been detected.

Assuming an average central black hole mass of $M_{\text{BH}} \sim 5 \times 10^8 M_\odot$ (following the results of D’Elia et al., 2003) for all radio-loud AGN, the Eddington accretion rate is $\dot{M}_{\text{Edd}} = 10 L_{\text{Edd}} / c^2 = 11 M_\odot/\text{yr}$, for a canonical efficiency of 10%. Then, in this case the accretion in strong-lined radio-loud AGN proceeds at $\sim 45\%$ of the Eddington rate, whereas this value is about half a per cent for weak-lined AGN. Narayan and Yi (1995) showed that advection-dominated solutions for the accretion flow occur for accretion rates below $\dot{M}_{\text{crit}} \approx \alpha^2 \dot{M}_{\text{Edd}}$, where α is the standard Shakura-Sunyaev viscosity parameter. If $\alpha = 0.1$, then advection-dominated accretion flows (ADAFs) occur at accretion rates below one per cent of the Eddington rate (e.g. Fabian and Rees, 1995). Therefore, it is likely that weak-lined AGN have advection-dominated accretion disks at their centers. ADAFs have very low radiative efficiencies (e.g. Rees et al., 1982; Narayan and Yi, 1995; Abramowicz et al., 1995), and have in fact already been invoked to explain the nuclear properties of some low-luminosity AGN, such as, e.g., M87 (Reynolds et al., 1996b; Di Matteo et al., 2002). Alternatively, central black hole masses of $M_{\text{BH}} \lesssim 2.5 \times 10^8 M_\odot$ would be required to render the accretion rate of weak-lined sources above 1% the Eddington rate. These values lie at the lower end of the black hole mass range of $10^8 - 10^9 M_\odot$ found recently by Barth et al. (2002) applying the correlation between stellar velocity dispersion and black hole mass defined for nearby galaxies to 11 BL Lac objects. On the other hand, most likely a standard stationary, geometrically thin accretion disk (e.g. Shakura and Sunyaev, 1973), usually invoked to explain the properties of powerful AGN, lies at the centers of strong-lined radio-loud AGN.

The discontinuity between weak- and strong-lined radio-loud AGN observed in

all emission line - jet power planes investigated in Section 4.4.3 emphasizes the presence of a true physical difference between these two groups, and suggests that this is related to their emission line production mechanism, and so accretion process, rather than to a property of their central engine which controls their jet power. For example, taking the mean NLR luminosity of weak-lined sources and the correlation between NLR luminosity and extended radio power observed for the strong-lined sources (Fig. 4.8, left panel) I get that weak-lined radio-loud AGN have on average more than three orders of magnitude (!) higher radio jet powers than expected if they were simply the low-luminosity counterparts of the strong-lined population. Moreover, Fig. 4.8, left panel, shows that the range in radio jet powers spanned by the weak- and strong-lined AGN is similar.

Therefore, it appears that the radiative power of their accretion disks which controls the power emitted by their emission lines is the most pronounced difference between these two classes. In this respect, assuming the presence of ADAFs in the weak-lined radio-loud AGN is not at odds with their observed jet powers. It has been argued that advection-dominated accretion flows possess a ‘vortex’ region near the rotation axis forming a natural channel which could readily be evacuated by an outflowing jet, e.g., via the Blandford-Znajek mechanism (e.g. Fabian and Rees, 1995) .

Considering the strong-lined sources, my work gives results similar to previous studies. Rawlings and Saunders (1991) showed for a sample of objects from the 3CR survey that there is a close relationship between radio jet power (derived from the extended radio luminosity) and narrow line region luminosity ($L_{\text{jet}} \propto L_{\text{NLR}}^{0.9 \pm 0.2}$) that extended over roughly four orders of magnitude. Based on this they concluded that all radio-source central engines channelled at least as much power into their jets as was radiated by accretion. Willott et al. (1999) confirmed their observed correlation using sources from the 3CRR sample and also from the much fainter 7C survey, and showed that this relation was indeed intrinsic and not induced by a common redshift dependence. Both these studies included mainly high-power radio sources with strong emission lines. The sample of Rawlings & Saunders included only 7 FR I radio galaxies and only sources with detected emission lines (with one exception), whereas FR I radio galaxies were excluded a priori in the studies of Willott et al. Moreover, BL Lacs were not present in these samples.

My work confirms for the strong-lined radio-loud AGN the result of Willott et al. that the relation between narrow line region luminosity and radio power for these sources is intrinsic rather than induced by a common redshift dependence. Furthermore, the resulting slope of 0.58 ± 0.08 is similar to the value of 0.72 ± 0.07

for their sample of quasars and weak quasars, but significantly flatter than the slope of 0.85 ± 0.04 for all their FR II sources. Willott et al. note that their marginal difference between the two slopes might be at least partly an artifact of the way in which quasars and radio galaxies are discriminated and discuss this further in Willott et al. (2000).

Rawlings and Saunders (1991) noted that a class of objects expected to not obey the observed correlation between NLR luminosity and radio jet power are the radio-quiet AGN. These have high NLR luminosities but negligible large-scale radio emission and are so expected to form a discontinuity in the emission line – jet power plane. In this respect, my studies show for the first time that a second discontinuity is formed in this plane by the weak-lined radio-loud AGN. This then emphasizes what has already been noted by Rawlings & Saunders, namely that the formation of radio jets requires specific physical attributes *independent* of the accretion rate.

This work included sources from the 2 Jy survey and I have used for these the X-ray data of Siebert et al. (1996). These authors find for 18 quasars, 30 FR II radio galaxies and 19 FR I radio galaxies from the 2 Jy survey that once the common redshift dependence is excluded a significant correlation between the [O III] line luminosity and X-ray power is only present for quasars but not for radio galaxies. For the observed correlation they get a slope of 0.92 ± 0.20 . Their result is similar to the analysis for strong-lined radio-loud AGN with Ca H&K break values $C = 0$ and $C > 0$. I find a significant correlation only for the first. Furthermore, the slope of the correlation is 0.86 ± 0.14 (assuming the NLR luminosity as independent variable in consistency with these authors), similar to their value. Of the objects with $C = 0$, only 33% (13/40) are in common with their sample of quasars, whereas 17 of their FR II radio galaxies and one quasar are among the 40 strong-lined sources with $C > 0$. Moreover, the slopes for the two correlations between NLR luminosity and radio and X-ray jet powers obtained from my studies are similar, implying that the narrow line region luminosity of strong-lined radio-loud AGN scales with jet power per se.

Celotti et al. (1997) investigated the relation between the BLR luminosity and jet kinetic power (derived from Very Large Baseline Interferometry (VLBI) radio data and X-ray luminosities) for a heterogenous sample of 64 quasars and 12 BL Lacs. They found only a weak correlation between these two quantities for quasars, but a highly significant correlation for their BL Lacs. However, the distributions of the ratios between the kinetic and BLR luminosities for different quasar subclasses had similar means of $L_{\text{KIN}}/L_{\text{BLR}} \approx 10$. Adopting a typical BLR covering factor of ~ 0.1 this then implied that the jet kinetic power of quasars was of the same order as their

ionizing radiation, in agreement with the results of Rawlings and Saunders (1991) for the NLR luminosity. The $L_{\text{KIN}}/L_{\text{BLR}}$ ratio values for BL Lacs were significantly higher than those of quasars.

Using two homogeneous samples of radio sources my studies confirm that the BLR luminosity of strong-lined AGN (once orientation effects are accounted for) scales with their radio and X-ray jet powers in a similar way as their NLR luminosity. This strengthens the conclusion of Celotti et al. that the accretion process and jet power supply are closely linked in these sources. A similar result to the one of Celotti et al. is also reached by the recent studies of D’Elia et al. (2003) who have investigated for the large majority (136 sources) of FSRQ from the DXRBS the relation between integrated accretion disk and jet power. If a relation between accretion process and jet power supply exists also in weak-lined AGN cannot be determined from the current data. The majority of these sources have only upper limits on their BLR luminosity, and so high quality spectroscopy which is expected to yield a larger number of detections is required in this respect.

The fact that weak-lined radio-loud AGN appear to have accretion disks with low radiative luminosities, which, however, can support powerful radio jets, possibly favors (jet-induced) shocks as the dominant excitation mechanism for their narrow emission lines. Nevertheless, in this respect spectra of high resolution and high S/N are needed to put more stringent constraints on their emission line luminosities and ratios. Also, if this scenario was true, we would expect the narrow emission line regions of weak-lined AGN to be relatively well aligned with their radio jet axis. Such optical – radio alignments have in fact been observed to occur to some extent in all radio galaxies, independently of redshift (e.g. McCarthy et al., 1987; Baum et al., 1992; Lacy et al., 1999; Best et al., 2000)

4.5.3 A New Classification Scheme for Blazars

This thesis has shown that the [O III] emission line distribution of radio-loud AGN is bimodal, possibly indicating the existence of two physically distinct classes: weak-lined radio-loud AGN with accretion disks of low radiative power (possibly ADAFs) allowing (jet-induced) shocks to be the main excitation mechanism for their narrow emission lines, and strong-lined radio-loud AGN with powerful accretion disks, whose strong narrow and broad emission lines are produced mainly via photoionization.

However, I do not want to propose a new classification scheme for blazars (and radio galaxies) in terms of nomenclature (the terminology zoo for AGN needs to be *decreased* and not the opposite), but rather want to encourage the use of the [O III] – [O II] equivalent plot in future studies of radio-loud AGN. This can help

us to disentangle orientation effects from intrinsic properties, which, as I believe, is the only correct approach to find answers to fundamental questions such as ‘What triggers the formation of jets in AGN?’ and ‘What is the true relation between accretion processes and jet properties?’

But, as I have already pointed out in the first Chapter, a discrepancy is inherent in our present classification scheme for radio-loud AGN. Blazars are separated into their subclasses based on emission line strengths, whereas we classify radio galaxies based on their radio morphology. And this discrepancy can only be reconciled if we adopt a uniform classification scheme for both. Nevertheless, such a classification scheme might not be necessary if only we have a method to discern orientation effects from intrinsic properties, and so can include without hesitation blazars and radio galaxies in any of our studies. The radio core dominance parameter could be used at radio frequencies, and this thesis has presented an invaluable tool for studies involving their emission line properties: optical viewing angle indicators, namely the Ca H&K break value and the $[\text{O II}] - [\text{O III}]$ equivalent width plane.

Chapter 5

Conclusions and Prospects

This thesis has made an effort to put the classification of blazars on firm physical grounds, and, in this respect, it represents a physical revision of the current classification scheme proposed by Marchã et al. (1996).

The approach chosen in this thesis was to first understand the physical meaning of the dilution of the Ca H&K break in radio-loud AGN, since this feature is currently used to separate radio galaxies and blazars (Chapter 3), and then to investigate if a bimodal distribution is present for the emission lines of radio-loud AGN, since their emission line strength is currently the criterion used to distinguish between the two blazar subclasses, BL Lacs and flat-spectrum radio quasars (Chapter 4).

For the studies on the Ca H&K break value I used a sample of ~ 90 BL Lacs and low-luminosity radio galaxies selected from the DXRBS, the survey at the basis of this thesis, and also from other radio and X-ray surveys available in the literature. The main result of this work was that the Ca H&K break value of radio-loud AGN is a suitable statistical indicator of orientation. This was argued based on the strong anticorrelations found between this feature and optical (Section 3.1), radio and X-ray jet luminosity, as well as radio core dominance parameter (Section 3.2), the latter believed to be a suitable indicator of orientation. I excluded the possibility that the range in jet power observed with Ca H&K break value was due to intrinsic variations based on the lack of a similarly strong anticorrelation between Ca H&K break value and extended radio jet power (Section 3.2).

The finding that the Ca H&K break value is a suitable statistical orientation in-

indicator is most important, since it offers the possibility to determine average viewing angles for samples of radio-loud AGN from such a simple (and common) observation as their optical spectra. The only other orientation indicator known so far is the radio core dominance parameter and its measurement requires dedicated radio observations. Therefore, my finding will be of considerable advantage for future studies of unified schemes.

Assuming the Ca H&K break value as a suitable orientation indicator, I constrained the typical Lorentz factor of BL Lacs and low-luminosity radio galaxies to values of $\Gamma \sim 2 - 4$ for both the radio and X-ray jet emission (Section 3.3). Additionally, I derived average viewing angles for the two BL Lac subclasses, low- and high-energy peaked BL Lacs, which turned out to be similar to each other and to the entire population of BL Lacs (Section 3.4). This result is in support of the scenario advocated by Padovani and Giommi (1995), namely that the main difference between the two BL Lac subclasses is the intrinsic shape of their spectral energy distributions, and undermines competing scenarios which attribute their differences mainly to orientation effects (e.g. Maraschi et al., 1986).

The main result of these studies relevant for the classification of blazars was that the transition in Ca H&K break value between blazars and radio galaxies, i.e. between sources viewed at smaller and larger viewing angles respectively, is continuous. However, using the critical angle which has been defined in the literature as the angle for which the radio core dominance parameter is equal to one (Urry and Padovani, 1995), I inferred a Ca H&K break value of $C \sim 0.35$ to be suitable to separate core- and lobe-dominated radio-loud AGN. This value is similar to that of $C = 0.4$ proposed Marchã et al. to separate blazars and radio galaxies, however, it has a more physical meaning now. From my studies it also directly follows that BL Lacs with intermediate Ca H&K break values (termed by Marchã et al. ‘BL Lac candidates’) are the long-sought population of BL Lacs with viewing angles intermediate between those of ‘classical’ BL Lacs and FR I radio galaxies. Therefore, a continuous transition in orientation similar to the one observed for powerful radio sources, namely FR II radio galaxies – steep-spectrum radio quasars – flat spectrum radio quasars (in order of decreasing viewing angle), exists also for the low-luminosity class.

I investigated the current separation of blazars into BL Lacs and FSRQ using a sample of blazars from the DXRBS (~ 130 sources). DXRBS is most suitable for this purpose since it offers a large (~ 350 sources) and homogenous sample of both blazar types, and its optical identification is nearly ($\sim 90\%$) complete (see Chapter 2). In the course of my PhD studies I significantly contributed to the spectroscopic

identification of this survey. I participated in three of the observing runs allocated to this project and reduced the large majority of the spectroscopic data.

My studies using blazars from DXRBS first showed that if we separate blazars into BL Lacs and FSRQ based on their strongest *observed* emission lines using the Ca H&K break – equivalent width plane and the diagonal line proposed by Marchã et al., $\sim 80\%$ of the high-redshift ($z \geq 0.4$) blazars have to be classified as FSRQ if they have emission lines as weak as $\sim 10 \text{ \AA}$, and $\sim 90\%$ of these sources have to be classified as such if they have emission lines at all (Section 4.3.1). Therefore, our current blazar classification scheme can account at least in part for the scarcity of high-redshift BL Lacs in present samples (see, e.g., Fig. 2.3).

Assuming the Ca H&K break value to be a suitable statistical orientation indicator, I argued that the Ca H&K break – equivalent width plane has to be applied to narrow emission lines only if it should be used to separate also blazars and radio galaxies. Only these emission lines are believed to be radiated (quasi-)isotropically and are common to both. Furthermore, I argued that a separation of blazars would be physically justified only if there existed a bimodality for any of the (narrow) emission lines inherent to the entire class of radio-loud AGN. Then, in order to search for such a bimodality I additionally included in my studies radio galaxies from DXRBS, and, since this survey has a radio spectral index cut of $\alpha_r \leq 0.7$ and therefore selects against most classical double-lobed radio galaxies, also a sample of ~ 50 radio galaxies and quasars from the 2 Jy survey.

My studies considered the strongest narrow emission lines typically seen in spectra of radio-loud AGN, namely [O II] $\lambda 3727$ and [O III] $\lambda 5007$, and yielded a bimodal distribution for the [O III] emission line only (Section 4.3.2). This is the first time that a bimodality is reported for any of the emission lines of radio-loud AGN. In fact, Scarpa and Falomo (1997) argued that the transition in emission line strength between blazar subclasses is continuous. However, their studies investigated the broad emission line Mg II $\lambda 2798$, which is believed to be radiated anisotropically and so is expected to be strongly affected by orientation effects. Moreover, these authors used a heterogeneous sample of (~ 70) blazars. In comparison, I used ~ 100 sources selected from two homogeneous, radio-flux limited samples of blazars and radio galaxies.

In the remainder of the thesis I investigated if the bimodality observed for the [O III] emission line possibly indicates the presence of two physically distinct classes of radio-loud AGN, thus allowing me to refine the present classification of blazars. For this purpose I first separated the entire sample of blazars and radio galaxies under study into sources with *intrinsically* weak and strong [O III] emission lines

(referred to as weak- [25 sources] and strong-lined radio-loud AGN [80 sources] respectively). I argued that the Ca H&K break – equivalent width plane did not offer the dynamic range necessary to distinguish at Ca H&K break values of $C = 0$ *intrinsically* weak-lined radio-loud AGN from strongly beamed strong-lined radio-loud AGN whose emission lines only *appeared* weak, and proposed rather the use of the [O III] – [O II] equivalent width plane to discern orientation effects from intrinsic properties in studies involving emission lines of radio-loud AGN (Section 4.4.1).

I then compared for weak- and strong-lined radio-loud AGN their narrow and broad emission line region luminosities (Section 4.4.2), their distribution in the emission line luminosity – jet power planes (Section 4.4.3), and their state of ionization (Section 4.4.4). This yielded three main results: 1. weak-lined radio-loud AGN have *considerably* less luminous narrow (a factor of ~ 300) and broad (a factor of ~ 70) emission line regions than strong-lined radio-loud AGN; 2. weak-lined sources do not form simply an extension of strong-lined radio-loud AGN to both lower line luminosities *and* jet powers; and 3. the dominant excitation mechanisms for the narrow emission lines of weak- and strong-lined radio-loud AGN might be different, namely (jet-induced) shocks and photoionization respectively.

I believe that from all these three results a consistent scenario emerges: the central engine of weak-lined radio-loud AGN has only a very low ionizing power (possibly due to the presence of an advection-dominated accretion flow [ADAF]), however, fairly luminous jets can exist in these sources which then excite material in the ambient medium via shocks. Strong-lined radio-loud AGN, on the other hand, most likely have powerful accretion disks which produce luminous narrow and broad emission lines via photoionization. In their case excitation induced by jet-cloud collisions is expected to have a small net effect on their total emission line flux.

In order to verify this scenario in future studies we need in particular high-quality spectroscopy of weak-lined radio-loud AGN, i.e. spectra with a high resolution and S/N, in order to detect in these sources even the faintest emission lines. This will allow us to reduce the number of upper limits in statistical studies (60% and 75% of the weak-lined AGN included in this study had only upper limits on their NLR and BLR luminosity respectively) and to put more stringent constraints on their emission line ratios and luminosities. In addition, optical and radio images with high spatial resolution would be necessary to determine if their narrow emission lines are indeed excited mainly via (jet-induced) shocks.

Bibliography

- Abramowicz, M. A., Chen, X., Kato, S., Lasota, J.-P., and Regev, O. (1995), “Thermal Equilibria of Accretion Disks,” *ApJ*, 438, L37.
- Akritas, M. G. and Siebert, J. (1996), “A Test for Partial Correlation with Censored Astronomical Data,” *MNRAS*, 278, 919.
- Albrecht, M. A., Brighton, A., Herlin, T., Biereichel, P., and Durand, D. (1997), <http://archive.eso.org/skycat>.
- Allen, M. G., Dopita, M. A., Tsvetanov, Z. I., and Sutherland, R. S. (1999), “Physical Conditions in the Seyfert Galaxy NGC 2992,” *ApJ*, 511, 686.
- Angel, J. R. P. and Stockman, H. S. (1980), “Optical and Infrared Polarization of Active Extragalactic Objects,” *ARA&A*, 18, 321.
- Antonucci, R. and Miller, J. S. (1985), “Spectropolarimetry and the Nature of NGC 1068,” *ApJ*, 297, 621.
- Ashman, K. M., Bird, C. M., and Zepf, S. E. (1994), “Detecting Bimodality in Astronomical Datasets,” *AJ*, 108, 2348.
- Augusto, P., Wilkinson, P. N., and Browne, I. W. A. (1998), “Flat-Spectrum Radio Sources with kpc-Scale Structure,” *MNRAS*, 299, 1159.
- Avni, Y. and Bahcall, J. N. (1980), “On the Simultaneous Analysis of Several Complete Samples: the V/V_{\max} and V_e/V_a Variables, with Applications to Quasars,” *ApJ*, 238, 800.
- Bade, N., Beckmann, V., Douglas, N. G., Barthel, P. D., Engels, D., Cordis, L., Nass, P., and Voges, W. (1998), “On the Evolutionary Behaviour of BL Lac Objects,” *A&A*, 334, 459.
- Baker, J. C. (1997), “Origin of the Viewing-Angle Dependence of the Optical Continuum Emission in Quasars,” *MNRAS*, 286, 23.

- Baker, J. C. and Hunstead, R. W. (1995), "Revealing the Effects of Orientation in Composite Quasar Spectra," *ApJ*, 452, L95.
- Baker, J. C., Hunstead, R. W., and Brinkmann, W. (1995), "Radio and X-Ray Beaming in Steep-Spectrum Quasars," *MNRAS*, 277, 553.
- Baldwin, J. A., Phillips, M. M., and Terlevich, R. (1981), "Classification Parameters for the Emission-Line Spectra of Extragalactic Objects," *PASP*, 93, 5.
- Barth, A. J., Ho, L. C., and Sargent, W. L. W. (2002), "The Black Hole Masses and Host Galaxies of BL Lac Objects," accepted by *ApJ*, astro-ph/0209562.
- Barthel, P. D. (1989), "Is Every Quasar Beamed?" *ApJ*, 336, 606.
- Baum, S. A., Heckman, T. M., and Van Breugel, W. (1992), "Spectroscopy of Emission-Line Nebulae in Powerful Radio Galaxies. Interpretation," *ApJ*, 389, 208.
- Baum, S. A., Zirbel, E. L., and O'Dea, C. P. (1995), "Toward Understanding the Fanaroff-Riley Dichotomy in Radio Source Morphology and Power," *ApJ*, 451, 88.
- Bennert, N., Falcke, H., Schulz, H., Wilson, A. S., and Wills, B. J. (2002), "Size and Structure of the Narrow-Line Region of Quasars," *ApJ*, 574, L105.
- Best, P. N., Röttgering, H. J. A., and Longair, M. S. (2000), "Ionization, Shocks and Evolution of the Emission-Line Gas of Distant 3CR Radio Galaxies," *MNRAS*, 311, 1.
- Bicknell, G. V. (1995), "Relativistic Jets and the Fanaroff-Riley Classification of Radio Galaxies," *ApJS*, 101, 29.
- Blandford, R. D. and Rees, M. J. (1978), "Some Comments on Radiation Mechanisms in Lacertids," in *Pittsburgh Conference on BL Lac Objects*, ed. A. M. Wolfe, p. 328, University of Pittsburgh, Pittsburgh.
- Blandford, R. D. and Znajek, R. L. (1977), "Electromagnetic Extraction of Energy from Kerr Black Holes," *MNRAS*, 179, 433.
- Bondi, M., Marchã, M. J. M., Dallacasa, D., and Stanghellini, C. (2001), "Intermediate BL Lac Objects," *MNRAS*, 325, 1109.
- Brinkmann, W., Siebert, J., and Boller, T. (1994), "The X-Ray AGN Content of the Molonglo 408 MHz Survey: Bulk Properties of Previously Optically Identified Sources," *A&A*, 281, 355.

-
- Brinkmann, W., Siebert, J., Reich, W., Fürst, E., Reich, P., Voges, W., Trümper, J., and Wielebinski, R. (1995), “The *ROSAT* AGN Content of the 87GB 5 GHz Survey: Bulk Properties of Previously Optically Identified Sources,” *A&AS*, 109, 147.
- Brinkmann, W., Siebert, J., Feigelson, E. D., Kollgaard, R. I., Laurent-Muehleisen, S. A., Reich, W., Fürst, E., Reich, P., et al. (1997), “Radio-Loud Active Galaxies in the Northern *ROSAT* All-Sky Survey. II. Multi-Frequency Properties of Unidentified Sources,” *A&A*, 323, 739.
- Browne, I. W. A. (1989), “BL Lac Objects, OVV/HPQs and Unified Models,” in *BL Lac Objects*, eds. L. Maraschi, T. Maccacaro, and M.-H. Ulrich, p. 401, Springer-Verlag, Heidelberg.
- Bruzual, A. G. (1983), “Spectral Evolution of Galaxies. I. Early-Type Systems,” *ApJ*, 273, 105.
- Caccianiga, A., Maccacaro, T., Wolter, A., Della Ceca, R., and Gioia, I. M. (1999), “The REX Survey: A Search for Radio-Emitting X-Ray Sources,” *ApJ*, 513, 51.
- Caccianiga, A., Maccacaro, T., Wolter, A., Della Ceca, R., and Gioia, I. M. (2000), “Emission Line AGNs from the REX Survey. Results from Optical Spectroscopy,” *A&AS*, 144, 247.
- Caccianiga, A., Marchã, M. J., Antón, S., Mack, K.-H., and Neeser, M. J. (2002), “The CLASS Blazar Survey. II. Optical Properties,” *MNRAS*, 329, 877.
- Capetti, A. and Celotti, A. (1999), “Testing the FR I/BL Lac Unifying Model with *HST* Observations,” *MNRAS*, 304, 434.
- Cassaro, P., Stanghellini, C., Bondi, M., Dallacasa, D., Della Ceca, R., and Zappalà, R. A. (1999), “Extended Radio Emission in BL Lac Objects. I. The Images,” *A&AS*, 139, 601.
- Celotti, A. and Fabian, A. C. (1993), “The Kinetic Power and Luminosity of Parsecscale Radio Jets - An Argument for Heavy Jets,” *MNRAS*, 264, 228.
- Celotti, A., Maraschi, L., Ghisellini, G., Caccianiga, A., and Maccacaro, T. (1993), “Unified Model for X-Ray- and Radio-Selected BL Lacertae Objects,” *ApJ*, 416, 118.
- Celotti, A., Padovani, P., and Ghisellini, G. (1997), “Jets and Accretion Processes in Active Galactic Nuclei: Further Clues,” *MNRAS*, 286, 415.

- Chiaberge, M., Celotti, A., Capetti, A., and Ghisellini, G. (2000), “Does the Unification of BL Lac and FR I Radio Galaxies Require Jet Velocity Structures?” *A&A*, 358, 104.
- Cohen, M. H., Ogle, P. M., Tran, H. D., Goodrich, R. W., and Miller, J. S. (1999), “Polarimetry and Unification of Low-Redshift Radio Galaxies,” *AJ*, 118, 1963.
- Condon, J. J., Helou, G., Sanders, D. B., and Soifer, B. T. (1996), “A 1.425 GHz Atlas of the *IRAS* Bright Galaxy Sample, Part II,” *ApJS*, 103, 81.
- Condon, J. J., Cotton, W. D., Greisen, E. W., Yin, Q. F., Perley, R. A., Taylor, G. B., and Broderick, J. J. (1998), “The NRAO VLA Sky Survey,” *AJ*, 115, 1693.
- Corbett, E. A., Robinson, A., Axon, D. J., Hough, J. H., Jeffries, R. D., Thurston, M. R., and Young, S. (1996), “The Appearance of Broad $H\alpha$ in BL Lacertae,” *MNRAS*, 281, 737.
- De Young, D. S. (1993), “On the Relation between Fanaroff-Riley Types I and II Radio Galaxies,” *ApJ*, 405, L13.
- D’Elia, V., Padovani, P., and Landt, H. (2003), “The Disc-Jet Relation in Strong-lined Blazars,” *MNRAS*, 339, 1081.
- Dennett-Thorpe, J. and Marchã, M. J. (2000), “Flat Radio-Spectrum Galaxies and BL Lacs. I. Core Properties,” *A&A*, 361, 480.
- Dennett-Thorpe, J., Barthel, P. D., and van Bemmel, I. M. (2000), “On the Viewing Angle to Broad-Lined Radio Galaxies,” *A&A*, 364, 501.
- Di Matteo, T., Allen, S. W., Fabian, A. C., Wilson, A. S., and Young, A. J. (2002), “Accretion onto the Supermassive Black Hole in M87,” accepted by *ApJ*, astro-ph/0202238.
- Dopita, M. A. and Sutherland, R. S. (1995), “Spectral Signatures of Fast Shocks. II. Optical Diagnostic Diagrams,” *ApJ*, 455, 468.
- Dressler, A. and Shectman, S. A. (1987), “Systematics of the 4000 Angstrom Break in the Spectra of Galaxies,” *AJ*, 94, 899.
- Drinkwater, M. J., Barnes, D. G., and Ellison, S. L. (1995), “Using the Cosmos/UKST Southern Sky Object Catalogue,” *PASA*, 12, 248.

-
- Evans, I., Koratkar, A., Allen, M., Dopita, M., and Tsvetanov, Z. (1999), “The Excitation Mechanism of Emission-Line Regions in Seyfert Galaxies,” *ApJ*, 521, 531.
- Fabian, A. C. and Rees, M. J. (1995), “The Accretion Luminosity of a Massive Black Hole in an Elliptical Galaxy,” *MNRAS*, 277, L55.
- Falomo, R., Scarpa, R., and Bersanelli, M. (1994), “Optical Spectrophotometry of Blazars,” *ApJS*, 93, 125.
- Fanaroff, B. L. and Riley, J. M. (1974), “The Morphology of Extragalactic Radio Sources of High and Low Luminosity,” *MNRAS*, 167, 31.
- Feigelson, E. D. and Nelson, P. I. (1985), “Statistical Methods for Astronomical Data with Upper Limits. I. Univariate Distributions,” *ApJ*, 293, 192.
- Fernini, I., Burns, J. O., and Perley, R. A. (1997), “VLA Imaging of Fanaroff-Riley II 3CR Radio Galaxies. II. Eight New Images and Comparisons with 3CR Quasars,” *AJ*, 114, 2292.
- Filippenko, A. V. (1982), “The Importance of Atmospheric Differential Refraction in Spectrophotometry,” *PASP*, 94, 715.
- Francis, P. J., Hewett, P. C., Foltz, C. B., Chaffee, F. H., Weymann, R. J., and Morris, S. L. (1991), “A High Signal-to-Noise Ratio Composite Quasar Spectrum,” *ApJ*, 373, 465.
- Gaskell, C. M., Shields, G. A., and Wampler, E. J. (1981), “Abundances of Refractory Elements in Quasars,” *ApJ*, 249, 443.
- Ghisellini, G. and Celotti, A. (2001), “The Dividing Line between FR I and FR II Radio Galaxies,” *A&A*, 379, L1.
- Ghisellini, G. and Maraschi, L. (1989), “Bulk Acceleration in Relativistic Jets and the Spectral Properties of Blazars,” *ApJ*, 340, 181.
- Gioia, I. M., Henry, J. P., Maccacaro, T., Morris, S. L., Stocke, J. T., and Wolter, A. (1990), “The Extended Medium Sensitivity Survey Distant Cluster Sample. X-ray Cosmological Evolution,” *ApJ*, 356, 35.
- Giommi, P., Ansari, S. G., and Micol, A. (1995), “Radio to X-Ray Energy Distribution of BL Lacertae Objects,” *A&AS*, 109, 267.

- Giommi, P., Menna, M. T., and Padovani, P. (1999), “The Sedentary Multifrequency Survey. I. Statistical Identification and Cosmological Properties of High-Energy Peaked BL Lacs,” *MNRAS*, 310, 465.
- Giovannini, G., Feretti, L., Gregorini, L., and Parma, P. (1988), “Radio Nuclei in Elliptical Galaxies,” *A&A*, 199, 73.
- Giovannini, G., Cotton, W. D., Feretti, L., Lara, L., and Venturi, T. (2001), “VLBI Observations of a Complete Sample of Radio Galaxies: 10 Years Later,” *ApJ*, 552, 508.
- Gopal-Krishna and Wiita, P. J. (1988), “Hot Gaseous Coronae of Early-Type Galaxies and their Radio Luminosity Function,” *Nature*, 333, 49.
- Gopal-Krishna and Wiita, P. J. (2001), “The Fanaroff-Riley Transition and the Optical Luminosity of the Host Elliptical Galaxy,” *A&A*, 373, 100.
- Gregory, P. C., Scott, W. K., Douglas, K., and Condon, J. J. (1996), “The GB6 Catalog of Radio Sources,” *ApJS*, 103, 427.
- Griffith, M. R. and Wright, A. E. (1993), “The Parkes-MIT-NRAO (PMN) Surveys. I. The 4850 MHz Surveys and Data Reduction,” *AJ*, 105, 1666.
- Hardcastle, M. J. and Worrall, D. M. (1999), “*ROSAT* X-Ray Observations of 3CRR Radio Sources,” *MNRAS*, 309, 969.
- Hardcastle, M. J., Alexander, P., Pooley, G. G., and Riley, J. M. (1998), “FR II Radio Galaxies with $z < 0.3$. I. Properties of Jets, Cores and Hotspots,” *MNRAS*, 296, 445.
- Heidt, J. and Wagner, S. J. (1996), “Statistics of Optical Intraday Variability in a Complete Sample of Radio-Selected BL Lacertae Objects,” *A&A*, 305, 42.
- Heidt, J. and Wagner, S. J. (1998), “Intraday Variability in X-Ray Selected BL Lacertae Objects,” *A&A*, 329, 853.
- Helfand, D. J., Schnee, S., Becker, R. H., White, R. L., and McMahon, R. G. (1999), “The FIRST Unbiased Survey for Radio Stars,” *AJ*, 117, 1568.
- Hes, R., Barthel, P. D., and Fosbury, R. A. E. (1996), “Emission Line Imaging of 3CR Quasars and Radio Galaxies,” *A&A*, 313, 423.
- Hill, G. J. and Lilly, S. J. (1991), “A Change in the Cluster Environments of Radio Galaxies with Cosmic Epoch,” *ApJ*, 367, 1.

-
- Impey, C. D. and Tapia, S. (1990), “The Optical Polarization Properties of Quasars,” *ApJ*, 354, 124.
- Irwin, M., Maddox, S., and McMahon, R. G. (1994), “The APM Sky Catalogues,” *Spectrum*, 2, 14.
- Isobe, T., Feigelson, E. D., and Nelson, P. I. (1986), “Statistical Methods for Astronomical Data with Upper Limits II. Correlation and Regression,” *ApJ*, 306, 490.
- Ivezić, Z., Menou, K., Knapp, G. R., Strauss, M. A., Lupton, R. H., Vanden Berk, D. E., Richards, G. T., Tremonti, C., et al. (2002), “Optical and Radio Properties of Extragalactic Sources Observed by the FIRST Survey and the Sloan Digital Sky Survey,” *AJ*, 124, 2364.
- Jannuzi, B. T., Smith, P. S., and Elston, R. (1994), “The Optical Polarization Properties of X-Ray-Selected BL Lacertae Objects,” *ApJ*, 428, 130.
- Jauncey, D. L., Batty, M. J., Gulkis, S., and Savage, A. (1982), “2.3 GHz Accurate Positions and Optical Identifications for Selected Parkes Radio Sources,” *AJ*, 87, 763.
- Kaiser, C. R. and Alexander, P. (1997), “A Self-Similar Model for Extragalactic Radio Sources,” *MNRAS*, 286, 215.
- Kollgaard, R. I., Wardle, J. F. C., Roberts, D. H., and Gabuzda, D. C. (1992), “Radio Constraints on the Nature of BL Lacertae Objects and Their Parent Population,” *AJ*, 104, 1687.
- Kühr, H. and Schmidt, G. D. (1990), “Complete Samples of Radio-Selected BL Lac Objects,” *AJ*, 99, 1.
- Lacy, M., Ridgway, S. E., Wold, M., Lilje, P. B., and Rawlings, S. (1999), “Radio-Optical Alignments in a Low Radio Luminosity Sample,” *MNRAS*, 307, 420.
- Laing, R. A., Jenkins, C. R., Wall, J. V., and Unger, S. W. (1994), “Spectrophotometry of a Complete Sample of 3CR Radio Sources: Implications for Unified Models,” in *The First Stromlo Symposium: The Physics of Active Galaxies*, eds. G. V. Bicknell, M. A. Dopita, and P. J. Quinn, p. 201, A.S.P., San Francisco.
- Landt, H., Padovani, P., Perlman, E. S., Giommi, P., Bignall, H., and Tzioumis, A. (2001), “The Deep X-Ray Radio Blazar Survey (DXRBS). II. New Identifications,” *MNRAS*, 323, 757.

- Landt, H., Padovani, P., and Giommi, P. (2002), “The Classification of BL Lacertae Objects: The Ca H&K Break,” *MNRAS*, 336, 945.
- Laurent-Muehleisen, S. A., Kollgaard, R. I., Ryan, P. J., Feigelson, E. D., Brinkmann, W., and Siebert, J. (1997), “Radio-Loud Active Galaxies in the Northern *ROSAT* All-Sky Survey. I. Radio Identifications,” *A&AS*, 122, 235.
- Laurent-Muehleisen, S. A., Kollgaard, R. I., Ciardullo, R., Feigelson, E. D., Brinkmann, W., and Siebert, J. (1998), “Radio-Loud Active Galaxies in the Northern *ROSAT* All-Sky Survey. III. New Spectroscopic Identifications from the RASS-Green Bank BL Lacertae Survey,” *ApJS*, 118, 127.
- Laurent-Muehleisen, S. A., Kollgaard, R., Feigelson, E. D., Brinkmann, W., and Siebert, J. (1999), “The RGB Sample of Intermediate BL Lacertae Objects,” *ApJ*, 525, 127.
- Lind, K. R. and Blandford, R. D. (1985), “Semidynamical Models of Radio Jets. Relativistic Beaming and Source Counts,” *ApJ*, 295, 358.
- Loveday, J. (1996), “The APM Bright Galaxy Catalogue,” *MNRAS*, 278, 1025.
- Lumsden, S. L., Heisler, C. A., Bailey, J. A., Hough, J. H., and Young, S. (2001), “Spectropolarimetry of a Complete Infrared-Selected Sample of Seyfert 2 Galaxies,” *MNRAS*, 327, 459.
- Malkan, M. A. (1983), “The Ultraviolet Excess of Luminous Quasars. II. Evidence for Massive Accretion Disks,” *ApJ*, 268, 582.
- Malkan, M. A. and Sargent, W. L. W. (1982), “The Ultraviolet Excess of Seyfert 1 Galaxies and Quasars,” *ApJ*, 254, 22.
- Maoz, D., Netzer, H., Peterson, B. M., Bechtold, J., Bertram, R., Bochkarev, N. G., Carone, T. E., Dietrich, M., et al. (1993), “Variations of the Ultraviolet Fe II and Balmer Continuum Emission in the Seyfert Galaxy NGC 5548,” *ApJ*, 404, 576.
- Maraschi, L., Ghisellini, G., Tanzi, E. G., and Treves, A. (1986), “Spectral Properties of Blazars. II. An X-Ray Observed Sample,” *ApJ*, 310, 325.
- Marchã, M. J., Caccianiga, A., Browne, I. W. A., and Jackson, N. (2001), “The CLASS Blazar Survey. I. Selection Criteria and Radio Properties,” *MNRAS*, 326, 1455.

-
- Marchã, M. J. M. and Browne, I. W. A. (1995), “The Recognition of BL Lac Objects: Effects on Redshift Distributions, Missing Objects and Cosmological Evolution,” *MNRAS*, 275, 951.
- Marchã, M. J. M., Browne, I. W. A., Impey, C. D., and Smith, P. S. (1996), “Optical Spectroscopy and Polarization of a New Sample of Optically Bright Flat Radio Spectrum Sources,” *MNRAS*, 281, 425.
- McCarthy, P. J., Van Breugel, W., Spinrad, H., and Djorgovski, S. (1987), “A Correlation between the Radio and Optical Morphologies of Distant 3CR Radio Galaxies,” *ApJ*, 321, L29.
- McLure, R. J. and Dunlop, J. S. (2001), “The Cluster Environments of Powerful Radio-Loud and Radio-Quiet Active Galactic Nuclei,” *MNRAS*, 321, 515.
- McLure, R. J., Kukula, M. J., Dunlop, J. S., Baum, S. A., O’Dea, C. P., and Hughes, D. H. (1999), “A Comparative *HST* Imaging Study of the Host Galaxies of Radio-Quiet Quasars, Radio-Loud Quasars and Radio Galaxies - I,” *MNRAS*, 308, 377.
- Meier, D. L. (1999), “A Magnetically Switched, Rotating Black Hole Model for the Production of Extragalactic Radio Jets and the Fanaroff and Riley Class Division,” *ApJ*, 522, 753.
- Morganti, R., Killeen, N. E. B., and Tadhunter, C. N. (1993), “The Radio Structures of Southern 2 JY Radio Sources,” *MNRAS*, 263, 1023.
- Morganti, R., Oosterloo, T. A., Reynolds, J. E., Tadhunter, C. N., and Migenes, V. (1997), “A Study of Cores in a Complete Sample of Radio Sources,” *MNRAS*, 284, 541.
- Morris, S. L., Stocke, J. T., Gioia, I. M., Schild, R. E., Wolter, A., Maccacaro, T., and Della Ceca, R. (1991), “The Luminosity Function and Cosmological Evolution of X-Ray-Selected BL Lacertae Objects,” *ApJ*, 380, 49.
- Murphy, D. W., Browne, I. W. A., and Perley, R. A. (1993), “VLA Observations of a Complete Sample of Core-Dominated Radio Sources,” *MNRAS*, 264, 298.
- Narayan, R. and Yi, I. (1995), “Advection-Dominated Accretion: Self-Similarity and Bipolar Outflows,” *ApJ*, 444, 231.
- Nass, P., Bade, N., Kollgaard, R. I., Laurent-Muehleisen, S. A., Reimers, D., and Voges, W. (1996), “BL Lacertae Objects in the *ROSAT* All-Sky Survey: New Objects and Comparison of Different Search Techniques,” *A&A*, 309, 419.

- O'Dea, C. P. (1998), "The Compact Steep-Spectrum and Gigahertz Peaked-Spectrum Radio Sources," *PASP*, 110, 493.
- Owen, F. N. and Ledlow, M. J. (1994), "The FR I/II Break and the Bivariate Luminosity Function in Abell Clusters of Galaxies," in *The First Stromlo Symposium: The Physics of Active Galaxies*, eds. G. V. Bicknell, M. A. Dopita, and P. J. Quinn, p. 319, A.S.P., San Francisco.
- Owen, F. N., Ledlow, M. J., and Keel, W. C. (1996), "Optical Spectroscopy of Radio Galaxies in Abell Clusters II. BL Lacs and FR I Unification," *AJ*, 111, 53.
- Padovani, P. (1997), "Gamma-ray Emitting AGN and Unified Schemes," in *Very High Energy Phenomena in the Universe*, eds. Y. Giraud-Héraud and J. Trâ Thanh Vân, p. 7.
- Padovani, P. (2001), "Deep Blazar Surveys," in *Blazar Demographics and Physics*, eds. P. Padovani and C. M. Urry, p. 163, A.S.P., San Francisco.
- Padovani, P. (2002), "Blazar Surveys," in *Blazars Astrophysics with BeppoSAX and Other Observatories*, eds. P. Giommi, E. Massaro, and G. Palumbo, in press.
- Padovani, P. and Giommi, P. (1995), "The Connection Between X-Ray- and Radio-Selected BL Lacertae Objects," *ApJ*, 444, 567.
- Padovani, P. and Giommi, P. (1996), "The *ROSAT* X-Ray Spectra of BL Lacertae Objects," *MNRAS*, 279, 526.
- Padovani, P. and Urry, C. M. (1990), "Fanaroff-Riley I Galaxies as the Parent Population of BL Lacertae Objects I. X-Ray Constraints," *ApJ*, 356, 75.
- Padovani, P. and Urry, C. M. (1991), "Fanaroff-Riley I Galaxies as the Parent Population of BL Lacertae Objects II. Optical Constraints," *ApJ*, 368, 373.
- Padovani, P. and Urry, C. M. (1992), "Luminosity Functions, Relativistic Beaming, and Unified Theories of High-Luminosity Radio Sources," *ApJ*, 387, 449.
- Padovani, P., Giommi, P., and Fiore, F. (1997), "A Multifrequency Database of Active Galactic Nuclei," *MmSAI*, 68, 147.
- Padovani, P., Perlman, E., Landt, H., Giommi, P., and Perri, M. (2002), "What Types of Jets Does Nature Make: A New Population of Radio Quasars," submitted to *ApJ*.

-
- Perley, R. A., Dreher, J. W., and Cowan, J. J. (1984), “The Jet and Filaments in Cygnus A,” *ApJ*, 285, L35.
- Perlman, E. S. and Stocke, J. T. (1993), “The Radio Structure Source of X-Ray-Selected BL Lacertae Objects,” *ApJ*, 406, 430.
- Perlman, E. S., Stocke, J. T., Schachter, J. F., Elvis, M., Ellingson, E., Urry, C. M., Potter, M., Impey, C. D., and Kolchinsky, P. (1996a), “The *EINSTEIN* Slew Survey Sample of BL Lacertae Objects,” *ApJS*, 104, 251.
- Perlman, E. S., Stocke, J. T., Wang, Q. D., and Morris, S. L. (1996b), “Soft X-Ray Observations of a Complete Sample of X-Ray-Selected BL Lacertae Objects,” *ApJ*, 456, 451.
- Perlman, E. S., Padovani, P., Giommi, P., Sambruna, R., Jones, L. R., Tzioumis, A., and Reynolds, J. (1998), “The Deep X-Ray Radio Blazar Survey. I. Methods and First Results,” *AJ*, 115, 1253.
- Perlman, E. S., Padovani, P., Landt, H., Stocke, J. T., Costamante, L., Rector, T., Giommi, P., and Schachter, J. F. (2001), “Surveys and the Blazar Parameter Space,” in *Blazar Demographics and Physics*, eds. P. Padovani and C. M. Urry, p. 200, A.S.P., San Francisco.
- Prestage, R. M. and Peacock, J. A. (1988), “The Cluster Environments of Powerful Radio Galaxies,” *MNRAS*, 230, 131.
- Rawlings, S. and Saunders, R. (1991), “Evidence for a Common Central-Engine Mechanism in All Extragalactic Radio Sources,” *Nature*, 349, 138.
- Rector, T. A. and Stocke, J. T. (2001), “The Properties of the Radio-Selected 1 Jy Sample of BL Lacertae Objects,” *AJ*, 122, 565.
- Rector, T. A., Stocke, J. T., and Perlman, E. S. (1999), “A Search for Low-Luminosity BL Lacertae Objects,” *ApJ*, 516, 145.
- Rector, T. A., Stocke, J. T., Perlman, E. S., Morris, S. L., and Gioia, I. M. (2000), “The Properties of the X-Ray-Selected EMSS Sample of BL Lacertae Objects,” *AJ*, 120, 1626.
- Rees, M. (1966), “Appearance of Relativistically Expanding Radio Sources,” *Nature*, 211, 468.
- Rees, M. J., Phinney, E. S., Begelman, M. C., and Blandford, R. D. (1982), “Ion-Supported Tori and the Origin of Radio Jets,” *Nature*, 295, 17.

- Reynolds, C. S., Fabian, A. C., Celotti, A., and Rees, M. J. (1996a), “The Matter Content of the Jet in M87: Evidence for an Electron-Positron Jet,” *MNRAS*, 283, 873.
- Reynolds, C. S., Di Matteo, T., Fabian, A. C., Hwang, U., and Canizares, C. R. (1996b), “The ‘Quiescent’ Black Hole in M87,” *MNRAS*, 283, L111.
- Rybicki, G. B. and Lightman, A. P. (1979), *Radiative Processes in Astrophysics*, John Wiley & Sons, New York.
- Sambruna, R. M., Maraschi, L., and Urry, C. M. (1996), “On the Spectral Energy Distributions of Blazars,” *ApJ*, 463, 444.
- Saunders, R., Baldwin, J. E., Rawlings, S., Warner, P. J., and Miller, L. (1989), “Spectrophotometry of FR II Radiogalaxies in an Unbiased, Low-Redshift Sample,” *MNRAS*, 238, 777.
- Scarpa, R. and Falomo, R. (1997), “Are High Polarization Quasars and BL Lacertae Objects Really Different? A Study of the Optical Spectral Properties,” *A&A*, 325, 109.
- Schmidt, M. (1963), “3C 273: A Star-Like Object with a Large Redshift,” *Nature*, 197, 1040.
- Schmidt, M. (1968), “Space Distribution and Luminosity Functions of Quasi-Stellar Radio Sources,” *ApJ*, 151, 393.
- Schmitt, H. R. and Kinney, A. L. (1996), “A Comparison between the Narrow-Line Regions of Seyfert 1 and Seyfert 2 Galaxies,” *ApJ*, 463, 498.
- Seyfert, C. K. (1943), “Nuclear Emission in Spiral Nebulae,” *ApJ*, 97, 28.
- Shakura, N. I. and Sunyaev, R. A. (1973), “Black Holes in Binary Systems. Observational Appearance,” *A&A*, 24, 337.
- Siebert, J., Brinkmann, W., Morganti, R., Tadhunter, C. N., Danziger, I. J., Fosbury, R. A. E., and di Serego Alighieri, S. (1996), “The Soft X-Ray Properties of a Complete Sample of Radio Sources,” *MNRAS*, 279, 1331.
- Siebert, J., Brinkmann, W., Drinkwater, M. J., Yuan, W., Francis, P. J., Peterson, B. A., and Webster, R. L. (1998), “X-Ray Properties of the Parkes Sample of Flat-Spectrum Radio Sources: Dust in Radio-Loud Quasars?” *MNRAS*, 301, 261.

-
- Sitko, M. L. and Junkkarinen, V. T. (1985), "Continuum and Line Fluxes of OJ287 at Minimum Light," *PASP*, 97, 1158.
- Spinrad, H., Marr, J., Aguilar, L., and Djorgovski, S. (1985), "A Third Update of the Status of the 3CR Sources. Further New Redshifts and New Identifications of Distant Galaxies," *PASP*, 97, 932.
- Stark, A. A., Gammie, C. F., Wilson, R. W., Bally, J., Linke, R. A., Heiles, C., and Hurwitz, M. (1992), "The Bell Laboratories H I Survey," *ApJS*, 79, 77.
- Stickel, M. and Kühr, H. (1994), "An Update of the Optical Identification Status of the S4 Radio Source Catalogue," *A&AS*, 103, 349.
- Stickel, M., Fried, J. W., Kühr, H., Padovani, P., and Urry, C. M. (1991), "The Complete Sample of 1 Jansky BL Lacertae Objects. I. Summary Properties," *ApJ*, 374, 431.
- Stickel, M., Meisenheimer, K., and Kühr, H. (1994), "The Optical Identification Status of the 1 Jy Radio Source Catalogue," *A&AS*, 105, 211.
- Stickel, M., Rieke, G. H., Kühr, H., and Rieke, M. J. (1996), "Flat-Spectrum Radio Sources with Faint Optical Counterparts," *ApJ*, 468, 556.
- Stocke, J. T., Morris, S. L., Gioia, I. M., Maccacaro, T., Schild, R., Wolter, A., Fleming, T. A., and Henry, J. P. (1991), "The *EINSTEIN OBSERVATORY* Extended Medium-Sensitivity Survey. II. The Optical Identifications," *ApJS*, 76, 813.
- Strittmatter, P. A., Serkowski, K., Carswell, R., Stein, W. A., Merrill, K. M., and Burbidge, E. M. (1972), "Compact Extragalactic Nonthermal Sources," *ApJ*, 175, L7.
- Sutherland, R. S., Bicknell, G. V., and Dopita, M. A. (1993), "Shock Excitation of the Emission-Line Filaments in Centaurus A," *ApJ*, 414, 510.
- Tadhunter, C. N., Morganti, R., di Serego-Alighieri, S., Fosbury, R. A. E., and Danziger, I. J. (1993), "Optical Spectroscopy of a Complete Sample of Southern 2 Jy Radio Sources," *MNRAS*, 263, 999.
- Tadhunter, C. N., Morganti, R., Robinson, A., Dickson, R., Villar-Martin, M., and Fosbury, R. A. E. (1998), "The Nature of the Optical-Radio Correlations for Powerful Radio Galaxies," *MNRAS*, 298, 1035.

- Taylor, G. B., Vermeulen, R. C., Readhead, A. C. S., Pearson, T. J., Henstock, D. R., and Wilkinson, P. N. (1996), "A Complete Flux-Density-Limited VLBI Survey of 293 Flat-Spectrum Radio Sources," *ApJS*, 107, 37.
- Ulrich, M. H. (1981), "The Appearance of Broad Emission Lines in the Spectrum of the BL Lac Object PKS 0521-36," *A&A*, 103, L1.
- Urry, C. M. (1998), "BL Lac Objects and Blazars: Past, Present and Future," in *BL Lac Phenomenon*, eds. L. O. Takalo and A. Sillanpää, p. 3, A.S.P., San Francisco.
- Urry, C. M. and Padovani, P. (1995), "Unified Schemes for Radio-Loud Active Galactic Nuclei," *PASP*, 107, 803.
- Urry, C. M. and Shafer, R. A. (1984), "Luminosity Enhancement in Relativistic Jets and Altered Luminosity Functions for Beamed Objects," *ApJ*, 280, 569.
- Urry, C. M., Padovani, P., and Stickel, M. (1991), "Fanaroff-Riley I Galaxies as the Parent Population of BL Lacertae Objects III. Radio Constraints," *ApJ*, 382, 501.
- Urry, C. M., Scarpa, R., O'Dowd, M., Falomo, R., Pesce, J. E., and Treves, A. (2000), "The *HST* Survey of BL Lacertae Objects. II. Host Galaxies," *ApJ*, 532, 816.
- Veilleux, S. and Osterbrock, D. E. (1987), "Spectral Classification of Emission-Line Galaxies," *ApJS*, 63, 295.
- Verdoes Kleijn, G. A., Baum, S. A., de Zeeuw, P. T., and O'Dea, C. P. (2002), "Core Radio and Optical Emission in the Nuclei of Nearby FR I Radio Galaxies," *AJ*, 123, 1334.
- Véron-Cetty, M.-P. and Véron, P. (2001), "A Catalogue of Quasars and Active Nuclei: 10th Edition," *A&A*, 374, 92.
- Voges, W., Aschenbach, B., Boller, T., Bräuninger, H., Briel, U., Burkert, W., Dennerl, K., Englhauser, J., et al. (1999), "The *ROSAT* All-Sky Survey Bright Source Catalogue," *A&A*, 349, 389.
- Wall, J. V. and Peacock, J. A. (1985), "Bright Extragalactic Radio Sources at 2.7 GHz. III. The All-Sky Catalogue," *MNRAS*, 216, 173.
- White, N. E., Giommi, P., and Angelini, L. (1995), <http://wgacat.gsfc.nasa.gov/wgacat/wgacat.html>.

-
- White, R. L. and Becker, R. H. (1992), “A New Catalog of 30 239 1.4 GHz Sources,” *ApJS*, 79, 331.
- Willott, C. J., Rawlings, S., Blundell, K. M., and Lacy, M. (1999), “The Emission Line-Radio Correlation for Radio Sources Using the 7C Redshift Survey,” *MNRAS*, 309, 1017.
- Willott, C. J., Rawlings, S., Blundell, K. M., and Lacy, M. (2000), “The Quasar Fraction in Low-Frequency-Selected Complete Samples and Implications for Unified Schemes,” *MNRAS*, 316, 449.
- Wills, B. J., Netzer, H., and Wills, D. (1985), “Broad Emission Features in QSOs and Active Galactic Nuclei. II. New Observations and Theory of Fe II and H I Emission,” *ApJ*, 288, 94.
- Wold, M., Lacy, M., Lilje, P. B., and Serjeant, S. (2000), “Clustering of Galaxies around Radio Quasars at $0.5 \leq z \leq 0.8$,” *MNRAS*, 316, 267.
- Wolter, A. and Celotti, A. (2001), “An X-Ray Selected Sample of Radio-Loud Quasars,” *A&A*, 371, 527.
- Wolter, A., Caccianiga, A., Maccacaro, T., Della Ceca, R., Gioia, I. M., Cavallotti, F., and Minoia, M. (2001), “Radio Properties of REX BL Lacs and Galaxies,” in *Blazar Demographics and Physics*, eds. P. Padovani and C. M. Urry, p. 190, A.S.P., San Francisco.
- Wurtz, R., Stocke, J. T., and Yee, H. K. C. (1996), “The Canada-France-Hawaii Telescope Imaging Survey of BL Lacertae Objects. I. Properties of the Host Galaxies,” *ApJS*, 103, 109.
- Wurtz, R., Stocke, J. T., Ellingson, E., and Yee, H. K. C. (1997), “The Canada-France-Hawaii Telescope Imaging Survey of BL Lacertae Objects. II. Clustering Environments,” *ApJ*, 480, 547.
- Zirbel, E. L. and Baum, S. A. (1995), “On the FR I/FR II Dichotomy in Powerful Radio Sources: Analysis of Their Emission-Line and Radio Luminosities,” *ApJ*, 448, 521.

Appendix A

Positional Information

The following tables give the positional information for the DXRBS sources. The first table includes the objects previously unclassified and meeting all DXRBS selection criteria (211 objects). These form together with the previously known sources the complete sample. The second table includes objects previously unclassified that do not meet all DXRBS selection criteria (22 low priority sources). A number of DXRBS sources were serendipitously observed by *ROSAT* on more than one occasion. For completeness, the WGACAT positions for all observations are given.

The columns of the tables are as follows:

(1): WGACAT name of the source; (2) and (3): WGACAT position; (4): source offset from the center of the PSPC field of view (in arc-minutes); (5) and (6): GB6 or PMN position; (7) and (8): position of the optical counterpart (which is taken as the position of the corresponding NVSS or ATCA source if within $\sim 3''$, otherwise the optical position was measured on the finder and a footnote is given); (9): offset between the WGACAT (X-ray) and NVSS/ATCA radio (or optical) position (in arc-seconds); (10): ratio between the latter offset (column 9) and the sum in quadrature of the X-ray and NVSS/ATCA radio (or optical) positional error (this value corresponds roughly to the significance in σ of the X-ray/radio mismatch). Positions are in equinox J2000.

I. DXRBS Complete Sample

Name	WGACAT Position		PSPC Center Offset	PMN or GB6 Position		Optical Position		Offset (X-O)	Offset/ Error
	RA	DEC	[arcmin]	RA	DEC	RA	DEC	[arcsec]	
(1)	(2)	(3)	(4)	(5)	(6)	(7)	(8)	(9)	(10)
WGAJ0010.5-3027	00 10 33.7	-30 27 14	47.4	00 10 33.5	-30 27 31	00 10 35.7	-30 27 46	41.1	1.0
WGAJ0010.7-3649	00 10 43.2	-36 49 29	26.4	00 10 42.2	-36 48 15	00 10 47.3	-36 48 49	63.4	2.2
WGAJ0011.2-3620	00 11 14.0	-36 20 35	3.2	00 11 15.5	-36 20 33	00 11 14.6	-36 20 39	8.3	0.6
WGAJ0012.5-1629	00 12 33.7	-16 29 01	45.9	00 12 33.2	-16 28 06	00 12 33.9	-16 28 07	54.1	1.3
	00 12 37.5	-16 28 23	44.8	00 12 33.2	-16 28 06	00 12 33.9	-16 28 07	54.2	1.3
WGAJ0014.5-3059	00 14 34.1	-30 59 22	37.8	00 14 35.8	-30 59 08	00 14 38.0	-30 59 19	50.2	1.4
WGAJ0015.5+3052	00 15 35.2	+30 52 19	34.7	00 15 36.1	+30 52 21	00 15 36.0	+30 52 30 ^a	15.1	0.4
	00 15 39.7	+30 52 43	33.3	00 15 36.1	+30 52 21	00 15 36.0	+30 52 30	49.4	1.4
WGAJ0023.6+0417	00 23 37.6	+04 17 02	15.6	00 23 39.4	+04 16 20	00 23 37.6	+04 16 42	20.0	1.1
WGAJ0029.0+0509	00 29 04.6	+05 09 42	22.9	00 29 03.8	+05 09 31	00 29 03.5	+05 09 34	18.3	0.6
WGAJ0032.5-2648	00 32 33.0	-26 48 54	24.3	00 32 37.7	-26 49 29	00 32 33.0	-26 49 17	23.0	0.8
WGAJ0032.5-2849	00 32 31.8	-28 49 48	34.8	00 32 31.2	-28 49 20	00 32 33.1	-28 49 19	33.7	0.9
WGAJ0034.4-2133	00 34 29.9	-21 33 24	9.1	00 34 30.5	-21 34 03	00 34 30.9	-21 33 53 ^b	32.2	2.3
WGAJ0040.4-2340	00 40 25.1	-23 40 05	6.4	00 40 25.3	-23 40 58	00 40 24.9	-23 39 60	5.7	0.4
WGAJ0043.3-2638	00 43 22.5	-26 38 57	32.4	00 43 24.0	-26 39 06	00 43 22.7	-26 39 07	10.4	0.3
WGAJ0049.5-2509	00 49 33.5	-25 09 44	28.7	00 49 34.2	-25 09 34	00 49 33.7	-25 09 34	10.4	0.4
WGAJ0057.3-2212	00 57 18.6	-22 12 30	8.9	00 57 21.8	-22 12 33	00 57 19.3	-22 12 37	12.0	0.9
	00 57 18.8	-22 12 17	9.1	00 57 21.8	-22 12 33	00 57 19.3	-22 12 37	21.2	1.5
	00 57 19.5	-22 12 32	8.9	00 57 21.8	-22 12 33	00 57 19.3	-22 12 37	5.7	0.4
WGAJ0100.1-3337	01 00 08.9	-33 37 21	6.0	01 00 07.6	-33 37 20	01 00 09.4	-33 37 32	12.7	0.9
WGAJ0106.7-1034	01 06 43.1	-10 34 03	36.1	01 06 43.6	-10 34 26	01 06 44.1	-10 34 10	16.3	0.4
WGAJ0110.5-1647	01 10 35.4	-16 47 56	28.3	01 10 36.3	-16 48 42	01 10 35.5	-16 48 28	32.0	1.1
WGAJ0125.0+0146	01 25 05.4	+01 46 33	5.0	01 25 04.1	+01 46 14	01 25 05.4	+01 46 26	7.0	0.5
WGAJ0126.2-0500	01 26 13.6	-05 00 49	28.8	01 26 09.1	-05 00 40	01 26 15.0	-05 01 23 ^b	39.9	1.4
WGAJ0136.0-4044	01 36 02.0	-40 44 46	17.0	01 36 06.3	-40 44 29	01 36 02.9	-40 44 50	11.0	0.6
WGAJ0143.2-6813	01 43 16.2	-68 13 06	25.5	01 43 22.9	-68 13 18	01 43 19.2	-68 13 27	26.8	0.9
WGAJ0146.2+0223	01 46 12.9	+02 23 00	35.3	01 46 15.1	+02 22 06	01 46 14.6	+02 22 08	57.9	1.6
WGAJ0152.5-1413	01 52 30.3	-14 13 00	30.6	01 52 31.7	-14 12 39	01 52 32.1	-14 12 38	34.2	0.9
WGAJ0154.4-1346	01 54 28.9	-13 46 45	23.4	01 54 29.3	-13 46 08	01 54 29.4	-13 46 36	11.6	0.4
WGAJ0204.8+1514	02 04 49.7	+15 14 20	28.7	02 04 50.8	+15 14 00	02 04 50.3	+15 14 11	12.5	0.4
WGAJ0208.1-3858	02 08 08.5	-38 58 15	33.9	02 08 11.1	-38 58 18	02 08 12.2	-38 58 08	43.7	1.2
WGAJ0210.0-1004	02 10 00.6	-10 04 07	9.1	02 09 59.4	-10 03 31	02 10 00.1	-10 03 54	15.0	1.1
WGAJ0210.1-3851	02 10 11.5	-38 51 32	38.8	02 10 07.6	-38 51 10	02 10 13.2	-38 51 22	22.2	0.6
WGAJ0211.9-7351	02 11 57.8	-73 51 20	24.1	02 12 15.7	-73 51 47	02 12 14.1	-73 51 28	68.5	2.4
WGAJ0216.6-7331	02 16 37.7	-73 31 35	32.9	02 16 47.3	-73 31 42	02 16 44.6	-73 31 40	29.8	0.8
WGAJ0217.7-7347	02 17 44.8	-73 47 31	17.4	02 17 48.2	-73 47 18	02 17 45.1	-73 47 23	8.1	0.4
	02 17 46.4	-73 46 21	18.6	02 17 48.2	-73 47 18	02 17 45.1	-73 47 23	62.2	3.3
WGAJ0227.5-0847	02 27 32.1	-08 47 35	37.3	02 27 32.6	-08 47 59	02 27 32.1	-08 48 13	38.0	1.0
WGAJ0230.0-1031	02 30 00.1	-10 31 39	31.1	02 29 55.6	-10 31 54	02 29 59.3	-10 31 17	25.0	0.7
WGAJ0245.2+1047	02 45 13.5	+10 47 20	34.9	02 45 14.7	+10 47 12	02 45 13.7	+10 47 23 ^c	4.2	0.1
WGAJ0251.9-2051	02 51 55.2	-20 51 42	15.4	02 51 55.9	-20 52 18	02 51 54.9	-20 51 49 ^d	8.2	0.4
WGAJ0253.3+0006	02 53 19.8	+00 06 45	27.1	02 53 21.6	+00 06 04	02 53 21.1	+00 06 02	47.2	1.6
WGAJ0258.5-5051	02 58 35.7	-50 51 54	31.0	02 58 38.9	-50 52 14	02 58 38.8	-50 52 04	31.0	0.9
	02 58 37.7	-50 52 16	30.9	02 58 38.9	-50 52 14	02 58 38.8	-50 52 04	15.9	0.4
WGAJ0259.4+1926	02 59 26.3	+19 26 23	43.1	02 59 29.9	+19 25 49	02 59 29.7	+19 25 45	61.3	1.5
WGAJ0304.9+0002	03 04 57.9	+00 02 28	30.6	03 04 58.8	+00 02 07	03 04 59.2	+00 02 33	20.1	0.6

Name	WGACAT Position		PSPC Center Offset	PMN or GB6 Position		Optical Position		Offset (X-O)	Offset/ Error
	RA	DEC	[arcmin]	RA	DEC	RA	DEC	[arcsec]	
(1)	(2)	(3)	(4)	(5)	(6)	(7)	(8)	(9)	(10)
WGAJ0305.3-2420	03 05 20.2	-24 20 39	29.5	03 05 20.9	-24 21 55	03 05 19.5	-24 21 34	55.8	1.9
WGAJ0307.7-4717	03 07 42.6	-47 17 20	33.4	03 07 38.2	-47 17 32	03 07 39.9	-47 17 43	35.8	1.0
WGAJ0312.3-6610	03 12 19.0	-66 10 28	38.6	03 12 20.1	-66 11 02	03 12 15.8	-66 10 58 ^e	35.7	1.0
WGAJ0314.4-6548	03 14 24.4	-65 48 20	45.7	03 14 19.3	-65 48 39	03 14 22.4	-65 48 25	13.3	0.3
	03 14 27.6	-65 48 21	45.5	03 14 19.3	-65 48 39	03 14 22.4	-65 48 25	32.2	0.8
WGAJ0321.6-6641	03 21 39.6	-66 41 47	25.6	03 21 52.1	-66 42 31	03 21 45.0	-66 42 00	39.4	1.4
	03 21 45.1	-66 41 40	26.8	03 21 52.1	-66 42 31	03 21 45.0	-66 42 00	30.0	1.0
WGAJ0322.1-5205	03 22 08.7	-52 05 32	17.9	03 22 11.5	-52 06 37	03 22 07.9	-52 05 36 ^e	8.4	0.5
WGAJ0322.2-5042	03 22 12.3	-50 42 26	22.9	03 22 10.3	-50 42 21	03 22 12.4	-50 42 33	7.1	0.2
WGAJ0322.6-1335	03 22 37.8	-13 35 15	12.1	03 22 39.2	-13 35 33	03 22 38.5	-13 35 18	10.6	0.6
WGAJ0324.9-2140	03 24 59.6	-21 40 41	32.6	03 25 01.3	-21 40 19	03 25 00.8	-21 40 41	16.7	0.5
WGAJ0325.0-4926	03 25 00.1	-49 26 44	18.9	03 25 03.5	-49 27 24	03 25 02.6	-49 27 05	32.2	1.7
	03 25 00.2	-49 27 05	18.9	03 25 03.5	-49 27 24	03 25 02.6	-49 27 05	23.4	1.2
	03 25 03.2	-49 26 44	19.4	03 25 03.5	-49 27 24	03 25 02.6	-49 27 05	21.8	1.2
WGAJ0340.4-2234	03 40 26.3	-22 34 49	38.3	03 40 26.1	-22 34 33	03 40 26.2	-22 34 54	5.2	0.1
WGAJ0340.8-1814	03 40 49.1	-18 14 00	21.9	03 40 45.5	-18 13 39	03 40 48.0	-18 14 00	15.7	0.5
WGAJ0343.6-1141	03 43 40.9	-11 41 42	13.3	03 43 43.3	-11 41 39	03 43 41.9	-11 41 37	15.5	0.8
WGAJ0355.6-1026	03 55 41.0	-10 26 44	29.4	03 55 40.3	-10 26 43	03 55 41.0	-10 26 58	14.0	0.5
WGAJ0357.6-4158	03 57 39.5	-41 58 57	31.4	03 57 36.8	-41 58 59	03 57 36.8	-41 59 01	30.4	0.8
WGAJ0411.0-1637	04 11 00.0	-16 37 00	51.0	04 10 59.4	-16 36 08	04 10 59.5	-16 36 11	49.5	0.9
WGAJ0414.0-1224	04 14 05.7	-12 24 30	18.4	04 14 03.1	-12 23 38	04 14 05.9	-12 24 17	13.3	0.3
WGAJ0414.0-1307	04 14 02.9	-13 07 13	24.4	04 14 02.3	-13 06 44	04 14 03.1	-13 06 39 ^f	34.1	1.2
WGAJ0421.5+1433	04 21 33.4	+14 33 44	11.8	04 21 33.1	+14 33 43	04 21 33.1	+14 33 54 ^g	10.9	0.6
WGAJ0424.6-3849	04 24 39.3	-38 49 02	30.3	04 24 34.1	-38 48 42	04 24 33.6	-38 48 42	69.6	1.9
WGAJ0427.2-0756	04 27 13.7	-07 56 01	24.2	04 27 17.9	-07 56 37	04 27 14.2	-07 56 24	24.2	0.8
WGAJ0428.8-3805	04 28 50.5	-38 05 44	11.4	04 28 52.6	-38 05 23	04 28 50.9	-38 05 52	9.3	0.5
WGAJ0431.9+1731	04 31 55.3	+17 31 44	28.8	04 31 57.1	+17 31 25	04 31 57.3	+17 31 35	30.0	1.0
	04 31 57.6	+17 31 37	6.7	04 31 57.1	+17 31 25	04 31 57.3	+17 31 35	4.7	0.4
WGAJ0434.3-1443	04 34 18.7	-14 43 01	5.9	04 34 19.0	-14 43 09	04 34 19.0	-14 42 55	7.4	0.5
WGAJ0435.1-0811	04 35 06.6	-08 11 05	28.6	04 35 05.9	-08 11 15	04 35 08.4	-08 11 04	26.8	0.9
WGAJ0438.7-4727	04 38 45.3	-47 27 51	23.1	04 38 47.4	-47 28 16	04 38 47.0	-47 28 01	19.9	0.7
WGAJ0441.8-4306	04 41 53.9	-43 06 21	31.6	04 41 48.7	-43 06 56	04 41 49.1	-43 06 60	65.5	1.7
WGAJ0447.9-0322	04 47 54.6	-03 22 28	38.4	04 47 57.5	-03 22 40	04 47 54.7	-03 22 43	15.1	0.4
WGAJ0448.2-2110	04 48 14.9	-21 10 18	30.4	04 48 18.0	-21 09 47	04 48 17.4	-21 09 45	48.1	1.3
WGAJ0448.6-2203	04 48 36.9	-22 03 41	44.3	04 48 32.6	-22 03 03	04 48 35.8	-22 03 28	20.1	0.5
WGAJ0500.0-3040	05 00 04.6	-30 40 49	26.4	05 00 07.5	-30 41 14	05 00 05.0	-30 41 09	20.7	0.7
WGAJ0500.9-3047	05 00 59.9	-30 47 07	32.2	05 01 06.4	-30 47 36	05 01 06.9	-30 47 37	95.1	2.6
WGAJ0510.0+1800	05 10 02.6	+18 00 48	9.6	05 10 02.4	+18 00 41	05 10 02.3	+18 00 41	8.2	0.6
WGAJ0518.2+0624	05 18 14.7	+06 24 17	26.3	05 18 15.8	+06 24 00	05 18 15.9	+06 24 22	18.6	0.6
WGAJ0528.5-5820	05 28 34.7	-58 20 12	33.4	05 28 33.2	-58 20 25	05 28 34.9	-58 20 20	8.2	0.2
WGAJ0533.6-4632	05 33 38.9	-46 32 24	24.7	05 33 38.8	-46 32 06	05 33 40.8	-46 32 15	21.6	0.8
WGAJ0533.7-5817	05 33 45.2	-58 17 46	18.9	05 33 43.3	-58 17 41	05 33 45.3	-58 18 02	16.0	0.9
WGAJ0534.9-6439	05 34 58.7	-64 39 02	2.1	05 35 01.1	-64 38 35	05 35 00.2	-64 38 57	10.8	0.8
WGAJ0535.1-0239	05 35 11.9	-02 39 05	11.5	05 35 10.8	-02 39 11	05 35 12.2	-02 39 06	4.6	0.2
WGAJ0536.4-3401	05 36 29.3	-34 01 06	37.7	05 36 28.8	-34 01 18	05 36 28.4	-34 01 11	12.3	0.3
WGAJ0539.0-3427	05 39 03.4	-34 27 12	25.2	05 39 06.2	-34 27 35	05 39 05.4	-34 27 13	24.8	0.9
WGAJ0544.1-2241	05 44 07.0	-22 41 16	17.2	05 44 05.7	-22 41 23	05 44 07.5	-22 41 10	9.2	0.5
WGAJ0546.6-6415	05 46 36.1	-64 15 06	52.8	05 46 42.9	-64 15 22	05 46 41.8	-64 15 22	40.4	0.8

Name	WGACAT Position		PSPC Center Offset	PMN or GB6 Position		Optical Position		Offset	Offset/
	RA	DEC	[arcmin]	RA	DEC	RA	DEC	(X-O)	Error
(1)	(2)	(3)	(4)	(5)	(6)	(7)	(8)	(9)	(10)
	05 46 40.5	-64 15 27	42.2	05 46 42.9	-64 15 22	05 46 41.8	-64 15 22	9.8	0.2
WGAJ0558.1+5328	05 58 09.6	+53 28 37	27.0	05 58 12.0	+53 28 32	05 58 11.6	+53 28 19	25.4	0.9
WGAJ0600.5-3937	06 00 31.0	-39 37 11	23.6	06 00 32.5	-39 36 60	06 00 31.4	-39 37 02	10.1	0.3
WGAJ0624.7-3229	06 24 43.0	-32 29 56	42.2	06 24 46.1	-32 31 07	06 24 44.9	-32 30 53	61.9	1.5
	06 24 47.3	-32 30 38	41.2	06 24 46.1	-32 31 07	06 24 44.9	-32 30 53	33.9	0.8
WGAJ0631.9-5404	06 31 59.6	-54 04 31	45.2	06 31 57.8	-54 05 02	06 32 01.7	-54 04 57	31.9	0.8
WGAJ0633.1-2333	06 33 11.8	-23 33 18	22.3	06 33 12.7	-23 33 05	06 33 12.8	-23 33 09	16.4	0.6
WGAJ0646.8+6807	06 46 49.8	+68 07 46	29.1	06 46 41.3	+68 07 40	06 46 42.4	+68 07 41 ^h	41.7	1.4
WGAJ0648.2-4347	06 48 16.7	-43 47 01	30.9	06 48 12.4	-43 46 39	06 48 13.4	-43 47 15	38.4	1.1
WGAJ0651.9+6955	06 51 56.3	+69 55 35	34.8	06 51 55.2	+69 55 16	06 51 54.6	+69 55 26	12.6	0.3
WGAJ0741.7-5304	07 41 42.2	-53 04 42	29.4	07 41 49.6	-53 05 16	07 41 49.8	-53 04 39	68.5	2.4
WGAJ0744.8+2920	07 44 51.6	+29 20 05	33.7	07 44 51.5	+29 20 27	07 44 51.2	+29 20 11	8.0	0.2
	07 44 51.8	+29 20 11	33.8	07 44 51.5	+29 20 27	07 44 51.2	+29 20 11	7.8	0.2
WGAJ0747.0-6744	07 47 03.6	-67 44 41	7.1	07 46 55.7	-67 44 57	07 47 05.0	-67 44 41 ⁱ	8.0	0.6
WGAJ0748.2-5257	07 48 13.2	-52 57 45	31.1	07 48 10.8	-52 58 29	07 48 12.7	-52 58 32	47.2	1.3
WGAJ0750.9-6726	07 50 55.1	-67 26 16	22.8	07 50 56.8	-67 26 36	07 50 59.5	-67 26 23	26.3	0.9
	07 51 02.4	-67 26 22	23.2	07 50 56.8	-67 26 36	07 50 59.5	-67 26 23	16.7	0.6
	07 51 04.2	-67 25 54	23.7	07 50 56.8	-67 26 36	07 50 59.5	-67 26 23	39.7	1.4
WGAJ0829.5+0858	08 29 30.4	+08 58 25	26.4	08 29 29.9	+08 58 19	08 29 30.3	+08 58 21	4.3	0.1
WGAJ0853.0+2004	08 53 02.3	+20 04 34	23.6	08 53 03.1	+20 04 22	08 53 02.7	+20 04 22	13.2	0.5
	08 53 02.7	+20 04 23	23.5	08 53 03.1	+20 04 22	08 53 02.7	+20 04 22	1.0	0.0
WGAJ0900.2-2817	09 00 14.0	-28 17 49	31.2	09 00 15.8	-28 17 60	09 00 15.4	-28 17 58	20.6	0.6
WGAJ0908.2+5031	09 08 17.4	+50 31 10	19.5	09 08 16.3	+50 31 06	09 08 16.9	+50 31 05	6.9	0.4
WGAJ0927.7-0900	09 27 44.9	-09 00 28	22.7	09 27 48.9	-09 01 04	09 27 46.9	-09 00 22	30.2	1.1
WGAJ0931.9+5533	09 31 58.2	+55 33 45	24.1	09 32 00.8	+55 33 34	09 32 00.2	+55 33 46 ^j	17.0	0.6
WGAJ0940.2+2603	09 40 14.0	+26 03 39	33.6	09 40 14.6	+26 03 38	09 40 14.7	+26 03 29	13.7	0.4
WGAJ0954.4-0503	09 54 26.7	-05 03 47	9.4	09 54 22.2	-05 03 04	09 54 27.0	-05 03 32	15.7	1.2
WGAJ1003.9+3244	10 03 58.1	+32 44 02	18.3	10 03 58.4	+32 44 03	10 03 57.5	+32 44 03	7.7	0.4
WGAJ1006.1+3236	10 06 08.3	+32 36 22	46.2	10 06 07.1	+32 36 20	10 06 07.7	+32 36 28	9.7	0.2
WGAJ1006.5+0509	10 06 34.1	+05 09 46	35.4	10 06 37.9	+05 09 50	10 06 37.6	+05 09 54	52.9	1.5
WGAJ1006.7-2014	10 06 44.9	-20 14 03	10.6	10 06 44.2	-20 14 21	10 06 44.8	-20 14 14	11.1	0.6
WGAJ1010.8-0201	10 10 52.6	-02 01 45	40.8	10 10 52.6	-02 00 57	10 10 51.6	-02 02 27	44.6	1.1
WGAJ1011.5-0423	10 11 30.1	-04 23 13	18.7	10 11 30.7	-04 23 33	10 11 30.2	-04 23 30	17.1	0.9
WGAJ1025.9+1253	10 25 56.0	+12 53 36	9.7	10 25 56.4	+12 53 48	10 25 56.4	+12 53 49	14.3	1.1
WGAJ1026.4+6746	10 26 29.1	+67 46 49	40.3	10 26 33.2	+67 46 02	10 26 34.0	+67 46 12 ^h	46.3	1.1
WGAJ1028.5-0236	10 28 33.2	-02 36 49	38.6	10 28 34.3	-02 37 12	10 28 34.1	-02 36 60	17.4	0.5
WGAJ1032.1-1400	10 32 06.6	-14 00 13	15.7	10 32 07.4	-14 00 19	10 32 06.3	-14 00 20	8.3	0.4
WGAJ1035.0+5652	10 35 04.8	+56 52 57	13.4	10 35 06.0	+56 52 57	10 35 05.9	+56 52 57	9.0	0.5
WGAJ1046.3+5354	10 46 23.7	+53 54 19	26.4	10 46 23.8	+53 54 38	10 46 24.0	+53 54 26	7.5	0.3
WGAJ1056.9-7649	10 56 54.3	-76 49 09	51.3	10 56 57.0	-76 49 23	10 56 54.6	-76 48 35	34.0	0.6
WGAJ1057.6-7724	10 57 41.0	-77 24 13	26.7	10 57 31.1	-77 24 24	10 57 32.7	-77 24 29	31.5	1.1
WGAJ1101.8+6241	11 01 53.2	+62 41 20	39.6	11 01 53.9	+62 41 55	11 01 53.4	+62 41 50 ^a	30.0	0.8
WGAJ1104.8+6038	11 04 53.0	+60 38 54	22.8	11 04 54.5	+60 38 57	11 04 53.6	+60 38 55	4.5	0.2
WGAJ1105.3-1813	11 05 18.9	-18 13 06	25.0	11 05 15.2	-18 13 04	11 05 19.2	-18 13 13	8.2	0.3
WGAJ1112.5-3745	11 12 34.7	-37 45 24	30.2	11 12 38.6	-37 45 49	11 12 36.8	-37 45 45	32.6	0.9
WGAJ1116.1+0828	11 16 08.9	+08 28 14	50.5	11 16 10.2	+08 29 19	11 16 10.0	+08 29 22	69.9	1.3
WGAJ1150.4+0156	11 50 24.5	+01 56 11	8.7	11 50 23.9	+01 56 02	11 50 24.8	+01 56 16	6.7	0.5
WGAJ1204.2-0710	12 04 16.1	-07 10 03	34.6	12 04 16.8	-07 10 34	12 04 16.7	-07 10 10	11.3	0.3

Name	WGACAT Position		PSPC Center Offset	PMN or GB6 Position		Optical Position		Offset (X-O)	Offset/ Error
	RA	DEC	[arcmin]	RA	DEC	RA	DEC	[arcsec]	
(1)	(2)	(3)	(4)	(5)	(6)	(7)	(8)	(9)	(10)
WGAJ1213.0+3248	12 13 03.8	+32 48 00	34.9	12 13 04.3	+32 47 42	12 13 03.8	+32 47 37	23.0	0.6
WGAJ1213.2+1443	12 13 14.0	+14 43 47	41.6	12 13 16.6	+14 44 14	12 13 14.9	+14 44 00 ^b	18.4	0.4
WGAJ1222.6+2934	12 22 39.5	+29 34 40	41.9	12 22 42.4	+29 34 39	12 22 43.1	+29 34 41	47.0	1.1
	12 22 42.5	+29 34 54	20.1	12 22 42.4	+29 34 39	12 22 43.1	+29 34 40	16.0	0.6
WGAJ1223.9+0650	12 23 53.2	+06 50 13	31.2	12 23 54.7	+06 50 13	12 23 54.7	+06 50 02	24.9	0.7
WGAJ1225.5+0715	12 25 30.8	+07 15 59	18.1	12 25 30.8	+07 15 49	12 25 31.2	+07 15 52	9.2	0.5
WGAJ1229.4+2711	12 29 29.0	+27 12 21	40.4	12 29 33.3	+27 11 57	12 29 34.3	+27 11 57	74.7	1.8
WGAJ1231.7+2848	12 31 46.8	+28 48 03	46.6	12 31 44.0	+28 48 03	12 31 43.7	+28 47 50	42.8	1.0
WGAJ1248.3-0631	12 48 23.0	-06 31 21	35.3	12 48 20.4	-06 31 56	12 48 23.0	-06 32 00	49.0	1.4
WGAJ1259.9+1206	12 59 58.2	+12 06 44	35.0	13 00 01.8	+12 06 07	13 00 01.9	+12 06 19	59.8	1.6
WGAJ1300.7-3253	13 00 42.3	-32 53 01	28.2	13 00 41.9	-32 53 02	13 00 42.4	-32 53 12	11.1	0.4
WGAJ1306.6-2428	13 06 40.3	-24 28 45	44.5	13 06 41.8	-24 27 23	13 06 41.2	-24 27 36	70.1	1.7
WGAJ1311.3-0521	13 11 22.3	-05 21 16	30.1	13 11 21.2	-05 21 05	13 11 17.8	-05 21 22	67.5	1.9
WGAJ1314.0-3304	13 14 03.0	-33 04 04	12.8	13 14 04.5	-33 03 07	13 14 03.4	-33 03 56 ^b	9.4	0.5
WGAJ1315.1+2841	13 15 10.3	+28 41 12	30.1	13 15 13.9	+28 40 59	13 15 13.6	+28 40 53	47.4	1.3
WGAJ1320.4+0140	13 20 26.5	+01 40 37	16.1	13 20 27.1	+01 40 48	13 20 26.8	+01 40 36	4.6	0.3
WGAJ1324.0-3623	13 24 02.6	-36 23 16	29.6	13 24 04.1	-36 23 51	13 24 03.5	-36 23 35	21.9	0.8
WGAJ1324.4-1049	13 24 25.7	-10 49 03	21.4	13 24 25.8	-10 49 19	13 24 25.9	-10 49 24	21.2	0.7
WGAJ1329.0+5009	13 29 00.8	+50 09 39	38.5	13 29 06.0	+50 09 21	13 29 05.8	+50 09 26	49.8	1.4
WGAJ1332.7+4722	13 32 46.0	+47 22 32	32.2	13 32 45.7	+47 22 26	13 32 45.3	+47 22 22	12.3	0.3
WGAJ1333.1-3323	13 33 07.2	-33 23 52	23.2	13 33 06.4	-33 24 18	13 33 08.9	-33 24 39	51.6	1.8
WGAJ1337.2-1319	13 37 13.1	-13 19 03	23.5	13 37 16.4	-13 19 04	13 37 14.9	-13 19 17	29.8	1.0
WGAJ1353.2-4720	13 53 14.9	-47 20 56	22.2	13 53 15.4	-47 20 53	13 53 16.7	-47 20 55	18.3	0.6
WGAJ1359.6+4010	13 59 36.1	+40 10 54	27.1	13 59 37.5	+40 11 42	13 59 38.1	+40 11 38	49.6	1.7
WGAJ1400.7+0425	14 00 46.4	+04 25 51	21.0	14 00 48.5	+04 25 33	14 00 48.4	+04 25 31	36.0	1.3
WGAJ1402.7-3334	14 02 43.5	-33 34 01	25.3	14 02 41.0	-33 34 59	14 02 41.4	-33 34 09	27.4	0.9
WGAJ1404.2+3413	14 04 15.8	+34 13 21	29.0	14 04 16.7	+34 13 13	14 04 16.7	+34 13 16	12.2	0.4
WGAJ1406.9+3433	14 06 54.4	+34 33 42	21.2	14 06 54.0	+34 33 28	14 06 53.9	+34 33 37	8.0	0.3
WGAJ1416.4+1242	14 16 26.8	+12 42 47	40.0	14 16 28.3	+12 42 26	14 16 28.6	+12 42 13	43.0	1.0
	14 16 28.3	+12 42 18	26.5	14 16 28.3	+12 42 26	14 16 28.6	+12 42 13	6.7	0.2
WGAJ1417.2+0608	14 17 16.8	+06 08 49	33.7	14 17 18.3	+06 08 08	14 17 19.0	+06 08 12 ^k	49.4	1.3
	14 17 17.4	+06 08 17	33.9	14 17 18.3	+06 08 08	14 17 19.0	+06 08 12	24.4	0.6
WGAJ1417.5+2645	14 17 30.2	+26 45 12	8.6	14 17 30.6	+26 45 07	14 17 30.4	+26 44 57	15.2	1.1
WGAJ1419.1+0603	14 19 09.6	+06 03 49	26.6	14 19 09.2	+06 03 34	14 19 09.3	+06 03 30	19.5	0.7
WGAJ1420.6+0650	14 20 40.0	+06 50 58	32.1	14 20 40.9	+06 50 57	14 20 41.0	+06 50 58 ^h	14.9	0.4
	14 20 40.6	+06 51 04	32.3	14 20 40.9	+06 50 57	14 20 41.0	+06 51 02	6.3	0.2
WGAJ1423.3+4830	14 23 18.0	+48 30 06	14.1	14 23 18.4	+48 30 17	14 23 18.0	+48 30 16	10.0	0.5
WGAJ1427.9+3247	14 27 56.8	+32 47 44	25.9	14 27 58.3	+32 47 41	14 27 58.8	+32 47 40 ^k	25.5	0.9
WGAJ1442.3+5236	14 42 21.3	+52 36 17	33.3	14 42 19.4	+52 36 20	14 42 19.6	+52 36 21	16.0	0.4
WGAJ1457.7-2818	14 57 42.0	-28 18 43	19.1	14 57 43.1	-28 19 19	14 57 44.6	-28 19 21	51.2	2.7
WGAJ1506.6-4008	15 06 36.0	-40 08 25	30.0	15 06 33.7	-40 07 35	15 06 37.2	-40 08 00	28.5	0.8
WGAJ1507.9+6214	15 07 55.9	+62 14 09	33.5	15 07 57.9	+62 13 44	15 07 57.3	+62 13 35	35.4	1.0
WGAJ1509.5-4340	15 09 35.8	-43 40 14	25.8	15 09 34.1	-43 40 41	15 09 35.7	-43 40 32	18.0	0.6
WGAJ1525.3+4201	15 25 22.5	+42 01 02	20.5	15 25 25.2	+42 01 15	15 25 23.6	+42 01 17	19.4	0.7
	15 25 23.9	+42 01 15	17.4	15 25 25.2	+42 01 15	15 25 23.6	+42 01 17	3.9	0.2
WGAJ1539.1-0658	15 39 09.8	-06 58 27	9.1	15 39 09.4	-06 58 29	15 39 09.6	-06 58 43	16.3	1.2
WGAJ1543.6+1847	15 43 40.7	+18 47 41	25.0	15 43 42.2	+18 47 07	15 43 43.8	+18 47 20	48.8	1.7
WGAJ1606.0+2031	16 06 05.3	+20 31 43	14.1	16 06 05.7	+20 32 14	16 06 05.9	+20 32 09	27.3	1.5

Name	WGACAT Position		PSPC Center Offset	PMN or GB6 Position		Optical Position		Offset (X-O)	Offset/ Error
	RA	DEC	[arcmin]	RA	DEC	RA	DEC	[arcsec]	
(1)	(2)	(3)	(4)	(5)	(6)	(7)	(8)	(9)	(10)
WGAI1615.2-0540	16 15 17.8	-05 40 24	27.6	16 15 20.9	-05 40 59	16 15 18.6	-05 40 21	12.3	0.4
	16 15 17.9	-05 40 53	27.1	16 15 20.9	-05 40 59	16 15 18.6	-05 40 21	33.7	1.2
WGAI1626.6+5809	16 26 37.3	+58 09 39	32.5	16 26 36.3	+58 09 14	16 26 37.2	+58 09 18 ^a	21.0	0.6
WGAI1629.7+2117	16 29 47.0	+21 17 16	14.3	16 29 47.6	+21 17 22	16 29 47.7	+21 17 16	9.8	0.5
WGAI1648.4+4104	16 48 28.3	+41 04 12	32.1	16 48 30.0	+41 04 07	16 48 29.3	+41 04 06	12.8	0.4
WGAI1656.6+5321	16 56 41.8	+53 21 48	24.3	16 56 41.3	+53 21 51	16 56 39.7	+53 21 49	18.8	0.7
WGAI1656.6+6012	16 56 41.7	+60 12 07	51.4	16 56 47.8	+60 12 28	16 56 48.3	+60 12 16	50.0	0.9
	16 56 48.1	+60 12 21	42.4	16 56 47.8	+60 12 28	16 56 48.3	+60 12 16	5.2	0.1
WGAI1722.3+3103	17 22 19.7	+31 03 17	8.8	17 22 18.7	+31 03 29	17 22 19.0	+31 03 23 ^b	10.8	0.8
WGAI1738.6-5333	17 38 37.5	-53 33 54	17.6	17 38 37.5	-53 34 05	17 38 38.8	-53 34 00	19.7	1.1
WGAI1744.3-0517	17 44 22.0	-05 17 47	24.6	17 44 17.8	-05 18 34	17 44 20.9	-05 18 41	56.4	2.0
WGAI1804.7+1755	18 04 42.8	+17 55 34	16.3	18 04 43.7	+17 55 36	18 04 42.5	+17 55 59	25.4	1.4
WGAI1808.2-5011	18 08 13.0	-50 11 38	18.4	18 08 13.2	-50 11 55	18 08 13.9	-50 11 54	18.2	1.0
WGAI1826.1-3650	18 26 07.4	-36 50 37	15.6	18 26 09.4	-36 51 12	18 26 08.1	-36 50 41 ^l	9.3	0.5
WGAI1827.1-4533	18 27 09.9	-45 33 07	23.9	18 27 11.8	-45 33 02	18 27 10.2	-45 33 00	4.4	0.2
WGAI1834.2-5948	18 34 15.8	-59 48 33	32.2	18 34 14.5	-59 48 51	18 34 13.6	-59 48 39	17.6	0.5
WGAI1834.4-5856	18 34 27.3	-58 56 11	31.7	18 34 28.1	-58 56 35	18 34 27.5	-58 56 36	25.0	0.7
	18 34 27.3	-58 56 43	4.5	18 34 28.1	-58 56 35	18 34 27.5	-58 56 36	7.2	0.5
WGAI1837.7-5848	18 37 44.9	-58 48 05	30.4	18 37 52.2	-58 48 14	18 37 53.8	-58 48 09	69.2	1.9
WGAI1840.9+5452	18 40 58.2	+54 52 29	43.3	18 40 56.8	+54 52 29	18 40 57.4	+54 52 14	16.5	0.4
WGAI1843.4-7430	18 43 26.4	-74 30 03	13.7	18 43 39.5	-74 30 46	18 43 40.2	-74 30 25	59.5	3.2
WGAI1911.8-2102	19 11 50.6	-21 02 21	31.2	19 11 53.8	-21 02 49	19 11 54.0	-21 02 44	52.8	1.5
WGAI1936.8-4719	19 36 53.1	-47 19 47	42.4	19 36 55.0	-47 19 38	19 36 56.1	-47 19 50	30.7	0.7
WGAI1938.4-4657	19 38 27.0	-46 57 54	34.2	19 38 26.4	-46 57 29	19 38 26.3	-46 57 26	28.9	0.8
WGAI2056.4-5819	20 56 29.1	-58 19 59	15.7	20 56 30.5	-58 20 15	20 56 30.6	-58 20 07	14.3	0.8
WGAI2109.7-1332	21 09 47.0	-13 32 15	21.0	21 09 51.6	-13 32 59	21 09 49.9	-13 32 46	52.4	1.8
WGAI2151.3-4233	21 51 20.6	-42 33 22	37.9	21 51 23.4	-42 33 41	21 51 21.9	-42 33 34 ^m	18.7	0.5
WGAI2154.1-1501	21 54 06.2	-15 01 53	47.3	21 54 08.6	-15 01 54	21 54 07.5	-15 01 31 ⁿ	27.2	0.6
	21 54 09.9	-15 02 12	47.7	21 54 08.6	-15 01 54	21 54 07.5	-15 01 31	54.0	1.3
WGAI2157.7+0650	21 57 42.7	+06 50 06	40.0	21 57 42.4	+06 49 21	21 57 43.2	+06 49 23	43.6	1.2
WGAI2159.3-1500	21 59 18.7	-15 00 33	18.8	21 59 18.3	-15 00 40	21 59 20.2	-15 00 37	22.1	1.2
	21 59 20.1	-15 00 40	19.1	21 59 18.3	-15 00 40	21 59 20.2	-15 00 37	3.3	0.2
WGAI2239.7-0631	22 39 46.5	-06 31 42	41.0	22 39 48.8	-06 31 48	22 39 46.9	-06 31 51 ^d	10.8	0.3
WGAI2248.6-2702	22 48 36.5	-27 02 34	13.0	22 48 37.5	-27 02 53	22 48 36.4	-27 02 55	21.0	1.1
WGAI2258.3-5525	22 58 18.1	-55 25 31	34.5	22 58 16.5	-55 26 14	22 58 19.0	-55 25 37	9.7	0.3
WGAI2303.5-5126	23 03 30.3	-51 26 31	8.7	23 03 29.6	-51 26 18	23 03 30.6	-51 26 42	11.4	0.9
WGAI2304.8-3624	23 04 53.3	-36 24 48	34.6	23 04 56.9	-36 25 42	23 04 56.3	-36 25 12	42.8	1.2
WGAI2317.4-4213	23 17 55.7	-42 13 29	7.9	23 17 52.3	-42 13 52	23 17 56.4	-42 13 33	8.7	0.6
WGAI2320.6+0032	23 20 38.5	+00 32 17	31.9	23 20 39.1	+00 31 16	23 20 38.0	+00 31 39	38.7	1.1
WGAI2322.0+2114	23 22 02.1	+21 14 02	15.8	23 22 03.3	+21 14 09	23 22 02.4	+21 13 54	9.0	0.5
	23 22 02.7	+21 13 36	15.4	23 22 03.3	+21 14 09	23 22 02.4	+21 13 54	18.5	1.0
WGAI2322.5-4221	23 22 35.2	-42 21 11	48.4	23 22 35.9	-42 21 10	23 22 40.4	-42 20 42	64.5	1.5
WGAI2329.0+0834	23 29 04.0	+08 34 51	22.0	23 29 05.5	+08 34 06	23 29 05.8	+08 34 15	44.8	1.6
WGAI2330.6-3724	23 30 36.9	-37 24 30	35.1	23 30 36.9	-37 24 43	23 30 35.8	-37 24 36	14.4	0.4
WGAI2333.2-0131	23 33 14.0	-01 31 29	30.0	23 33 16.3	-01 31 07	23 33 16.7	-01 31 08	45.6	1.3
WGAI2347.6+0852	23 47 36.3	+08 52 10	45.9	23 47 38.1	+08 52 52	23 47 38.1	+08 52 46 ^o	44.8	1.1
WGAI2349.9-2552	23 49 59.6	-25 52 30	28.8	23 49 58.8	-25 52 05	23 50 02.4	-25 52 19	39.4	1.4
	23 50 00.7	-25 52 20	29.0	23 49 58.8	-25 52 05	23 50 02.4	-25 52 19	23.0	0.8

Name	WGACAT Position		PSPC Center Offset	PMN or GB6 Position		Optical Position		Offset (X-O)	Offset/ Error
	RA	DEC	[arcmin]	RA	DEC	RA	DEC	[arcsec]	
(1)	(2)	(3)	(4)	(5)	(6)	(7)	(8)	(9)	(10)
WGAJ2354.2-0957	23 54 05.0	-09 57 11	25.3	23 54 06.6	-09 57 52	23 54 05.6	-09 57 48	38.1	1.3
WGAJ2356.4-3223	23 56 26.8	-32 23 46	35.3	23 56 30.3	-32 23 03	23 56 30.3	-32 22 22	95.2	2.6

II. DXRBS Low Priority Sources

Name	WGACAT Position		PSPC Center Offset	PMN or GB6 Position		Optical Position		Offset (X-O)	Offset/ Error
	RA	DEC	[arcmin]	RA	DEC	RA	DEC	[arcsec]	
(1)	(2)	(3)	(4)	(5)	(6)	(7)	(8)	(9)	(10)
WGAJ0247.9+1845	02 47 56.7	+18 45 13	38.7	02 47 52.5	+18 44 59	02 47 52.0	+18 44 27	81.1	2.2
WGAJ0313.9+4115	03 13 56.9	+41 15 37	16.9	03 13 58.0	+41 15 21	03 13 57.8	+41 15 23	17.3	0.9
WGAJ0449.4-4349	04 49 24.6	-43 49 39	2.0	04 49 24.3	-43 50 04	04 49 24.7	-43 50 09	30.0	2.3
WGAJ0513.8+0156	05 13 52.3	+01 56 59	14.9	05 13 52.7	+01 56 50	05 13 51.8	+01 56 29 ^P	30.6	1.7
	05 13 52.3	+01 56 59	14.9	05 13 52.7	+01 56 50	05 13 49.4	+01 55 52 ^P	79.9	1.7
	05 13 53.4	+01 56 21	14.3	05 13 52.7	+01 56 50	05 13 51.8	+01 56 29	25.3	1.4
	05 13 53.4	+01 56 21	14.3	05 13 52.7	+01 56 50	05 13 49.4	+01 55 52	66.6	1.4
WGAJ0605.8-7556	06 05 51.4	-75 56 21	38.3	06 05 51.3	-75 56 49	06 05 56.6	-75 56 59	43.6	1.2
WGAJ0628.4-3208	06 28 27.9	-32 08 11	25.7	06 28 32.6	-32 07 35	06 28 30.7	-32 08 14	35.7	1.2
	06 28 28.4	-32 08 06	25.8	06 28 32.6	-32 07 35	06 28 30.7	-32 08 14	30.3	1.1
WGAJ0724.3-0715	07 24 19.0	-07 15 56	34.3	07 24 16.3	-07 15 23	07 24 17.3	-07 15 20	38.4	1.1
WGAJ0816.0-0736	08 16 01.7	-07 36 16	20.2	08 16 04.1	-07 36 42	08 16 04.3	-07 35 57	43.2	1.5
WGAJ0847.2+1133	08 47 13.0	+11 34 30	48.1	08 47 10.3	+11 34 24	08 47 12.9	+11 33 50	40.0	1.0
WGAJ0937.1+5008	09 37 10.9	+50 08 54	32.0	09 37 11.9	+50 08 44	09 37 12.3	+50 08 52	13.6	0.4
	09 37 11.2	+50 09 02	31.9	09 37 11.9	+50 08 44	09 37 12.3	+50 08 52	13.2	0.4
	09 37 12.1	+50 08 53	25.5	09 37 11.9	+50 08 44	09 37 12.3	+50 08 52	2.2	0.1
	09 37 12.1	+50 09 02	24.4	09 37 11.9	+50 08 44	09 37 12.3	+50 08 52	10.2	0.4
	09 37 13.6	+50 08 56	24.4	09 37 11.9	+50 08 44	09 37 12.3	+50 08 52	14.0	0.5
WGAJ1028.6-0336	10 28 39.4	-03 36 52	35.6	10 28 39.5	-03 35 57	10 28 40.4	-03 36 19	45.5	1.3
WGAJ1120.4+5855	11 20 26.2	+58 55 57	18.4	11 20 27.7	+58 56 22	11 20 27.7	+58 56 12	18.5	1.0
	11 20 27.3	+58 56 19	16.3	11 20 27.7	+58 56 22	11 20 27.7	+58 56 12	6.1	0.3
WGAJ1206.2+2823	12 06 17.5	+28 23 19	35.7	12 06 20.5	+28 23 02	12 06 19.6	+28 22 54	37.7	1.1
WGAJ1217.1+2925	12 17 09.3	+29 25 28	29.2	12 17 08.6	+29 25 56	12 17 08.1	+29 25 32	14.4	0.5
WGAJ1401.5-1134	14 01 34.2	-11 34 17	26.9	14 01 35.4	-11 35 29	14 01 41.8	-11 36 25 ^q	169.9	5.9
WGAJ1457.9-2124	14 57 55.3	-21 24 12	32.3	14 57 54.8	-21 25 08	14 57 54.1	-21 24 58	55.2	1.5
	14 57 55.3	-21 24 56	32.4	14 57 54.8	-21 25 08	14 57 54.1	-21 24 58	11.8	0.3
WGAJ1520.7+0732	15 20 44.8	+07 32 28	19.3	15 20 44.7	+07 32 27	15 20 45.8	+07 32 28	1.8	0.1
	15 20 46.2	+07 32 52	18.7	15 20 44.7	+07 32 27	15 20 45.8	+07 32 28	22.3	1.0
WGAJ1610.3-3958	16 10 20.5	-39 58 22	22.1	16 10 21.9	-39 58 59	16 10 22.0	-39 58 58	40.4	1.4
	16 10 21.1	-39 58 53	5.8	16 10 21.9	-39 58 59	16 10 22.0	-39 58 58	11.0	0.8
	16 10 22.1	-39 58 37	14.0	16 10 21.9	-39 58 59	16 10 22.0	-39 58 58	22.1	1.2

Name	WGACAT Position		PSPC Center Offset	PMN or GB6 Position		Optical Position		Offset (X-O)	Offset/ Error
(1)	RA	DEC	[arcmin]	RA	DEC	RA	DEC	[arcsec]	(10)
	16 10 23.9	-39 58 28	23.8	16 10 21.9	-39 58 59	16 10 22.0	-39 58 58	38.6	1.3
WGAI1835.5-6539	18 35 31.2	-65 39 34	26.8	18 35 33.4	-65 40 23	18 35 35.0	-65 40 27	57.9	2.0
WGAI2131.9-0556	21 31 55.9	-05 56 30	24.8	21 31 55.9	-05 57 15	21 31 53.8	-05 56 00	43.4	1.5
WGAI2201.6-5646	22 01 37.5	-56 46 22	12.8	22 01 40.4	-56 46 45	22 01 38.4	-56 46 32	10.8	0.6
	22 01 37.6	-56 46 18	9.9	22 01 40.4	-56 46 45	22 01 38.4	-56 46 32	14.0	1.0
WGAI2205.2-0004	22 05 13.6	-00 04 00	25.7	22 05 13.3	-00 04 22	22 05 13.5	-00 04 32	32.0	1.1

^aoptical counterpart 6'' off NVSS position

^boptical counterpart 4'' off NVSS position

^coptical counterpart 26'' off NVSS position

^doptical counterpart 7'' off NVSS position

^eoptical counterpart 8'' off ATCA position

^foptical counterpart 8'' (10'') off NVSS (ATCA) position

^goptical counterpart 9'' off NVSS position; NVSS source extended

^hoptical counterpart 5'' off NVSS position

ⁱoptical counterpart 4'' off ATCA position

^jthree NVSS sources; optical counterpart in between two of them; possible double-lobed source

^ktwo NVSS sources; optical counterpart in between them; possible double-lobed source

^loptical counterpart 8'' off NVSS position

^moptical counterpart 7'' off PARKES position

ⁿATCA position; NVSS position 15'' off

^ooptical counterpart 12'' off NVSS position; NVSS source extended

^pthree NVSS sources; northernmost optical counterpart in between the two strongest sources, southernmost counterpart is 5'' off the faintest NVSS source

^qoptical counterpart 160'' off NVSS position; NVSS source extended

Appendix B

Spectroscopic Observations

The following table gives the observational information for the DXRBS sources. The table includes all previously unclassified sources listed in Appendix A with the exception of 11 objects, namely WGAJ0040.4–2340, WGAJ0152.5–1413, WGAJ0154.4–1346, WGAJ0208.1–3858, WGAJ0230.0–1031, WGAJ0340.4–2234, WGAJ0536.4–3401, WGAJ1248.3–0631, WGAJ1324.4–1049, WGAJ1401.5–1134, and WGAJ1520.7+0732, that have been observed by other groups. The reduced and calibrated spectra of the sources are shown in Appendix D.

The columns of the table are as follows:

(1): WGACAT name of the source; (2): name of the telescope; (3): date of the observation; (4): exposure time (in seconds). The telescope names have been abbreviated as follows: Cerro Tololo Inter-American Observatory (CTIO), Tololo, Chile; European Southern Observatory (ESO), La Silla, Chile; Kitt Peak National Observatory (KPNO), Kitt Peak, Arizona; Multiple Mirror Telescope (MMT) 4.5 m, Mount Hopkins, Arizona; Very Large Telescope (VLT) 8 m, Paranal, Chile.

Name	Observatory	Date	Exp [sec]	Name	Observatory	Date	Exp [sec]
(1)	(2)	(3)	(4)	(1)	(2)	(3)	(4)
WGAJ0010.5-3027	ESO 3.6 m	1998 Sep	900	WGAJ0357.6-4158	ESO 3.6 m	1996 Dec	900
WGAJ0010.7-3649	ESO 3.6 m	2000 Aug	600	WGAJ0411.0-1637	KPNO 2.1 m	1996 Dec	1200
WGAJ0011.2-3620	ESO 3.6 m	1996 Dec	900	WGAJ0414.0-1224	ESO 2.2 m	1996 Dec	900
WGAJ0012.5-1629	KPNO 2.1 m	1996 Dec	1200	WGAJ0414.0-1307	ESO 3.6 m	1996 Dec	900
WGAJ0014.5-3059	ESO 3.6 m	1998 Sep	1200	WGAJ0421.5+1433	ESO 3.6 m	1998 Feb	1200
WGAJ0015.5+3052	MMT	1996 Dec	900	WGAJ0424.6-3849	ESO 3.6 m	2000 Aug	900
WGAJ0023.6+0417	ESO 3.6 m	2000 Aug	1200	WGAJ0427.2-0756	ESO 3.6 m	1998 Feb	1200
WGAJ0029.0+0509	KPNO 2.1 m	1996 Dec	2400	WGAJ0428.8-3805	ESO 2.2 m	1996 Dec	1200
WGAJ0032.5-2648	KPNO 2.1 m	1996 Dec	2400	WGAJ0431.9+1731	VLT	1999 Sep	2400
WGAJ0032.5-2849	ESO 3.6 m	1996 Dec	240	WGAJ0434.3-1443	ESO 3.6 m	1996 Dec	900
WGAJ0034.4-2133	ESO 3.6 m	1998 Sep	3600	WGAJ0435.1-0811	KPNO 2.1 m	1996 Dec	3600
WGAJ0043.3-2638	CTIO 1.5 m	1997 Jan	1800	WGAJ0438.7-4727	ESO 3.6 m	1999 Mar	2700
WGAJ0049.5-2509	ESO 3.6 m	1996 Dec	1500	WGAJ0441.8-4306	ESO 3.6 m	2000 Aug	3600
WGAJ0057.3-2212	ESO 3.6 m	1996 Dec	900	WGAJ0447.9-0322	KPNO 2.1 m	1996 Dec	1200
WGAJ0100.1-3337	ESO 3.6 m	1996 Dec	900	WGAJ0448.2-2110	KPNO 2.1 m	1996 Dec	2400
WGAJ0106.7-1034	KPNO 2.1 m	1998 Jun	1200	WGAJ0448.6-2203	ESO 3.6 m	2000 Aug	1800
WGAJ0110.5-1647	KPNO 2.1 m	1996 Dec	1200	WGAJ0449.4-4349	CTIO 4 m	1996 Jan	900
WGAJ0125.0+0146	KPNO 2.1 m	1996 Dec	2400	WGAJ0500.0-3040	ESO 2.2 m	1996 Dec	1800
WGAJ0126.2-0500	ESO 3.6 m	1998 Sep	900	WGAJ0500.9-3047	ESO 3.6 m	2000 Aug	600
WGAJ0136.0-4044	ESO 3.6 m	1996 Dec	900	WGAJ0510.0+1800	ESO 3.6 m	1996 Dec	720
WGAJ0143.2-6813	ESO 3.6 m	1996 Dec	900	WGAJ0513.8+0156	ESO 3.6 m	1999 Mar	600
WGAJ0146.2+0223	ESO 3.6 m	2000 Aug	1200	WGAJ0518.2+0624	ESO 3.6 m	1996 Dec	480
WGAJ0204.8+1514	ESO 3.6 m	1996 Dec	1200	WGAJ0528.5-5820	ESO 3.6 m	1999 Mar	900
WGAJ0210.0-1004	ESO 2.2 m	1996 Dec	1500	WGAJ0533.6-4632	ESO 3.6 m	2001 Jul	3600
WGAJ0210.1-3851	ESO 3.6 m	2000 Aug	1200	WGAJ0533.7-5817	ESO 3.6 m	1999 Mar	900
WGAJ0211.9-7351	ESO 3.6 m	2000 Aug	1200	WGAJ0534.9-6439	ESO 3.6 m	1999 Mar	900
WGAJ0216.6-7331	ESO 3.6 m	1996 Dec	1200	WGAJ0535.1-0239	ESO 2.2 m	1996 Dec	1200
WGAJ0217.7-7347	ESO 3.6 m	1996 Dec	600	WGAJ0539.0-3427	ESO 2.2 m	1996 Dec	1800
WGAJ0227.5-0847	ESO 3.6 m	1998 Sep	900	WGAJ0544.1-2241	KPNO 2.1 m	1996 Dec	1200
WGAJ0245.2+1047	MMT	1996 Dec	900	WGAJ0546.6-6415	CTIO 1.5 m	1997 Jan	1800
WGAJ0247.9+1845	ESO 3.6 m	2000 Aug	1200	WGAJ0558.1+5328	KPNO 2.1 m	1996 Dec	1200
WGAJ0251.9-2051	ESO 3.6 m	1999 Mar	600	WGAJ0600.5-3937	ESO 2.2 m	1996 Dec	1200
WGAJ0253.3+0006	VLT	2000 Dec	1800	WGAJ0605.8-7556	VLT	2000 Nov	2400
WGAJ0258.5-5051	VLT	1999 Sep	2700	WGAJ0624.7-3229	CTIO 1.5 m	1997 Jan	2400
WGAJ0259.4+1926	ESO 3.6 m	2000 Aug	1200	WGAJ0628.4-3208	ESO 3.6 m	1996 Dec	360
WGAJ0304.9+0002	MMT	1996 Dec	1120	WGAJ0631.9-5404	CTIO 1.5 m	1997 Jan	1200
WGAJ0305.3-2420	KPNO 4 m	1999 Feb	600	WGAJ0633.1-2333	ESO 3.6 m	1996 Dec	1200
WGAJ0307.7-4717	ESO 3.6 m	1999 Mar	2700	WGAJ0646.8+6807	KPNO 4 m	1999 Feb	2400
WGAJ0312.3-6610	ESO 3.6 m	2000 Aug	1800	WGAJ0648.2-4347	ESO 2.2 m	1996 Dec	1200
WGAJ0313.9+4115	KPNO 2.1 m	1996 Dec	1200	WGAJ0651.9+6955	KPNO 4 m	1999 Feb	1800
WGAJ0314.4-6548	CTIO 1.5 m	1997 Jan	3600	WGAJ0724.3-0715	CTIO 1.5 m	1997 Jan	2400
WGAJ0321.6-6641	ESO 3.6 m	2000 Aug	1200	WGAJ0741.7-5304	ESO 3.6 m	1999 Mar	3600
WGAJ0322.1-5205	ESO 3.6 m	1998 Feb	300	WGAJ0744.8+2920	CTIO 1.5 m	1997 Jan	600
WGAJ0322.2-5042	ESO 2.2 m	1996 Dec	1200	WGAJ0747.0-6744	ESO 3.6 m	1999 Mar	1800
WGAJ0322.6-1335	ESO 3.6 m	1998 Feb	2400	WGAJ0748.2-5257	ESO 2.2 m	1996 Dec	1200
WGAJ0324.9-2140	ESO 2.2 m	1996 Dec	600	WGAJ0750.9-6726	ESO 2.2 m	1996 Dec	900
WGAJ0325.0-4926	ESO 2.2 m	1996 Dec	1200	WGAJ0816.0-0736	ESO 2.2 m	1996 Dec	900
WGAJ0340.8-1814	ESO 3.6 m	1996 Dec	1500	WGAJ0829.5+0858	ESO 3.6 m	1998 Feb	1800
WGAJ0343.6-1141	VLT	2000 Dec	2700	WGAJ0847.2+1133	ESO 2.2 m	1997 May	900
WGAJ0355.6-1026	VLT	1999 Sep	4800	WGAJ0853.0+2004	ESO 3.6 m	1998 Feb	300

Name	Observatory	Date	Exp [sec]	Name	Observatory	Date	Exp [sec]
(1)	(2)	(3)	(4)	(1)	(2)	(3)	(4)
WGAJ0900.2-2817	ESO 3.6 m	1996 Dec	900	WGAJ1337.2-1319	ESO 2.2 m	1997 May	1500
WGAJ0908.2+5031	KPNO 4 m	1999 Feb	1200	WGAJ1353.2-4720	ESO 3.6 m	1999 Mar	1200
WGAJ0927.7-0900	KPNO 4 m	1999 Feb	1800	WGAJ1359.6+4010	KPNO 2.1 m	1998 Jun	1200
WGAJ0931.9+5533	KPNO 4 m	1999 Feb	1200	WGAJ1400.7+0425	ESO 3.6 m	1998 Feb	900
WGAJ0937.1+5008	KPNO 4 m	1999 Feb	600	WGAJ1402.7-3334	ESO 3.6 m	1998 Feb	1800
WGAJ0940.2+2603	KPNO 2.1 m	1996 Dec	2400	WGAJ1404.2+3413	KPNO 4 m	1999 Feb	1200
WGAJ0954.4-0503	VLT	2000 Dec	2700	WGAJ1406.9+3433	KPNO 2.1 m	1998 Jun	1200
WGAJ1003.9+3244	KPNO 2.1 m	1996 Dec	3600	WGAJ1416.4+1242	ESO 2.2 m	1997 May	900
WGAJ1006.1+3236	ESO 2.2 m	1997 May	900	WGAJ1417.2+0608	ESO 3.6 m	2000 Aug	600
WGAJ1006.5+0509	ESO 2.2 m	1997 May	1800	WGAJ1417.5+2645	ESO 2.2 m	1997 May	1800
WGAJ1006.7-2014	VLT	1999 May	2700	WGAJ1419.1+0603	ESO 2.2 m	1997 May	1800
WGAJ1010.8-0201	ESO 3.6 m	1998 Feb	900	WGAJ1420.6+0650	ESO 2.2 m	1997 May	900
WGAJ1011.5-0423	ESO 2.2 m	1996 Dec	1200	WGAJ1423.3+4830	KPNO 2.1 m	1998 Jun	2400
WGAJ1025.9+1253	KPNO 2.1 m	1996 Dec	3600	WGAJ1427.9+3247	KPNO 4 m	1999 Feb	1200
WGAJ1026.4+6746	KPNO 4 m	1999 Feb	1200	WGAJ1442.3+5236	KPNO 2.1 m	1998 Jun	2700
WGAJ1028.5-0236	ESO 3.6 m	1998 Feb	1200	WGAJ1457.7-2818	ESO 2.2 m	1997 May	1200
WGAJ1028.6-0336	ESO 3.6 m	1999 Mar	1200	WGAJ1457.9-2124	ESO 3.6 m	1998 Feb	1200
WGAJ1032.1-1400	CTIO 1.5 m	1997 Jan	2400	WGAJ1506.6-4008	ESO 2.2 m	1997 May	900
WGAJ1035.0+5652	KPNO 2.1 m	1996 Dec	3600	WGAJ1507.9+6214	KPNO 4 m	1999 Feb	1200
WGAJ1046.3+5354	KPNO 2.1 m	1996 Dec	2400	WGAJ1509.5-4340	ESO 2.2 m	1997 May	1800
WGAJ1056.9-7649	ESO 2.2 m	1997 May	2100	WGAJ1525.3+4201	Lick 3 m	1995 Jun	300
WGAJ1057.6-7724	ESO 3.6 m	1999 Mar	1200	WGAJ1539.1-0658	ESO 3.6 m	1998 Feb	900
WGAJ1101.8+6241	KPNO 4 m	1999 Feb	1200	WGAJ1543.6+1847	ESO 2.2 m	1997 May	1200
WGAJ1104.8+6038	KPNO 2.1 m	1996 Dec	2400	WGAJ1606.0+2031	KPNO 2.1 m	1998 Jun	1800
WGAJ1105.3-1813	ESO 2.2 m	1997 May	1200	WGAJ1610.3-3958	ESO 2.2 m	1997 May	1500
WGAJ1112.5-3745	ESO 2.2 m	1996 Dec	900	WGAJ1615.2-0540	VLT	1999 Aug	2400
WGAJ1116.1+0828	ESO 2.2 m	1997 May	1200	WGAJ1626.6+5809	KPNO 2.1 m	1998 Jun	1200
WGAJ1120.4+5855	KPNO 4 m	1999 Feb	600	WGAJ1629.7+2117	ESO 2.2 m	1997 May	1800
WGAJ1150.4+0156	ESO 3.6 m	1996 Dec	300	WGAJ1648.4+4104	KPNO 2.1 m	1998 Jun	2700
WGAJ1204.2-0710	KPNO 2.1 m	1998 Jun	1200	WGAJ1656.6+5321	KPNO 4 m	1999 Feb	900
WGAJ1206.2+2823	ESO 2.2 m	1997 May	1200	WGAJ1656.6+6012	KPNO 2.1 m	1998 Jun	2400
WGAJ1213.0+3248	ESO 2.2 m	1997 May	1200	WGAJ1722.3+3103	KPNO 2.1 m	1998 Jun	2400
WGAJ1213.2+1443	ESO 2.2 m	1997 May	1200	WGAJ1738.6-5333	ESO 2.2 m	1997 May	1200
WGAJ1217.1+2925	ESO 2.2 m	1997 May	1200	WGAJ1744.3-0517	VLT	1999 Jul	1200
WGAJ1222.6+2934	KPNO 4 m	1999 Feb	1200	WGAJ1804.7+1755	ESO 3.6 m	1998 Sep	600
WGAJ1223.9+0650	ESO 2.2 m	1997 May	1800	WGAJ1808.2-5011	ESO 3.6 m	1999 Mar	1800
WGAJ1225.5+0715	ESO 3.6 m	1998 Feb	1200	WGAJ1826.1-3650	ESO 3.6 m	1998 Sep	3600
WGAJ1229.4+2711	KPNO 4 m	1999 Feb	1200	WGAJ1827.1-4533	ESO 3.6 m	1998 Sep	1200
WGAJ1231.7+2848	CTIO 1.5 m	1997 Jan	1200	WGAJ1834.2-5948	VLT	2000 Nov	1800
WGAJ1259.9+1206	ESO 3.6 m	2001 Jul	3600	WGAJ1834.4-5856	ESO 3.6 m	1999 Mar	1800
WGAJ1300.7-3253	CTIO 1.5 m	1997 Jan	1800	WGAJ1835.5-6539	VLT	1999 Jun	1800
WGAJ1306.6-2428	VLT	2001 Feb	2400	WGAJ1837.7-5848	ESO 2.2 m	1997 May	1800
WGAJ1311.3-0521	ESO 3.6 m	1999 Mar	900	WGAJ1840.9+5452	KPNO 2.1 m	1998 Jun	2700
WGAJ1314.0-3304	ESO 2.2 m	1997 May	900	WGAJ1843.4-7430	ESO 3.6 m	2001 Jul	2400
WGAJ1315.1+2841	KPNO 4 m	1999 Feb	2700	WGAJ1911.8-2102	ESO 3.6 m	1999 Mar	1800
WGAJ1320.4+0140	ESO 3.6 m	1999 Mar	1200	WGAJ1936.8-4719	ESO 3.6 m	2000 Aug	1200
WGAJ1324.0-3623	CTIO 1.5 m	1997 Jan	1200	WGAJ1938.4-4657	VLT	2001 Mar	1800
WGAJ1329.0+5009	KPNO 4 m	1999 Feb	1800	WGAJ2056.4-5819	ESO 3.6 m	2000 Aug	600
WGAJ1332.7+4722	KPNO 2.1 m	1998 Jun	2400	WGAJ2109.7-1332	KPNO 2.1 m	1998 Jun	1800
WGAJ1333.1-3323	ESO 3.6 m	1999 Mar	1800	WGAJ2131.9-0556	ESO 3.6 m	2000 Aug	300

Name	Observatory	Date	Exp [sec]	Name	Observatory	Date	Exp [sec]
(1)	(2)	(3)	(4)	(1)	(2)	(3)	(4)
WGAJ2151.3-4233	ESO 2.2 m	1997 May	900	WGAJ2317.4-4213	ESO 3.6 m	1996 Dec	480
WGAJ2154.1-1501	ESO 2.2 m	1997 May	600	WGAJ2320.6+0032	ESO 3.6 m	1999 Aug	900
WGAJ2157.7+0650	ESO 3.6 m	2000 Aug	1800	WGAJ2322.0+2114	KPNO 2.1 m	1996 Dec	1200
WGAJ2159.3-1500	ESO 2.2 m	1997 May	600	WGAJ2322.5-4221	ESO 3.6 m	2001 Jul	600
WGAJ2201.6-5646	ESO 2.2 m	1997 May	1200	WGAJ2329.0+0834	ESO 3.6 m	1998 Sep	1800
WGAJ2205.2-0004	VLT	1999 Aug	1800	WGAJ2330.6-3724	ESO 3.6 m	2000 Aug	900
WGAJ2239.7-0631	ESO 3.6 m	1999 Aug	600	WGAJ2333.2-0131	ESO 3.6 m	1996 Dec	900
WGAJ2248.6-2702	ESO 3.6 m	2000 Aug	3600	WGAJ2347.6+0852	KPNO 2.1 m	1996 Dec	1200
WGAJ2258.3-5525	ESO 2.2 m	1997 May	1200	WGAJ2349.9-2552	ESO 3.6 m	2000 Aug	1200
WGAJ2303.5-5126	ESO 3.6 m	2000 Aug	600	WGAJ2354.2-0957	VLT	1999 Aug	1200
WGAJ2304.8-3624	VLT	2001 Jul	1800	WGAJ2356.4-3223	VLT	2001 Jul	5400

Appendix C

Classifications and Redshifts

The following tables give the radio, optical and X-ray fluxes, radio spectral index, classification, and redshift for the DXRBS sources. The first table includes the objects previously known (108 sources). The second table includes the objects previously unclassified and meeting all DXRBS selection criteria (211 objects). These form together with the previously known sources the complete sample (319 sources). The third table includes objects previously unclassified that do not meet all DXRBS selection criteria (22 low priority sources). A number of DXRBS sources were serendipitously observed by *ROSAT* on more than one occasion. For completeness, the information for all observations is given.

The columns of the tables are as follows:

(1): WGACAT name of the source; (2): *ROSAT* count rate; (3): 0.1 - 2.0 keV X-ray flux (not corrected for galactic extinction); (4): unabsorbed X-ray flux at 1 keV (both X-ray fluxes have been derived from the *ROSAT* count rates using the observed hardness ratio and assuming galactic N_{H}); (5): ratio between the 0.3 – 3.5 keV X-ray flux and the radio flux at 6 cm; (6): radio flux at 6 cm; (7): radio spectral index (a footnote is given for sources with $\Delta\alpha = \alpha_{\text{ATCA}} - \alpha_{\text{PMN-NVSS}} \gtrsim 0.6$, which are possibly Gigahertz peaked-spectrum (GPS) sources (e.g. O’Dea, 1998), and for sources with $\alpha_{\text{ATCA}} > 0.7$). In Table I (8): V magnitude; (9) classification and (10) redshift from the AGN catalogue of Padovani et al. (1997). In Tables II and III: (8): B_j magnitude from COSMOS; (9): O magnitude from APM; (10): E magnitude from APM; (11): current classification; (12): redshift. For most of the faint objects the magnitude comes from other sources and a footnote is given. The redshift was computed, whenever possible, by taking the mean of the values derived from the narrow lines. Where only a single (broad) emission line was observed, it was assumed to be Mg II $\lambda 2798 \text{ \AA}$.

I. DXRBS Previously Known Sources

Name	ROSAT counts	$f_{0.1-2.0\text{keV}}$ [erg/s/cm ²]	$f_{1\text{keV}}$ [μJy]	\log f_x/f_r	$f_{6\text{cm}}$ [mJy]	α_r	V	Class	z
(1)	(2)	(3)	(4)	(5)	(6)	(7)	(8)	(9)	(10)
B2 0834+25	0.035	4.08e-13	0.108	-11.94	458	0.14	18.0	FSRQ	1.122
B2 1048+34	0.011	8.63e-14	0.015	-12.56	312	0.44	19.0	FSRQ	2.520
B2 1147+24	0.017	1.52e-13	0.022	-12.72	645	-0.02	6.2	BL Lac	...
B2 1211+33	0.039	2.47e-13	0.041	-12.44	627	0.54	17.9	SSRQ	1.598
B2 1215+33	0.007	4.88e-14	0.004	-12.67	117	0.46	18.1	FSRQ	2.605
B2 1422+26B	0.045	4.72e-13	0.084	-11.93	367	0.55	17.6	RG	0.037
B2 1506+33A	0.007	5.53e-14	0.005	-12.57	115	0.14	18.5	FSRQ	2.200
B3 0923+398	0.010	7.41e-14	0.008	-12.27	92	0.42	19.5	RG	0.392
DW 1211+13	0.011	9.83e-14	0.023	-12.89	894	0.42	18.1	FSRQ	1.137
EXO 0556.4-3838	0.956	1.15e-11	3.005	- 9.73	68	0.29	17.1	BL Lac	...
EXO 1811.7+3143	0.036	4.77e-13	0.090	-11.45	127	0.17	17.4	BL Lac	0.117
GB 1231+482	0.140	8.65e-13	0.036	-11.93	268	0.27	17.4	FSRQ	0.375
GB 1428+4217	0.031	3.00e-13	0.040	-12.18	337	0.13	22.5	FSRQ	4.715
HBQS 0050-28	0.014	1.13e-13	0.018	-12.26	179	0.18	18.3	FSRQ	1.650
I 0115	0.005	6.52e-14	0.019	-12.82	671	0.64	14.0	RG	0.043
MC 1524+101	0.024	2.37e-13	0.043	-12.15	316	0.26	19.0	FSRQ	1.358
MH 2136-428	0.120	9.66e-13	0.113	-11.17	108	-0.13	16.2	BL Lac	...
MS 02255-105	0.029	3.08e-13	0.050	-11.35	58	0.65	19.3	SSRQ	1.038
MS 14428+634	0.022	1.71e-13	0.030	-12.43	442	0.36	17.2	FSRQ	1.380
NGC 5232	0.010	1.06e-13	0.020	-12.72	529	-0.09	13.0	RG	0.021
NGC 6061	0.048	5.25e-13	0.105	-11.71	258	0.61	13.6	RG	0.038
OJ 297	0.004	5.80e-14	0.022	-13.40	2216	-0.17	16.6	FSRQ	2.160
ON 325	0.382	2.72e-12	0.270	-11.44	478	0.09	15.6	BL Lac	0.237
OS 319	0.103	1.17e-12	0.220	-12.31	2324	0.18	17.5	FSRQ	1.401
OY 106	0.008	7.15e-14	0.016	-13.73	4271	0.36	19.5	FSRQ	0.618
PKS 0027-426	0.046	5.52e-13	0.144	-11.80	419	0.00	19.0	FSRQ	1.660
PKS 0035+23	0.012	1.60e-13	0.032	-12.49	463	0.54	19.0	SSRQ	2.270
PKS 0041+007	0.009	1.06e-13	0.029	-12.02	152	0.58	16.5	RG	0.112
PKS 0100-270	0.030	2.74e-13	0.045	-11.92	201	0.42	18.1	FSRQ	1.597
PKS 0142-278	0.050	5.64e-13	0.139	-12.01	833	-0.03	19.0	FSRQ	1.157
PKS 0234-301	0.022	1.96e-13	0.044	-12.32	470	-0.19	17.7	FSRQ	2.102
PKS 0247-207	0.029	3.29e-13	0.092	-11.90	389	0.54	15.5	RG	0.087
PKS 0256-005	0.023	3.42e-13	0.102	-12.04	500	-0.59	17.2	FSRQ	1.995
PKS 0335-364	0.048	4.88e-13	0.070	-12.19	583	-0.39	18.0	FSRQ	1.537
PKS 0406-127	0.013	1.32e-13	0.021	-12.63	517	0.22	19.0	FSRQ	1.563
PKS 0422-380	0.064	6.74e-13	0.105	-12.49	1706	-2.06	18.1	FSRQ	0.782
PKS 0439-433	0.100	1.00e-12	0.156	-11.53	285	0.19	16.4	FSRQ	0.593
PKS 1240-294	0.042	5.92e-13	0.166	-11.83	472	0.31	17.7	FSRQ	1.133
PKS 1324-300	0.031	3.98e-13	0.097	-11.96	406	0.59	18.0	RG	0.200
PKS 1937-101	0.029	4.64e-13	0.177	-12.15	750	0.09	17.0	FSRQ	3.787
PKS 2058-425	0.097	9.96e-13	0.200	-11.86	721	0.56	17.2	SSRQ	0.221
PKS 2059+034	0.041	6.47e-13	0.213	-12.22	1362	-0.72	17.8	FSRQ	1.013
PKS 2212-299	0.032	2.10e-13	0.022	-12.54	450	0.30	17.4	FSRQ	2.706
PKS 2316-423	0.207	1.70e-12	0.337	-11.52	595	0.43	14.5	BL Lac	0.055
PKS 2319+07	0.013	1.86e-13	0.047	-12.63	857	0.18	18.5	FSRQ	2.090
PKS 2329-384	0.019	1.90e-13	0.048	-12.47	784	-0.05	17.0	FSRQ	1.195
PKS 2352-342	0.182	1.20e-12	0.114	-11.53	241	0.62	16.4	SSRQ	0.702
PKS 2357-318	0.037	3.22e-13	0.085	-12.19	747	-1.62	17.6	FSRQ	0.991

Name	ROSAT counts	$f_{0.1-2.0\text{keV}}$ [erg/s/cm ²]	$f_{1\text{keV}}$ [μJy]	log f_x/f_r	$f_{6\text{cm}}$ [mJy]	α_r	V	Class	z
(1)	(2)	(3)	(4)	(5)	(6)	(7)	(8)	(9)	(10)
PKS 2357-326	0.007	4.11e-14	0.003	-13.37	535	0.02	18.7	FSRQ	1.275
PMN J0630-24	0.060	9.72e-13	0.322	-11.05	130	-0.16	15.9	BL Lac	...
PMN J1218+05	0.073	7.95e-13	0.129	-11.60	271	0.63	14.0	RG	0.075
RGB J1715+36	0.011	1.33e-13	0.021	-11.91	93	0.23	20.7	FSRQ	0.555
RRSIV4	0.027	1.85e-13	0.021	-12.44	347	-0.29	19.0	FSRQ	1.185
RX J09168+523	0.252	2.23e-12	0.360	-10.55	69	0.58	18.9	BL Lac	0.190
RX J12368+25	0.083	8.08e-13	0.102	-11.26	109	0.54	17.6	SSRQ	0.546
S4 0024+34	0.025	3.34e-13	0.091	-12.09	463	0.47	18.0	RG	0.333
S4 0206+355	0.022	3.06e-13	0.086	-12.39	976	0.68	13.0	RG	0.037
S4 0537+531	0.007	8.26e-14	0.040	-12.82	668	-0.02	18.0	FSRQ	1.275
S4 0847+37	0.066	9.11e-13	0.235	-11.52	391	0.37	19.5	RG	0.407
S4 0955+476	0.036	3.44e-13	0.028	-12.77	1005	-0.32	18.0	FSRQ	1.873
S4 1656+34	0.035	3.24e-13	0.096	-11.95	474	0.06	17.4	FSRQ	1.936
S4 1656+571	0.021	1.98e-13	0.037	-12.61	764	0.04	17.6	FSRQ	1.293
S4 1806+456	0.027	3.04e-13	0.077	-11.99	351	-0.68	19.0	FSRQ	0.830
S5 0743+74	0.009	1.23e-13	0.034	-12.45	445	-0.19	19.3	FSRQ	1.629
S5 0916+718	0.026	3.64e-13	0.094	-11.78	295	0.22	19.5	FSRQ	0.594
S5 1027+74	0.066	8.42e-13	0.223	-11.38	250	0.19	17.2	FSRQ	0.123
TEX 0109+200	0.017	2.38e-13	0.058	-12.01	281	0.31	17.0	FSRQ	0.746
TEX 0237+185	0.017	2.54e-13	0.084	-12.14	446	-0.05	18.7	FSRQ	1.297
TEX 0836+182	0.031	2.61e-13	0.033	-12.21	310	0.17	17.0	BL Lac	...
TEX 1235-117	0.075	9.15e-13	0.210	-10.95	87	0.25	17.7	FSRQ	1.320
UM 320	0.010	1.15e-13	0.031	-12.22	259	0.13	18.6	FSRQ	2.280
UM 416	0.016	1.91e-13	0.043	-11.80	134	0.04	18.0	FSRQ	1.490
WGA 1012+06	0.021	2.07e-13	0.055	-12.03	300	0.45	16.8	BL Lac	...
WGA 1202+44	0.210	1.26e-12	0.112	-10.98	69	1.43	18.1	BL Lac	...
1ES 1212+078	0.506	5.42e-12	0.945	-10.37	117	-0.04	16.0	BL Lac	0.130
1Jy 0112-017	0.026	3.64e-13	0.092	-12.56	1540	-0.48	17.4	FSRQ	1.381
1Jy 0119+041	0.024	2.61e-13	0.050	-12.70	1235	-0.24	19.5	FSRQ	0.637
1Jy 0122-003	0.066	7.62e-13	0.200	-12.11	1234	0.09	16.7	FSRQ	1.070
1Jy 0514-459	0.067	8.40e-13	0.160	-12.10	990	0.44	17.5	FSRQ	0.194
1Jy 0839+187	0.051	5.38e-13	0.104	-12.23	898	0.24	16.4	FSRQ	1.272
1Jy 0850+581	0.023	2.80e-13	0.071	-12.51	1184	0.15	18.0	FSRQ	1.322
1Jy 0859+470	0.032	2.68e-13	0.044	-12.73	1264	0.48	18.7	FSRQ	1.462
1Jy 1145-071	0.031	3.74e-13	0.093	-12.27	791	-0.22	18.0	FSRQ	1.342
1Jy 1255-316	0.019	2.26e-13	0.061	-12.74	1410	0.09	18.7	FSRQ	1.924
1Jy 1435+638	0.078	8.85e-13	0.130	-12.02	757	0.51	16.1	SSRQ	2.068
1Jy 1502+106	0.023	2.19e-13	0.032	-13.14	2325	-0.33	18.6	FSRQ	0.563
1Jy 1637+574	0.105	1.02e-12	0.188	-12.24	1750	-0.29	17.0	FSRQ	0.750
1Jy 1638+398	0.028	2.59e-13	0.050	-12.61	1117	-0.44	16.5	FSRQ	1.666
1Jy 1725+044	0.049	6.95e-13	0.178	-12.07	885	-0.44	17.0	FSRQ	0.293
1Jy 2344+092	0.085	1.27e-12	0.359	-11.97	1392	0.32	16.0	FSRQ	0.673
3C 345	0.317	3.55e-12	0.753	-12.31	8719	-0.08	16.0	FSRQ	0.594
4C 19.34	0.103	1.19e-12	0.279	-11.75	765	-0.11	17.5	FSRQ	0.828
4C 38.41	0.100	1.03e-12	0.148	-12.61	3221	-0.44	18.0	FSRQ	1.814
4C 45.34	0.042	5.45e-13	0.169	-11.65	461	0.70	17.4	SSRQ	0.646
4C +47.44	0.032	3.23e-13	0.087	-12.43	1244	-0.22	17.5	FSRQ	0.740
4C 50.47	0.023	3.75e-13	0.112	-11.93	345	0.53	17.9	SSRQ	1.098
4C 55.17	0.076	4.60e-13	0.034	-12.94	2015	0.33	16.5	BL Lac	0.909
4C +66.16	0.047	5.40e-13	0.151	-11.41	217	0.64	17.3	SSRQ	0.629

Name	ROSAT counts	$f_{0.1-2.0\text{keV}}$ [erg/s/cm ²]	$f_{1\text{keV}}$ [μJy]	log f_x/f_r	$f_{6\text{cm}}$ [mJy]	α_r	V	Class	z
(1)	(2)	(3)	(4)	(5)	(6)	(7)	(8)	(9)	(10)
4C 72.16	0.034	4.86e-13	0.130	-12.03	858	0.44	17.9	FSRQ	1.460
5C 02.56	0.004	3.23e-14	0.006	-12.52	100	0.50	20.0	FSRQ	2.396
7C 1159+2813	0.043	3.44e-13	0.036	-11.70	107	0.16	20.5	FSRQ	0.672
7C 1555+3538	0.226	2.84e-12	0.547	-10.44	80	0.68	14.7	RG	0.158
7C 1753+6543	0.020	2.25e-13	0.046	-11.92	186	0.61	17.4	SSRQ	0.140
0822+27W1	0.054	6.38e-13	0.155	-11.31	150	-0.03	17.7	FSRQ	2.060
0959+68W1	0.029	4.19e-13	0.114	-11.18	86	0.41	15.9	FSRQ	0.773
1104+72W1	0.008	9.91e-14	0.026	-12.26	271	0.30	18.9	FSRQ	2.100
1308+328	0.014	1.22e-13	0.027	-12.76	870	-0.62	19.5	FSRQ	1.650
1601+1720	0.032	3.77e-13	0.077	-11.95	343	0.58	13.5	RG	0.034

II. DXRBS Complete Sample

Name	ROSAT counts	$f_{0.1-2.0\text{keV}}$ [erg/s/cm ²]	$f_{1\text{keV}}$ [μJy]	log f_x/f_r	$f_{6\text{cm}}$ [mJy]	α_r	B_j	O	E	Class	z
(1)	(2)	(3)	(4)	(5)	(6)	(7)	(8)	(9)	(10)	(11)	(12)
WGAJ0010.5-3027	0.022	0.14e-12	0.011	-12.72	391	-0.15	19.1	19.5	18.8	FSRQ	1.190
WGAJ0010.7-3649	0.012	0.77e-13	0.006	-12.25	73	0.15	18.0	18.3	18.2	FSRQ	2.080
WGAJ0011.2-3620	0.002	0.17e-13	0.003	-12.73	96	-0.29	22.4	21.9	21.3 ^d	FSRQ	2.324
WGAJ0012.5-1629	0.097	0.13e-11	0.292	-10.53	50	0.50 ^k	17.6	15.0	14.4	FSRQ	0.151
	0.123	0.18e-11	0.374	-10.42							
WGAJ0014.5-3059	0.015	0.13e-12	0.022	-12.08	140	0.25		19.7	18.9	FSRQ	2.785
WGAJ0015.5+3052	0.019	0.28e-12	0.083	-11.38	89	0.62		17.2	16.3	SSRQ	1.619
	0.023	0.32e-12	0.095	-11.35							
WGAJ0023.6+0417	0.006	0.64e-13	0.015	-12.07	91	0.65		21.2	18.9	BL Lac	0.100
WGAJ0029.0+0509	0.006	0.63e-13	0.014	-12.71	377	0.00		19.3	18.1	FSRQ	1.633
WGAJ0032.5-2648	0.015	0.11e-12	0.028	-11.67	71	0.50 ^l	18.3			FSRQ	1.467
WGAJ0032.5-2849	0.016	0.18e-12	0.047	-11.74	146	0.08	18.9	17.7	16.7	BL Lac	0.324
WGAJ0034.4-2133	0.003	0.26e-13	0.009	-12.17	82	0.56 ^m			22.9 ^a	SSRQ	0.764
WGAJ0040.4-2340	0.008	0.61e-13	0.009	-12.00	48	0.09	19.1	17.8	16.3	BL Lac	0.213
WGAJ0043.3-2638	0.054	0.40e-12	0.062	-11.37	81	-0.03	17.3	17.6	17.3	BL Lac	1.002
WGAJ0049.5-2509	0.007	0.58e-13	0.013	-11.98	68	0.27		23.8 ^a		FSRQ	1.472
WGAJ0057.3-2212	0.007	0.49e-13	0.004	-12.40	70	0.29		>23.0	20.6	FSRQ	2.140
	0.007	0.66e-13	0.013	-12.00							
	0.007	0.58e-13	0.016	-11.89							
WGAJ0100.1-3337	0.008	0.62e-13	0.010	-12.39	127	-0.42	20.2			BL Lac	0.875
WGAJ0106.7-1034	0.039	0.44e-12	0.091	-11.63	188	0.35	17.0	17.7	17.7	FSRQ	0.469
WGAJ0110.5-1647	0.161	0.12e-11	0.176	-10.87	72	0.35	15.6	15.9	16.2	FSRQ	0.781
WGAJ0125.0+0146	0.016	0.19e-12	0.046	-11.65	95	0.59	19.8	19.6	19.0	SSRQ	1.559
WGAJ0126.2-0500	0.027	0.31e-12	0.076	-11.19	54	0.21	18.3			FSRQ	0.411
WGAJ0136.0-4044	0.017	0.16e-12	0.039	-11.84	137	-0.54	20.7	21.2	20.1	FSRQ	0.649
WGAJ0143.2-6813	0.006	0.54e-13	0.002	-12.37	51	0.10	21.2	21.6	20.0	FSRQ	1.223
WGAJ0146.2+0223	0.016	0.15e-12	0.020	-11.95	104	0.46	21.1	20.0	19.5	FSRQ	2.048

Name	ROSAT counts	$f_{0.1-2.0\text{keV}}$ [erg/s/cm ²]	$f_{1\text{keV}}$ [μJy]	log f_x/f_r	$f_{6\text{cm}}$ [mJy]	α_r	B_j	O	E	Class	z
(1)	(2)	(3)	(4)	(5)	(6)	(7)	(8)	(9)	(10)	(11)	(12)
WGAJ0152.5-1413	0.040	0.36e-12	0.047	-12.23	445	0.41	19.8	19.6	19.6	FSRQ	1.350
WGAJ0154.4-1346	0.005	0.43e-13	0.004	-12.55	82	-0.08		>23.0		FSRQ	1.010
WGAJ0204.8+1514	0.020	0.26e-12	0.077	-12.94	3073	0.32			21.3 ^f	RG	0.833
WGAJ0208.1-3858	0.020	0.17e-12	0.026	-11.65	64	0.57	17.2			RG	0.100
WGAJ0210.0-1004	0.006	0.68e-13	0.015	-12.50	244	0.45		19.7	19.5	FSRQ	1.976
WGAJ0210.1-3851	0.010	0.70e-13	0.006	-12.16	58	-0.02	20.5			FSRQ	1.877
WGAJ0211.9-7351	0.005	0.54e-13	0.016	-11.48	23	0.59		19.8	19.1	SSRQ	0.789
WGAJ0216.6-7331	0.006	0.59e-13	0.013	-11.98	62	0.21		20.0	19.7	FSRQ	2.679
WGAJ0217.7-7347	0.013	0.15e-12	0.039	-11.87	143	0.36		20.7	20.2	FSRQ	1.234
	0.002	0.17e-13	0.005	-12.84							
WGAJ0227.5-0847	0.019	0.22e-12	0.051	-11.69	115	-0.34 ^z	17.3			FSRQ	2.228
WGAJ0230.0-1031	0.016	0.18e-12	0.047	-11.34	53	0.08	18.0			FSRQ	1.135
WGAJ0245.2+1047	0.053	0.78e-12	0.262	-11.24	217	0.55		15.7		BL Lac	0.070
WGAJ0251.9-2051	0.015	0.13e-12	0.037	-11.45	53	0.65 ⁿ	18.5			SSRQ	0.761
WGAJ0253.3+0006	0.006	0.72e-13	0.023	-12.19	158	-0.17			22.4 ^c	FSRQ	1.339
WGAJ0258.5-5051	0.016	0.15e-12	0.038	-12.37	452	0.24	24.2		22.5 ^d	FSRQ	0.834
	0.029	0.36e-12	0.076	-12.07							
WGAJ0259.4+1926	0.016	0.28e-12	0.089	-11.76	159	0.16		19.0	18.6	FSRQ	0.544
WGAJ0304.9+0002	0.026	0.40e-12	0.121	-11.14	75	0.40 ^o		17.8	18.4	FSRQ	0.563
WGAJ0305.3-2420	0.013	0.10e-12	0.008	-12.25	102	-0.15	18.8	17.9	16.7	RG	0.211
WGAJ0307.7-4717	0.024	0.22e-12	0.042	-11.76	123	0.70	23.2			SSRQ	0.599
WGAJ0312.3-6610	0.016	0.16e-12	0.036	-11.50	56	0.40	19.8			FSRQ	1.384
WGAJ0314.4-6548	0.023	0.24e-12	0.021	-12.07	179	0.11	19.0			FSRQ	0.636
	0.083	0.96e-12	0.208	-11.26							
WGAJ0321.6-6641	0.010	0.11e-12	0.010	-11.75	40	0.54	20.4			SSRQ	0.546
	0.018	0.18e-12	0.009	-11.64							
WGAJ0322.1-5205	0.156	0.12e-11	0.262	-10.48	40	-0.27	16.8			FSRQ	0.416
WGAJ0322.2-5042	0.025	0.26e-12	0.057	-11.45	78	-0.66	18.2			FSRQ	0.651
WGAJ0322.6-1335	0.004	0.47e-13	0.008	-12.58	164	0.38		22.0 ^a		FSRQ	1.468
WGAJ0324.9-2140	0.014	0.11e-12	0.007	-12.03	59	0.41	17.8	18.1	17.5	FSRQ	2.828
WGAJ0325.0-4926	0.023	0.19e-12	0.027	-11.64	67	0.89	18.9			SSRQ	0.259
	0.018	0.16e-12	0.039	-11.54							
	0.089	0.72e-12	0.112	-11.03							
WGAJ0340.4-2234	0.027	0.23e-12	0.027	-11.51	52	0.51	17.7			SSRQ	1.680
WGAJ0340.8-1814	0.002	0.31e-13	0.005	-12.75	148	0.56 ^p	19.6	18.8	16.7	RG	0.195
WGAJ0343.6-1141	0.003	0.29e-13	0.008	-12.11	46	0.21		>22.5	22.7 ^a	FSRQ	2.259
WGAJ0355.6-1026	0.008	0.72e-13	0.013	-11.90	57	0.68 ^q		>22.0	23.0 ^a	SSRQ	0.965
WGAJ0357.6-4158	0.012	0.11e-12	0.024	-11.99	118	0.19	20.9	20.3	19.6	FSRQ	1.271
WGAJ0411.0-1637	0.034	0.39e-12	0.087	-11.45	124	0.31	16.4	17.1	17.2	FSRQ	0.622
WGAJ0414.0-1224	0.021	0.25e-12	0.060	-11.17	42	0.63	18.3			SSRQ	0.569
WGAJ0414.0-1307	0.007	0.79e-13	0.026	-12.01	152	0.57		22.2	20.3	SSRQ	0.463
WGAJ0421.5+1433	0.003	0.35e-13	0.017	-12.42	114	0.63		18.8	15.2	RG	0.059
WGAJ0424.6-3849	0.019	0.17e-12	0.011	-12.58	309	0.43	17.8	18.4	18.7	FSRQ	2.340
WGAJ0427.2-0756	0.012	0.14e-12	0.042	-11.52	56	0.27	21.0			FSRQ	1.375
WGAJ0428.8-3805	0.010	0.76e-13	0.004	-12.22	51	0.58 ^f	18.8	17.3	15.7	BL Lac	0.150
WGAJ0431.9+1731	0.006	0.82e-13	0.035	-12.30	300	0.30			21.3 ^c	BL Lac	0.143
	0.006	0.70e-13	0.030	-12.37							
WGAJ0434.3-1443	0.004	0.60e-13	0.009	-12.85	281	-0.25		20.2	19.8	FSRQ	1.899
WGAJ0435.1-0811	0.011	0.13e-12	0.028	-11.75	73	-0.27	21.1	21.1	19.5	FSRQ	0.791
WGAJ0438.7-4727	0.023	0.20e-12	0.041	-11.78	130	0.54	20.5	20.5	19.7	SSRQ	1.445

Name	ROSAT counts	$f_{0.1-2.0\text{keV}}$ [erg/s/cm ²]	f_{likeV} [μJy]	log f_x/f_r	$f_{6\text{cm}}$ [mJy]	α_r	B_j	O	E	Class	z
(1)	(2)	(3)	(4)	(5)	(6)	(7)	(8)	(9)	(10)	(11)	(12)
WGAJ0441.8-4306	0.041	0.43e-12	0.086	-11.47	129	-1.43			21.1 ^b	FSRQ	0.872
WGAJ0447.9-0322	0.103	0.14e-11	0.348	-10.54	56	0.47 ^s	16.0			FSRQ	0.774
WGAJ0448.2-2110	0.008	0.11e-12	0.028	-12.25	227	0.12	18.4	18.7	18.5	FSRQ	1.971
WGAJ0448.6-2203	0.019	0.25e-12	0.045	-11.56	81	0.00	18.9	19.6	19.5	FSRQ	0.496
WGAJ0500.0-3040	0.010	0.66e-13	0.017	-12.07	108	0.78	19.4			RG	0.417
WGAJ0500.9-3047	0.016	0.11e-12	0.011	-12.08	86	0.92	18.2			SSRQ	1.756
WGAJ0510.0+1800	0.027	0.34e-12	0.209	-12.23	796	0.10		20.6 ^a		FSRQ	0.416
WGAJ0518.2+0624	0.007	0.97e-13	0.037	-12.30	230	0.62		19.5 ^a		SSRQ	0.891
WGAJ0528.5-5820	0.014	0.14e-12	0.031	-11.80	99	0.70	18.7	17.8	16.7	BL Lac	0.254
WGAJ0533.6-4632	0.006	0.72e-13	0.022	-12.09	126	0.60	20.6			BL Lac	0.332
WGAJ0533.7-5817	0.009	0.11e-12	0.029	-11.68	66	0.94	17.9	18.5	18.4	SSRQ	0.757
WGAJ0534.9-6439	0.016	0.21e-12	0.057	-11.48	76	0.77	20.5			SSRQ	1.463
WGAJ0535.1-0239	0.009	0.11e-12	0.051	-11.48	42	0.10	18.7			FSRQ	1.033
WGAJ0536.4-3401	0.080	0.92e-12	0.212	-11.80	663	0.01	18.3	17.8	16.2	FSRQ	0.683
WGAJ0539.0-3427	0.014	0.18e-12	0.042	-11.95	195	0.15		21.8	19.3	FSRQ	0.263
WGAJ0544.1-2241	0.043	0.46e-12	0.085	-11.74	234	-0.44 ^{aa}	15.0			FSRQ	1.537
WGAJ0546.6-6415	0.221	0.42e-11	1.224	-10.75	287	-0.67		16.0 ^g	14.7 ^g	FSRQ	0.323
	0.341	0.58e-11	1.681	-10.57							
WGAJ0558.1+5328	0.006	0.84e-13	0.040	-12.31	234	0.59		14.4 ^g	10.9 ^g	BL Lac	0.036
WGAJ0600.5-3937	0.029	0.41e-12	0.117	-12.08	623	-0.22	18.6	18.7	19.1	FSRQ	1.661
WGAJ0624.7-3229	0.037	0.45e-12	0.137	-11.12	86	-0.53 ^{ab}	19.6			BL Lac	0.672
	0.062	0.82e-12	0.210	-10.95							
WGAJ0631.9-5404	0.141	0.23e-11	0.715	-10.76	155	0.35	18.5			FSRQ	0.193
WGAJ0633.1-2333	0.003	0.45e-13	0.017	-12.16	99	0.64	22.8			SSRQ	2.928
WGAJ0646.8+6807	0.008	0.89e-13	0.009	-12.03	72	0.56			19.7 ^c	SSRQ	0.927
WGAJ0648.2-4347	0.026	0.37e-12	0.107	-11.44	126	0.36	18.3			FSRQ	1.029
WGAJ0651.9+6955	0.017	0.21e-12	0.067	-11.67	132	0.63		20.0	19.3	SSRQ	1.367
WGAJ0741.7-5304	0.005	0.71e-13	0.024	-11.79	44	0.77	22.2			SSRQ	3.743
WGAJ0744.8+2920	0.035	0.49e-12	0.121	-11.54	179	0.40		16.4	15.9	FSRQ	1.168
	0.041	0.55e-12	0.078	-11.60							
WGAJ0747.0-6744	0.005	0.68e-13	0.023	-11.59	27	0.16	19.7			FSRQ	1.025
WGAJ0748.2-5257	0.006	0.93e-13	0.035	-12.28	230	-0.29	18.4			FSRQ	1.802
WGAJ0750.9-6726	0.011	0.16e-12	0.059	-11.45	52	0.05	17.7			FSRQ	1.237
	0.018	0.27e-12	0.101	-11.23							
	0.008	0.12e-12	0.039	-11.65							
WGAJ0829.5+0858	0.019	0.24e-12	0.058	-11.82	180	0.60		21.5 ^a		SSRQ	0.866
WGAJ0853.0+2004	0.010	0.86e-13	0.022	-11.73	60	0.60		18.2	18.0	SSRQ	1.930
	0.010	0.83e-13	0.019	-11.80							
WGAJ0900.2-2817	0.022	0.37e-12	0.139	-11.74	234	0.62 ^t	20.3			SSRQ	0.894
WGAJ0908.2+5031	0.008	0.63e-13	0.010	-12.20	86	0.59		20.8	19.6	SSRQ	0.917
WGAJ0927.7-0900	0.014	0.20e-12	0.052	-11.82	181	-0.14	21.3			FSRQ	0.254
WGAJ0931.9+5533	0.045	0.43e-12	0.105	-11.00	53	0.66		16.7	16.0	SSRQ	0.266
WGAJ0940.2+2603	0.037	0.35e-12	0.082	-11.83	292	0.05		20.9	19.2	BL Lac	...
WGAJ0954.4-0503	0.003	0.32e-13	0.009	-11.96	43	-0.07			21.0 ^c	FSRQ	0.660
WGAJ1003.9+3244	0.006	0.46e-13	0.006	-13.01	371	0.20		18.8	18.2	FSRQ	1.682
WGAJ1006.1+3236	0.052	0.43e-12	0.046	-11.91	231	0.62		18.7	18.1	SSRQ	1.020
WGAJ1006.5+0509	0.015	0.16e-12	0.037	-11.99	179	0.12		21.7		FSRQ	1.216
WGAJ1006.7-2014	0.008	0.11e-12	0.030	-11.96	152	0.56			23.0 ^a	SSRQ	1.535
WGAJ1010.8-0201	0.063	0.82e-12	0.164	-12.02	826	0.32	18.9	19.9	18.9	FSRQ	0.896
WGAJ1011.5-0423	0.006	0.64e-13	0.019	-12.22	189	-0.14	18.6			FSRQ	1.588

Name	ROSAT counts	$f_{0.1-2.0\text{keV}}$ [erg/s/cm ²]	$f_{1\text{keV}}$ [μJy]	log f_x/f_r	$f_{6\text{cm}}$ [mJy]	α_r	B_j	O	E	Class	z
(1)	(2)	(3)	(4)	(5)	(6)	(7)	(8)	(9)	(10)	(11)	(12)
WGAJ1025.9+1253	0.028	0.33e-12	0.076	-12.25	631	0.34		18.7	18.2	FSRQ	0.663
WGAJ1026.4+6746	0.034	0.38e-12	0.069	-11.55	129	0.49		16.9 ^j	17.9 ^j	FSRQ	1.181
WGAJ1028.5-0236	0.019	0.24e-12	0.068	-11.53	94	-0.06	21.9	>22.0	19.6	FSRQ	0.476
WGAJ1032.1-1400	0.012	0.14e-12	0.040	-12.12	223	-0.10		18.4	18.8	FSRQ	1.039
WGAJ1035.0+5652	0.005	0.28e-13	0.001	-13.38	205	0.24		19.8	19.1	FSRQ	0.577
WGAJ1046.3+5354	0.016	0.15e-12	0.023	-12.34	271	0.38		19.2	18.4	FSRQ	1.704
WGAJ1056.9-7649	0.019	0.34e-12	0.113	-11.38	98	0.00	20.9			RG	0.193
WGAJ1057.6-7724	0.005	0.71e-13	0.020	-12.76	431	0.71		21.4 ^a		RG	0.181
WGAJ1101.8+6241	0.070	0.46e-12	0.038	-12.46	693	0.12		17.9	17.7	FSRQ	0.663
WGAJ1104.8+6038	0.018	0.13e-12	0.015	-12.32	187	0.18		19.0	18.1	FSRQ	1.373
WGAJ1105.3-1813	0.006	0.80e-13	0.023	-11.77	59	-0.77		18.5	20.1	FSRQ	0.578
WGAJ1112.5-3745	0.023	0.36e-12	0.119	-11.47	132	-0.34	17.9			FSRQ	0.979
WGAJ1116.1+0828	0.014	0.22e-12	0.063	-11.98	282	-0.08		22.4 ^a		FSRQ	0.486
WGAJ1150.4+0156	0.018	0.16e-12	0.019	-11.93	95	0.35	22.7		19.5 ^d	FSRQ	1.502
WGAJ1204.2-0710	0.058	0.45e-12	0.070	-11.50	128	0.22	18.0			BL Lac	0.185
WGAJ1213.0+3248	0.015	0.12e-12	0.022	-11.70	61	0.70		19.9	19.2	SSRQ	2.502
WGAJ1213.2+1443	0.044	0.48e-12	0.100	-11.08	61	0.50		21.0	19.9	FSRQ	0.714
WGAJ1222.6+2934	0.016	0.15e-12	0.029	-11.59	60	0.55		19.5	18.7	SSRQ	0.787
	0.016	0.15e-12	0.033	-11.54							
WGAJ1223.9+0650	0.018	0.18e-12	0.030	-12.18	251	0.11		21.2		FSRQ	1.189
WGAJ1225.5+0715	0.010	0.84e-13	0.016	-11.96	75	0.54		21.3	>20.0	SSRQ	1.120
WGAJ1229.4+2711	0.024	0.28e-12	0.079	-11.56	165	0.16		>22.0	19.2	RG	0.490
WGAJ1231.7+2848	0.117	0.11e-11	0.150	-11.14	114	0.52		16.4	15.6	BL Lac	1.000
WGAJ1248.3-0631	0.021	0.22e-12	0.023	-12.49	433	0.12	19.5			FSRQ	0.762
WGAJ1259.9+1206	0.031	0.31e-12	0.031	-11.96	178	-0.16		20.8 ^g	19.4 ^g	FSRQ	0.627
WGAJ1300.7-3253	0.017	0.22e-12	0.059	-11.98	238	0.02	18.5	18.5	18.1	FSRQ	1.256
WGAJ1306.6-2428	0.013	0.20e-12	0.055	-11.69	103	-0.21	21.1	22.1	>20.0	FSRQ	0.666
WGAJ1311.3-0521	0.027	0.28e-12	0.040	-11.31	46	0.36	18.7			BL Lac	0.160
WGAJ1314.0-3304	0.026	0.33e-12	0.092	-11.50	125	0.50 ^u	19.3			FSRQ	0.484
WGAJ1315.1+2841	0.017	0.12e-12	0.008	-12.20	95	0.36		20.2	19.9	FSRQ	1.576
WGAJ1320.4+0140	0.022	0.20e-12	0.036	-12.46	541	0.01	20.8	20.8	>20.0	BL Lac	1.235
WGAJ1324.0-3623	0.022	0.28e-12	0.074	-11.82	202	0.19	16.6			FSRQ	0.739
WGAJ1324.4-1049	0.047	0.69e-12	0.163	-11.66	857	-1.09 ^{ac}		22.5	20.7	FSRQ	0.872
WGAJ1329.0+5009	0.023	0.16e-12	0.018	-12.08	133	0.68		20.1	19.2	SSRQ	2.650
WGAJ1332.7+4722	0.033	0.33e-12	0.056	-12.05	333	0.54		19.3	18.9	SSRQ	0.668
WGAJ1333.1-3323	0.005	0.55e-13	0.014	-12.33	140	0.22	21.7			FSRQ	2.240
WGAJ1337.2-1319	0.022	0.32e-12	0.085	-11.30	71	0.38 ^v		19.8	18.8	FSRQ	3.475
WGAJ1353.2-4720	0.019	0.30e-12	0.128	-11.63	198	0.66	21.4			SSRQ	0.550
WGAJ1359.6+4010	0.014	0.13e-12	0.020	-12.41	281	-0.76		19.2	17.6	FSRQ	0.407
WGAJ1400.7+0425	0.009	0.80e-13	0.008	-12.73	267	0.06		21.3		FSRQ	2.550
WGAJ1402.7-3334	0.042	0.61e-12	0.172	-11.00	88	-0.02	23.0			FSRQ	2.140
WGAJ1404.2+3413	0.011	0.78e-13	0.012	-11.98	62	0.67		18.6	17.6	SSRQ	0.937
WGAJ1406.9+3433	0.014	0.11e-12	0.010	-12.51	204	0.27		18.7	17.9	FSRQ	2.556
WGAJ1416.4+1242	0.100	0.95e-12	0.058	-11.36	98	0.30		18.1	17.7	FSRQ	0.335
	0.098	0.87e-12	0.148	-11.09							
WGAJ1417.2+0608	0.016	0.16e-12	0.016	-11.95	93	0.67		15.6	14.2	RG	0.117
	0.020	0.22e-12	0.054	-11.53							
WGAJ1417.5+2645	0.006	0.51e-13	0.010	-12.17	77	0.29		21.9	>20.0	FSRQ	1.455
WGAJ1419.1+0603	0.009	0.97e-13	0.022	-12.33	240	0.01			20.5 ^d	FSRQ	2.389
WGAJ1420.6+0650	0.028	0.33e-12	0.076	-11.80	241	0.56		20.1		SSRQ	0.236

Name	ROSAT counts	$f_{0.1-2.0\text{keV}}$ [erg/s/cm ²]	f_{1keV} [μJy]	\log f_x/f_r	$f_{6\text{cm}}$ [mJy]	α_r	B_j	O	E	Class	z
(1)	(2)	(3)	(4)	(5)	(6)	(7)	(8)	(9)	(10)	(11)	(12)
	0.033	0.35e-12	0.042	-12.00							
WGAJ1423.3+4830	0.022	0.20e-12	0.037	-11.72	100	0.55		19.4	19.1	SSRQ	0.569
WGAJ1427.9+3247	0.052	0.38e-12	0.055	-11.32	65	0.66		18.1	17.6	SSRQ	0.568
WGAJ1442.3+5236	0.016	0.14e-12	0.036	-11.77	111	0.32		19.3	18.5	FSRQ	1.800
WGAJ1457.7-2818	0.007	0.89e-13	0.019	-12.19	136	0.40 ^w	18.8			FSRQ	1.999
WGAJ1506.6-4008	0.018	0.27e-12	0.064	-11.60	110	0.31		19.6 ^a		FSRQ	1.031
WGAJ1507.9+6214	0.018	0.12e-12	0.008	-12.52	213	0.69		18.5	18.1	SSRQ	1.478
WGAJ1509.5-4340	0.016	0.24e-12	0.081	-11.83	165	-0.40	19.2			FSRQ	0.776
WGAJ1525.3+4201	0.015	0.15e-12	0.031	-11.80	103	0.24		18.0	17.2	FSRQ	1.189
	0.019	0.18e-12	0.042	-11.66							
WGAJ1539.1-0658	0.005	0.70e-13	0.018	-12.03	76	-0.27 ^{ad}	20.0			BL Lac	...
WGAJ1543.6+1847	0.011	0.13e-12	0.035	-12.26	300	0.13		19.5	18.8	FSRQ	1.396
WGAJ1606.0+2031	0.006	0.66e-13	0.018	-12.31	196	0.32			18.3	FSRQ	0.383
WGAJ1615.2-0540	0.019	0.27e-12	0.088	-11.53	92	-0.46 ^{ae}	23.1	22.3 ^a		FSRQ	3.380
	0.010	0.15e-12	0.056	-11.69							
WGAJ1626.6+5809	0.032	0.32e-12	0.067	-11.95	315	0.55			17.5	SSRQ	0.748
WGAJ1629.7+2117	0.013	0.14e-12	0.035	-11.81	105	0.50		21.5	>20.0	FSRQ	0.833
WGAJ1648.4+4104	0.061	0.61e-12	0.109	-11.54	197	0.52		19.8	19.0	SSRQ	0.851
WGAJ1656.6+5321	0.014	0.15e-12	0.033	-11.94	145	0.09			19.1 ^c	FSRQ	1.555
WGAJ1656.6+6012	0.032	0.29e-12	0.029	-11.99	184	-0.33		19.0 ^g	18.4 ^g	FSRQ	0.623
	0.032	0.23e-12	0.007	-12.37							
WGAJ1722.3+3103	0.014	0.16e-12	0.036	-11.50	53	0.58		21.2	18.7	SSRQ	0.305
WGAJ1738.6-5333	0.015	0.19e-12	0.072	-12.10	307	-0.10		18.4 ^a		FSRQ	1.721
WGAJ1744.3-0517	0.004	0.54e-13	0.024	-12.18	82	0.69			21.6 ^b	BL Lac	0.310
WGAJ1804.7+1755	0.009	0.11e-12	0.036	-11.84	92	0.29		19.4	18.7	FSRQ	0.435
WGAJ1808.2-5011	0.011	0.14e-12	0.042	-12.44	425	-0.33		20.4 ^a		FSRQ	1.606
WGAJ1826.1-3650	0.016	0.20e-12	0.078	-12.35	552	-0.06			18.8 ^e	FSRQ	0.888
WGAJ1827.1-4533	0.023	0.33e-12	0.104	-12.09	451	0.00	18.1			FSRQ	1.244
WGAJ1834.2-5948	0.014	0.21e-12	0.062	-11.66	105	0.63	21.1			BL Lac	0.435
WGAJ1834.4-5856	0.011	0.15e-12	0.046	-12.25	399	0.00	19.7			BL Lac	...
	0.023	0.35e-12	0.102	-12.03							
WGAJ1837.7-5848	0.012	0.19e-12	0.053	-12.02	211	-0.08	19.3			FSRQ	3.040
WGAJ1840.9+5452	0.040	0.58e-12	0.179	-11.53	252	0.39		19.4	18.8	BL Lac	0.646
WGAJ1843.4-7430	0.003	0.29e-13	0.005	-11.97	25	0.39	21.0			BL Lac	...
WGAJ1911.8-2102	0.018	0.30e-12	0.084	-12.17	443	0.28		17.7 ^g	17.9 ^g	FSRQ	1.450
WGAJ1936.8-4719	0.202	0.34e-11	0.936	-10.17	60	-0.11	20.3			BL Lac	0.264
WGAJ1938.4-4657	0.010	0.14e-12	0.029	-12.11	174	0.11		21.0		FSRQ	0.805
WGAJ2056.4-5819	0.023	0.29e-12	0.083	-12.10	454	0.53	19.0	18.1	17.4	SSRQ	1.139
WGAJ2109.7-1332	0.014	0.16e-12	0.034	-11.49	51	0.16	19.3	18.2	17.8	FSRQ	1.226
WGAJ2151.3-4233	0.030	0.26e-12	0.031	-12.16	265	0.51	16.1 ^h			RG	0.061
WGAJ2154.1-1501	0.033	0.36e-12	0.072	-11.78	219	0.30		16.5	16.4	FSRQ	1.208
	0.033	0.35e-12	0.091	-11.71							
WGAJ2157.7+0650	0.021	0.28e-12	0.083	-11.62	144	0.24		21.0	>20.0	FSRQ	0.625
WGAJ2159.3-1500	0.005	0.49e-13	0.013	-12.16	86	0.01 ^x	18.2	18.9	18.4	FSRQ	2.270
	0.013	0.13e-12	0.027	-11.82							
WGAJ2239.7-0631	0.069	0.97e-12	0.259	-10.72	64	0.54		20.1	18.8	SSRQ	0.264
WGAJ2248.6-2702	0.006	0.53e-13	0.008	-12.31	84	0.22			20.9	FSRQ	2.750
WGAJ2258.3-5525	0.167	0.14e-11	0.201	-10.66	51	0.10	17.9			BL Lac	0.479
WGAJ2303.5-5126	0.004	0.33e-13	0.006	-12.33	64	0.51	15.8			RG	0.426
WGAJ2304.8-3624	0.016	0.11e-12	0.013	-12.50	242	0.16			21.6 ⁱ	FSRQ	0.962

Name	ROSAT counts	$f_{0.1-2.0\text{keV}}$ [erg/s/cm ²]	$f_{1\text{keV}}$ [μJy]	log f_x/f_r	$f_{6\text{cm}}$ [mJy]	α_r	B_j	O	E	Class	z
(1)	(2)	(3)	(4)	(5)	(6)	(7)	(8)	(9)	(10)	(11)	(12)
WGAJ2317.4-4213	0.003	0.24e-13	0.006	-12.58	133	0.53	15.4			RG	0.056
WGAJ2320.6+0032	0.013	0.16e-12	0.036	-11.71	87	0.45	18.9			FSRQ	1.894
WGAJ2322.0+2114	0.011	0.15e-12	0.041	-11.68	100	0.31		17.1	16.9	FSRQ	0.707
	0.019	0.24e-12	0.064	-11.57							
WGAJ2322.5-4221	0.060	0.37e-12	0.019	-11.58	66	0.02	16.2			BL Lac	0.089
WGAJ2329.0+0834	0.004	0.61e-13	0.020	-12.35	273	0.06			20.5 ⁱ	FSRQ	0.948
WGAJ2330.6-3724	0.032	0.27e-12	0.038	-12.05	238	0.19	16.6			BL Lac	0.279
WGAJ2333.2-0131	0.013	0.16e-12	0.043	-12.21	314	-0.14	18.3	19.5	18.7	FSRQ	1.062
WGAJ2347.6+0852	0.043	0.64e-12	0.176	-10.91	60	0.58		17.1	16.2	SSRQ	0.292
WGAJ2349.9-2552	0.016	0.12e-12	0.009	-11.99	60	0.39 ^y			19.0	FSRQ	0.844
	0.016	0.14e-12	0.021	-11.72							
WGAJ2354.2-0957	0.010	0.98e-13	0.025	-12.01	131	0.35	22.0 ⁱ			FSRQ	0.989
WGAJ2356.4-3223	0.017	0.16e-12	0.023	-11.93	106	0.65			22.8 ^b	SSRQ	2.830

III. DXRBS Low Priority Sources

Name	ROSAT counts	$f_{0.1-2.0\text{keV}}$ [erg/s/cm ²]	$f_{1\text{keV}}$ [μJy]	log f_x/f_r	$f_{6\text{cm}}$ [mJy]	α_r	B_j	O	E	Class	z
(1)	(2)	(3)	(4)	(5)	(6)	(7)	(8)	(9)	(10)	(11)	(12)
WGAJ0247.9+1845	0.020	0.29e-12	0.093	-11.31	70	0.41			18.5	RG	0.301
WGAJ0313.9+4115	0.024	0.31e-12	0.112	-11.15	48	-0.04			15.0 ^e	BL Lac	0.029
WGAJ0449.4-4349	0.497	0.35e-11	0.477	-10.92	242	0.15	15.9	15.6	14.9	BL Lac	...
WGAJ0513.8+0156	0.031	0.42e-12	0.123	-11.26	131	0.45			14.3	RG	0.092
	0.023	0.30e-12	0.095	-11.49							
WGAJ0605.8-7556	0.014	0.22e-12	0.075	-11.04	25	0.77			22.7	RG	0.458
WGAJ0628.4-3208	0.019	0.26e-12	0.075	-11.44	86	0.78	18.5			SSRQ	2.077
	0.008	0.99e-13	0.032	-11.77							
WGAJ0724.3-0715	0.017	0.28e-12	0.234	-12.29	482	-0.28		19.8 ^g	17.2 ^g	FSRQ	0.271
WGAJ0816.0-0736	0.008	0.12e-12	0.040	-11.55	61	0.80	16.1			BL Lac	0.040
WGAJ0847.2+1133	1.290	0.16e-10	3.954	-9.24	32	0.03		17.8	16.6	BL Lac	0.199
WGAJ0937.1+5008	0.056	0.51e-12	0.063	-11.95	315	-0.42		19.6	18.0	FSRQ	0.275
	0.069	0.74e-12	0.167	-11.52							
	0.056	0.53e-12	0.127	-11.64							
	0.072	0.67e-12	0.160	-11.53							
	0.058	0.50e-12	0.082	-11.85							
WGAJ1028.6-0336	0.008	0.76e-13	0.009	-11.99	61	0.74	19.1	20.5		SSRQ	1.781
WGAJ1120.4+5855	0.008	0.60e-13	0.005	-12.19	46	0.61		18.5	16.0	RG	0.158
	0.026	0.21e-12	0.033	-11.40							
WGAJ1206.2+2823	0.013	0.89e-13	0.002	-11.96	21	0.41		19.5	18.9	FSRQ	0.708
WGAJ1217.1+2925	0.012	0.94e-13	0.014	-11.80	49	0.27		19.9	19.2	FSRQ	0.974
WGAJ1401.5-1134	0.004	0.48e-13	0.013	-13.06	636	0.58		8.8	9.6	RG	0.038
WGAJ1457.9-2124	0.035	0.54e-12	0.166	-11.38	146	0.79	21.3	21.6	18.3	RG	0.319
	0.040	0.61e-12	0.191	-11.32							

Name	ROSAT counts	$f_{0.1-2.0\text{keV}}$ [erg/s/cm ²]	$f_{1\text{keV}}$ [μJy]	log f_x/f_r	$f_{6\text{cm}}$ [mJy]	α_r	B_j	O	E	Class	z
(1)	(2)	(3)	(4)	(5)	(6)	(7)	(8)	(9)	(10)	(11)	(12)
WGAJ1520.7+0732	0.016	0.16e-12	0.037	-11.74	100	0.34		18.6	17.9	FSRQ	1.070
	0.006	0.60e-13	0.014	-12.17							
WGAJ1610.3-3958	0.026	0.40e-12	0.209	-12.09	882	0.19	20.9			FSRQ	0.518
	0.011	0.17e-12	0.086	-12.69							
	0.023	0.29e-12	0.165	-12.31							
	0.022	0.30e-12	0.208	-12.34							
WGAJ1835.5-6539	0.005	0.67e-13	0.021	-12.43	244	1.02			22.8 ^b	RG	0.554
WGAJ2131.9-0556	0.011	0.14e-12	0.033	-11.46	43	0.65 ^{af}	15.3	17.2	14.8	RG	0.085
WGAJ2201.6-5646	0.047	0.45e-12	0.077	-11.23	67	0.71	17.5			SSRQ	0.410
	0.022	0.22e-12	0.049	-11.44							
WGAJ2205.2-0004	0.008	0.11e-12	0.027	-12.21	180	0.83			21.3 ^b	RG	0.827

^a V_{mag} from ESO image

^b R_{mag} from ESO image

^c R_{mag} from WYIN image

^d R_{mag} from CTIO image

^e R_{mag} from spectrum

^f R_{mag} from Stickel et al. (1996)

^gmagnitude from USNO

^hmagnitude from the APM Bright Galaxy Catalogue (Loveday, 1996)

ⁱmagnitude from DSS 2

^jtwo merged obj. in APM, given magnitudes assume a flux ratio of ~ 2

^k $\alpha_{\text{ATCA}} = 0.83$

^l $\alpha_{\text{ATCA}} = 1.00$

^m $\alpha_{\text{ATCA}} = 1.91$, possibly GPS

ⁿ $\alpha_{\text{ATCA}} = 1.70$, possibly GPS

^o $\alpha_{\text{ATCA}} = 0.71$

^p $\alpha_{\text{ATCA}} = 0.80$

^q $\alpha_{\text{ATCA}} = 0.90$

^r $\alpha_{\text{ATCA}} = 1.98$, possibly GPS

^s $\alpha_{\text{ATCA}} = 0.91$

^t $\alpha_{\text{ATCA}} = 1.44$, possibly GPS

^u $\alpha_{\text{ATCA}} = 0.97$

^v $\alpha_{\text{ATCA}} = 0.87$

^w $\alpha_{\text{ATCA}} = 0.72$

^x $\alpha_{\text{ATCA}} = 1.46$, possibly GPS

^y $\alpha_{\text{ATCA}} = 1.48$

^z $\alpha_{\text{ATCA}} = 0.36$, possibly GPS

^{aa} $\alpha_{\text{ATCA}} = 0.31$, possibly GPS

^{ab} $\alpha_{\text{ATCA}} = 0.29$, possibly GPS

^{ac} $\alpha_{\text{ATCA}} = -0.47$, possibly GPS

^{ad} $\alpha_{\text{ATCA}} = 0.47$, possibly GPS

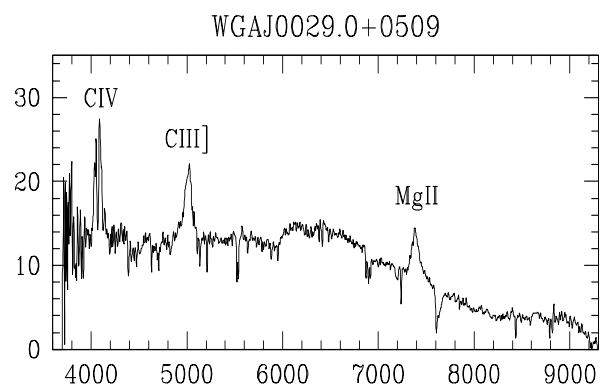
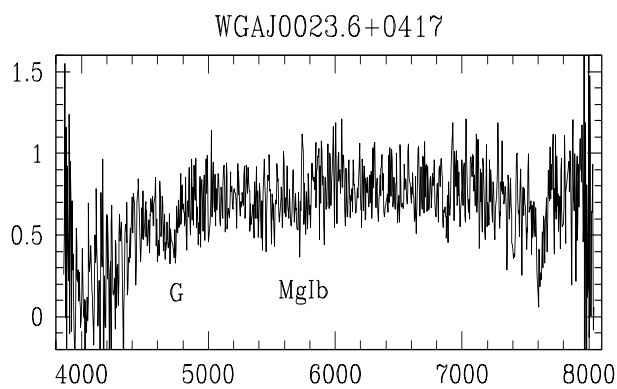
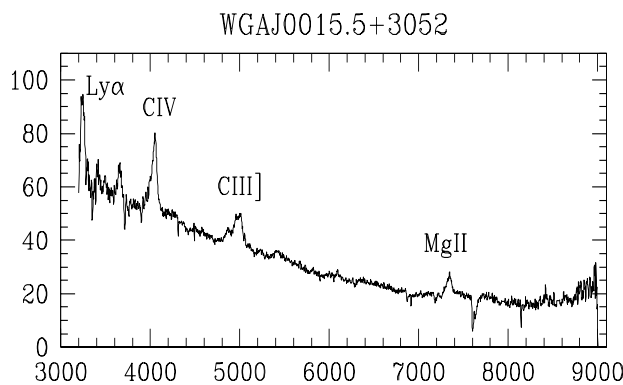
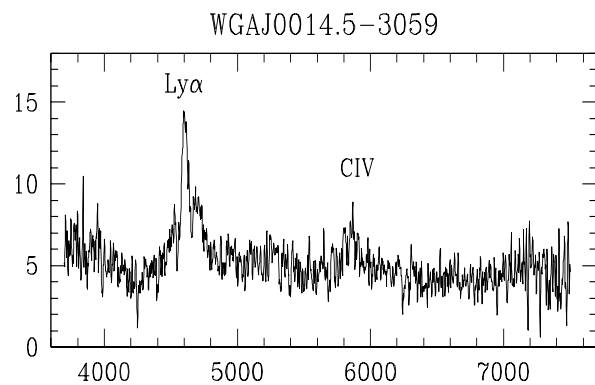
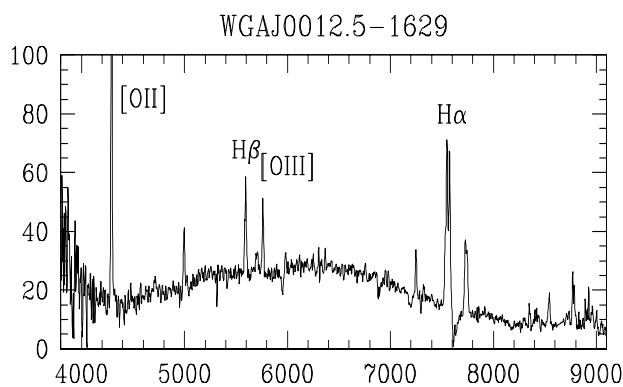
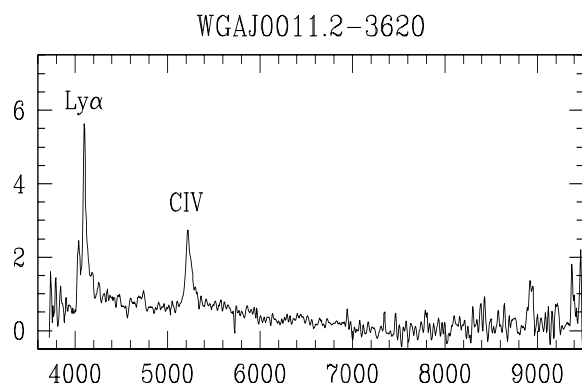
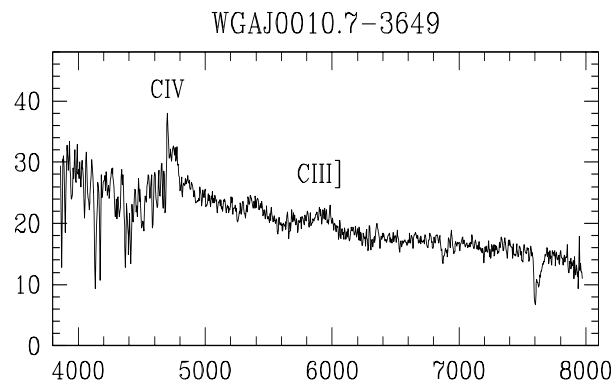
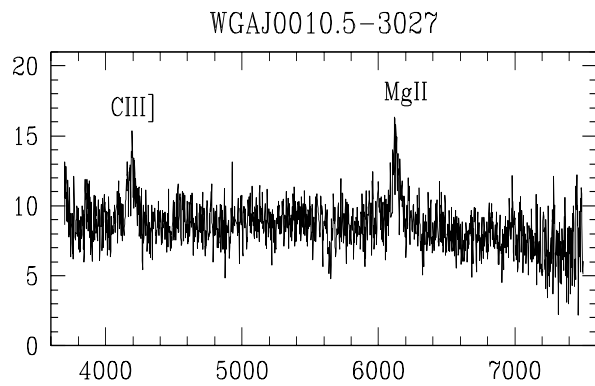
^{ae} $\alpha_{\text{ATCA}} = 0.55$, possibly GPS

^{af} $\alpha_{\text{ATCA}} = 0.82$

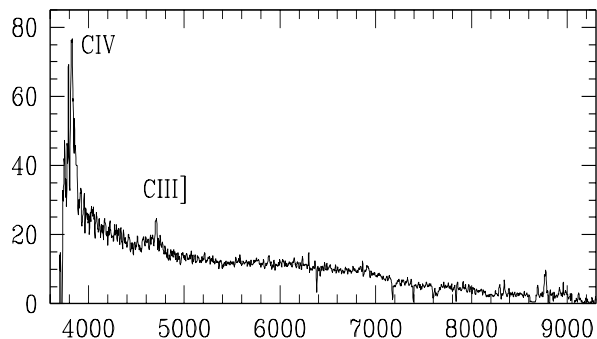
Appendix D

Optical Spectra

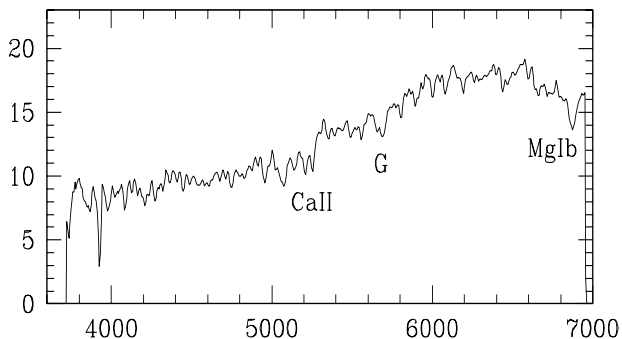
Following are presented the reduced and calibrated spectra of the DXRBS sources listed in Appendix B. The spectra are plotted as wavelength flux in units of 10^{-17} erg s⁻¹ cm⁻² Å⁻¹ versus wavelength in units of Å.



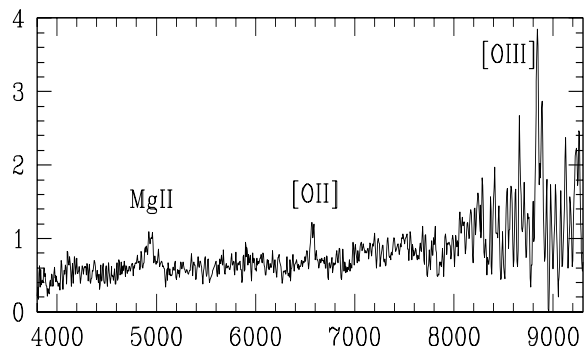
WGAJ0032.5-2648



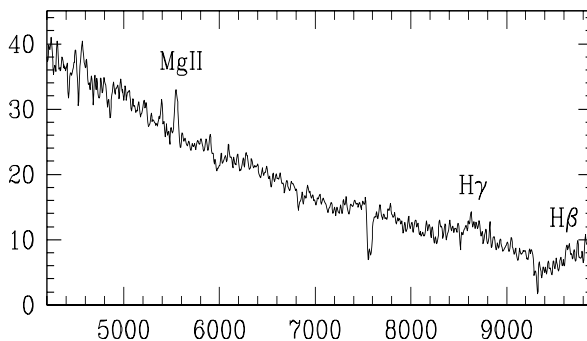
WGAJ0032.5-2849



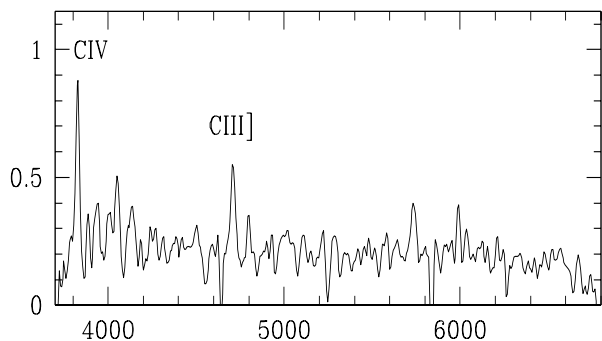
WGAJ0034.4-2133



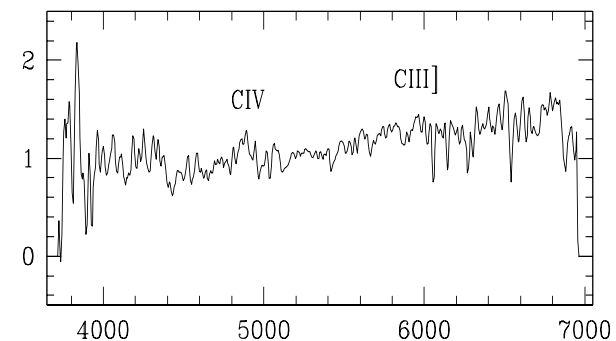
WGAJ0043.3-2638



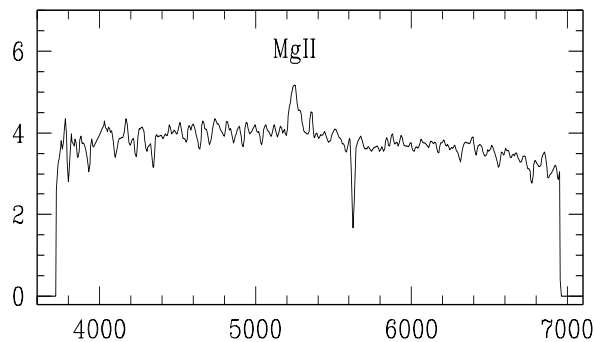
WGAJ0049.5-2509



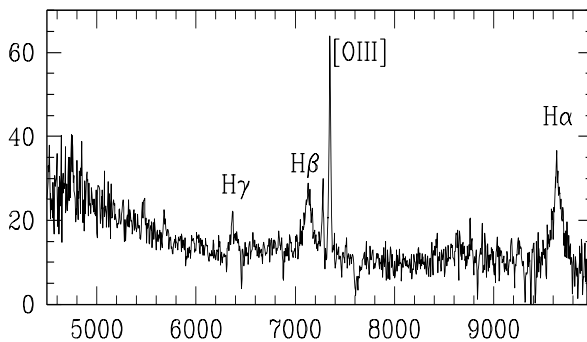
WGAJ0057.3-2212

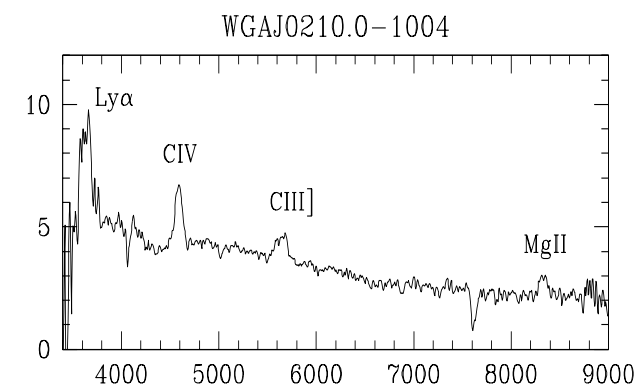
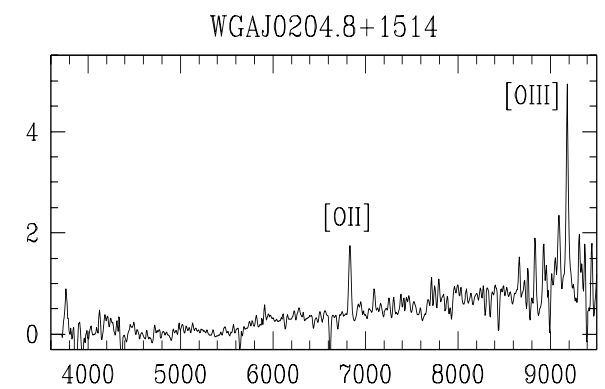
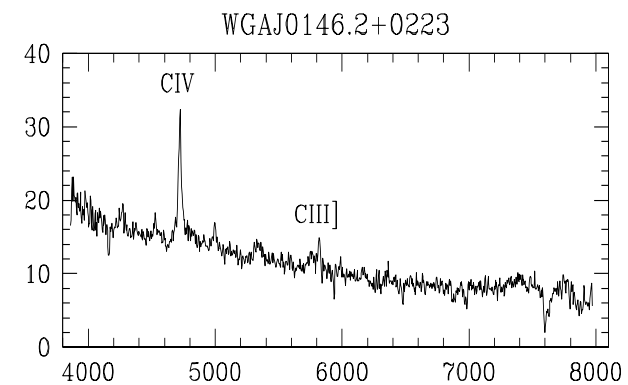
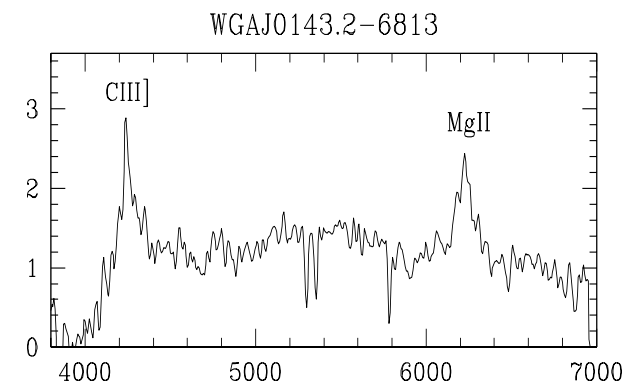
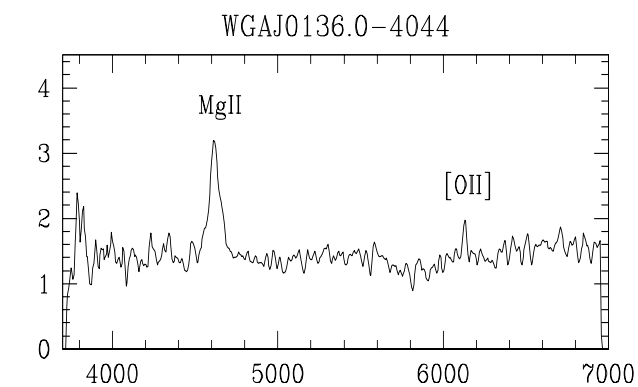
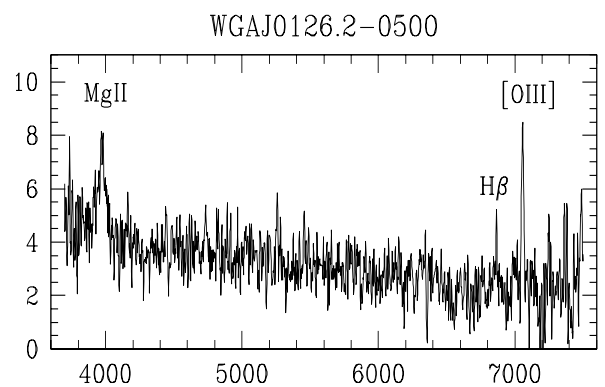
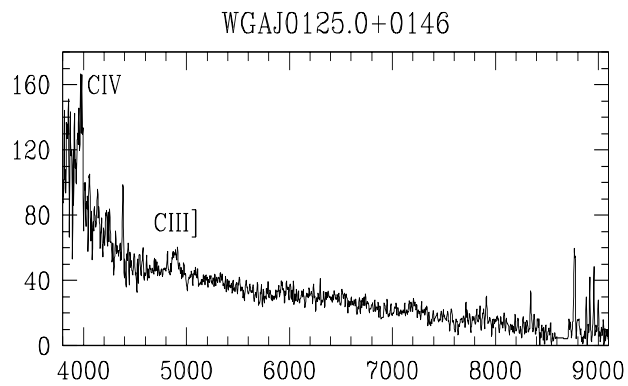
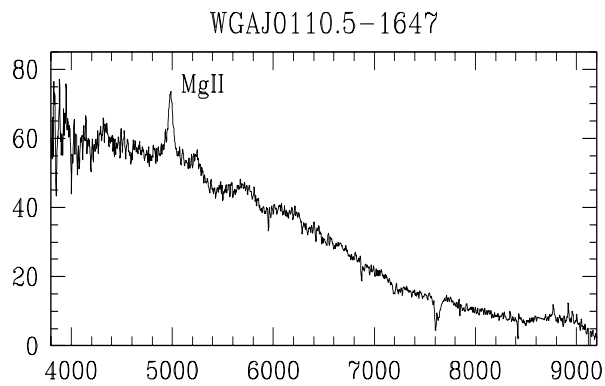


WGAJ0100.1-3337

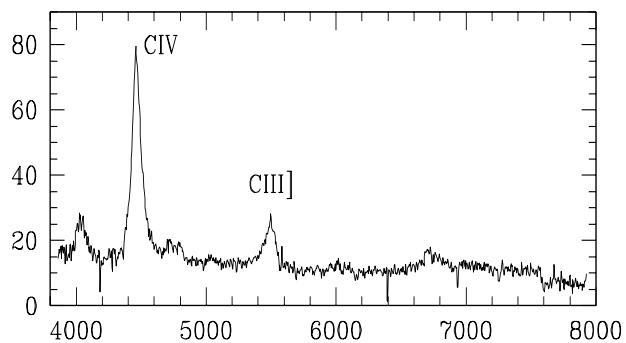


WGAJ0106.7-1034

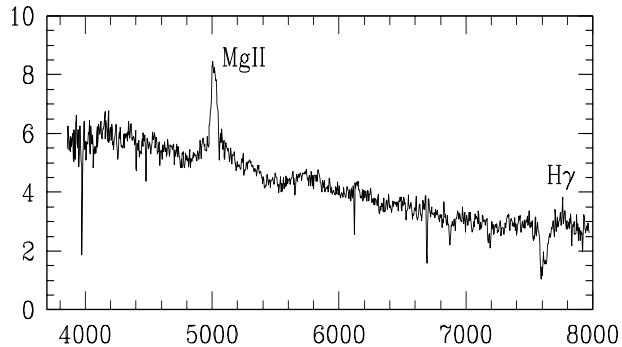




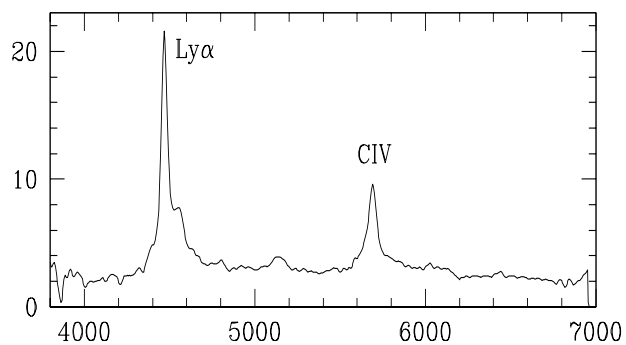
WGAJ0210.1-3851



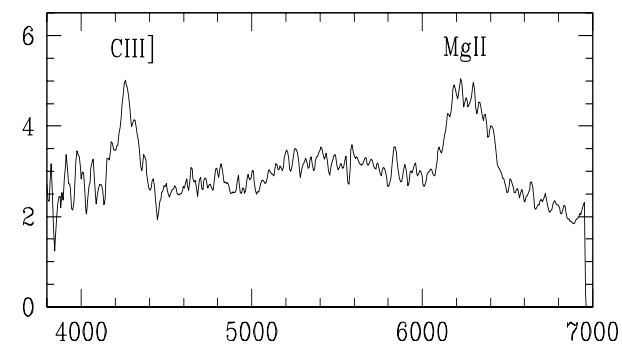
WGAJ0211.9-7351



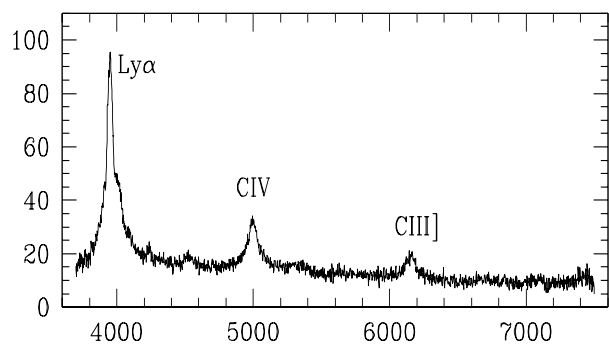
WGAJ0216.6-7331



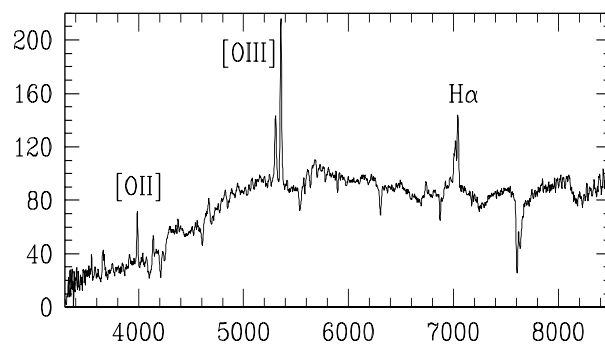
WGAJ0217.7-7347



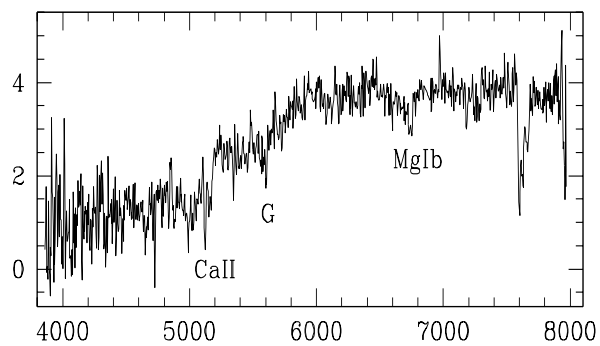
WGAJ0227.5-0847



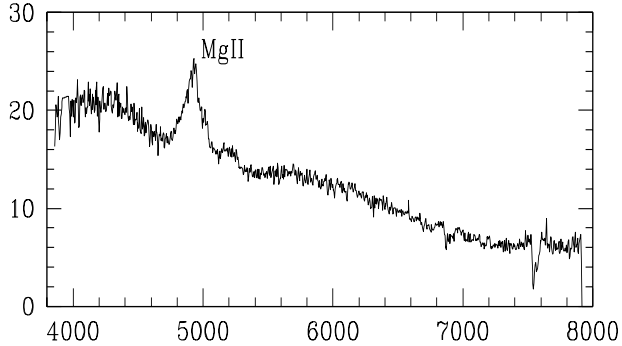
WGAJ0245.2+1047



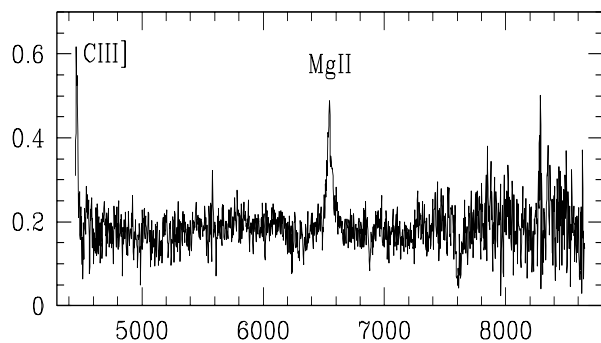
WGAJ0247.9+1845



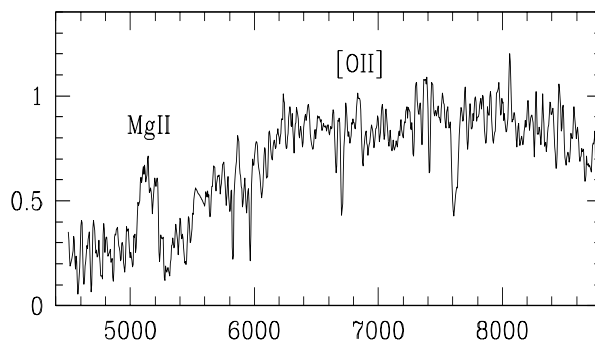
WGAJ0251.9-2051



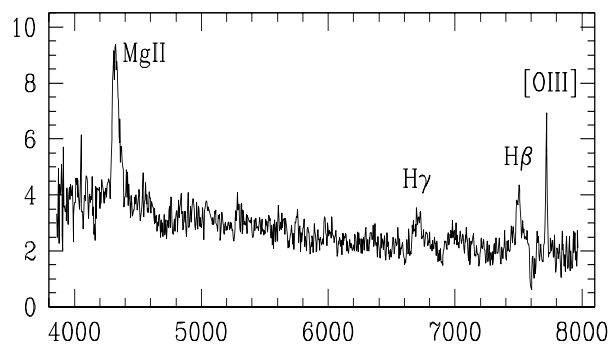
WGAJ0253.3+0006



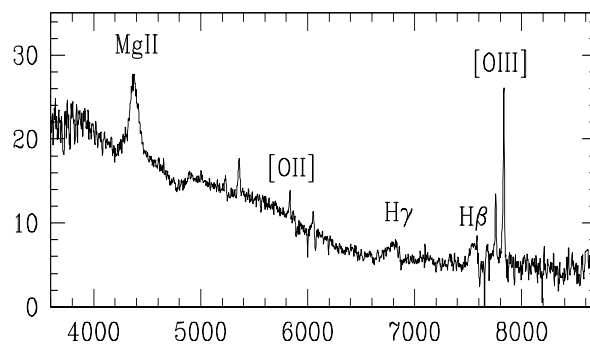
WGAJ0258.5-5051



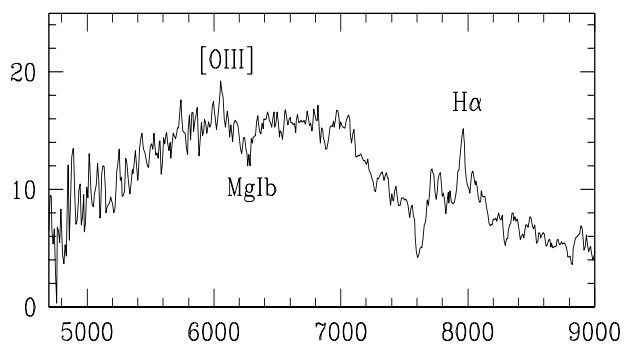
WGAJ0259.4+1926



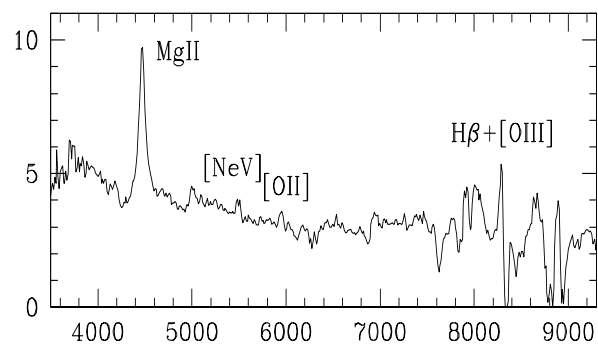
WGAJ0304.9+0002



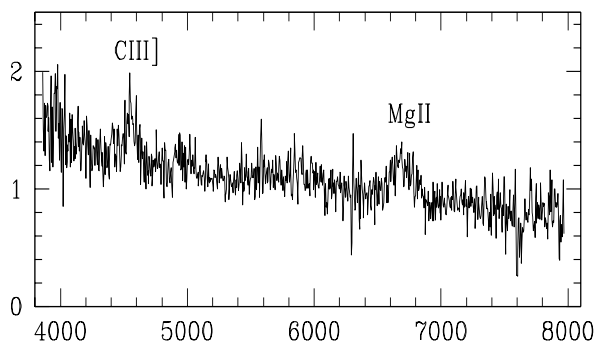
WGAJ0305.3-2420



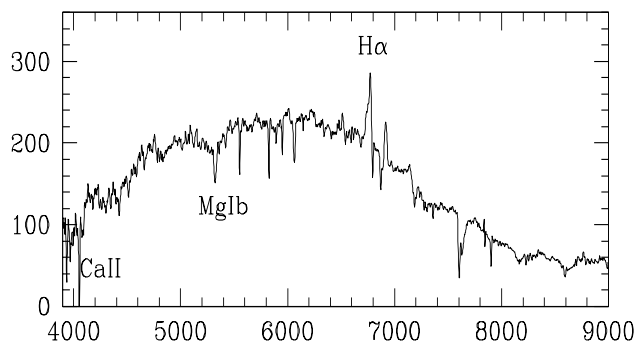
WGAJ0307.7-4717



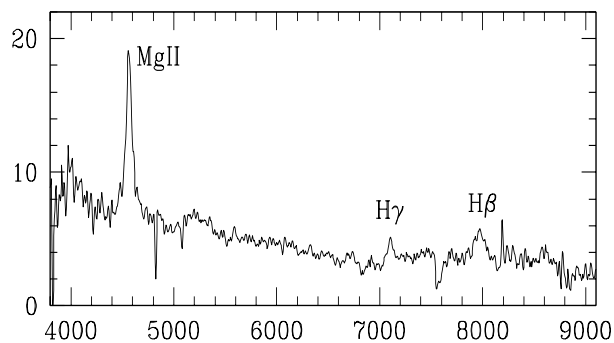
WGAJ0312.3-6610



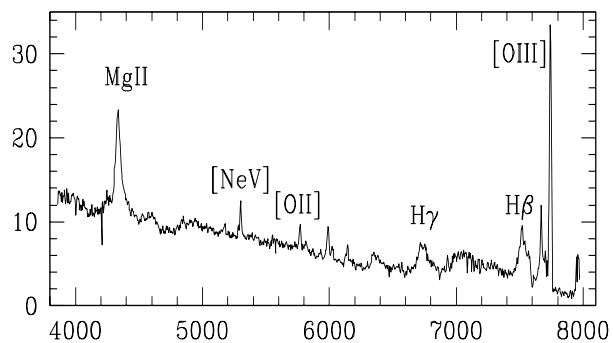
WGAJ0313.9+4115



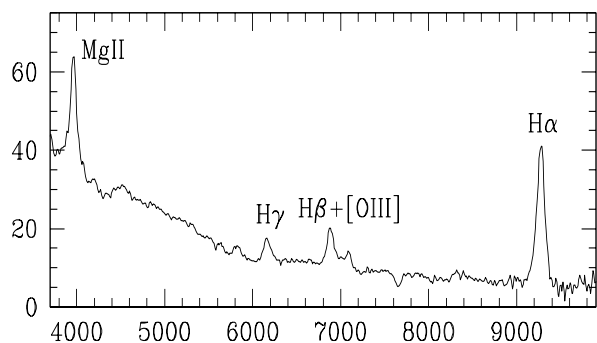
WGAJ0314.4-6548



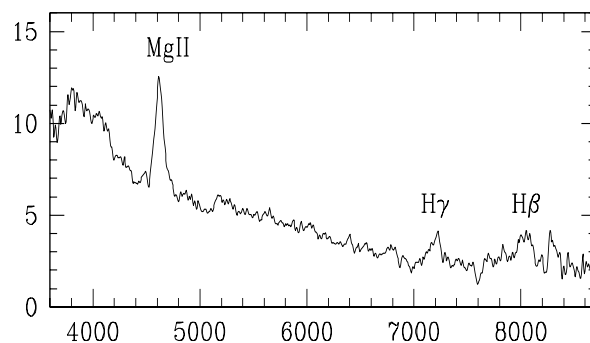
WGAJ0321.6-6641



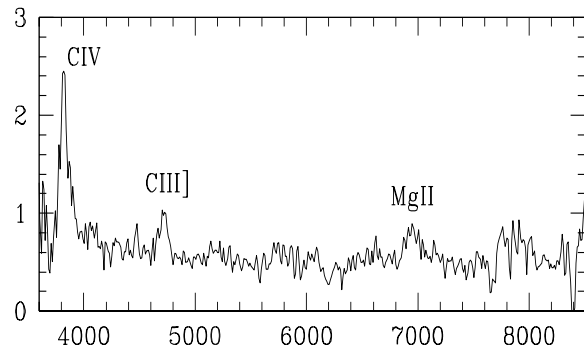
WGAJ0322.1-5205



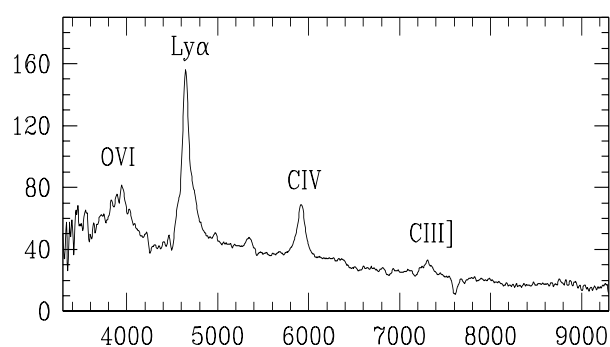
WGAJ0322.2-5042



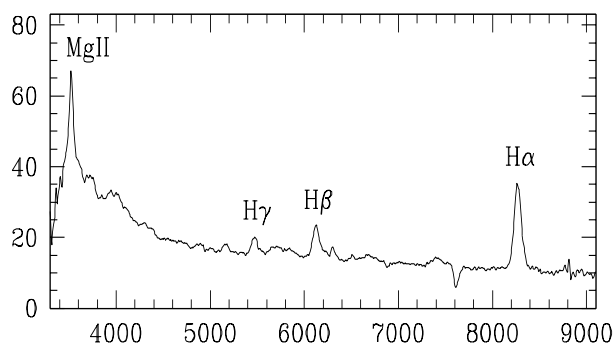
WGAJ0322.6-1335



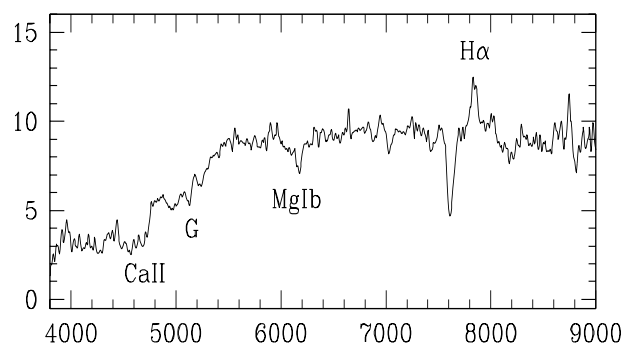
WGAJ0324.9-2140

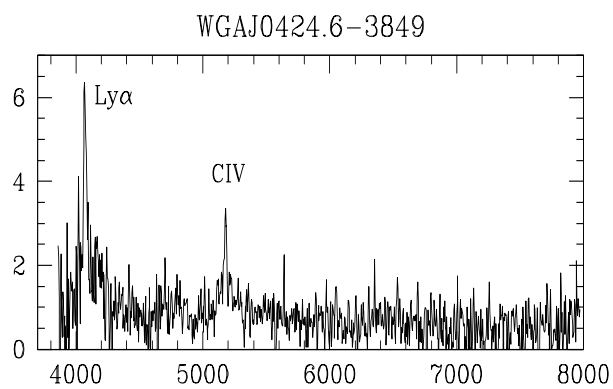
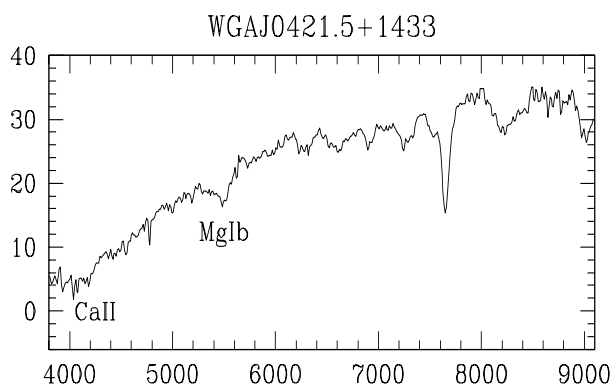
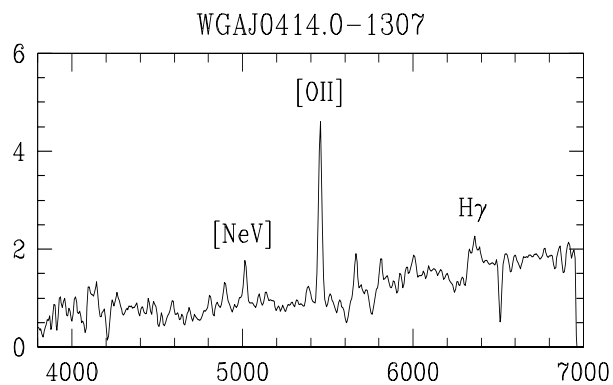
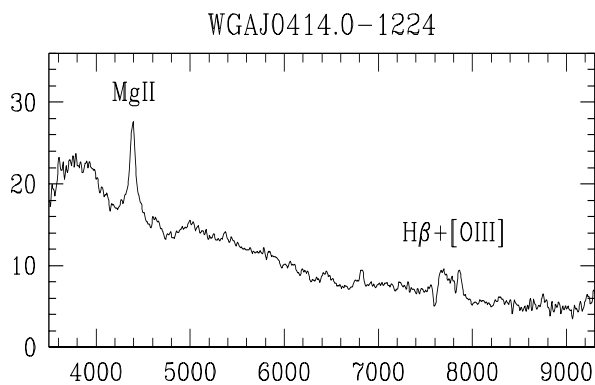
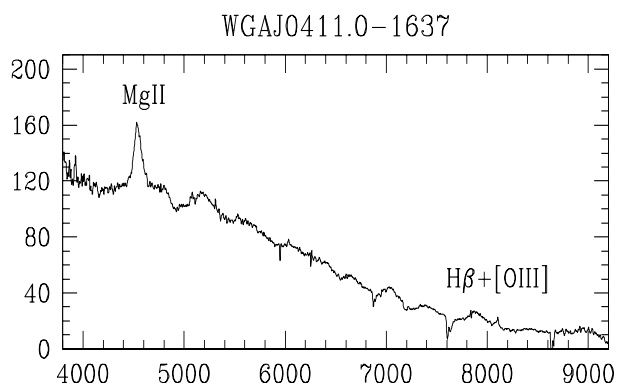
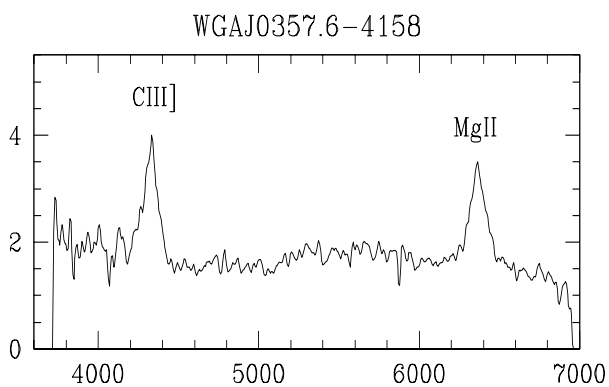
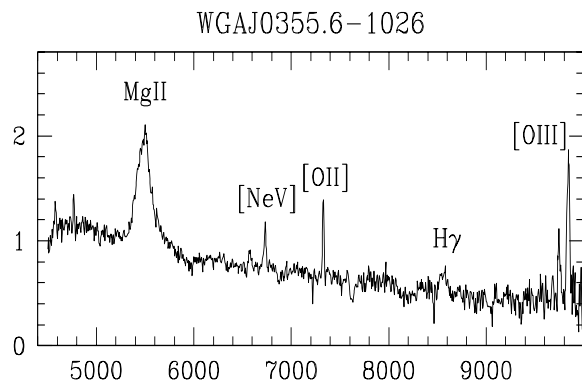
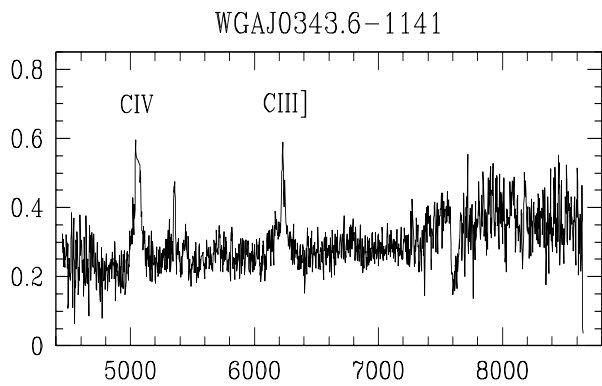


WGAJ0325.0-4926

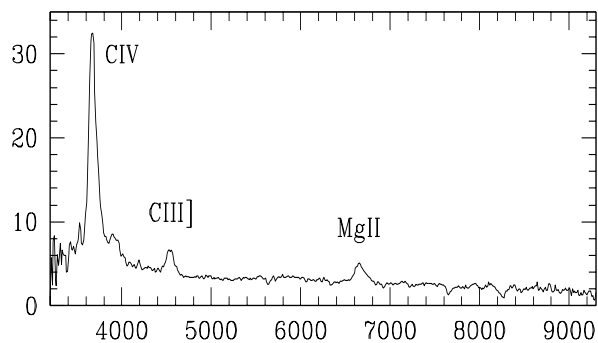


WGAJ0340.8-1814

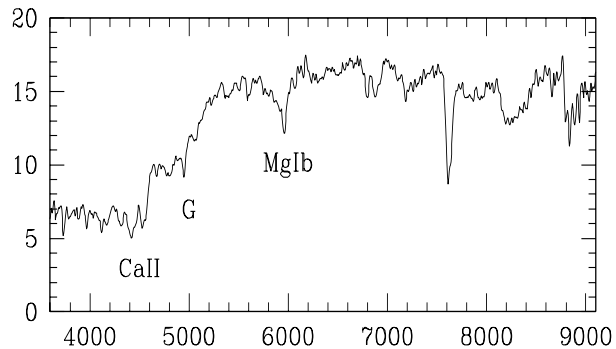




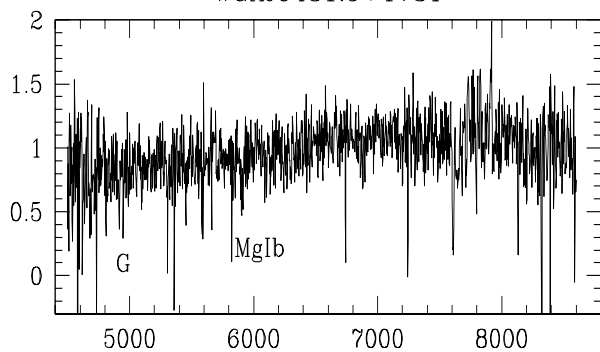
WGAJ0427.2-0756



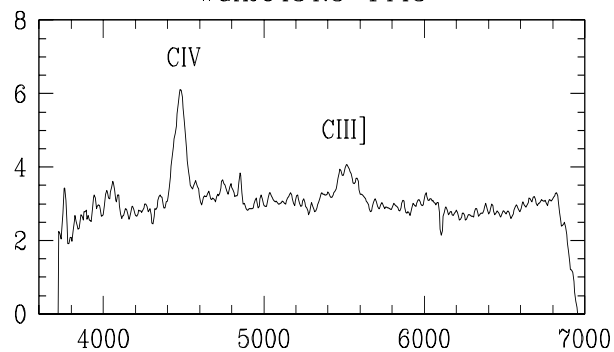
WGAJ0428.8-3805



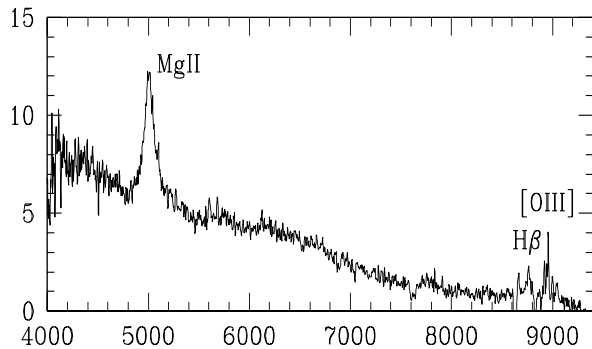
WGAJ0431.9+1731



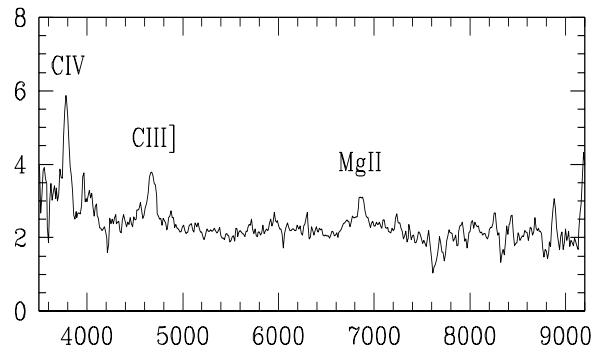
WGAJ0434.3-1443



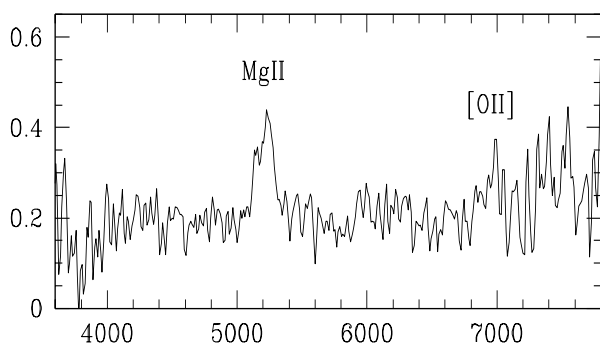
WGAJ0435.1-0811



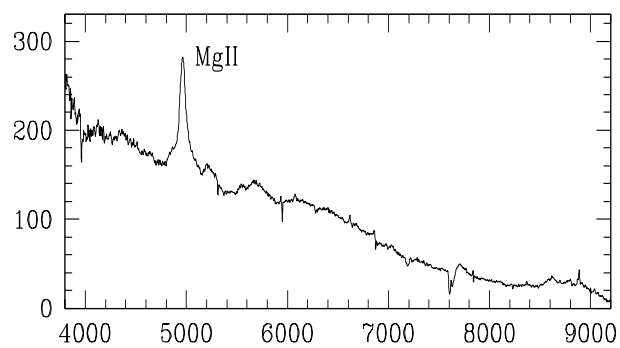
WGAJ0438.7-4727

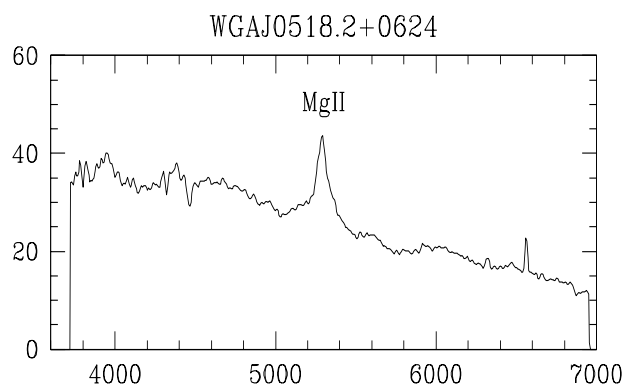
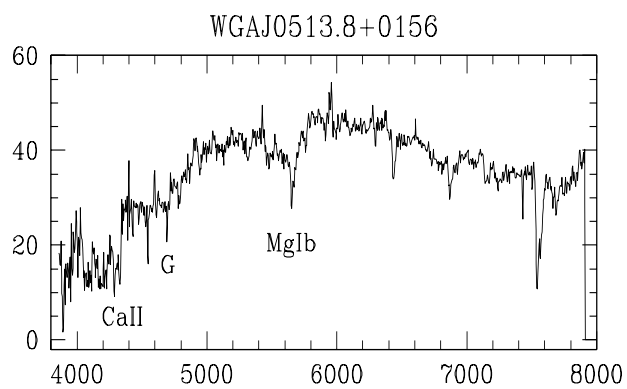
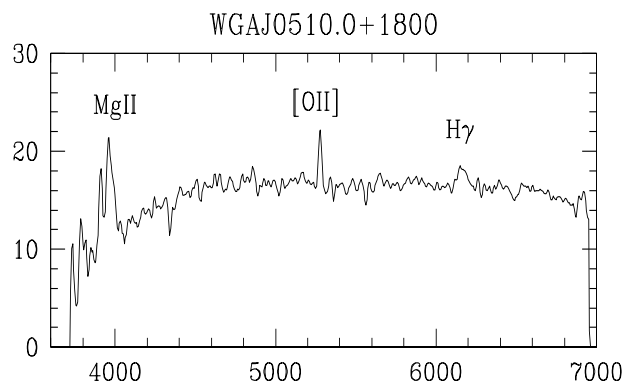
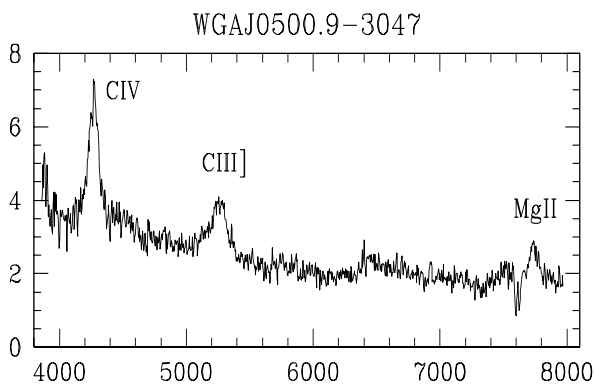
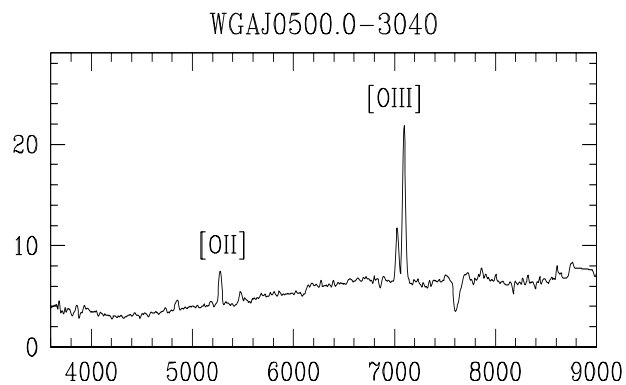
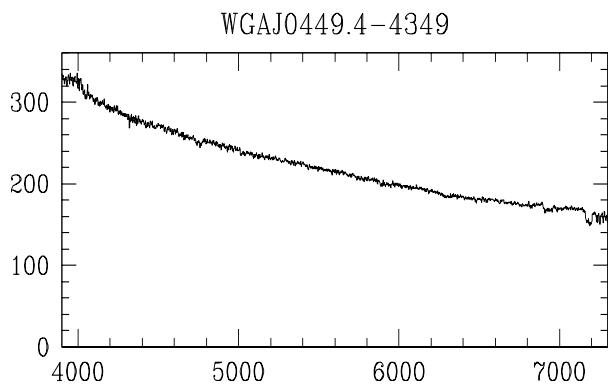
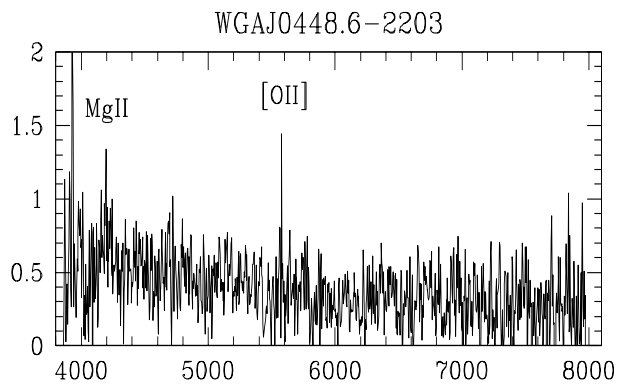
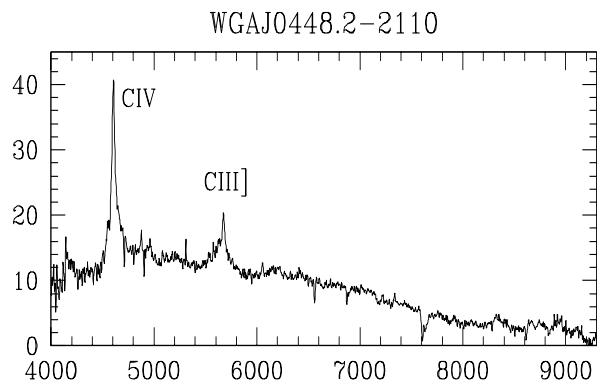


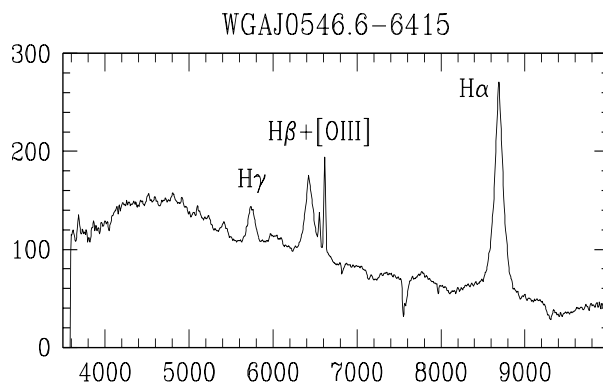
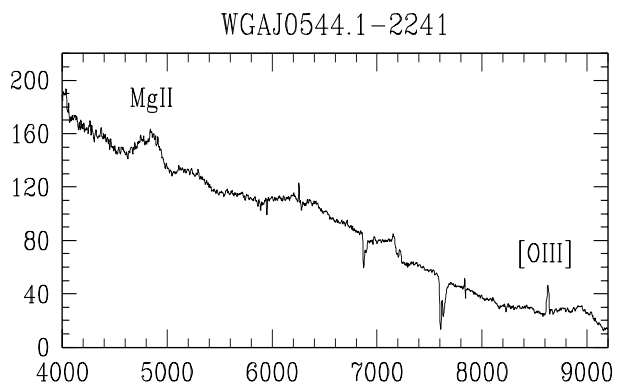
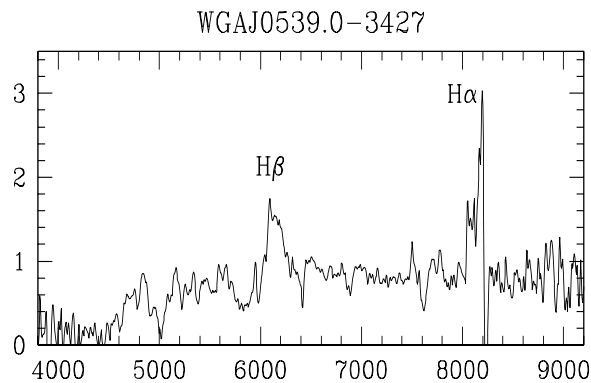
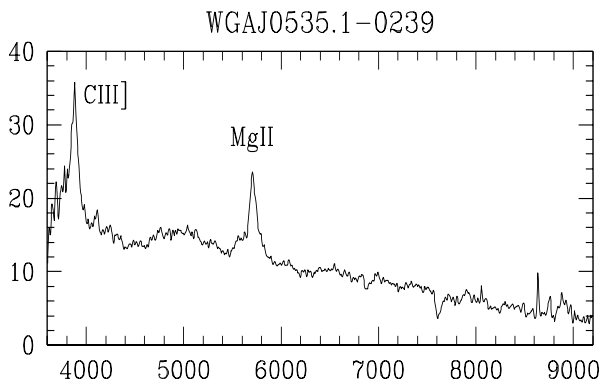
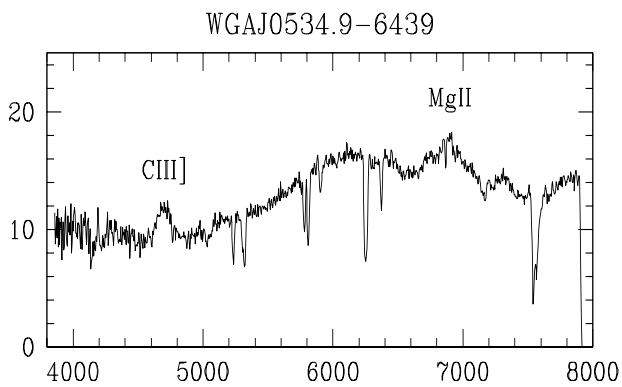
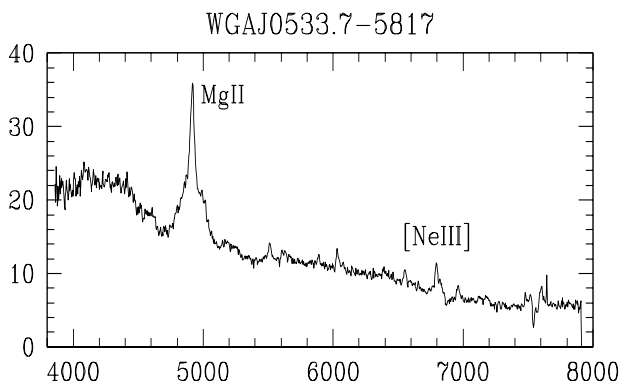
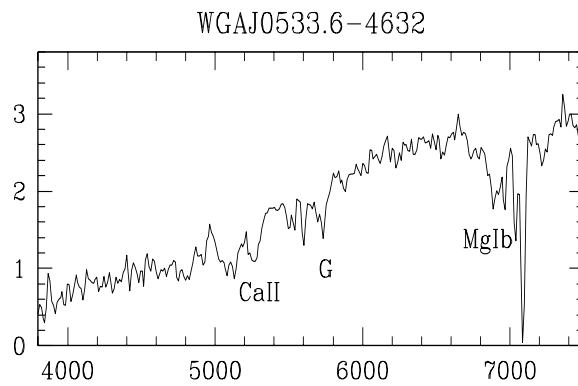
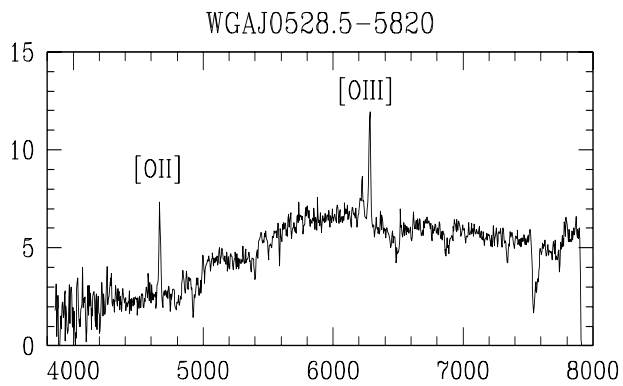
WGAJ0441.8-4306

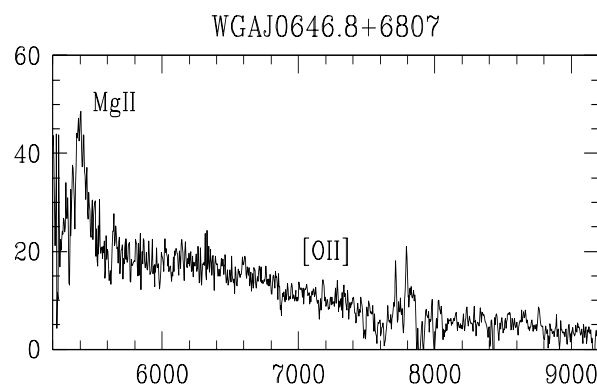
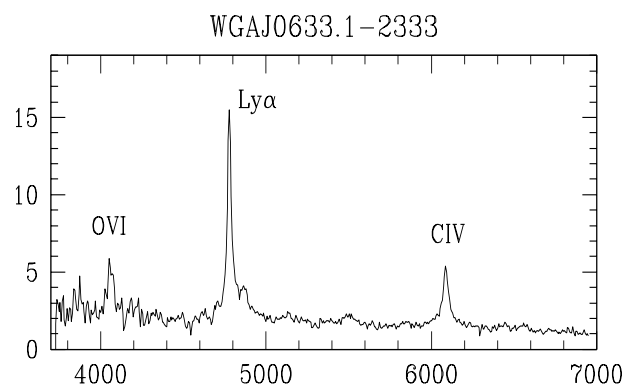
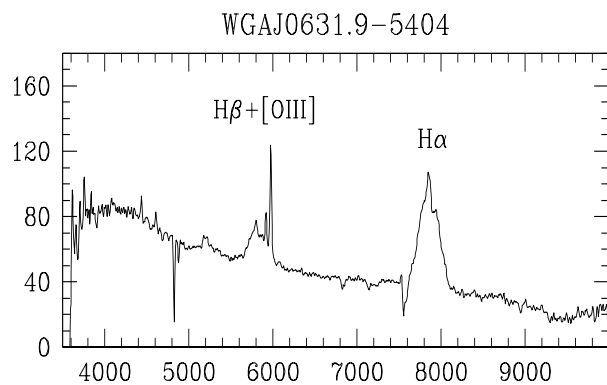
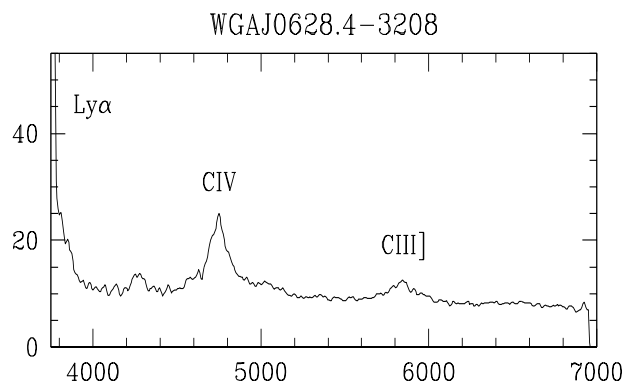
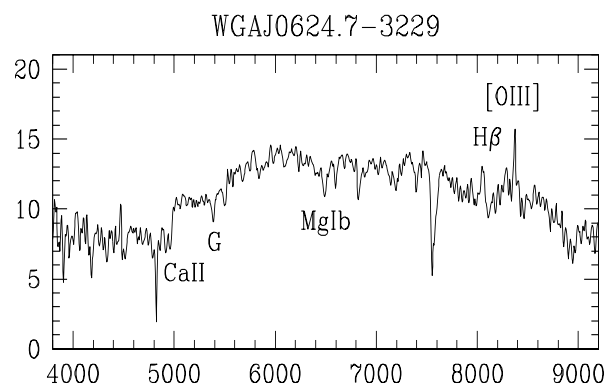
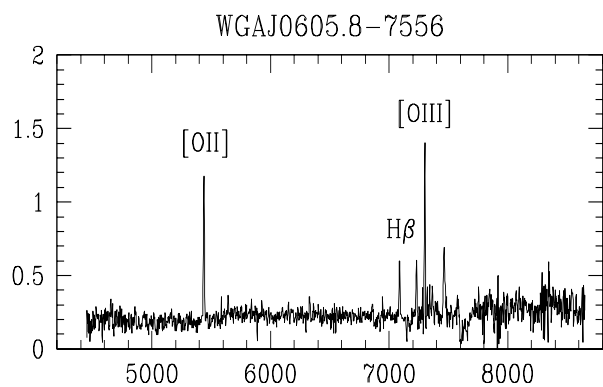
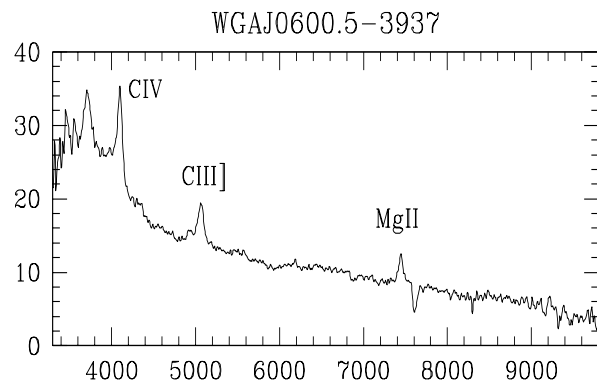
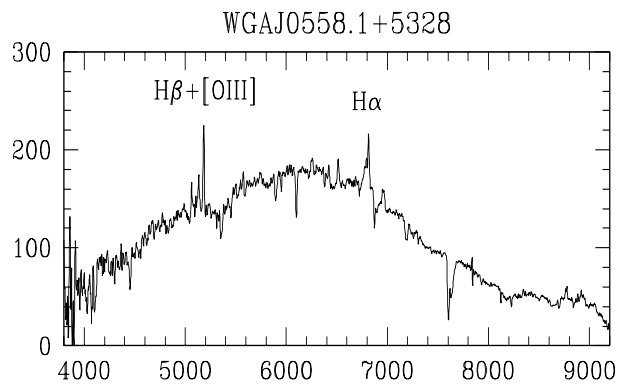


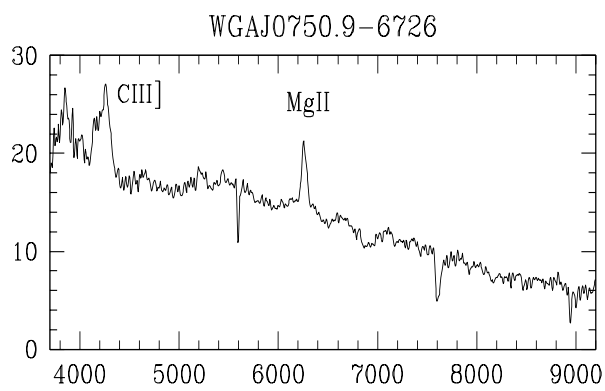
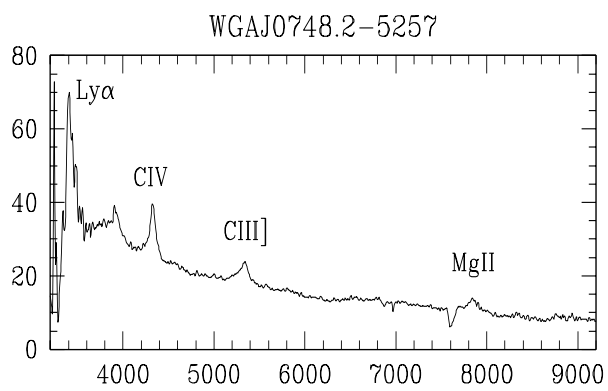
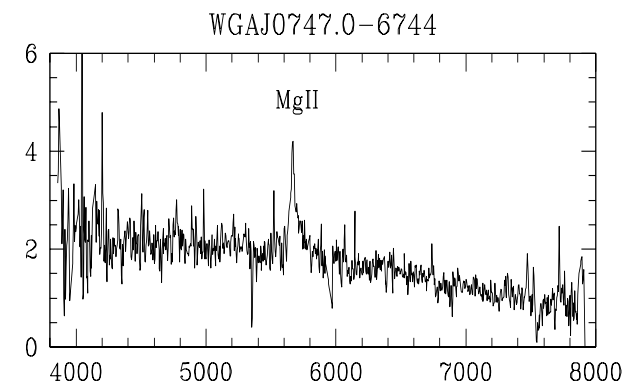
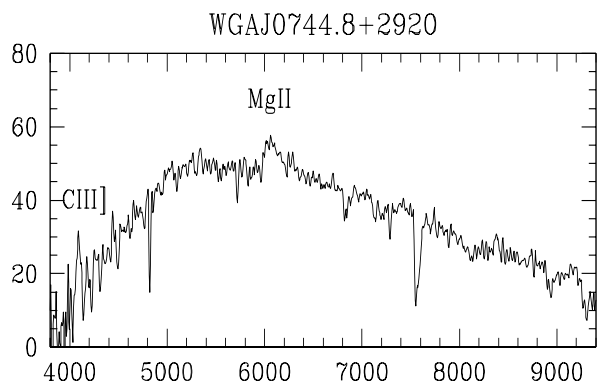
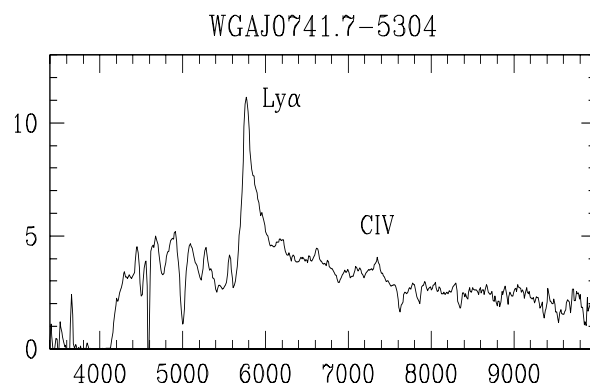
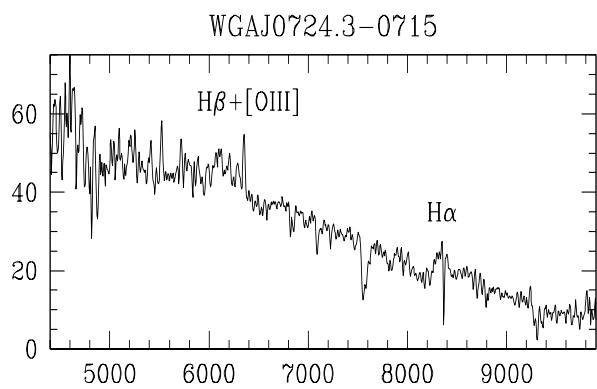
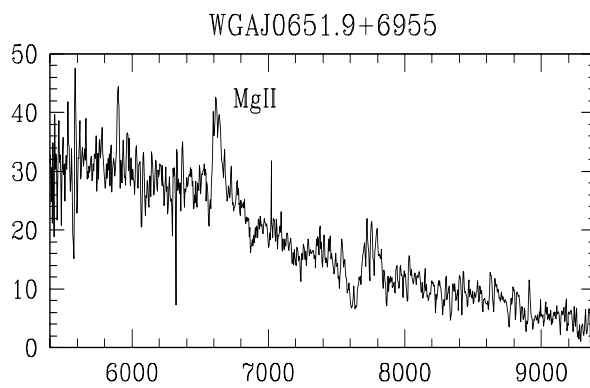
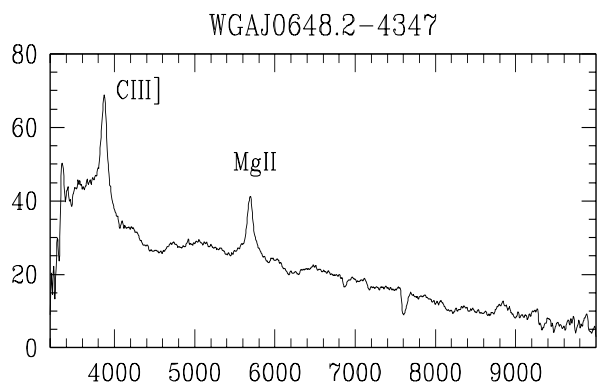
WGAJ0447.9-0322

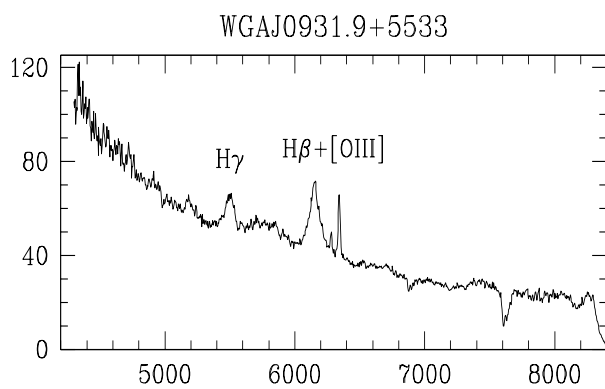
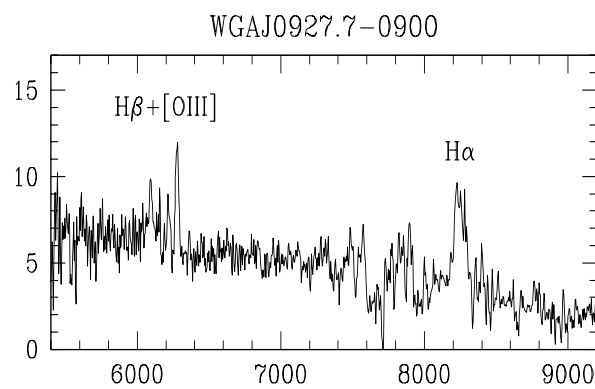
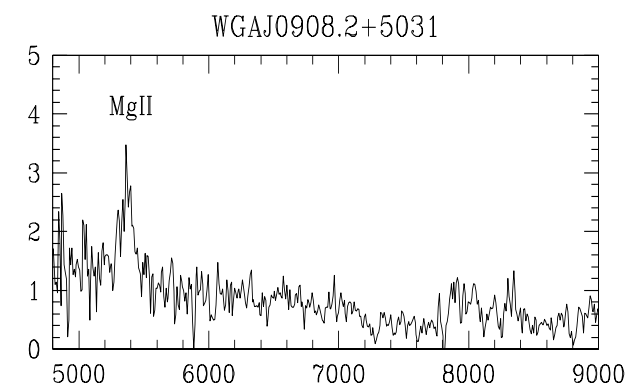
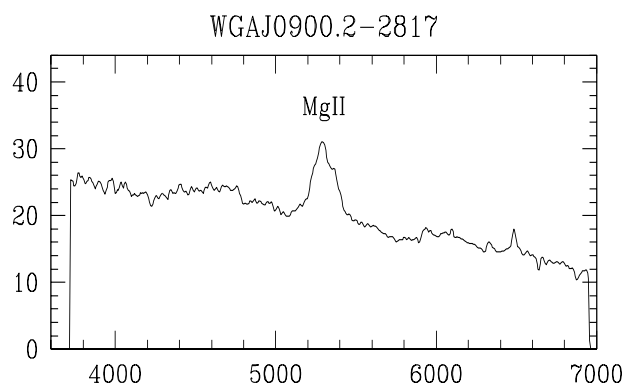
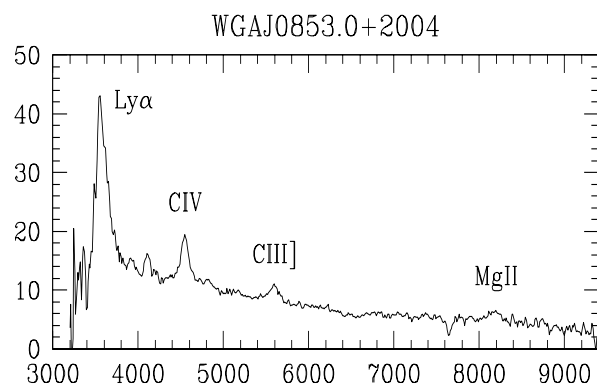
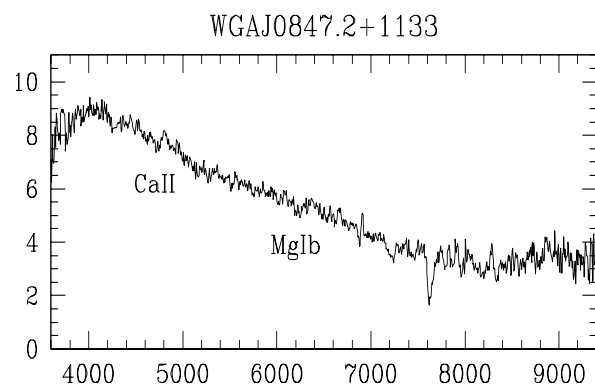
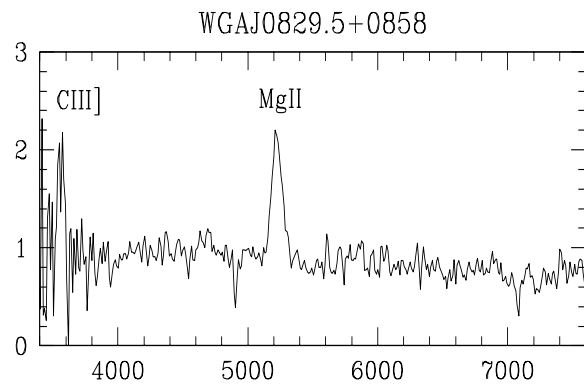
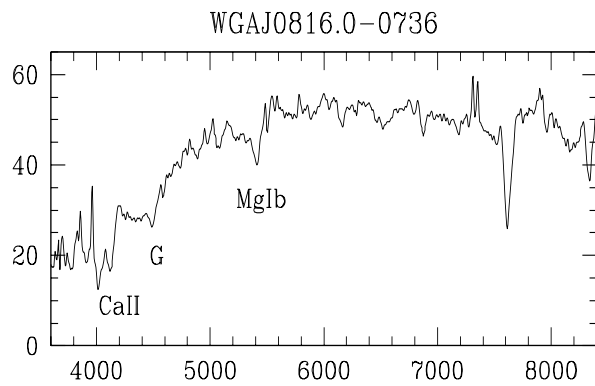




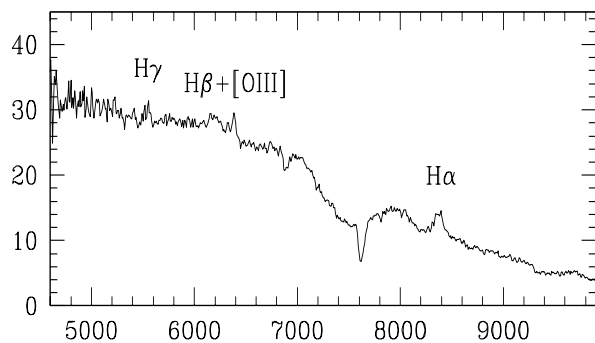




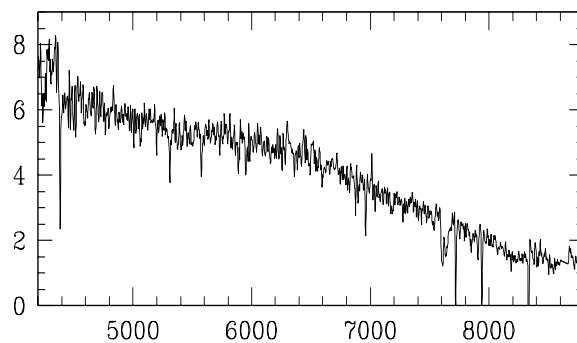




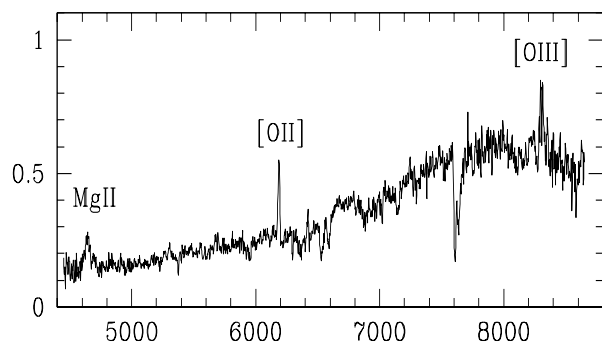
WGAJ0937.1+5008



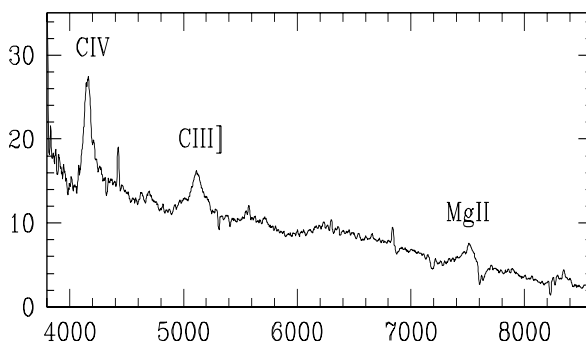
WGAJ0940.2+2603



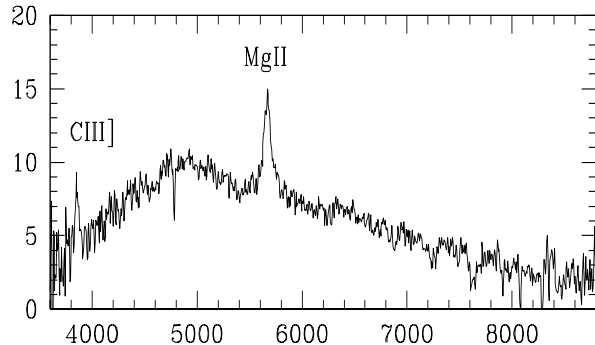
WGAJ0954.4-0503



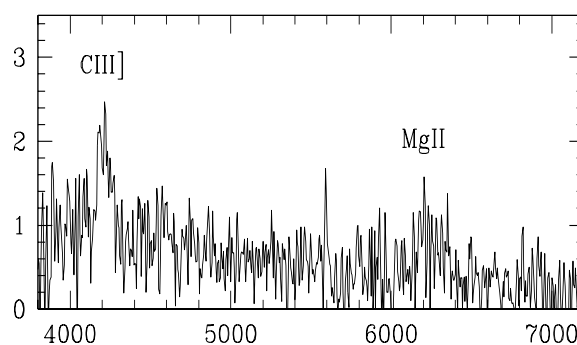
WGAJ1003.9+3244



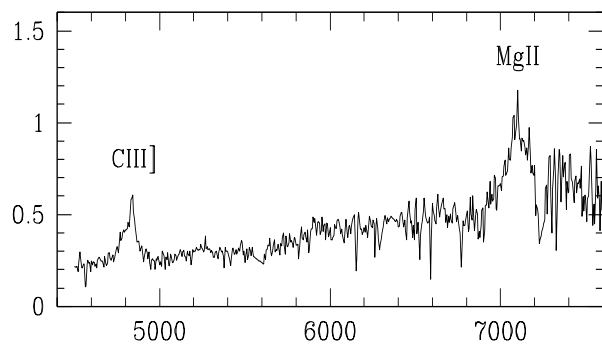
WGAJ1006.1+3236



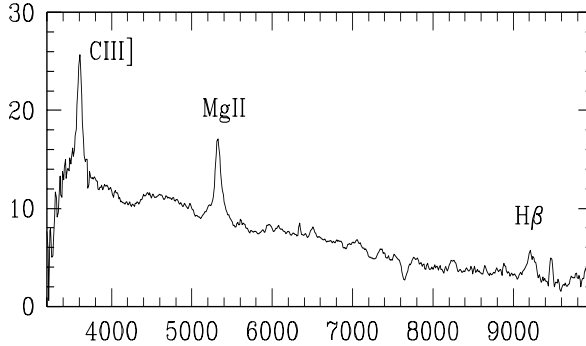
WGAJ1006.5+0509

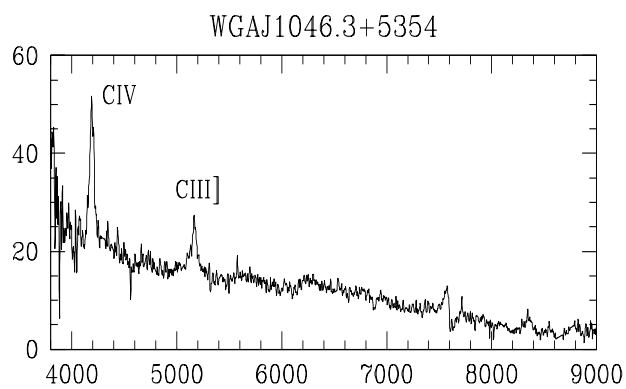
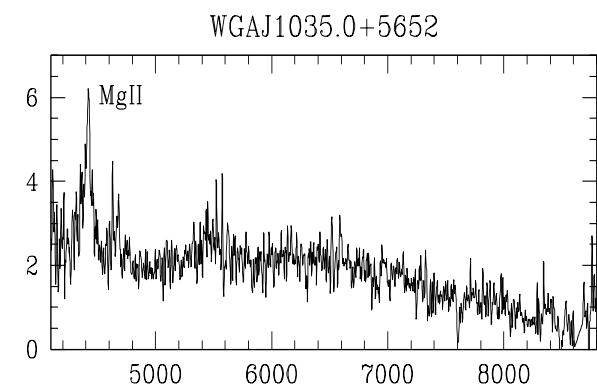
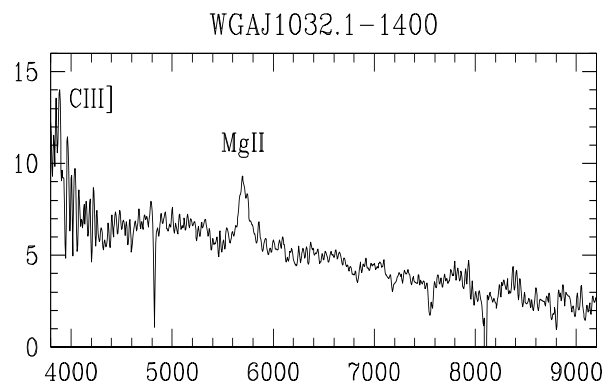
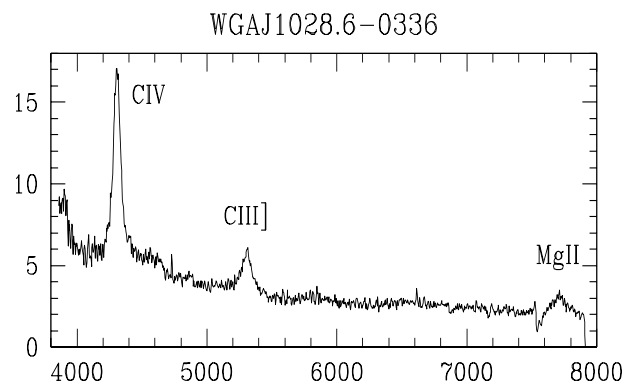
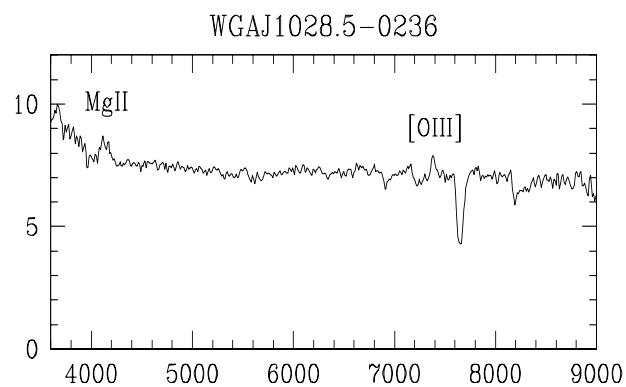
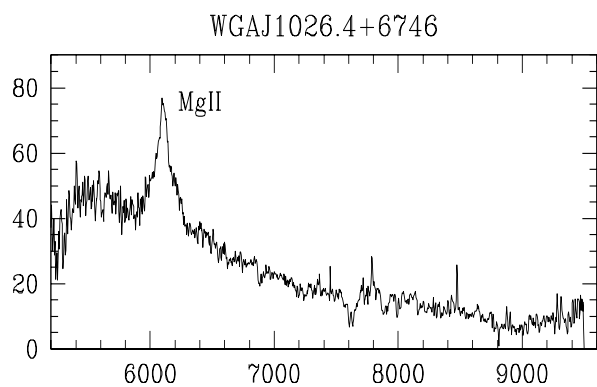
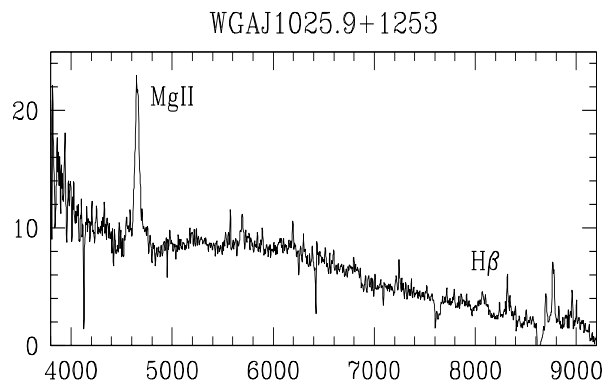
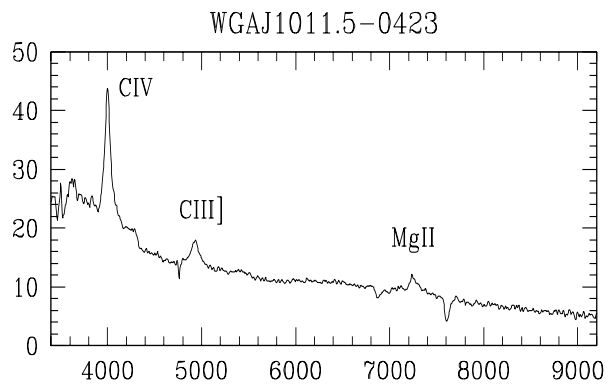


WGAJ1006.7-2014

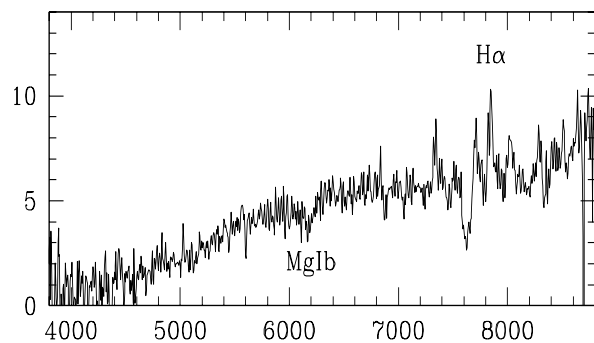


WGAJ1010.8-0201

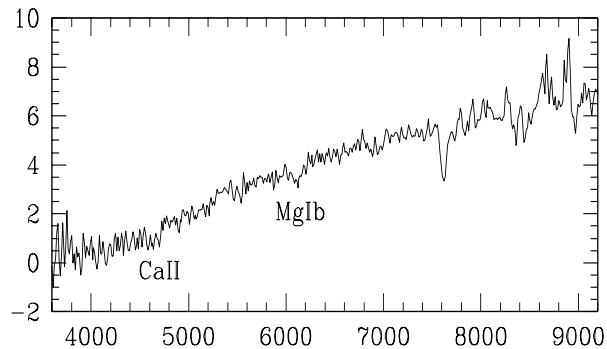




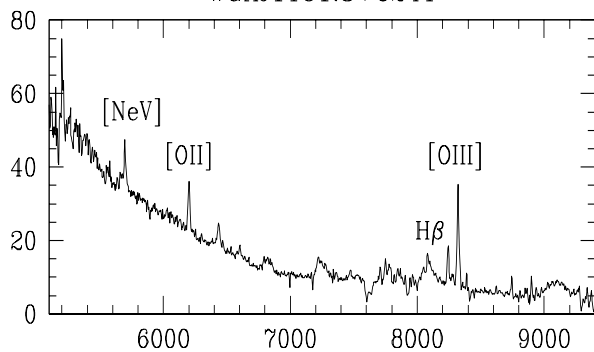
WGAJ1056.9-7649



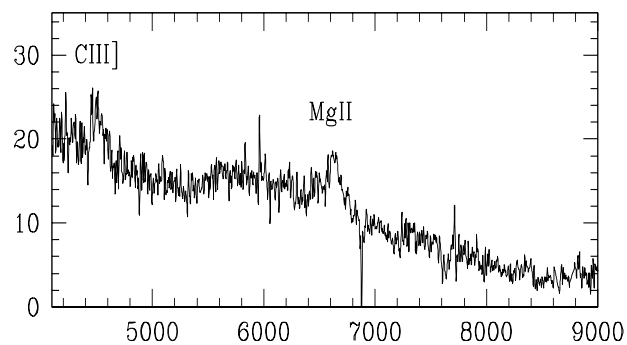
WGAJ1057.6-7724



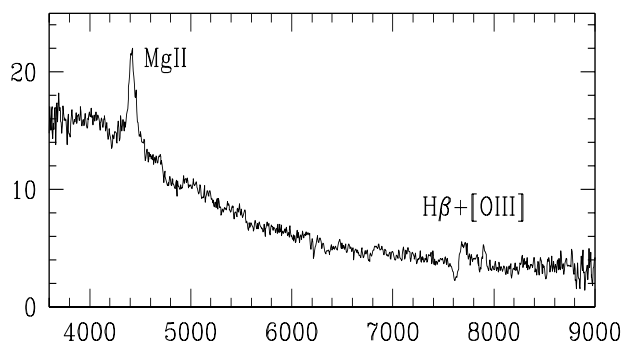
WGAJ1101.8+6241



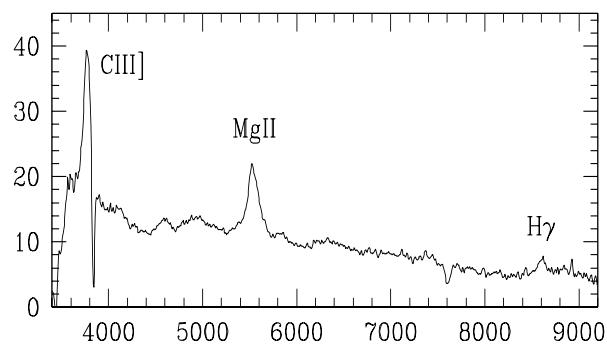
WGAJ1104.8+6038



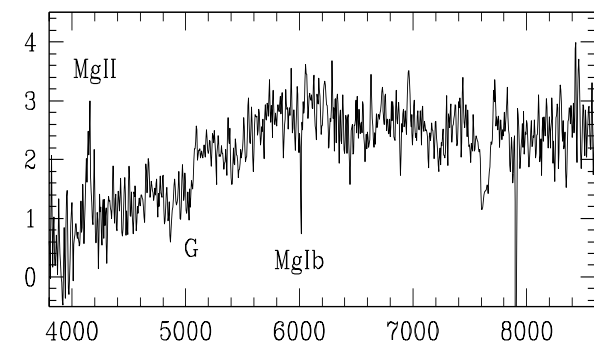
WGAJ1105.3-1813



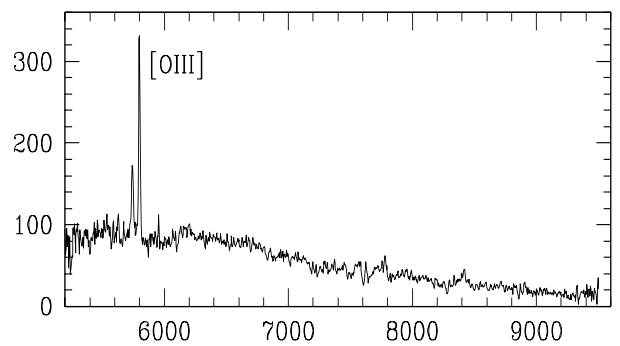
WGAJ1112.5-3745

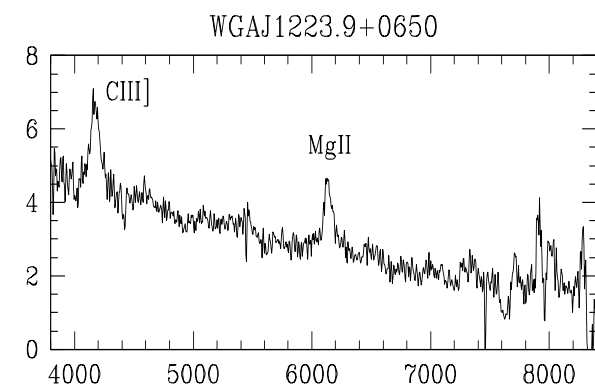
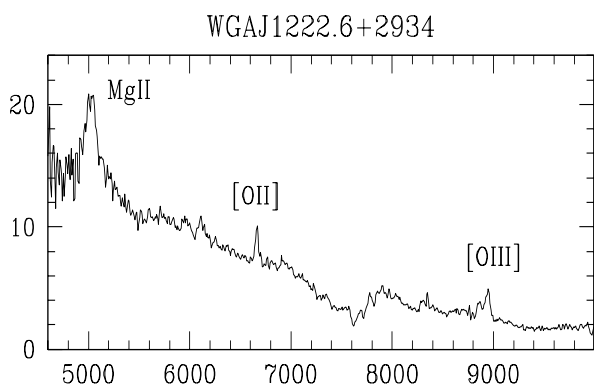
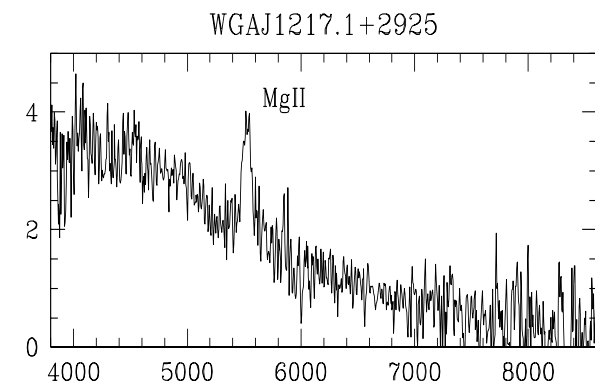
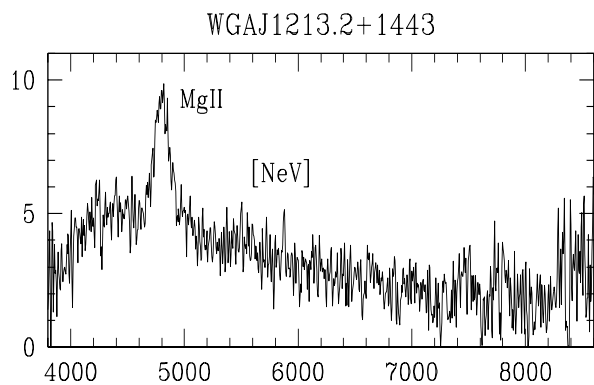
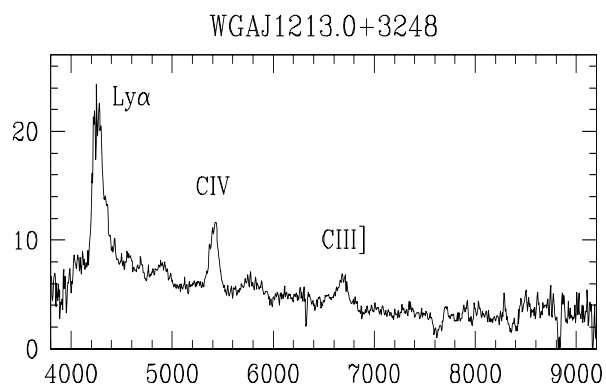
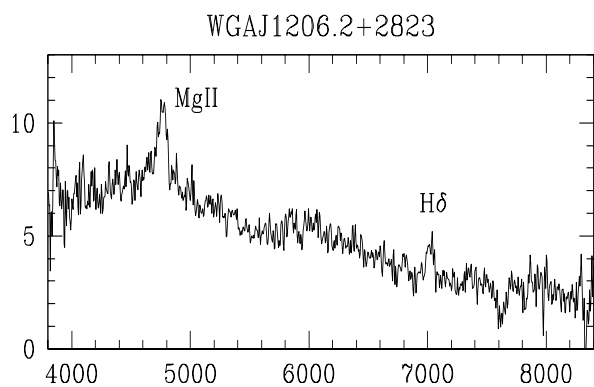
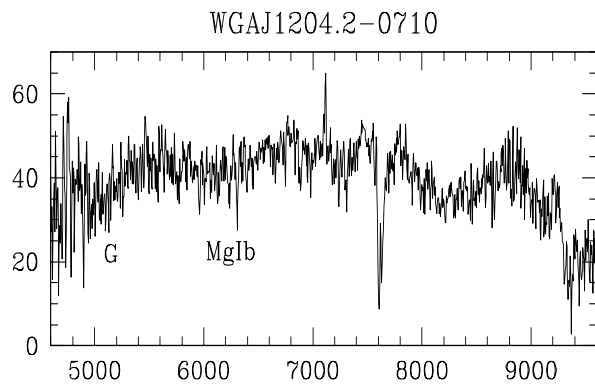
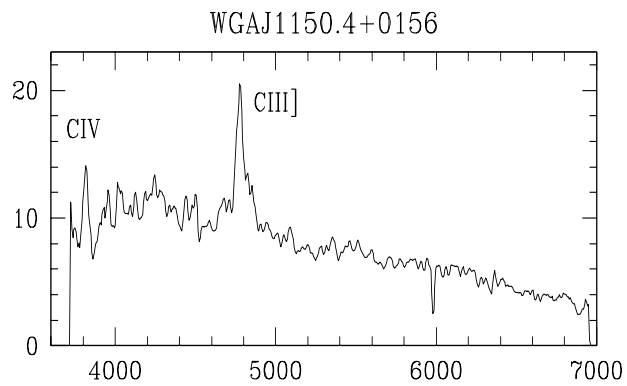


WGAJ1116.1+0828

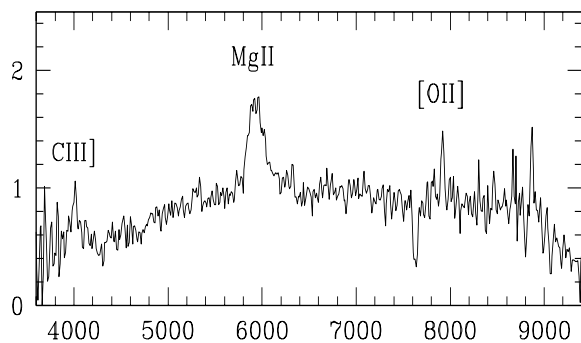


WGAJ1120.4+5855

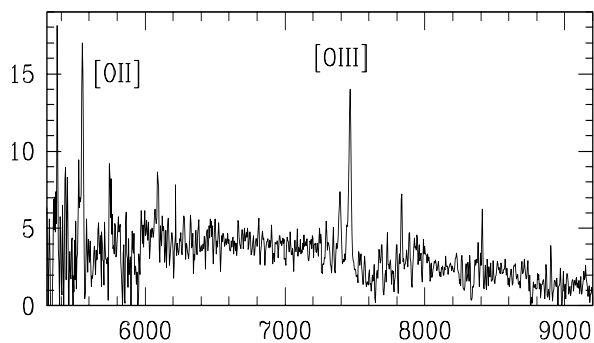




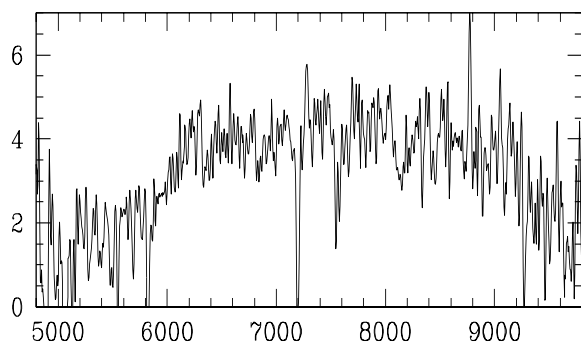
WGAJ1225.5+0715



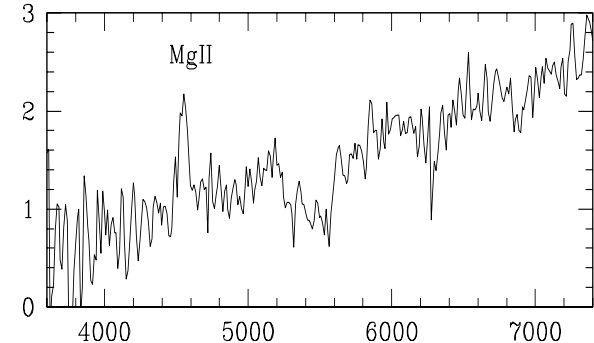
WGAJ1229.4+2711



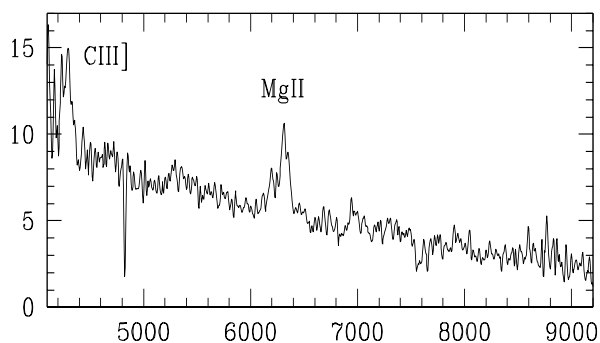
WGAJ1231.7+2848



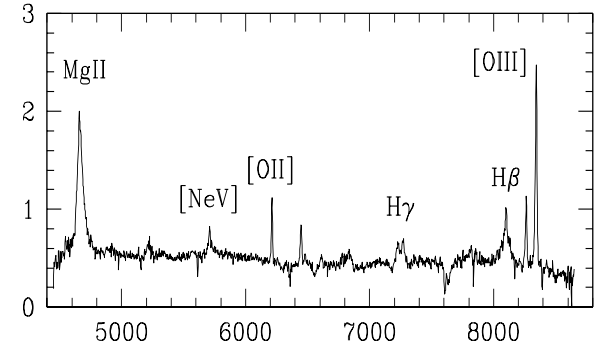
WGAJ1259.9+1206



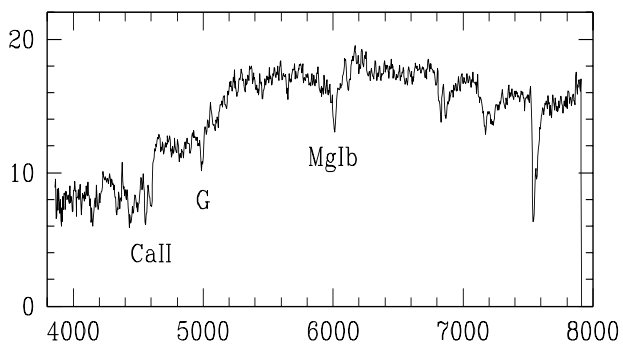
WGAJ1300.7-3253



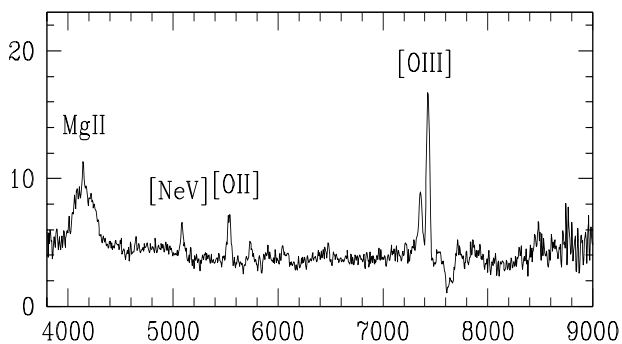
WGAJ1306.6-2428



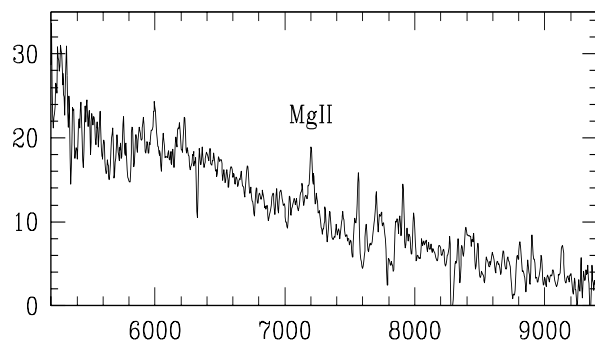
WGAJ1311.3-0521



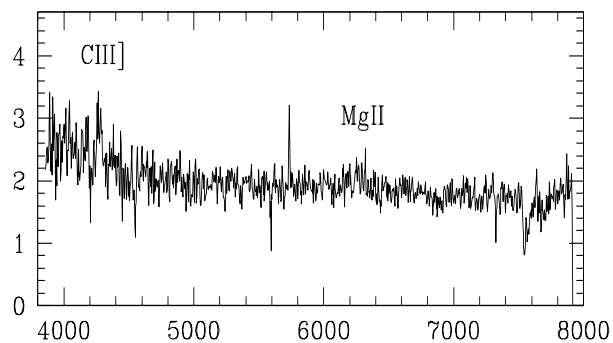
WGAJ1314.0-3304



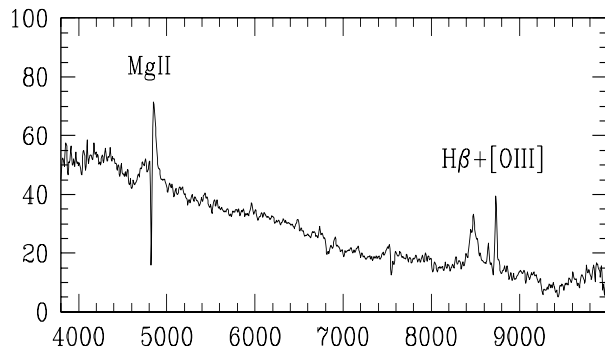
WGAJ1315.1+2841



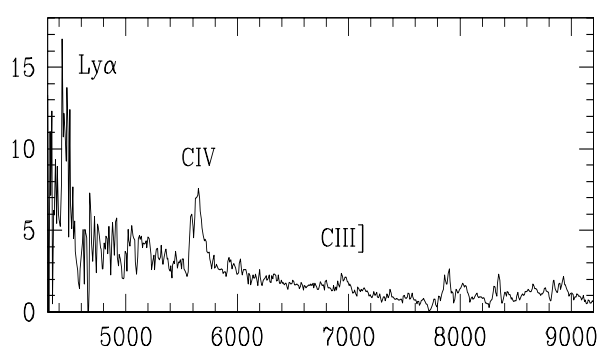
WGAJ1320.4+0140



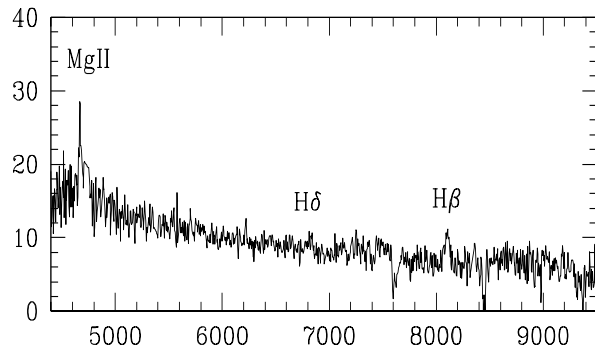
WGAJ1324.0-3623



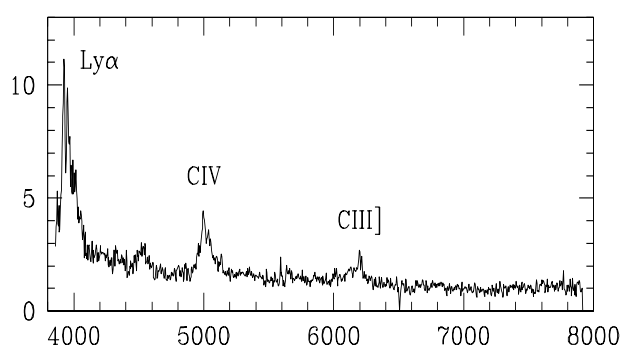
WGAJ1329.0+5009



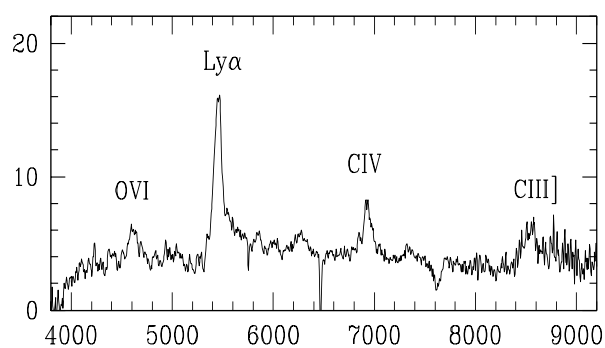
WGAJ1332.7+4722



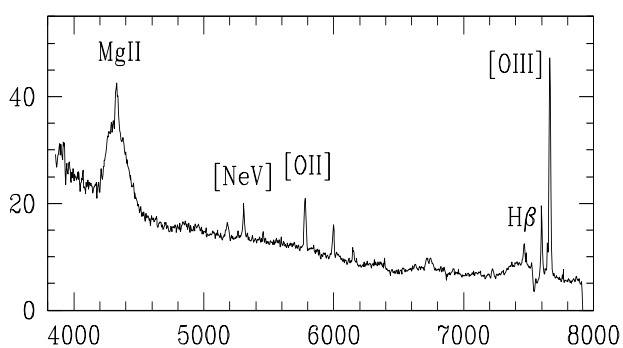
WGAJ1333.1-3323



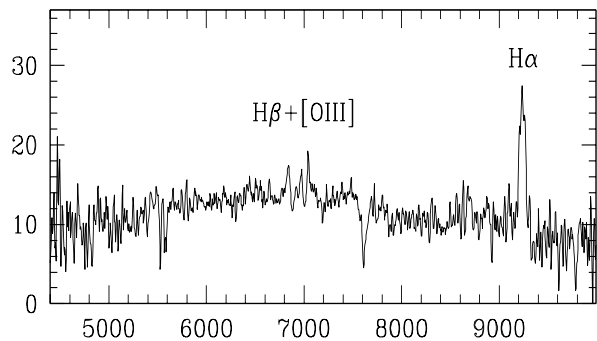
WGAJ1337.2-1319



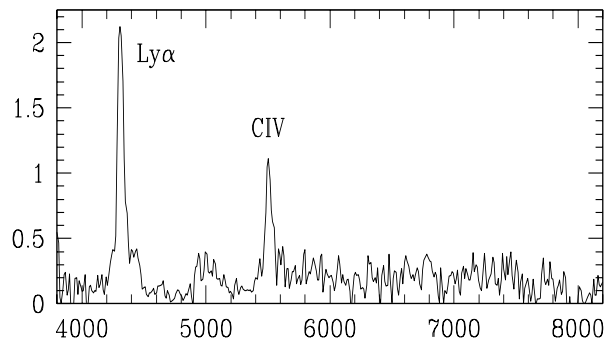
WGAJ1353.2-4720



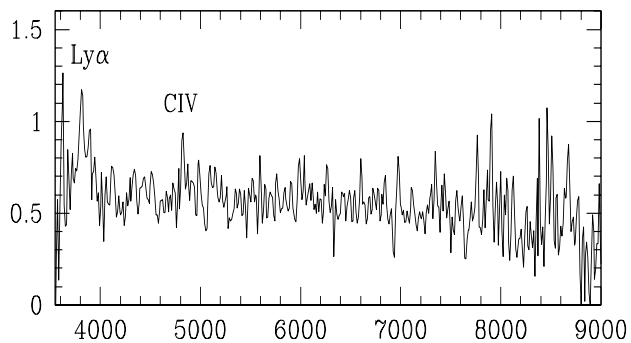
WGAJ1359.6+4010



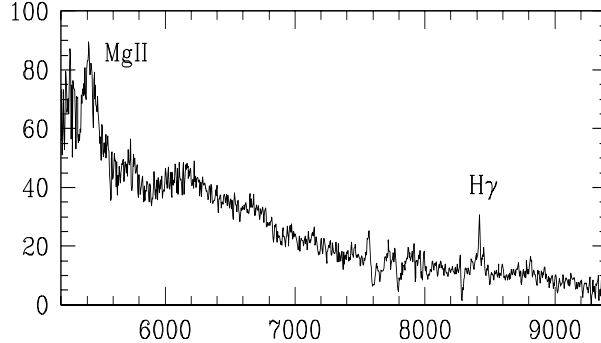
WGAJ1400.7+0425



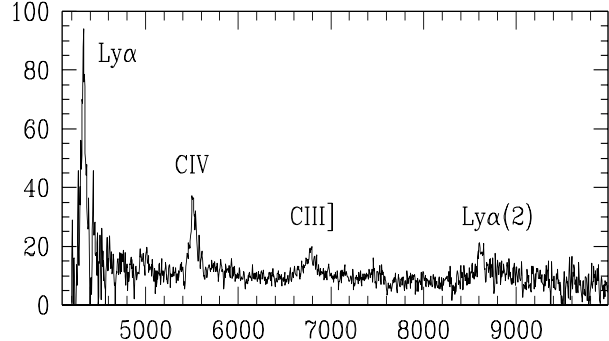
WGAJ1402.7-3334



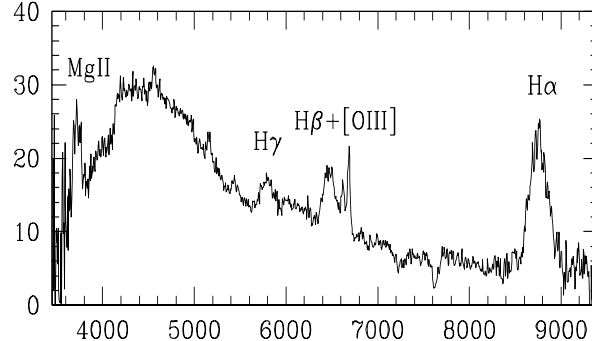
WGAJ1404.2+3413



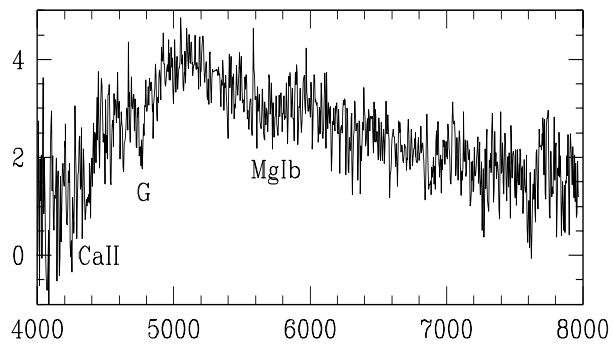
WGAJ1406.9+3433



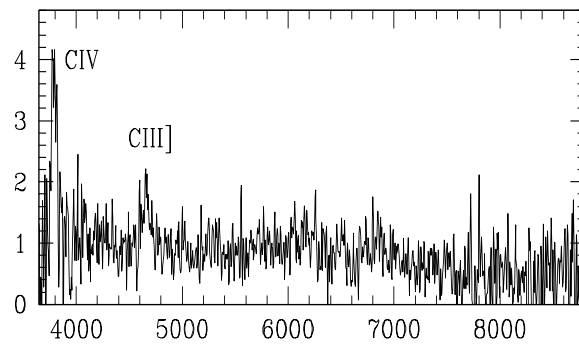
WGAJ1416.4+1242

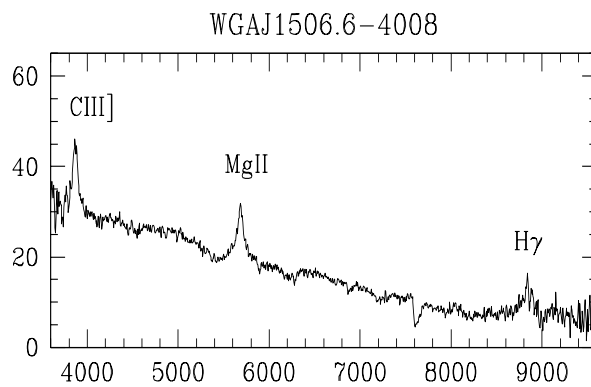
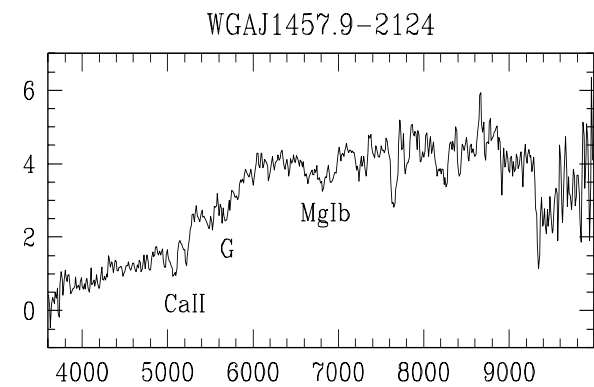
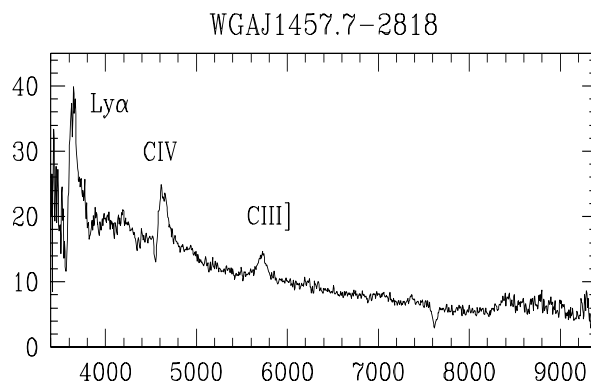
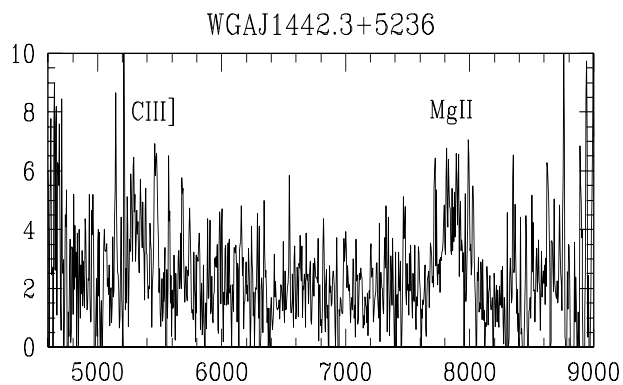
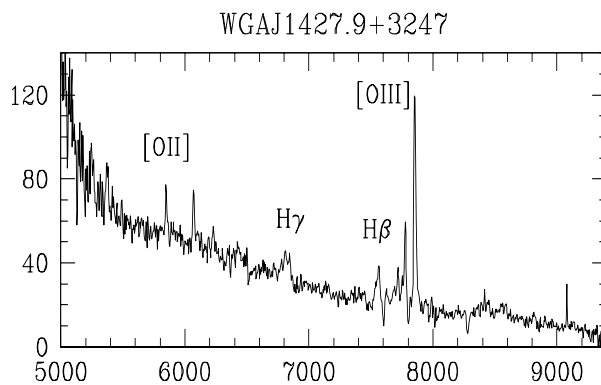
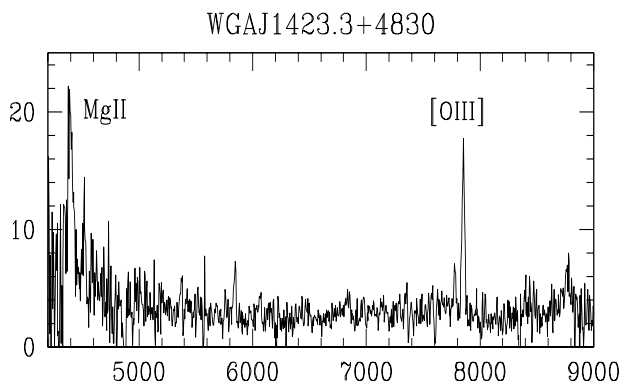
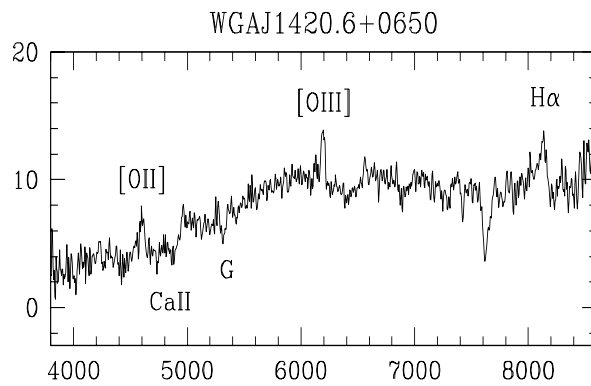
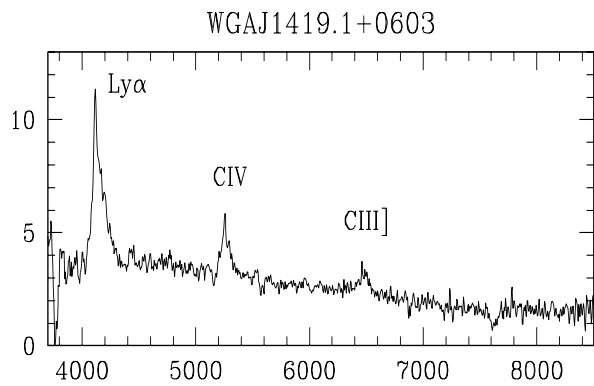


WGAJ1417.2+0608

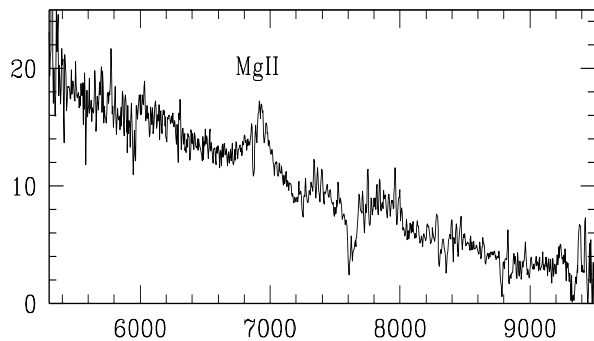


WGAJ1417.5+2645

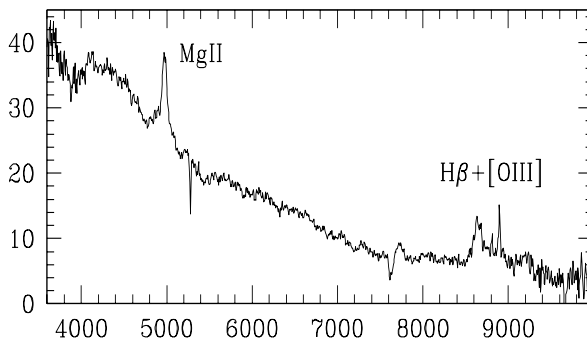




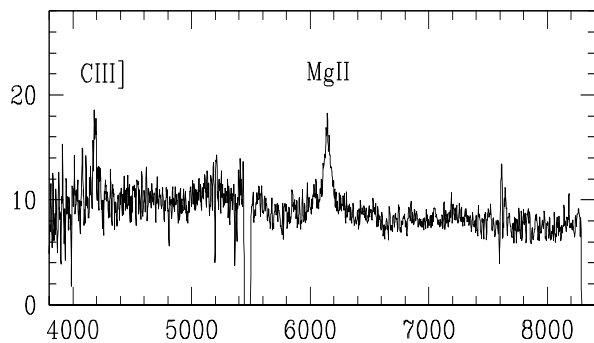
WGAJ1507.9+6214



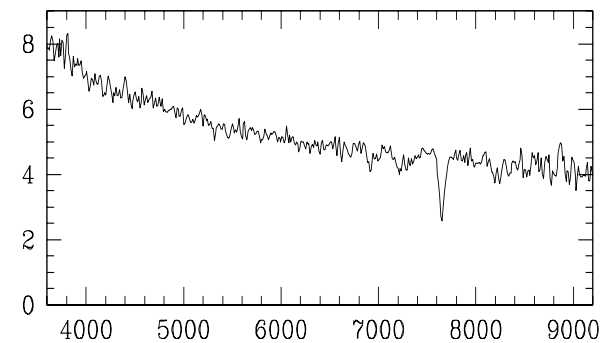
WGAJ1509.5-4340



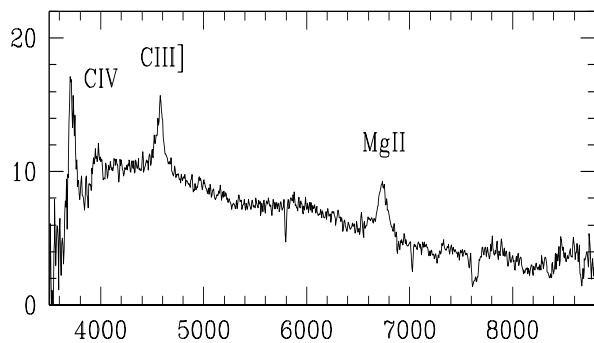
WGAJ1525.3+4201



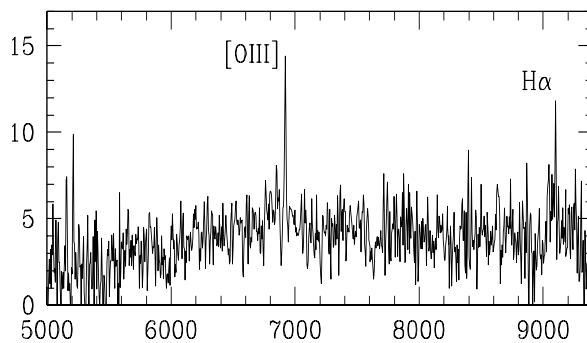
WGAJ1539.1-0658



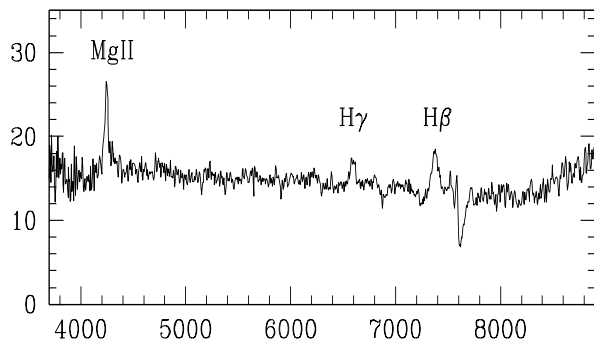
WGAJ1543.6+1847



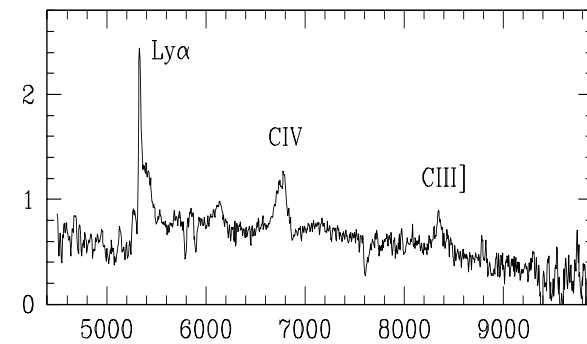
WGAJ1606.0+2031

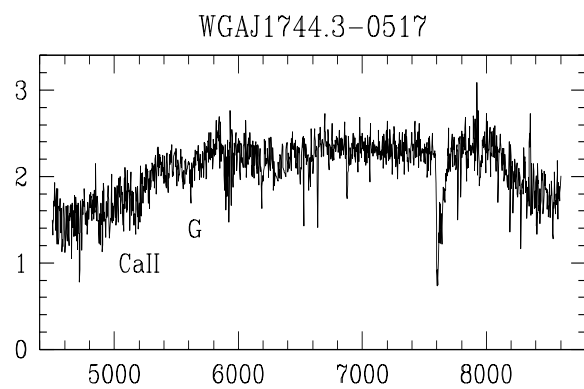
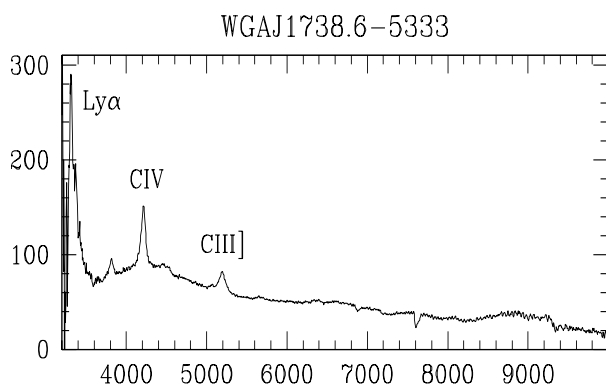
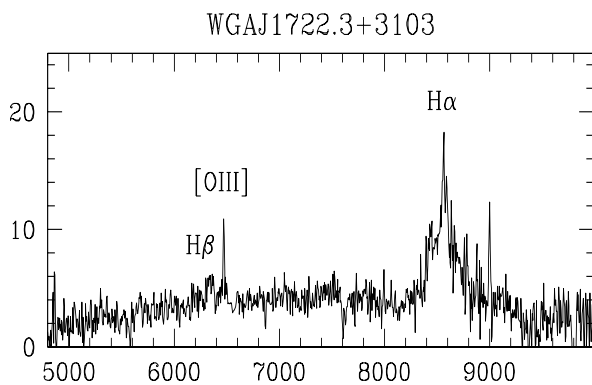
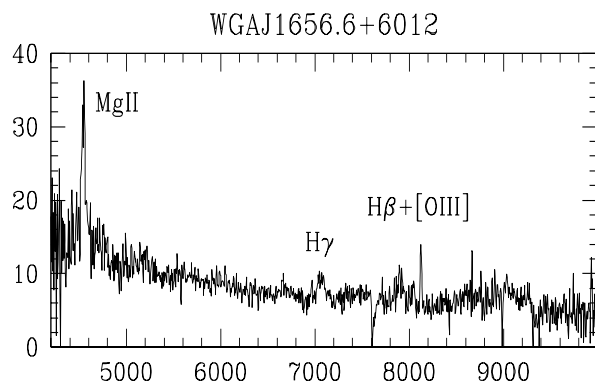
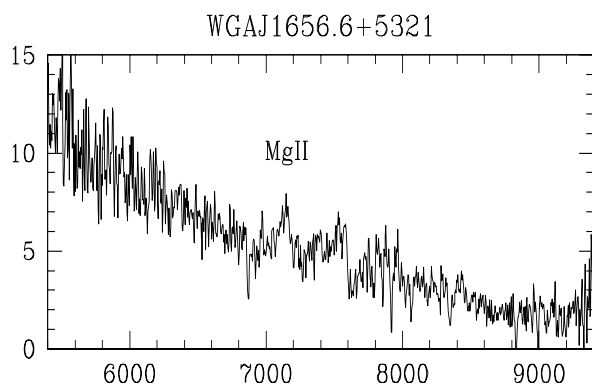
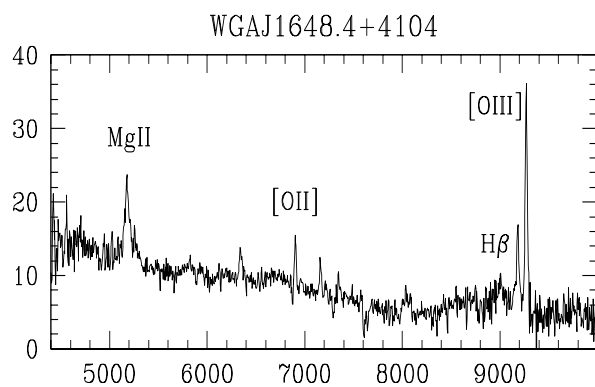
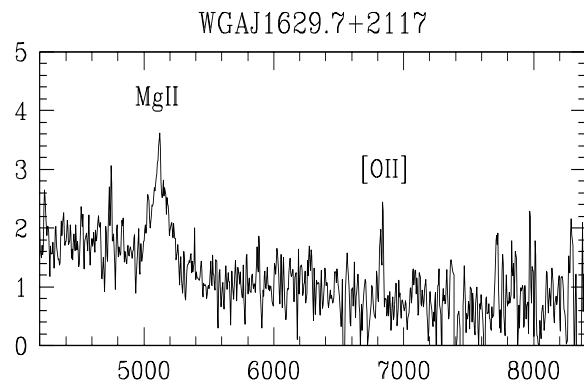
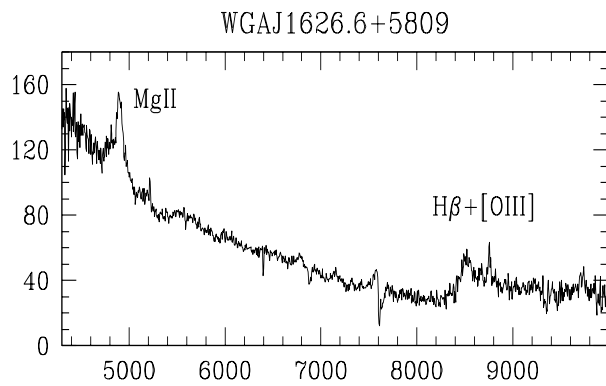


WGAJ1610.3-3958

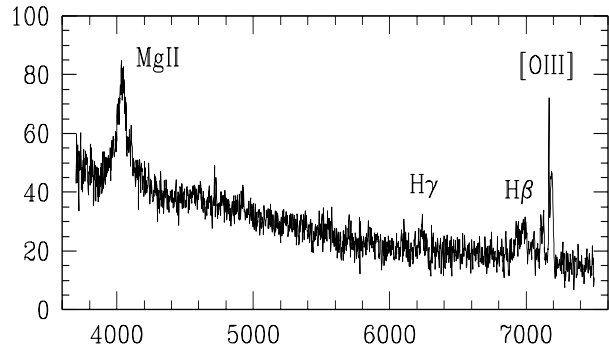


WGAJ1615.2-0540

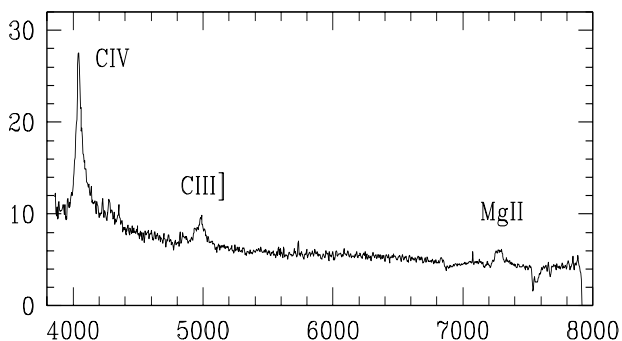




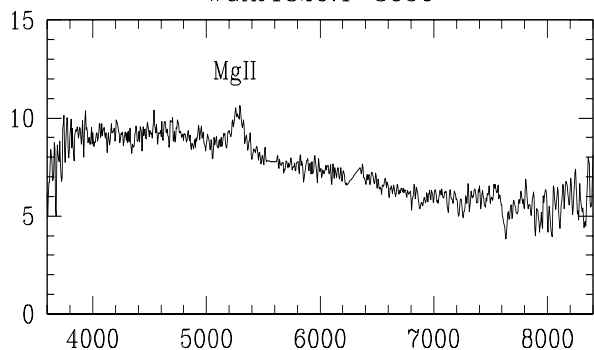
WGAJ1804.7+1755



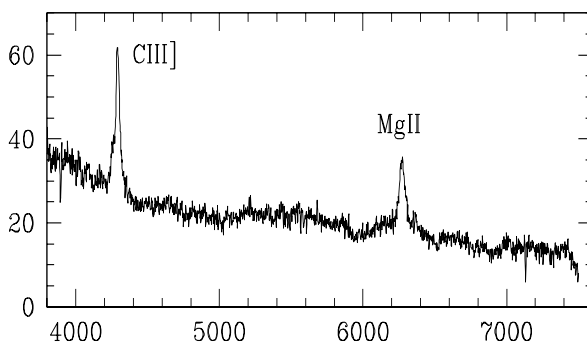
WGAJ1808.2-5011



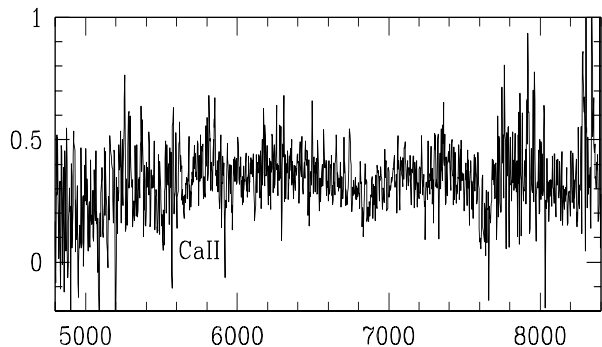
WGAJ1826.1-3650



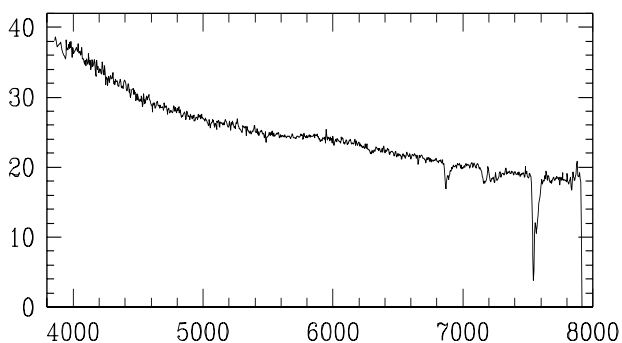
WGAJ1827.1-4533



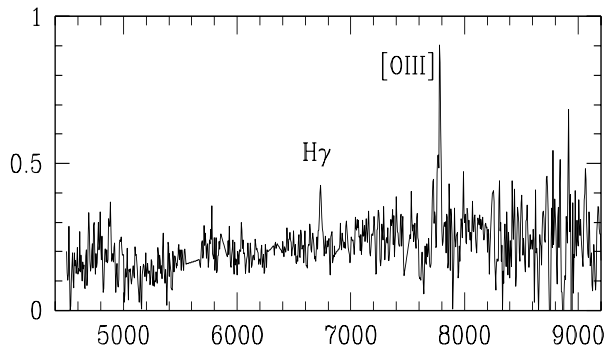
WGAJ1834.2-5948



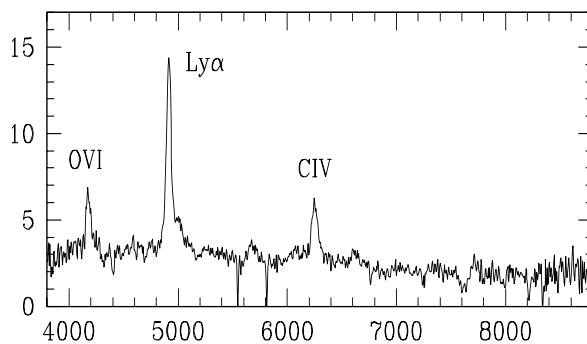
WGAJ1834.4-5856

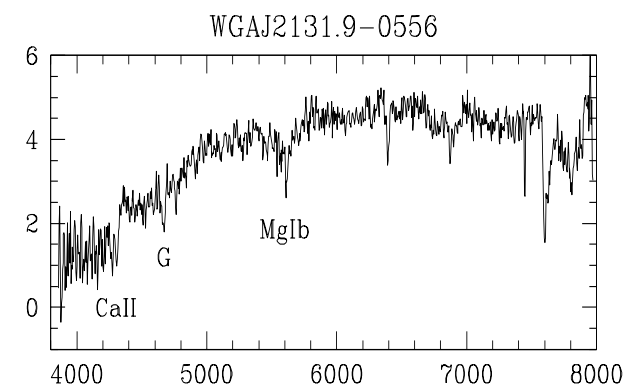
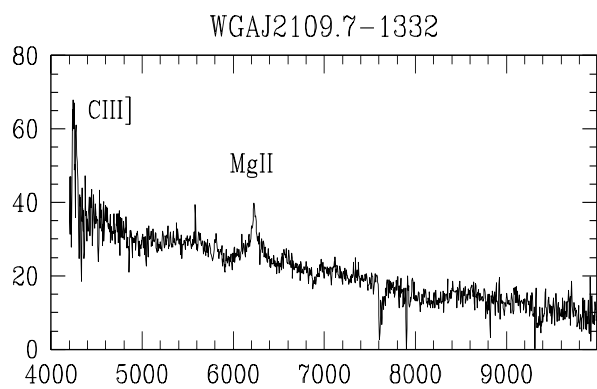
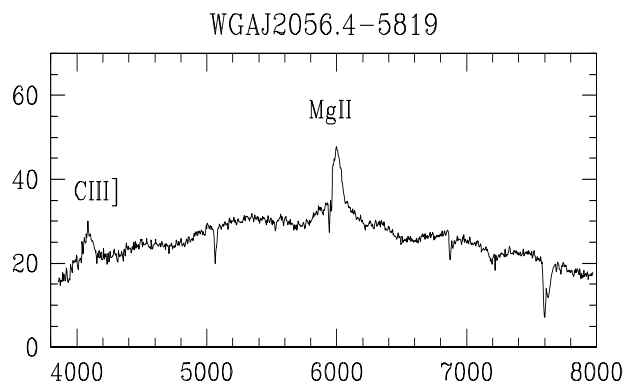
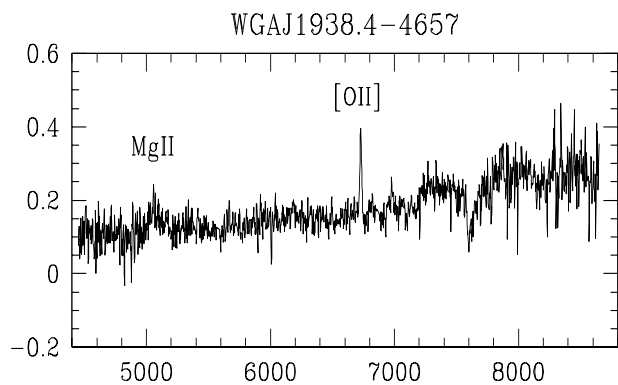
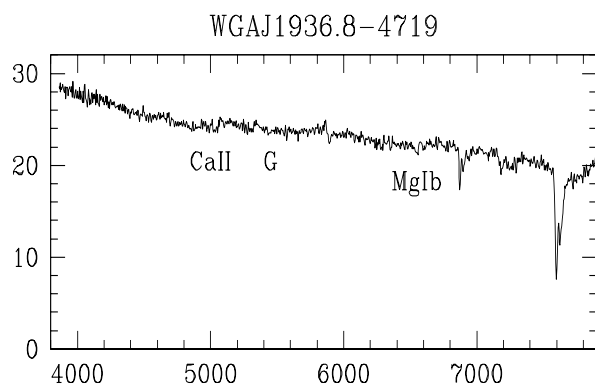
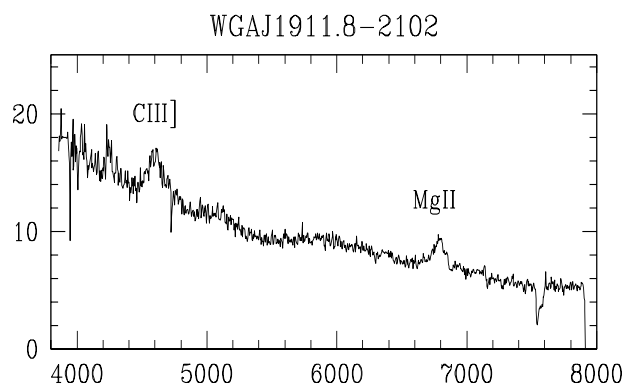
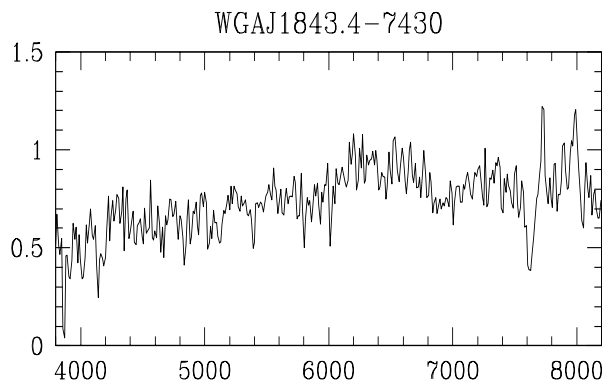
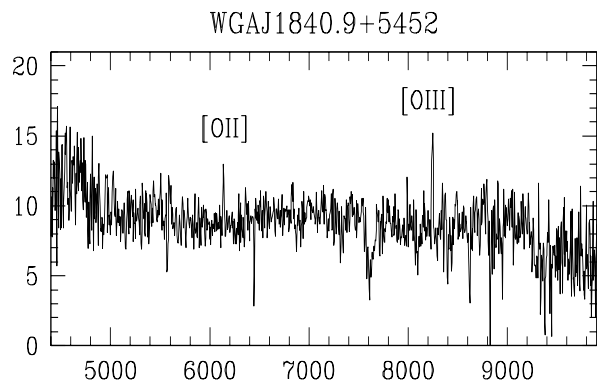


WGAJ1835.5-6539

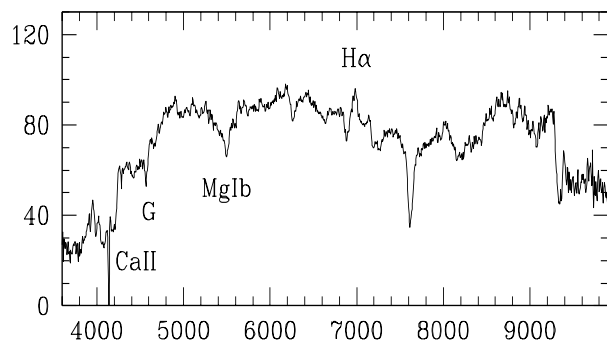


WGAJ1837.7-5848

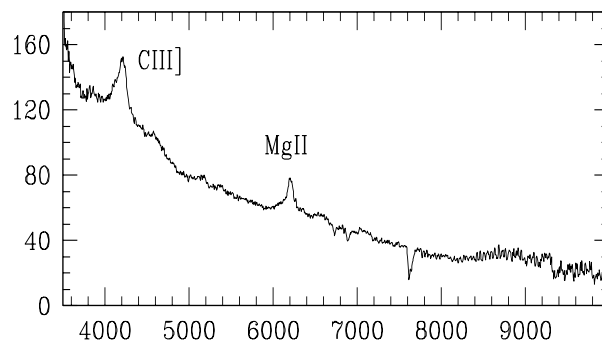




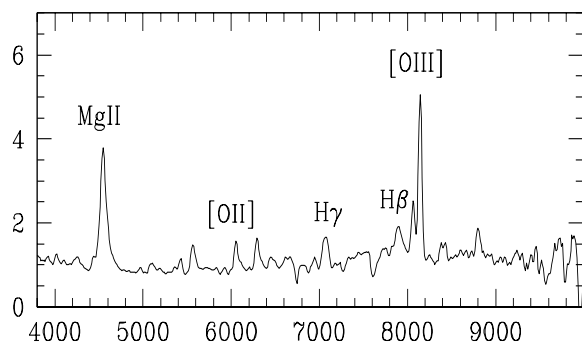
WGAJ2151.3-4233



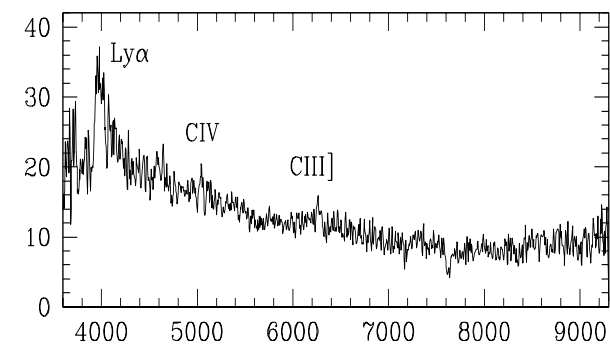
WGAJ2154.1-1501



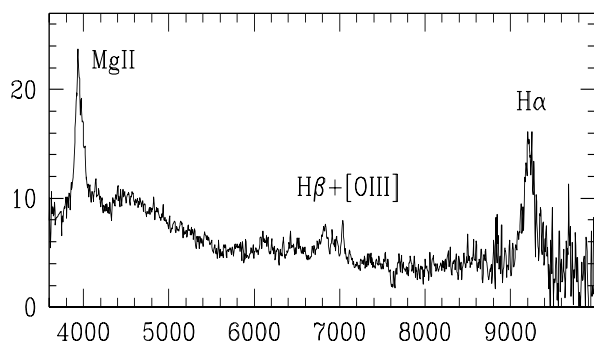
WGAJ2157.7+0650



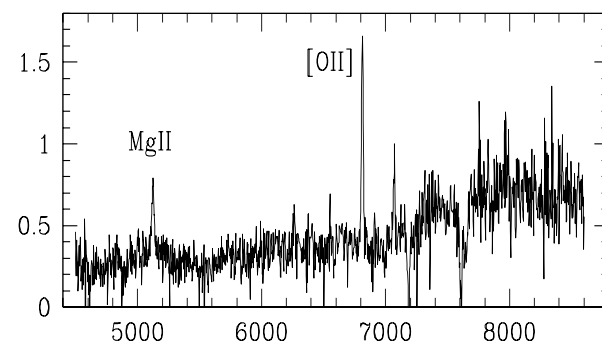
WGAJ2159.3-1500



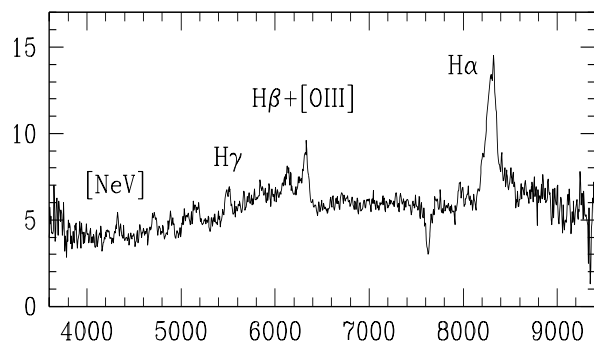
WGAJ2201.6-5646



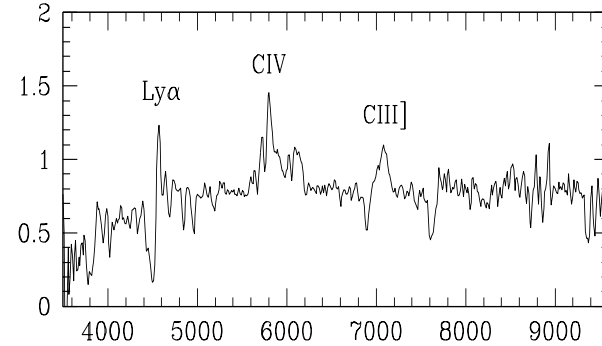
WGAJ2205.2-0004

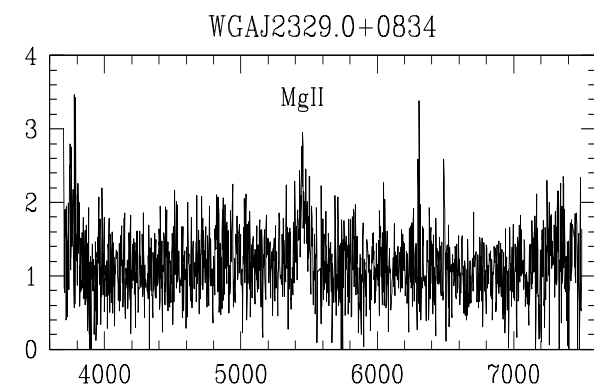
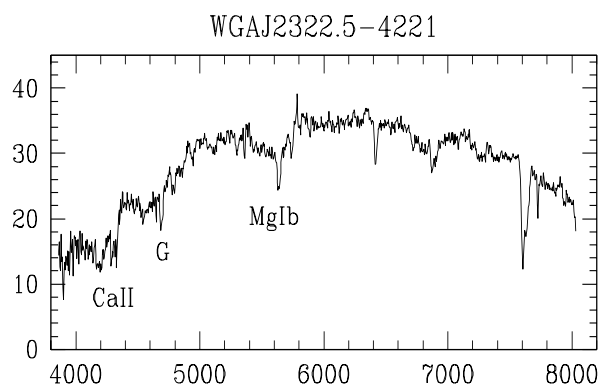
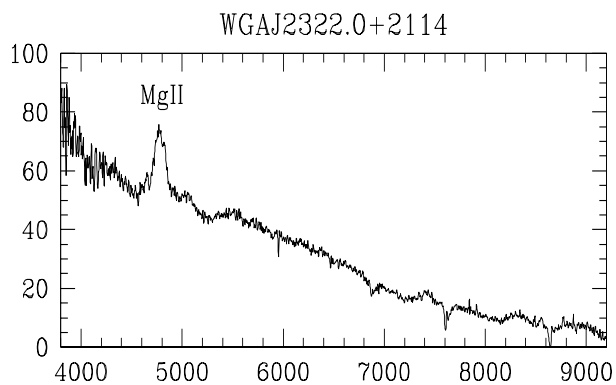
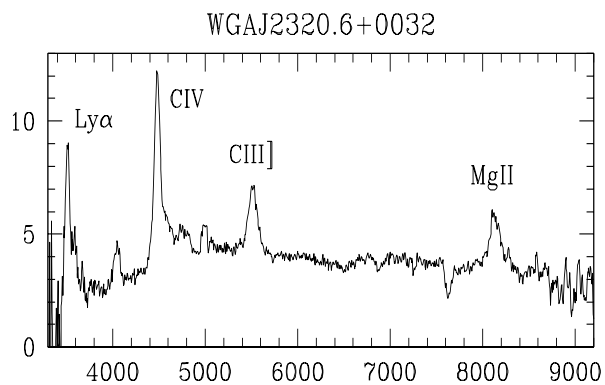
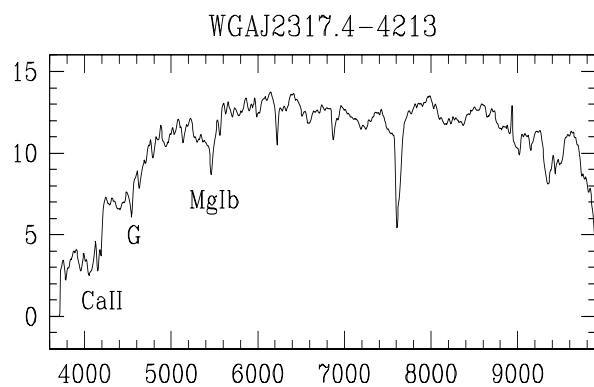
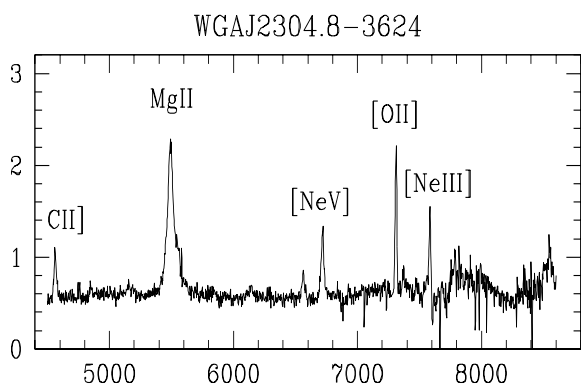
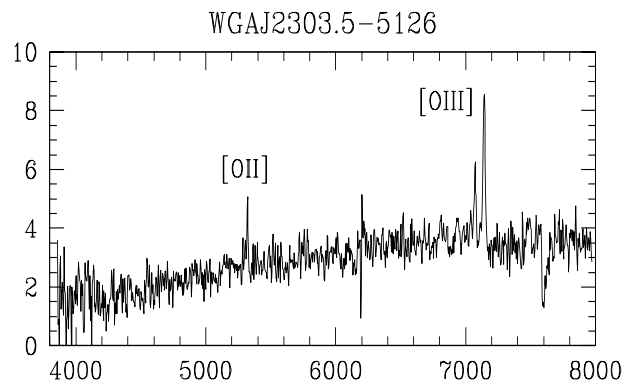
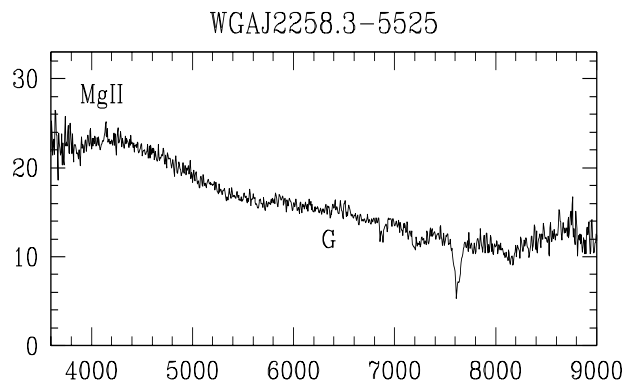


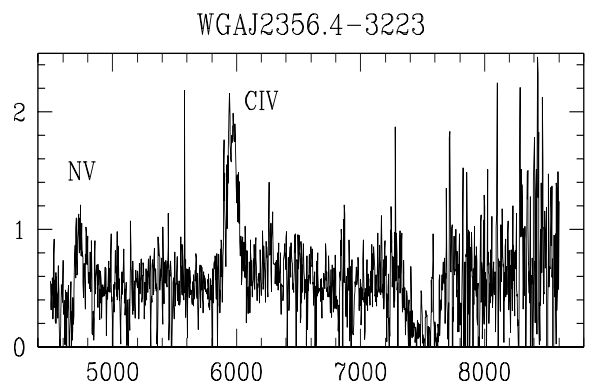
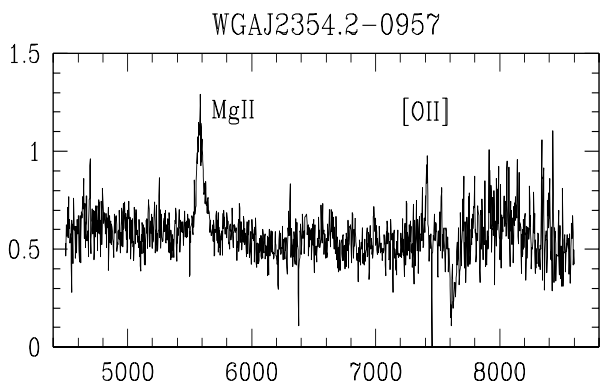
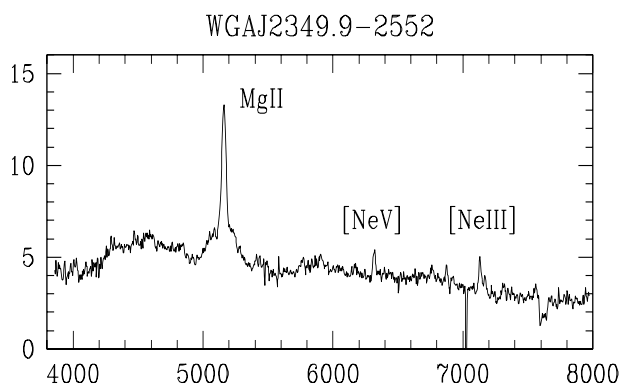
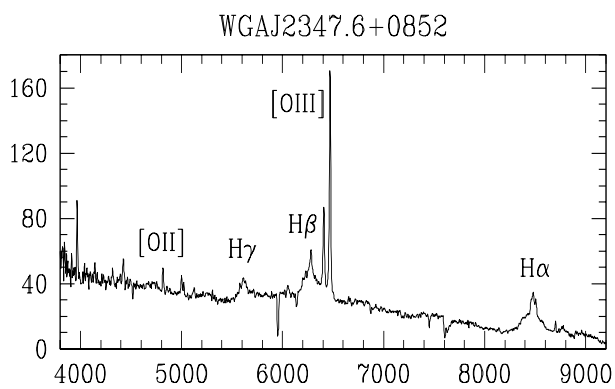
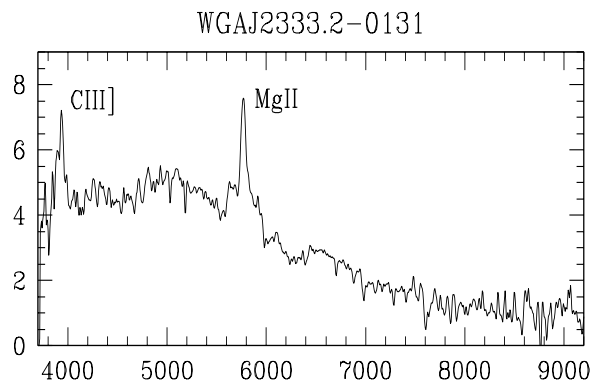
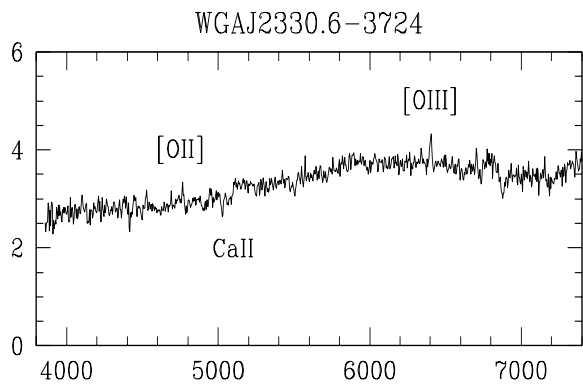
WGAJ2239.7-0631



WGAJ2248.6-2702







Acknowledgements

I approached this PhD thesis with an inexhaustible enthusiasm and I would like to thank my supervisor Paolo Padovani from all my heart for preserving this feeling in me till the very last moment of this (unexpectedly) difficult enterprise. I also hope to never forget at any moment of my future scientific career that any success I owe to his effort to teach me his knowledge to the largest possible extent and in the best way he could. For giving me unconditional love and support whenever I was about to lose the ground under my feet in the struggle of growing-up I would like to thank my mother. She fully understood always and everything.

My gratitude goes out to Eric Perlman for teaching me the tools of an observer and to him and Paolo Giommi for numerous scientific discussions which I not only enjoyed at any time, but which allowed me to gain a complete (and most up-to-date) picture of blazars. Of my old friends left behind in Germany and new friends found in Baltimore, who eased my life during the four years of my PhD thesis, I can only name a few: Andre (I thank for letting me go when he needed me most), Biggi, Andrea and Havana (my oldest friends I have and hopefully will have), Jayadev (his advice ‘The PhD thesis is just a driver’s license. You will drive later.’ and of course all the fun and good Indian meals we had together will remain unforgettable), Luigi (who joined me in my experience of the first cultural shock), Sissy, Chelsea, Glen and David (my American friends I found most common ground with), Ravi, Jason and Jim (I thank for the endless fun we had together especially in the final and most strenuous period of my thesis), Nicole (I thank for her selfless help without which I could not have finished this thesis in such a pleasant way), and of course I will never forget my officemates at the ‘Tute’: Gijs, Tomasso, and Cristiano (the first epoch), Claudia, Chris, Valerio, Björn and Alvaro (the second epoch).

Finally, I am more than thankful for the opportunity to conduct my PhD research in the wonderful scientific atmosphere of the Space Telescope Science Institute in Baltimore, USA. For the hospitality during the last months of my thesis and for the official supervision of this work I would like to thank the Hamburg Observatory, in particular Prof. Dieter Reimers and Dieter Engels. This PhD thesis received financial support from the STScI DDRF grants D0001.82236, D0001.82260 and D0001.82299, and from Deutscher Akademischer Austauschdienst (DAAD).